Liquid Phase Catalytic Hydrogenation of Carbon Dioxide

Thesis submitted in accordance with the requirement of Cardiff University for the degree of Doctor of Philosophy

Claire E. Mitchell

School of Chemistry

Cardiff University

2016-2020

Abstract

Concerns of global warming and climate change have dominantly been the consequence of rising anthropogenic carbon dioxide (CO_2) atmospheric concentration. One method of reducing CO_2 emissions is unlocking the potential of CO_2 as a chemical C-1 feedstock, converting this current waste compound into high value chemicals and fuels. The research presented in this thesis addresses the utilisation of CO_2 using catalysis to form formate.

This work can be divided into three catalytic materials, hence, 3 results chapters. First, a series of Pd/Mo_2C catalysts were synthesised, optimised and evaluated for CO_2 hydrogenation, achieving TON of 109. The role of base and the pH of the reaction medium is importantly identified, having an impact on the intermediates essential for the reaction process. A key message conveyed is the crucial role of adding Ru to Pd in enhancing catalytic stability.

The two next chapters of research were inspired by the origin of life theory. First investigated is the iron sulphide pyrrhotite, ($Fe_{1-x}S$), and its ability as a catalyst towards the hydrogenation of CO_2. Controlled oxidation of the material was found to increase the surface oxygen content, creating new oxygen containing Fe and S species, having a positive effect on the catalytic activity increasing formate productivity from 0.3 µmol to 1.0 µmol. The material was characterised, and catalyst preparation optimised for catalytic activity. In the next chapter, iron nickel sulphide was then investigated under the same study. Violarite $(Fe,Ni)_3S_4$ was synthesised, characterised, and the synthesis procedure was optimised. Again, calcination is required for the optimal catalytic activity, creating vital oxygen containing species. Violarite achieved a superior catalytic performance than pyrrhotite, producing 4.9 µmol of formate.

Overall, this work was intended to investigate novel materials for the catalytic hydrogenation of CO_2. Catalyst characterisation has been crucial for understanding the catalytic properties of such materials, and this work hopes to convey their importance within this globally significant reaction process.

Acknowledgements

Firstly, I would like to thank my supervisor Dr Sankar Meenakshisundaram, for his guidance and support. His patience, cheerful anecdotes and confidence in me, allowed me to grow as a researcher and tackle a tricky project from its infancy into a piece of work I am quite proud of.

My second supervisor Prof. Nora H. de Leeuw, who gave the opportunity to work on such an interesting PhD project. Her passion and infectious energy that she drove into the project did not go unnoticed and certainly helped maintain the motivation within my work.

Without both my supervisors, I would never of had the opportunities to work in China and South Africa. Experiences I will never forget.

I would like to thank Susana and Maha, with me from the very beginning of my PhD, who's tenacity and enthusiasm are quite inspirational, I wish them both the very best for the future.

I have to thank the CCI team, my PhD wouldn't have been so enjoyable without such an amazing bunch of people (far too many to list!), with special thanks to all the postdocs, staff of the CCI and Rhodri, my first student although I learnt a lot more from him than he did from me.

Special thanks to my family, for supporting every decision I make and allowing me the freedom to make those decisions. To Carlos, a breath of fresh air and fuelling my adventure for life beyond the thesis. And finally, to my Cardiff friends, 6 and a half years of laughter and amazing memories, thank you!

Table of Contents

1 Introduction

This chapter involves an introduction to the work presented in this thesis; CO_2 hydrogenation. The discussion will begin with the CO_2 crisis, rising CO_2 emissions, its contribution to climate change. Current industrial tactics to control this problem will be discussed, including control of CO_2 emissions, and CO_2 capture and storage methodologies. The focus will then move onto the significance of converting CO_2 into higher value compounds, focusing on formic acid in particular. Analysing the pioneering research reported within CO_2 hydrogenation towards formic acid, providing insight into the catalytic system chosen for this PhD project. The inspiration of this research, a theory based on the 'Origin of Life', a concept involving the conversion of CO_2 and H_2 catalysed by earth abundant minerals will also be introduced and discussed.

1.1 CO_2 emissions and climate change

Climate change is the current rapid warming of the Earth's climate, predominantly caused by anthropogenic pollution. Since the mid-20th century, many unequivocal changes due to global warming have been observed, as the atmosphere and ocean have warmed, snow and ice have diminished, sea levels have risen, and extreme weather events have occurred. In consequence if ignored, climate change poses a huge threat to human civilisation and the ecosystems on this planet. This warming is caused by the emission of certain gases remaining semi-permanently in the atmosphere and preventing heat from escaping, creating a 'greenhouse effect', such gases are effectively termed as greenhouse gases[1]. Carbon dioxide (CO_2) constitutes to 72% of the totally emitted greenhouse gases and seen as the main gas responsible for climate change. Initially, before the industrial era, the increase in atmospheric CO_2 was caused by the release of carbon into the atmosphere from deforestation and other land-use change activities. Since 1950, emissions from combustion of fossil fuels became the dominant source of anthropogenic emissions driven by a robust global economy creating a higher demand for fuels[2]. The growing demand for natural gas and petroleum based feedstock for

power generation, transport and chemicals production has resulted in an unsustainable increase in CO_2 emissions[3,4]. Ten countries, including the United States, China, India, Russia, Japan, Germany, South Korea, Canada, Iran and the United Kingdom constitute the world's major greenhouse gas emitters, accounting for nearly two-thirds of total emissions[4]. Fossil fuels in the form of coal, oil and natural gas comprise 80% of the world's energy utilisation[5]. Coal-fired power generation continues to be the single largest emitter of CO_2, accounting for 30% of all energy-related carbon dioxide emissions, and despite attempts to mitigate emissions, the world saw more than 100% growth in annual CO_2 emissions since 1950. The international environment agency (IEA) reported that global energy-related CO_2 emissions, Figure 1.1, have reached a historic high of 33.1 gigatons (Gt) in the year 2018, a 1.7% increase since 2010 [6], resulting in an annual surface temperature increase of 0.3 ^oC.

Countries that work together on climate change under the umbrella of the United Nations Framework Convention of Climate Change (UNFCCC), an organisation of which created the Paris Agreement. The Paris Agreement in December 2015 marked the restriction of increase in the global average temperature to less than 2 ^oC compared to the pre-industrial level, and to pursue the limiting of global warming to 1.5 ^oC[7]. The Parties also undertook to achieve this goal by reducing net emissions 'to achieve a balance between anthropogenic sources and removals by sinks of greenhouse gases in the second half of this century'. A recent report by UNEP (United Nations Environment Programme), studying present global greenhouse gas emissions, states if no firm global action is taken against climate change, temperatures may increase by 2°C by 2050[8]. In order to prevent this, the European Council confirmed the EU objective of reducing greenhouse gas emissions by 80-95% by 2050 compared to 1990[8]. One way of combating this, the European Union has set a target of reducing its primary energy consumption by 20% by 2020[9]. Investments totalling €270 billion annually are set out to ensure a low carbon future have been taken in China, India and Korea amongst many others.

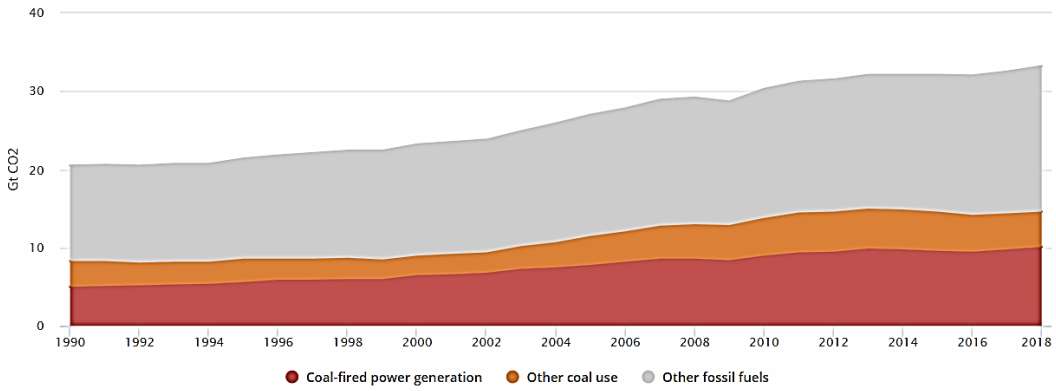

Figure 1.1: IEA reported global energy-related carbon dioxide emissions by source 1990-2018. Reproduced from reference [6] Source: IEA (2018) Global Energy and CO_2 Status Report. All rights reserved.

Natural CO_2 sinks, such as vegetation and oceans remove about half of all emissions from human activities. If no anthropogenic action is taken however, *Energy Technology Perspectives 2008* believe CO_2 emissions with increase by 130% above 2005 levels by 2050[10]. Emission targets set out by the Paris Agreement are certainly challenging, but not yet impossible to meet. The seriousness and urgency of the problem has been more widely acknowledged, atmospheric CO_2 can be reduced in three ways; (i) control of CO_2 emissions (ii) CO_2 capture and storage (iii) chemical conversion and utilisation of CO_2. These will be discussed in section 1.2.

1.2 Minimising CO_2 Emissions

1.2.1 Control of CO_2 emissions

The most obvious, yet fundamental challenge facing policy makers is the need for all or most of the world's leading countries to co-operate in restricting greenhouse gas emissions. The contributions to limit CO_2 emissions can be focused on greater energy efficiency of technological equipment, increased renewable energies and nuclear power, and the near-decarbonisation of fossil fuel-based power generation[10]. As well as technological changes, changing in the behaviour of society will also reduce CO_2 emissions, by limiting structural

changes i.e. reducing the need for private transportation and reducing use of electronic household appliances[11]. All key components to form a future of low carbon emissions, however, developing the technologies and infrastructure will take many years to make a significant effect.

1.2.2 CO_2 capture and storage

Carbon capture and storage (CCS) is considered as a more immediate solution for reducing atmospheric CO_2. CCS is defined as the capture of CO_2 from an industrial or power-sector point source combined with its transport and geological storage. It is an important part of the lowest-cost greenhouse gas mitigation portfolio[10] and if no CCS technologies are available, the overall cost to achieve a 50% reduction in CO_2 emissions by 2050 will increase by 70%. For the first time in almost a decade, 2018 saw an increase in plans to develop large-scale carbon capture, utilisation and storage (CCUS) facilities, contributing from 43 different projects[6]. With these recent advances in carbon capture technologies, cost-competitive pure CO_2 is becoming available for its conversion to value-added chemicals [12].

CO_2 capture technologies are used in industries to remove CO_2 from gas streams. There are currently 3 methods for CO_2 capture[10];

(1) Post-combustion, involves scrubbing of CO_2 out of flue gases from combustion processes. Here, an amine solvent is used to capture significant amounts of CO_2 from flue gas streams and is the most established CO_2 capture method and used in several facilities.

(2) Pre-combustion, the feedstock (fossil fuel) is partially oxidised at high temperatures, undergoing a gasification process forming syngas, this is followed by CO_2 separation to yield a hydrogen fuel gas. This process has not yet been demonstrated in an applicable power plant, however, shows potential from other industrial processes.

(3) Oxy-fuel, where the combustion of fuel in recycled flue gas is enriched with oxygen to produce CO_2-rich exhaust gas. A process which is commonly demonstrated in the steel manufacturing industry.

After the CO_2 has been captured, it is transported predominantly via high-pressure pipeline networks but also pressurised road and sea tankers. Transportation presents a number of challenges including access, public acceptance, and planning.

Once arrived, the storage of CO_2 involves the injection of CO_2 into porous geologic formations deep underground, typically several kilometres under the surface. The pressure and temperature of these conditions causes carbon dioxide to be in the liquid or 'supercritical phase'. Three options for CO_2 storage include saline formations (porous rock filled with salty water), oil and gas reservoirs, and deep unminable coal seams, CO_2 can be trapped by the following 3 methods[13]:

(1) Physical trapping, by immobilising CO_2 in a gaseous or supercritical phase. This involves static trapping in structural traps or residual-gas trapping in a porous structure.

(2) Chemical trapping in formation fluids, such as water of hydrocarbons, either by dissolution or by ionic trapping. Once dissolved, the CO_2 can react chemically with minerals in the formation or adsorb onto the mineral surface.

(3) Hydrodynamic trapping, through the upward migration of CO_2 at extremely low velocities leading to its trapping in intermediate layers. Migration to the surface would take millions of years and large quantities can be stored using this mechanism.

Despite the attraction of a 'quick fix' to the CO_2 crisis, carbon storage has a number of disadvantages. Firstly, there is a large energy penalty; the whole process of capture, transport and storage is a considerable expense[14], with UK estimates ranging from £33 to £330/tCO_2[15]. Additionally, many countries including the UK do not have sufficient storage capacity, or only have storage potential offshore, increasing the expense. The most negative impact, however, is the endangerment of leakage. Leakage may occur via natural geological media, or through existing man-made pathways such as wells[16] and can accumulate in formations overlying the storage reservoir, causing interference with other subsurface activities, groundwater contamination, or reach land surface and escape into the atmosphere[17]. Any leakages and

accidents that happen must be covered financially by the store manager, or likely passed on to future generations of taxpayers[18]. Due to the large energy penalty, cost and risk of leakage, storage of CO_2 is therefore not a sustainable long term solution[19]. As an alternative to CO_2 storage, recent advances have positioned *in situ* mineral carbonation as a viable technology[20]. For this process, captured CO_2 is stored through its injection into reactive rocks containing high concentrations of Ca^{2+}, Mg^{2+} and Fe^{2+} cations. Thus, proceeding rapid mineralization to calcite ($CaCO_3$), dolomite ($CaMg(CO_3)_2$) or magnesite ($MgCO_3$). This results in negligible risk of CO_2 migrating back into the atmosphere. Mineral carbonation can be considered a safe and economical option for CO_2 storage, to date the only ongoing industrial-scale injection is at Hellisheiði, Iceland[21].

1.2.3 CO_2 utilisation

Rather than treating CO_2 as waste, it can be regarded as a C-1 chemical feedstock for the synthesis of other chemicals that do not rely on a petrochemical source. Despite the large amount of fundamental research that has been performed regarding the conversion of CO_2 into higher value products, there are only few examples of industrially viable processes. CO_2 is a highly oxidised and thermodynamically stable molecule with the standard formation enthalpy of $-393.5\ kJ\,mol^{-1}$ [22]. Thus, overcoming the thermodynamic barrier and utilising CO_2 commercially is a challenge, as there are limited sufficient catalysts that have the ability to activate the molecule. Many of the available transformations of CO_2 consume lots of fossil-fuel derived energy, generating significant amounts of waste heat. Therefore, the challenge of converting CO_2 waste streams into useful products is to develop processes that require minimal amounts of non-renewable energy, economically competitive, and provide substantial reductions in greenhouse gas emissions compared with existing technology[23]. The potential of such a cheap, non-toxic and abundant feedstock for organic compounds, as well as the possibility to balance out CO_2 emissions whilst reducing the demand for CO_2 storage in

order to achieve CO_2 net negative emissions, makes CO_2 utilisation a forever expanding topic of research.

In 1975 CO_2 was shown to be active by transition metal complexes[24], and since then development of CO_2 conversion continues to grow. The industry uses approximately 200 Mt of CO_2 per year[25], however this is only 0.6% of the anthropogenic CO_2 emissions, totalling to 33 Gt per year[26]. Currently, toxic carbon monoxide is used in industry because CO_2 is perceived to be less reactive. The most promising large-scale use for CO_2 is for the synthesis of hydrocarbons and alcohols, via its hydrogenation. Commercially, CO_2 utilisation is thus far limited to the production of a few chemicals, the largest use of CO_2 is for the synthesis of urea, $CO(NH_2)_2$ [27] for nitrogen fertilisers and plastics, converting 110 million tonnes of CO_2. However, when used as fertiliser and applied to the soil, an equal amount of the utilized CO_2 is emitted to the atmosphere therefore not a method for permanent CO_2 storage. Urea is also used as an intermediate in organic syntheses such as the production of melamine and urea resins, used for adhesives and bonding agents. Other examples of industrial CO_2 utilisation include polycarbonates [28] (for plastics), salicylic acid (pharmaceutical ingredient) [29] and methanol [30]. Figure 1.2 summarises examples of organic synthesis starting from CO_2.

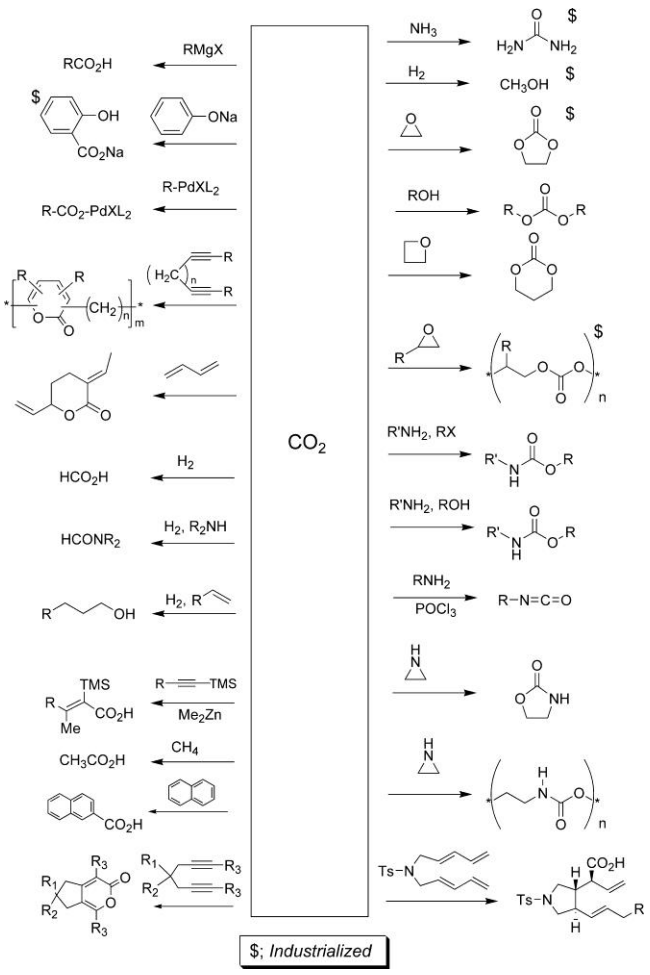

Figure 1.2: Utilisation of CO_2 in synthetic chemistry. Reprinted with permission from (Chem. Rev., 2007, 107, 2365–2387) [reference 31*]. Copyright (2020) American Chemical Society.*

To overcome the thermodynamic barrier to activate CO_2, there are 4 main methodologies to transform CO_2 into useful chemicals: [31]

(1) Use high-energy starting materials, such as hydrogen, unsaturated compounds, small-membered ring compounds and organometallics

(2) Choose oxidised low-energy synthetic targets such as organic carbonates

(3) Shift the equilibrium to the product side by removing a particular compound

(4) Supply external energy such as light or electricity

Selecting appropriate reactions can lead to a negative Gibbs free energy of the reaction, however selecting the reaction is not enough to overcome the thermodynamic barrier of CO_2. The employment of a catalyst is a necessary tool for reducing the thermodynamic barrier for

CO_2 activation, reducing the energy required to run the reaction, allowing a more sustainable process (Figure 1.3). Therefore, using an appropriate catalyst reduces the cost and time of the reaction. It is estimated that 90% of all commercially produced chemical products involve catalysis at some stage in the process of their manufacture[32]. Industrial catalysis can be classified into two main categories: homogeneous and heterogeneous. Homogeneous catalysis is identified where the catalyst is in the same phase as the reactants and products, e.g. a liquid catalyst within liquid reactants and products. Heterogeneous catalysis is identified where the catalyst is in a different phase to the reactants and products; e.g. a solid catalyst within gaseous or liquid reactants and products. Their critical role within the hydrogenation of CO_2 will be discussed throughout this review.

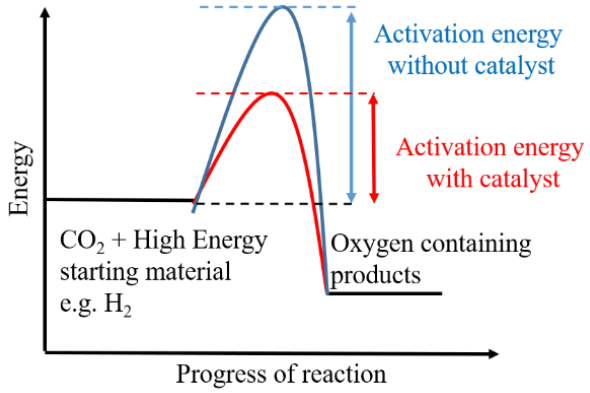

Figure 1.3: Schematic representation of organic synthesis using CO_2, with and without the presence of a catalyst.

Among all the possible transformations, CO_2 hydrogenation to acids, alcohols and hydrocarbons using H_2 derived from non-fossil feedstock is the most promising strategy [33]. Unlike fossil fuels, hydrogen is not readily available in nature. Great progress has already been made in water electrolysis to produce H_2 using electricity generated from renewable sources, i.e. solar or wind, and water splitting using electrolysis, thermolysis and photoelectrolysis

processes[34,35]. H_2 production from water electrolysis has successfully been an established industrial technology with energy efficiencies of 70%[36].

The simplest hydrogenation of CO_2 is the formation of formic acid (HCOOH), requiring only 2 hydrogen atoms, Eq. 1.1.

$$CO_2 + H_2 \rightarrow \mathrm{HCOOH} \qquad \textit{Eq. 1.1}$$

Although formic acid is a very simple molecule, it is widely used in many industrial processes, holds potential as a method for hydrogen storage, and supplies an alternative to portable batteries (formic acid applications will be discussed in detail in section 1.3). Nevertheless, formic acid derived directly from CO_2 has not yet found industrial application. Conventionally produced formic acid utilises fossil fuel derived feedstocks and high energy consumption amongst other limitations including slow reaction rate, undesirable by-products and high cost. Therefore, it is not surprising that utilisation of CO_2 is gaining momentum in the scientific community in order to shift from conventional fossil-based processes, toward environmentally friendly direct hydrogenation of CO_2 to formic acid.

1.3 Uses of Formic Acid

Current annual production of formic acid is around 600000 tons and this is projected to grow by 22% annually[37]. Due to its acidic nature and its strong reducing properties; formic acid finds applications in textiles, pharmaceuticals and food chemicals. In 2013, the global demand for formic acid was 579 kt, 34% of that contributing to animal feed, 32% accounted for leather tanning, and textile dying for 13%[38–41]. It is also used to promote the fermentation of acetic acid, as coagulants in rubber synthesis, an antibacterial agent in animal feed and as de-icing agent in many manufacturing industries[42].

The hydrogenation of CO_2 to formic acid can also be considered as a strategy to store H_2 chemically; using appropriate catalysts, it can be controllably converted back into to H_2 for immediate use. The CO_2 can then be removed and reused even at room temperature[43]. This process applies reversible CO_2 hydrogenation-dehydration enabling a carbon-neutral

hydrogen storage. Formic acid has a volumetric hydrogen density of 53g of H_2 per litre (4.4 H_2 wt%), it also possesses low-toxicity and is a liquid under ambient conditions, thus an easily transportable safe storage option as opposed to pure H_2. Therefore, can be seen an ideal hydrogen storage material for many applications[40,44–46]. Hydrogenation of CO_2 into HCOOH is very atomically efficient, as 100% of hydrogen is converted for storage, unlike methanol (66%) or methane (50%), where some hydrogen gets lost as water. Its dehydrogenation to H_2 and CO_2 is thermodynamically favourable by ΔG = -32.9 kJ mol^{-1} at room temperature[40]. In 2012, Boddien *et al.* demonstrated a highly reversible hydrogen storage system bases on Ru-catalysed formic acid (de)hydrogenation, appropriately named a 'hydrogen battery'[47].

Formic acid can also be seen as a H_2 replacement within fuel cells. Polymer electrolyte membrane (PEM) fuel cells are viewed as viable candidates to replace batteries in portable power devices. Traditionally H_2-PEM fuel cells followed by direct methanol fuel cells (DMFCs) are dominant choices[48]. However, limitations of such methods include high cost and potential dangers of hydrogen containers for H_2-PEMFCs and methanol's toxicity reducing the cell performance within DMFCs. Formic acid is a strong electrolyte, hence facilitates both electronic and proton transport within the anode compartment of the fuel cell. The use of formic acid as an alternative fuel to methanol in direct fuel cells is being actively investigated[49]. In only a few years of research, direct formic acid fuel cell (DFAFC) technology has shown electrocatalytic oxidation activity far superior to DMFCs, in some cases performances approaching those of H_2-PEM fuel cells[50]. With the need to reduce the size and weight of power sources, DFAFCs have higher potential for miniaturisation because it has high power output compared to other liquid fuel cells like methanol[51]. More advantages of using formic acid liquid fuel included fast electro-oxidation, low fuel cross over, non-flammable, non-toxic and ease of fuel availability. Thus, for many systems, the advantages if DFAFCs can outweigh those of its primary-liquid fuel contender the DMFC. However, DFAFCs possess challenges with decreasing cell performance. This is the result of a number of limitations including diffusion of formic acid across the cell membrane, constraints in mass

transfer caused by loss in formic acid concentration, water accumulation flooding the cathode and catalyst poisoning of CO[51]. Therefore, further development of DFAFCs are still required if they are to be considered as an alternative to H_2-PEM fuel cells.

1.4 Synthesis of formic acid and proposed reaction mechanisms

The production of formic acid can be classified into four groups; methyl formate hydrolysis, oxidation of hydrocarbons, hydrolysis of formamide and preparation of formic acid from formates. Current industrial technology for the production of formic acid involves the hydrolysis of methyl formate, with a capacity estimated at 770 kton a year[52]. A homogeneous reaction in the presence of a basic catalyst, $NaOCH_3$, catalysing a two-step process; an indirect carbonylation of water via methyl formate as an intermediate[53] as presented in Figure 1.4. First methanol is carbonylated with CO, to form methyl formate (Eq. 1.2). This is then hydrolysed in the presence of water to methanol and formic acid (Eq. 1.3), thereafter methanol can be separated by distillation and injected back into the reactor feed. However, this comes with difficulties, in order to shift the equilibrium towards formic acid for higher conversions, excess of water is needed, causing a diluted final product, requiring an extra process to separate the product away from the excess of reactant.

$$CO + CH_3OH \rightarrow HCOOCH_3 \qquad \textit{Eq. 1.2}$$

$$HCOOCH_3 + H_2O \leftrightarrow CH_3OH + HCOOH \qquad \textit{Eq. 1.3}$$

Scheme 1.1: The current most prominent process of formic acid production from CO and water via methyl formate.

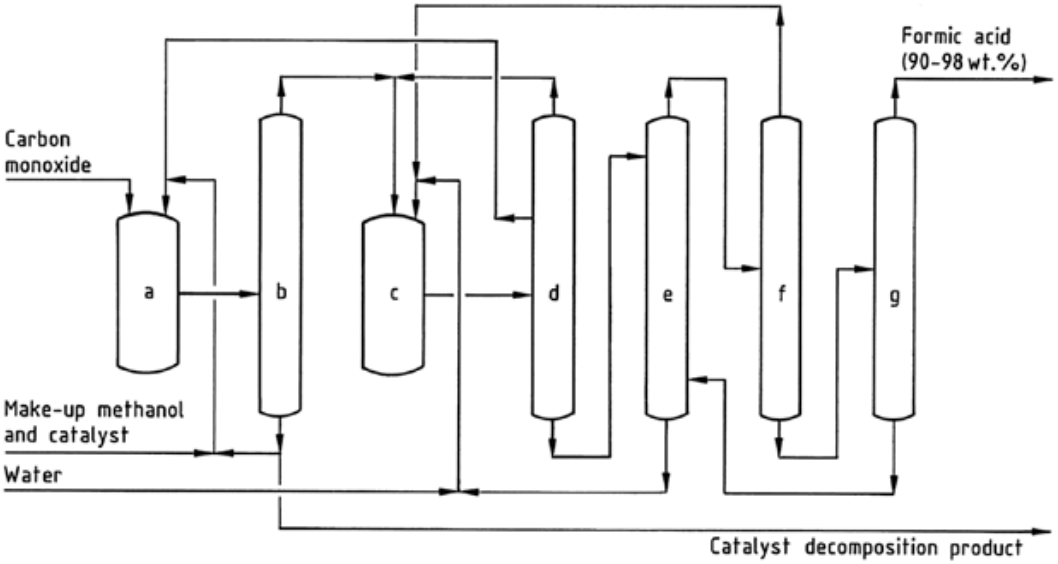

Figure 1.4: Production of formic acid (BASF process): a) Methyl formate reactor; b) Methyl formate column; c) Hydrolysis reactor; d) Low-boiler column; e) Extraction unit; f) Dehydration column; g) Pure acid column. Reprinted with permission from (H. Kiecza, Wiley Books, 2000) [reference 53*] Copyright (2020) John Wiley and Sons.*

The synthesis process from CO_2 and H_2 using homogeneous catalysts have been granted different patents to companies including BP and BASF[54]. BASF, with a yearly capacity of 230,000 tons, is the world market leader in formic acid production, and has been operational in industry since 1981[53]. They have developed a multiphase liquid-liquid process which combines catalyst recycling with isolation of formic acid. The process is divided into three steps; (1) hydrogenation, (2) catalyst extractions, and (3) product separation[55]. Despite the fact that homogeneous catalysis exhibits excellent catalytic efficiencies for the hydrogenation of CO_2 to formic acid/formate, the main hindrance is the laborious removal of catalyst and solvent. Advantages of heterogeneous catalysis over homogeneous include easy separation of fluid from solid catalyst, convenient handling in a fixed-, fluidised- or moving-bed reactors, regeneration of catalyst and established reactor designed principles[29], making the process a lot more attractive for large-scale production.

The hydrogenation of CO_2 to CO, hydrocarbons and alcohol is thermodynamically favourable because of the subsequent production of water. However, CO_2 hydrogenation to form formic acid involves the conversion of gaseous substances into liquid products. Hence, if performed

in the gas phase, the reaction is thermodynamically unfavourable by $\Delta G = +33$ kJ mol^{-1}, due to reduction in entropy (Eq. 1.4). To improve the enthalpy, the equilibrium can shift towards the product side using certain bases, such as ammonia (NH_3) and triethylamine (NEt_3) (Eq. 1.5)[56], exothermic protonation of the base by formic acid delivers enough energy to make the reaction favourable. In addition, if performed in the liquid phase, i.e. a solvent of dimethyl sulfoxide (DMSO) or water, the reaction becomes exothermic as the entropy is improved due the dissolution of gases and the reaction continues within the liquid phase (Eq. 1.6).

$CO_{2(g)} + H_{2(g)}$	$\rightarrow$	$HCO_2H_{(l)}$	$\Delta G° = 32.9$ kJ/mol	*Eq. 1.4*
$CO_{2(g)} + H_{2(g)} + NH_{3(aq)}$	$\rightarrow$	$HCO_2^-{}_{(aq)} + NH_4^+{}_{(aq)}$	$\Delta G° = -9.5$ kJ/mol	*Eq. 1.5*
$CO_{2(aq)} + H_{2(aq)} + NH_{3(aq)}$	$\rightarrow$	$HCO_2^-{}_{(aq)} + NH_4^+{}_{(aq)}$	$\Delta G° = -35.4$ kJ/mol	*Eq. 1.6*

Scheme 1.2: CO_2 hydrogenation to formic acid. Thermodynamic comparisons in aqueous solvents and the presence of base.

There have been many publications on the hydrogenation of CO_2 to formic acid/formate using homogeneous catalysis, however, only a few studies have been reported using heterogeneous catalysis, specifically in an alkaline media. This is possibly due to unfavourable reaction conditions (high temperature and pressure) compared to homogeneous catalysts, also the low chemoselectivity of heterogeneous processes, as formic acid can act as an intermediate to form methanol or methane[57]. For example, the industrial methanol synthesis with syngas over Cu-ZnO-Al_2O_3 catalyst[58] is thought to work *via* formation of surface formate as an intermediate. This review will summarise the pioneering research conducted using homogeneous catalysis; leading into the progress achieved for heterogeneous catalysis in alkaline aqueous media, conditions I have continued with for this project.

1.4.1 'Formic Acid' and 'CO_2' terminology

Formic acid is what is known as a weak acid, therefore when dissolved in water formic acid can deprotonate to form formate ($HCOO^-$). Formic acid and formate is known as a "conjugate pair" and forms an equilibrium (Eq. 1.7).

$$HCOOH + H_2O \leftrightarrow HCOO^- + H_3O^+ \qquad \textit{Eq. 1.7}$$

Formic acid has a small Ka therefore in water (pH 7), the protonated form (HCOOH) is favoured. However, within an alkaline solvent and an excess of OH^- ions, the equilibrium will shift towards the deprotonated form, forming $HCOO^-$.

Moreover, when concerning the dissolution of CO_2 within an aqueous media, the chemical equilibrium of reactant can be situated as a number of carbon species; CO_2, bicarbonate (HCO_3^-) and carbonate (CO_3^{2-}). This is discussed in detail in section 3.1.2. The specific carbon species is influenced by many parameters, such as temperature, CO_2 pressure, kind of base, and pH. Thus, the actual form of the substrate within aqueous conditions is ambiguous.

Henceforth, the term 'hydrogenation of CO_2 to formic acid' being used in this review may actually involve HCO_3^-/CO_2^{2-} as the substrate, and $HCOO^-$ as the product, therefore terms are used subjectively.

1.5 Development of catalysis for CO_2 hydrogenation to formic acid

1.5.1 Homogeneous catalysis

Homogeneous catalysts have been the most successful in the reduction of CO_2 to formic acid derivatives, such as formamides of formates. Since the discovery of phosphine-based Ru complexes by Inoue *et al.*[59] published in 1976, the formation of formic acid from CO_2 has

been extensively studied as a homogeneous process, namely Ir[60–62], Ru[63–65] and Rh[66] complexes containing sophisticated ligands (N-heterocyclic carbenes, pincer ligands and phosphines). This process has been carried out in organic solvents[44], water[44,64,67] or ionic liquids, or else directly in supercritical CO_2 ($scCO_2$) [63,68,69]. For formic acid to be stabilised and yields improved, reagents such as a base, alcohols or epoxides can be used, giving formate salts, formate esters or diols, respectively[56]. Noyori and co-workers utilised $scCO_2$, celebrating its high miscibility with hydrogen, high mixing rates and weak molecular association, resulting in high reactivity of catalysts and reactants. Using Ru(II)-phosphine complex, they obtained ammonium formate, alkyl formate, and formamide in high yields[68]. They obtained formic acid with a turnover frequency (TOF) of 1,400 h^{-1}, using additives such as methanol or dimethyl sulphoxide (DMSO) improved the yield to TOF=4000 h^{-1} [69], which were thought to have promoting effects due to water dissolution. In the absence of amine, no formic acid was produced. Within $scCO_2$ conditions, the highest TOF of 95,000 h^{-1} has been achieved using $RuCl(OAc)(PMe_3)_4$ catalyst, accounted for its solubility in $sc(CO_2)$[63]. Despite the impressive results obtained from $scCO_2$, it also exhibits some inherent disadvantages; obtaining the high critical pressure guarantees higher capital costs relative to using a conventional solvent, as well as the need for specialised equipment[70]. Alternatives to $scCO_2$ includes organic or aqueous solvents with additives such as amines or organic bases to optimise gaseous CO_2 dissolution and conversion. Joó *et al*. investigated the hydrogenation of carbon dioxide and its derivatives in aqueous solutions as a function of pH[66]. They previously established the strong pH-dependance of the formation of water soluble hydrides of ruthenium(II) such as $[H_2Ru(tppms)_4]$ and $HRuCl(tppms)_2]_2$ from $[RuCl_2(tppms)_2]_2$, tppms and H_2, and their distribution in aqueous solution, leading to opposite selectivities in acidic and basic solutions during the biphasic hydrogenation of unsaturated aldehydes[65]. The reaction was selective for C=C hydrogenation at low pH while in alkaline conditions, selectivity for the hydrogenation of the aldehyde was also observed. Continuing their work, they investigated the hydrogenation of carbon dioxide and its derivatives using water-soluble platinum group metal phosphine complexes in $NaHCO_3$ aqueous solutions, they report that the substrate bicarbonate can be

produced *in situ* in the reaction of carbonates and CO_2. This was the first homogeneous catalytic hydrogenation of HCO_3^- in aqueous solutions to be reported in literature. A 1M $NaHCO_3$ solution corresponding to pH 8.3 rapidly yields water soluble hydrides of ruthenium(II)-phosphine complexes, optimally catalysing the hydrogenation of HCO_3^- to HCO_2^- with TOF up to 262 h^{-1}. Katho *et al.* regulated the pH through the CO_2/HCO_3^- buffer by varying CO_2 pressure in the $CO_2/HCO_3^-/CO_3^{2-}$ reaction system. In this way, there was no use for amines or other organic bases. Increasing proton concentration increased the catalyst activity for HCO_2^- formation, achieving a maximum TOF of 807 h^{-1} at 10% HCO_3^-/90% CO_2. The reaction rate was dramatically dropped when all bicarbonate was converted to formate, in pure CO_2/H_2O, the residual rate was found at TOF 1.8 h^{-1}. When exploring the mechanism of the catalytic process, the rate of formation of HCO_2^- as a function of $[RuCl_2(PTA)_4]$ concentration was found to be first order with respect to [Ru(II)], levelled off with increasing $[HCO_3^-]$, allowing the assumption that the real substrate of the hydrogenation is the bicarbonate anion. In similar aqueous systems, the main role of amine additives can be to increase $[HCO_3^-]$, as found by Leitner *et al.*[71], shifting the pH in favour of the formation of bicarbonate. Initiated in 2009, Nozaki *et al.* investigated the Ir(III)- catalysed hydrogenation of CO_2 in basic medium. The iridium trihydride pincer complex $[Ir(H)_3(P^{iPr}N^{Py}P^{iPr})$ achieved excellent activity (TOF 150,000 h^{-1} at 200 °C, 50 bar) and productivity, turn over number (TON) = 3,500,000 at 120°C in aqueous KOH[60,61]. This has been the most active catalyst for the hydrogenation of CO_2 to formate to date.

1.5.2 Moving from Homogeneous to Heterogeneous catalysis

Despite impressive yields of formic acid from the hydrogenation of CO_2 via homogeneous catalysis, these catalysts require a complicated synthesis and/or handling procedures and the separation of formic acid from catalyst and bases also remains a challenge, hence, industries are reluctant to use homogeneous catalysis for large-scale production. Importantly, these homogeneous catalysts also known to promote decomposition of the generated formic acid

back into CO_2 and H_2 during the separation step(s)[72]. Despite the obvious practical advantage in separation of heterogeneous catalysis from the final reaction mixture, development lags significantly, therefore progress is highly desirable.

The activation of CO_2 is challenging and as an acidic oxide, has a strong affinity towards nucleophiles and electron-donating reagents. Using homogeneous catalysis, CO_2 conversions can be achieved using expensive electron-donating ligands on the metal active sites, which are prone to leaching. Without this ligand promotion in a heterogeneous catalytic system, CO_2 is always activated in a bent conformation by the interaction between the dissolved base with CO_2[73]. CO_2 can chemically react with an aqueous base such as KOH or NaOH to give bicarbonates (HCO_3^-), the precursor for further hydrogenation to formate. However, evolution of CO_2 to formate through the bicarbonate intermediate experiences a thermodynamic sink in the reaction. This is because the bicarbonate species is considerably more stable than that the parent CO_2 and final formate. Therefore, further hydrogenation of bicarbonate is thermodynamically disfavoured, necessitating enhanced heterogeneous ability of a heterogeneous catalyst[73].

Development of heterogeneous catalysts for CO_2 hydrogenation in liquid solutions has lacked due to the low activity of these catalysts. The synthesis of formic acid/formate anion by the hydrogenation of CO_2 was first discovered by Farlow and Adkins in 1935 using Raney nickel (finely grained Ni-Al alloy) as the catalyst in the presence of an amine[74], yielding 55% formic acid based on the amine at 80-170 °C under high pressures of 20-40 MPa in an ethanol/phenol solvent system. Despite that fact that the reaction was not catalytic (turn over number < 1), a new field of research was initiated. Using electrochemical processes Mahmood and co-workers in 1987 found that formic acid was produced at low rates at electrodes impregnated with either manganese, copper of zinc phthalocyanine[75]. CO_2 reduction to formic acid via heterogeneous catalysis has only really advanced within the last 15 years. Zhang *et al.* invited this idea in 2004 when they immobilised a homogeneous catalyst at the surface of a support[76]. Ruthenium immobilised on functionalised silica was used as a catalyst precursor, and then

ruthenium complexes catalysts were formed *in situ* at the reaction process of formic acid synthesis. TOF of 1384 h^{-1} and 100% selectivity was achieved in CO_2 expanded ethanol over Si-$(CH_2)_3$-$NH(CH_2)_3CH_3$-Ru, using NH_3 as a base. In comparison with the homogeneous system, the activity of the immobilised catalyst was greatly enhanced, almost three times higher. This can be credited to so-called site-isolation; attaching the catalyst to the support in such a way dispersed the catalytic sites, preventing the dimerisation or oglimerisation to less reactive sites, a process present with their homogeneous counterparts. An increase in electron-donating ability from the amine functionalised support to the metal is shown to improve the stability of the Ru-N bond, therefore also increasing the activity of the catalyst. The best known homogeneous catalytic systems have been based on the metal complexes of second and third row transition metals such as ruthenium and rhodium, usually combined with halides or hydrides as anionic ligands, or phosphines as neutral ligands. Other methods involving immobilising homogeneous catalysts onto heterogeneous supports for the CO_2 hydrogenation to formic acid have since been studied, Wesselbaum *et al.* used an immobilised ruthenium organometallic catalyst[77], and work from Hicks's group[78,79], where they found silica-tethered iridium catalysts offered high activities for formic acid production. However, the TOFs of there pseudo-heterogeneous catalysts decreased to one or two orders of magnitude compared to the homogeneous counterparts[63,80].

1.5.3 Supported metal catalysts

Preti *et al.* reported a gold (AUTO*lite*) supported on titania[81], the first gold catalyst for the hydrogenation of CO_2 to formates in the liquid phase, a robust catalyst for the production of $HCOOH/NEt_3$ adducts from CO_2, H_2 and neat NEt_3. They demonstrate a continuous process for catalyst- and solvent-free adducts, as NEt_3 is quantitatively converted into $HCOOH/NEt_3$ showing little drop in productivity over 37 days. In many homogeneous studies, it was found that ruthenium-hydride species was the initial active species during the catalytic cycle. Moreover, for the conversion of CO_2 to formic acid, hydroxyl groups, i.e. KOH would also

improve the catalytic activity. Hao *et al.* has applied the same idea and found ruthenium hydroxide species achieved by impregnating Ru onto γ-Al_2O_3, an effective catalyst for CO_2 hydrogenation[82]. It is shown that the interaction of the active ruthenium with the hydroxyl of the support through the formation of Ru-OH bonds is crucial for the reaction. To confirm the claim of Ru-OH being the active species, activated carbon and MgO were also tested as a support for ruthenium. Ruthenium species proved inactive in the presence of MgO, attributing to the only Ru species present on the surface being RuO_2. Activated carbon as a support, allowed for immobilisation of hydroxyl groups, improved the formic acid yield, but not as much as γ-Al_2O_3, which was found to have the highest concentration of superficial hydroxyl groups, confirming its importance for CO_2 hydrogenation. RuO_2 species, formed on the surface of γ-Al_2O_3 with increased metal weight loading (<2%), and high pH (pH 13), resulting in reduced catalysts activity. The optimal TON of formic acid of 139 was achieved over γ-Al_2O_3 supported ruthenium catalyst with a 2.0 wt.% prepared at a pH of 12.8. For the reaction mechanism, they proposed Ru-OH is hydrogenated to a ruthenium hydride species, and much like any other reported mechanism involving Ru-H, CO_2 is inserted into the ruthenium hydride bond to generate metal formate. Formic acid is released and the catalyst regenerated, restoring the activity of Ru-OH. Later applying the same system, Liu *et al.* employed γ-Al_2O_3 nanorods to support ruthenium hydroxide species (Ru/γ-Al_2O_3)[83]. The increased surface area of the nanorods compared to conventional γ-Al_2O_3, lead to highly dispersed Ru species and abundant hydroxyl groups thus improving formic acid yield. Umegaki *et al.* produced the first study using metallic ruthenium for the heterogeneous catalytic conversion of CO_2 to formic acid[84], without the common aid of any ligands. Metallic ruthenium nanoparticles prepared in methyl alcohol solution under solvothermal conditions showed an improved catalytic activity with the addition of water to the suspension of methyl alcohol and triethylamide. By using supercritical carbon dioxide, the TOF of the reaction increased with increasing partial pressure of carbon dioxide. Umegaki found that pre-reduced catalysts had a much higher TON than catalysts without the pre-reduction treatment, as Ru(III) species were not active for CO_2

hydrogenation. A very specific amount of water was required for the optimum TON, addition of 2 mL of water achieved the best TON of 1629. Increasing the amount of water to 4 mL decreased the TON, as a result of water oxidation forming of Ru(III) species, deactivating the catalyst. These results suggest a specific amount of water is required to promote the hydrogenation reaction, however, water must be limited to maintain the ruthenium species in its metallic state. As well as producing impressive yields of formic acid, this work also helped open the door towards using nanoparticle supported catalysts for the hydrogenation of CO_2. In 2015 PdNi alloyed nanoparticles as an efficient catalyst for the hydrogenation of CO_2 into formic acid without any base were studied by Nguyen and co-workers[85]. The PdNi alloy is supported on carbon nanotube-graphene (PdNi/CNT-GR) composite. GR and CNT, despite having a high surface area, can easily stack spontaneously or bundle together, hence not effective as a catalyst support. However, when CNT-GR composite is formed, they serve as a spacer for each other, preventing any stacking or bundling, exposing their own high surface areas. They found that Pd-Ni bimetallic catalyst has a synergistic effect on HCOOH yield, improving the catalytic activity compared to their monometallic counterparts, achieving respectable TON (5.4) and TOF (1.0×10^{-4} s^{-1}) when considering the reaction conditions; CO_2+H_2 50 bar (1:1) and 40 ºC. Using a nitrogenase base in a polar solvent, ammonium formate salts can be obtained.

1.5.4 Aqueous conditions

The majority of organic based solvents are derived from fossil fuel origin and come with more disadvantages such as toxicity and high cost. Water on the other hand is extremely safe, cheap and environmentally friendly, making it a lot more attractive solvent of choice. As a method for avoiding that HCO_3^- thermodynamic sink when converting CO_2 into formic acid, mentioned previously, a base is commonly used to consume the generated formate; thus, thermodynamically shifting the equilibrium forward. It is well accepted that a bicarbonate ion (HCO_3^-) is the common intermediate during the hydrogenation of CO_2 in aqueous alkaline

solutions. Previously, Stalder *et al.*[86] studied the conversion of $NaHCO_3$ to formate with Pd supported on a series of supports ($BaSO_4$, γ-Al_2O_3 and carbon), Pd/C showing the maximum TON of 115 at 25 ºC. Su *et al*. studied the conversion of bicarbonate salts under high H_2 pressures using palladium supported on porous carbon material (activated carbon)[87]. The activated carbon support was superior to other supports tested (Al_2O_3, $CaCO_3$, $BaSO_4$) due to increased dispersion of Pd nanoparticles, and its hydrophobic property for H_2 storage within the carbon channels, increasing the concentration of localised H_2 on the surface of the catalyst[88], in this way impressive turn over frequencies of 782 h^{-1} were achieved. Screening various carbonates (Na_2CO_3, K_2CO_3, $(NH_4)_2CO_3$) and bicarbonates ($NaHCO_3$, $KHCO_3$, $(NH_4)HCO_3$), they found that hydrogenation of carbonate salts was much more difficult than bicarbonate salts, due to protonation of carbonate ions as the rate limiting step. Of all bicarbonate salts, $(NH_4)HCO_3$ achieved the highest yields, resulting from the higher equilibrium concentration of HCO_3^- ions over CO_3^{2-} ions. This process of reacting CO_2 with ammonia leads to the production of both ammonium carbonate ($(NH_4)_2CO_3$) and ammonium carbamate ($NH_2CO_2NH_4$), an interesting alternative to the carbonate intermediate. In industry, these are intermediates or products during urea production processes and carbon capture and storage processes, respectively. Analysing this in more detail, Su *et al.* reported that ammonium carbamate was readily reduced using H_2 to produce ammonium formate over Pd on carbon in aqueous alcohol solutions without the need for base additives[80], yielding formate at 91.7% and TONs reaching 845. They found that adding water to the ethanol solution, increased solubility, which increased to yield of the formate. However, increasing H_2O any more than 30 wt%, decreased the formate yield. Comparing the hydrogenation efficiency of ammonium carbamate/carbonates with $NaHCO_3$ in ethanol-water solutions provided contrasting results. In pure water, the hydrogenation of $NaHCO_3$ was the fastest, while in pure ethanol, the same reaction was completely suppressed. However, the hydrogenation of $NH_2CO_2NH_4$ or $(NH_4)_2CO_3$ produced opposite results, here the hydrogenation was faster in pure ethanol than in water. These findings open a valuable insight of comparing CO_2

hydrogenation with ammonium carbamate/carbonate, and sodium carbonate intermediates within aqueous and ethanol solutions.

1.5.5 *State-of-the-art* methods for liquid phase CO_2 hydrogenation to formate

Within the last 4 years the field of CO_2 hydrogenation heterogeneous catalysis improved greatly. It should be mentioned, a rhodium catalyst, as reported by Maru and co-workers[89] in 2017 has found to have a superior activity for formic acid synthesis, rhodium hydrotalcite (Rh-HT) achieved TON of 15840 (TOF 660 h^{-1}) under conditions of 60 ^{o}C, 50 bar within a methanol/water solvent (5/1). However, I will continue to focus on the formation of formic acid within a liquid phase alkaline media, an area particularly underexplored, in which Pd and Ru nanoparticles as the catalytic metal has dominated. Very recently Zhang *et al.* investigated palladium supported on the common metal oxides CeO_2 and ZnO[90], the synergetic effects between the support and the metal facilitated the reaction. The basic sites on the support promoted CO_2 activation, forming surface adsorbed carbonaceous intermediates, which react further with hydrogen atoms on the palladium to form formic acid. ZnO possesses a lower density of basic sites, thus when selected as the support, CO_2 activation is seen as the rate determining step. CeO_2 possesses a higher density of basic sites therefore for Pd/CeO_2 the rate determining step is influenced by the nature of Pd species on the support. Song *et al.* reported a palladium catalyst supported on chitin[91] (the second most abundant biopolymer), as an effective catalyst for CO_2 hydrogenation. The structure of chitin is rich in hydroxyl groups and acetamide groups. The lone pairs on the nitrogen within the acetamido groups and the hydroxyl groups act as chelating agents, immobilising the palladium nanoparticles for catalytic application. Under optimised conditions, 0.25 weight percentage of palladium exhibited to the best catalytic activity achieved TOF of 257 h^{-1} at temperatures as low as 60 ^{o}C, and 40 bar pressure, as it was found that chitin maintained a good dispersion of the nanoparticles along the surface. As mentioned previously, Hao *et al.* hypothesised that the

hydroxyl groups on the surface of a support may enhance the adsorption of CO_2 and the catalytic efficiency of the catalyst[82], this was studied further by Mori *et al.* with a single-site Ru catalyst on the surface of a layered doubled hydroxide (LDH)[92]. The electronegativity was enhanced by the special location of the ^{-}OH ligands, which have an ordered arrangement on the LDH surface. The electron donating ability of these strong Brønsted hydroxyl ligands was found crucial for an active electron-rich Ru centre, boosting CO_2 adsorption in the vicinity of the Ru centre, enhancing CO_2 hydrogenation at relatively mild conditions of 100 ^{o}C, 20 bar, achieving high TON (698) and TOF (29 h^{-1}) with NaOH as the alkaline solvent. Continuing their work, Mori *et al.* moved on to investigate PdAg nanoparticles supported on titania[93], within the same reaction conditions as their previous work (20 bar, 100 ^{o}C, $NaHCO_3$ solvent). Alloying the Pd with Ag provided a synergistic effect exhibiting maximum TON of 14839 (TOF 618 h^{-1}), based on surface exposed Pd atoms. The ratio of Pd and Ag atoms were tuned in such a way forming a core shell structure, with Ag residing at the core and Pd atoms being exposed on the surface. The Ag atoms caused an electronic ligand effect, enhancing the electronegativity of the catalytic sites, the Pd atoms. This facilitated the adsorption of HCO_3^- species, the rate determining step of this reaction, as evidenced by kinetic and DFT calculations. Mori and co-worker's reported work has thus far achieved the highest TON/TOF for the hydrogenation of CO_2 to formic acid within alkaline conditions.

1.6 Research motivation - Origin of Life Theory

Moving away from finely tuned and heavily researched artificial catalysts, nature has already developed a sophisticated, efficient process for the selective reduction of CO_2 into carbon monoxide and formic acid, which is further reduced and combined with CO to generate an acetyl-CoA intermediate as part of the acetyl-CoA pathway. This pathway enables organisms to use hydrogen as an electron donor and carbon dioxide as an electron acceptor as a building block for biosynthesis. Involved in this reaction, are two specific enzymes; carbon monoxide dehydrogenase (CODH) and acetyl Co-A synthetase. Within the active sites of these enzymes

facilitating the reaction, unique (Fe,Ni)S clusters can be found[94,95] in the form of cubane-type [4Fe-4S] clusters and asymmetric [Ni-4Fe-5S] clusters[96]. In 1992 Wächtershäuser and co-workers[97] hypothesised the involvement of iron sulphide minerals structurally similar to these (Fe,Ni)S centres found in CO_2 reducing enzymes, in the 'Origin of Life' theory. To introduce this idea briefly, the Origin of Life theory proposes that prebiotic molecules have been formed from the conversion of aqueous CO_2 and H_2 molecules, a catalytic process occurring within deep-sea hydrothermal vents in the primordial ocean[94] by composite sulphide structures with catalytic transition metal centres (predominantly Fe and Ni). Russel adds a significant factor to these ideas, bringing to attention the structural similarities of the Fe_4S_4 'cubane' unit cell which can be found in the iron sulphide greigite (Fe_3S_4) and in ferredoxin, a [FeNi]-hydrogenase, a catalytic protein found within the acetyl-CoA pathway[98] as presented in Figure 1.5. Greigite can be found continually precipitating within a colloidal membrane of FeS in the chimney cavities of hydrothermal vents along the ocean floor. These hydrothermal vents act as chemical reactors, providing acidic and alkaline effluents[99], this contrast in pH aids a natural chemiosmotic potential, providing the driving force of the initial thermodynamically unfavourable CO_2 reduction step.

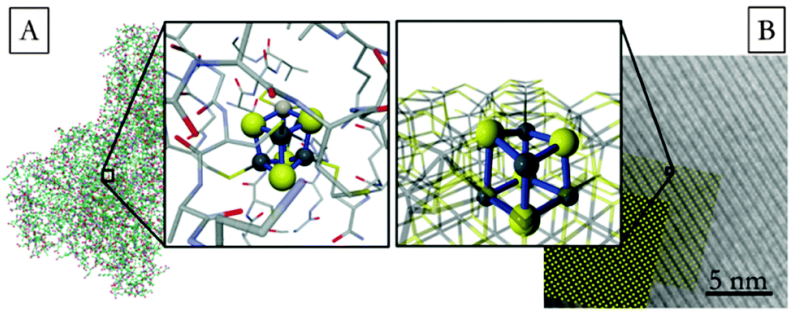

Figure 1.5: Schematic representation of the structural similarities between (Fe,Ni)S centres in enzymes and in minerals. (A) [Fe_4S_4] 'thiocubane' units in ferredoxin, the proposed active site of carbon monoxide dehydrogenase enzyme (B) Structure of the [Fe_4S_4] 'cubane' unit in greigite. Reproduced from Chem Comm, 2015, 51, 7501–7504 [reference 100*] with permission from the Royal Society of Chemistry.*

Yamaguchi *et al.*[101] investigated the hypothesis that Ni/greigite could be the evolutionary origin for the $NiFe_3S_4$ cluster in CODH. Specifically, they tested the role of Ni in the electroactivation of CO_2 by replacing an Fe atom in greigite with Ni. Mimicking the aqueous conditions of CO_2-saturated early ocean (pH 5.5), this material was shown to catalyse CO_2 to CH_4 and CO, but no solution-based products were detected. Work from Roldan *et al.* also involved replicating and adapting this theory of catalytic greigite for the reduction of CO_2, mainly via mechanistic studies[100,102,103]. They found within mild electrochemical conditions, greigite effectively reduced CO_2 to formic acid as well as acetic acid, methanol and pyruvic acid. This provided evidence for the first crucial step in the pathway towards shaping pre-biotic chemistry preceding the onset of life.

1.7 Aims of this thesis

It is clear that CO_2 utilisation is a highly prioritised topic of research, with certain areas still much to explore. Expanding on ideas previously mentioned, the work in this thesis aims to cover the development of 3 new catalytic materials capable for the hydrogenation of CO_2 to formate under aqueous, mild and environmentally benign conditions. These three catalytic materials will be discussed over 3 chapters. This research aims to contribute prominent ideas towards the challenging and necessary target for an efficient and sustainable catalytic material aiding industrial CO_2 conversion and utilisation. Looking deeper, Chapters 4 and 5 aims to give more insight into the theory of the 'Origin of life', using iron and nickel sulphide materials and testing their ability for CO_2 hydrogenation.

The aims of this thesis are outline below:

- Chapter 3 – Transition metal supported on Mo_2C will be tested for catalytic CO_2 hydrogenation into formate in the liquid aqueous phase. Specifically, the activity of palladium nanoparticles will be compared to ruthenium (among other metals), monometallic and bimetallic catalysis. In turn, catalyst synthesis will be modified and optimised. In addition, the influence of sodium-based solutions as reaction solvents

will be compared and explored in detail. The reusability of the catalyst will be tested, and characterised, in order to analyse how the catalyst is affected under reaction conditions. Bimetallic nanoparticles can act as a method to improve catalytic stability, a concept that will also be investigated in this work. Finally, the role of the reactant gases will be investigated using continuous flow conditions. This will give more information regarding the solubility of the gases in solution, and their behaviour within the reaction.

- Chapter 4 - The iron sulphide has previously shown interesting results concerning CO_2 hydrogenation into formate, to support the 'Origin of Life' theory. This chapter will investigate pyrrhotite, $Fe_{1-x}S$. First, the synthesis of pyrrhotite will be optimised and the material characterised. I will then investigate the effect of how oxidising the surface of the material has on the activity of the catalyst. The pyrrhotite synthesis and calcination conditions will be optimised to improve the catalytic activity of the material. Extensive characterisation of the bulk and surface will be analysed to give an insight into understanding the catalytic nature of the material.
- Chapter 5 - In an effort to improve the activity of iron sulphide, the influence of nickel within the iron sulphide structure will be tested and investigated. Ni will be introduced into the crystal structure using the same synthesis procedure as $Fe_{1-x}S$, creating $Fe_xNi_yS_z$ structures. The effect of calcination on the material's catalytic ability will be tested and optimised. Again, to understand the catalytic nature of the material and structural characteristics, extensive surface and bulk characterisation of the materials will be employed and analysed.

2 Materials and Methods

This section methodically lists the materials used in the work presented in this thesis. It then explains the reaction procedure for catalyst preparation, all of said catalysts are tested and characterised within this report. The following section will then briefly go through the theory behind the characterisation techniques used in this project, including the experimental details of the analysis.

2.1 Materials

Table 2.1. Chemical materials used in this thesis.

Material	Supplier	Purity
$PdCl_2$	Sigma Aldrich	99.9%
$RuCl_3.xH_2O$	Sigma Aldrich	99.9%
β-Mo_2C	Alfa Aesar	99.5%
$Fe(acac)_2$	Molekula	99.5%
$Ni(acac)_2$	Sigma Aldrich	95%
Sulphur *sublimed*	Alfa Aesar	99.5%
Oleylamine	Sigma Aldrich	70%
Toluene	Sigma Aldrich	99.8%
Formic Acid	Sigma Aldrich	99%
NaOH *pellets, anhydrous*	Sigma Aldrich	98%
$NaHCO_3$	Sigma Aldrich	99.7%
Na_2CO_3	Sigma Aldrich	99%
CO_2	BOC gases	99.999%
H_2	BOC gases	99.999%
5%H_2/Ar	BOC gases	n.a.
HCl	Sigma Aldrich	37%

HNO_3	Sigma Aldrich	70%
Poly vinyl alcohol	Sigma Aldrich	n.a.
M_w 9000-10000 g/mol, 80% hydrolysed		
$NaBH_4$	Sigma Aldrich	99.99%
Fe_2O_3	Sigma Aldrich	96%
Fe_3O_4	Sigma Aldrich	95%
$NiSO_4.6H_2O$	Sigma Aldrich	98%
$FeSO_4.7H_2O$	Sigma Aldrich	99%

2.2 Catalyst Preparation

2.2.1 Preparation of M/Mo_2C (M = Pd, Ru)

2.2.1.1 Modified Wet Impregnation

Modified wet-impregnation is a very common method for the synthesis of supported metal catalysts[104].

Preparing 2 g of catalyst

Separate aqueous solutions of $PdCl_2$ and $RuCl_3.xH_2O$ were prepared at approx. 6 mg/mL. The exact metal concentration was calculated by MP-AES (section 2.3.11). $PdCl_2$ solution was acidified with HCl to a specific concentration (0.58 M & 2 M). In a typical synthesis of 2 g of 1 wt. % M/Mo_2C catalyst, the requisite amount of the aqueous metal precursor (metal chloride) solution (equivalent to 0.02 g of metal; in the case of bimetallic catalyst, the two metals were taken in a equimolar ratio) was added to 16 mL of deionised water in a 50 mL glass round bottom flask with vigorous stirring. To this precursor solution, Mo_2C (1.98 g) was added

slowly and steadily with constant stirring at 25 ºC. After the completion of the addition of Mo_2C, the reaction slurry was left to stir for 15 minutes, the temperature was then raised to 60 °C and left to stir for another 30 minutes. Finally, the temperature was raised to 95 °C and left overnight (16 hours) under continuous stirring, for the complete evaporation of water. After 16 h, the remaining dry, dark-grey solid was ground thoroughly and this dried material was reduced in a furnace under 5 vol. % H_2 in Argon at 400 °C for 4 hours with a heating rate of 10 °C/min.

Preparing 15 g of catalyst

Pd/Mo_2C catalysts were prepared using the same synthesis as above, however on a larger scale. The usual Pd/Cl_2 precursor was prepared at approx. 6 mg/mL, acidified with 2 M HCl. 15 g of 1 wt. % and 5 wt. % Pd/Mo_2C prepared using the requisite amount of aqueous metal precursor, added to a 250 mL glass round bottom flask, deionised water was added to total 100 mL of liquid solution. The appropriate amount of Mo_2C support was added, and the usual synthesis procedure was applied. The dried material was reduced in a furnace under 90 vol. % H_2 in Argon at 400 ºC for 4 hours with a heating rate of 5 ºC/min.

2.2.1.2 Sol-Immobilisation method

Sol-Immobilisation is another very common technique for the synthesis of supported metal catalysts[105].

An aqueous solution of acidified $PdCl_2$ was prepared (as mentioned above). Polyvinyl alcohol (PVA) and an aqueous solution of $NaBH_4$ (0.1 M) were also freshly prepared. In a typical synthesis, of 1 g of 1 wt. % M/Mo_2C catalyst, the requisite amount of an aqueous solution of $PdCl_2$ was added to 400 mL of water. The required amount of PVA solution (1 wt. %) (PVA/(Pd) (w/w) = 1.3) was added. $NaBH_4$ (0.1 M, $NaBH_4$ /(Pd) (mol/mol) = 5) was then added as a reductant to form a dark-brown metallic solution. After 30 min of sol-generation, the colloid was immobilised by adding the support material, Mo_2C (0.99 g). 5 drops of

concentrated H_2SO_4 was added under vigorous stirring to obtain an acidic pH. After 2 h, the slurry was filtered, and the catalyst was washed thoroughly with 2 L of distilled water (until the mother liquor was neutral) and then dried at 120 °C overnight under static air in an oven. No further heat treatment was used.

2.2.2 Iron (Nickel) Sulphide Synthesis

Iron (nickel) sulphides were synthesised via an adapted methodology reported by Beal *et al.* [106].

Reactions were carried out in a three-necked flask equipped with a condenser, temperature probe and magnetic stirrer bar. Oleylamine (60 cm^3) was initially degassed by bubbling nitrogen rapidly through for 30 minutes. $Fe(acac)_2$, and/or $Ni(acac)_2$ (totalling 4.5 mmol) and sulphur (0.147 g, 4.5 mmol) were placed in a flask, and flushed with nitrogen. The degassed oleylamine was added to the flask, fitted to the condenser and stirred to produce a dark red suspension. While constantly bubbling nitrogen through the reaction mixture, the suspension was rapidly heated to the required reaction temperature and held for a certain amount of time before being cooled to room temperature. Experiments were performed at either 280 °C or 310 °C, and the heating period between 30 and 720 minutes. To remove the oleylamine, acetone was added (40 cm^3), followed by centrifugation and the organic brown supernatant layer was removed. To wash the black iron sulphide nanocrystals, the solid was then resuspended in toluene, followed by centrifugation and solvent removal. This step was repeated until the supernatant layer was clear and colourless. The sample was then left in a vacuum oven at room temperature overnight and stored as a powder. Any calcined samples were placed in a furnace and heated to a specified temperature under flowing air, for 4 hours. The samples were then cooled to room temperature, stored in a glass vial and flushed with N_2 to remove any air.

2.3 Catalyst Characterisation

2.3.1 X-ray Diffraction

X-ray diffraction (XRD) is a useful technique to quantify bulk crystal phases, monitor the kinetics of bulk transformations, to estimate particle sizes, and to identify the crystallographic phases present in the material. In a diffraction experiment, X-rays are typically generated from an electronically heated filament, that emits high energy electrons. A metallic target (usually Cu Kα) is bombarded with these accelerated high-energy electrons. The collision causes ejection of electrons from an inner shell of the target, which are immediately replaced by electrons from a higher shell, causing incident X-ray photons to arise[107]. These photons are shot into a material and the crystal of the material causes the beam of the X-ray to diffract as elastic scattering. The scattered waves formed within the same phase (constructive interference) provide a diffraction pattern, geometrically relating to the lattice spacing (crystal structure) of the material (Figure 2.1). This relationship is summarised by the Bragg's law, Eq. 2.1.

$$n\lambda = 2d\sin\theta; \quad n = 1,2,3 \ldots \qquad \textit{Eq. 2.1}$$

Where:

n = an integer called the order of reflection

λ = wavelength of the X-rays

d = the distance between the two lattice planes

θ = angle (in degrees) between the incoming X-rays and the normal to the reflecting lattice plane

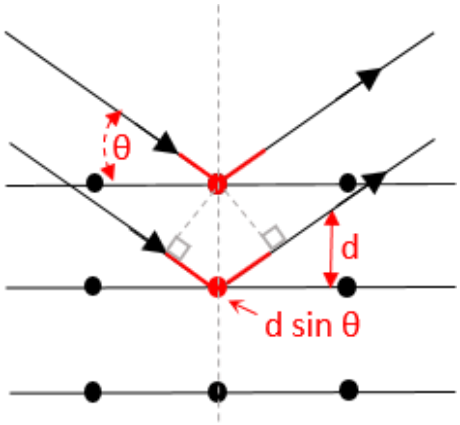

Figure 2.1: Schematic diagram of X-ray diffraction.

For a powder sample, the detector is rotated around the material to scan the intensity of the diffracted radiation as a function of the angle 2 θ between the incoming and diffracted beams. The diffraction pattern is possible because a small fraction of crystals are oriented in such a way that their plane is at the right angle (θ) with the incident beam to create constructive interference. The sample is constantly spinning throughout analysis to increase the probability of a photon hitting a crystallite orientated at a right angle, therein increasing the intensity of the signals[107].

The signals obtained in an XRD pattern can be compared with previously reported diffraction patterns in large data-bank, *via* JCPS files, allowing identification of the crystalline phases present in the sample.

Experimental

Conventional powder X-ray diffraction (PXRD) analysis of the materials was performed on a (θ-θ) PANalytical X'pert Pro powder diffractometer with a Ni filtered CuKα radiation source operating at 40 keV and 40 mA, calibrated against a Si standard. Samples were loaded onto a silicon wafer, to enhance diffraction intensity and reduce background noise, in this case only a small quantity of sample is needed. Patterns were recorded over the 2θ angular range 10-80 ° using a step size of 0.016 °. Determination of materials were carried out by direct comparison with JCPDS cards sourced from the international centre for diffraction data.

2.3.2 *In Situ* X-ray Diffraction

Using the same diffraction method as mentioned in section 2.3.1, XRD can be used to study materials *in-situ* under experimentally controlled conditions. In this instance, sample is loaded into a cell, which allows gas flow and temperature control. *In situ* XRD analysis can proceed while the sample is heated to a specific temperature for a specific amount of time, under a selected gas. This method is particularly useful for understanding how the crystal structure of a material behaves during a heat treatment.

Experimental

In-situ XRD was performed on a Panalytical X'Pert diffractometer with an Anton Paar 900 K *in-situ* cell. In this work, catalytic samples are treated in synthetic air at increasing temperatures to observe any structural changes of the material. The XRD spectra were collected at temperatures between 25 °C and 800 °C under an air flow (10 mL/min). The sample was heated at a rate of 5 °C/min and was kept for 5 min at a certain temperature before the spectra were collected.

2.3.3 X-ray Absorption Fine Spectroscopy

X-ray diffraction has an important limitation: clear diffraction peaks are only observed when the sample possesses sufficient long-range order. Therefore crystallite sizes below 100 nm causes incomplete destructive (out-of phase) interference in scattering directions, causing line broadening and smaller, less easy to determine peaks[107].

X-ray absorption fine spectroscopy (XAFS) is another absorption technique based on the photoelectric effect and is one of the leading tools for investigating the local structure environment, mostly due to the use of synchrotron radiation sources. One key attraction is that it can be used regardless of the physical form of the sample, in particular, non-crystalline materials without the need for long-range order, exceeding the limits with XRD. Analysis can

yield the numbers and types of atoms in the immediate environment of the absorbing atom. The technique is based on the absorption of X-rays and the creation of photoelectrons (ejection of a core electron), which are scattered by nearby atoms in a lattice. Each core electron has a well-defined binding energy, when the energy of an incident X-ray is scanned across one of these energies, there is an immediate increase in the absorption coefficient; this is called the 'absorption edge'. At certain energies, photoelectrons can be excited into higher energy electron orbitals, generating core holes. In order to return to the ground state, the core holes are filled by an electron from a higher energy orbital, this transition is accompanied by a release of energy. When the sample absorbs X-rays the absorption coefficient (a) can be obtained from the Beer-Lambert law (Eq. 2.2), in which I and I_0 is the intensity of the incident and transmitted radiation, respectively, and ℓ is the pathlength of the absorbing sample.

$$a\ell = log_{10}\left(\frac{I_0}{I}\right) \qquad \textit{Eq. 2.2}$$

XAFS derives from the fact that there is fine structure superimposed on the absorption edge. This fine structure is divided into two structures. Structure well above the absorption edge is referred to as extended X-ray absorption fine structure (EXAFS), providing information about metal site ligation. Structure in the immediate vicinity of the edge is referred to as X-ray absorption near edge structures (XANES), providing information primarily about geometry and oxidation state[108], the nature of XAFS is presented in Figure 2.2. The analysis of XAFS and XANES are usually two separate procedures.

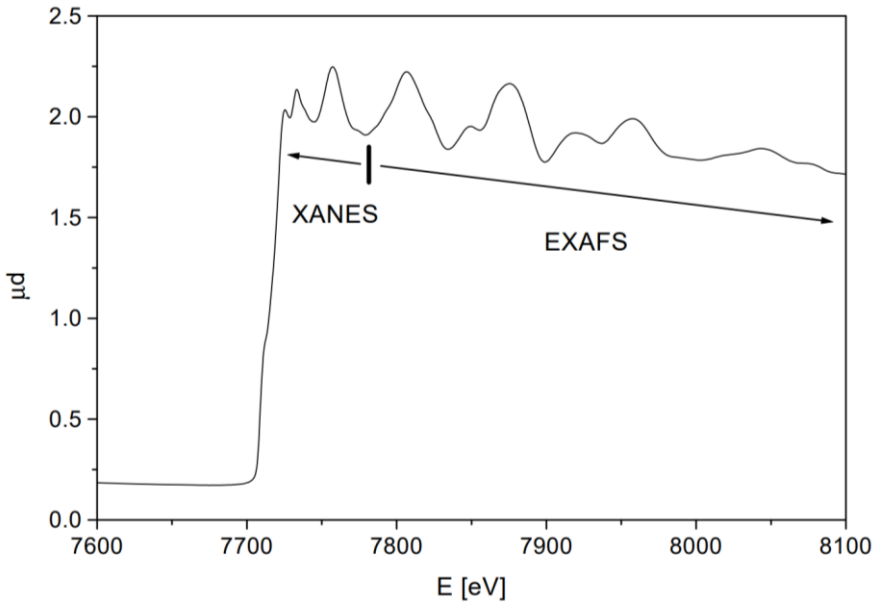

*Figure 2.2: The K-shell absorption edge of cobalt, displaying the XANES and EXAFS regions. Reproduced from reference[*109*].*

2.3.4 Extended X-Ray Absorption Fine Structure

Fine structure can be observed, in cases of X-ray absorption by diatomic molecules, in the form of intensity variations superimposed on the otherwise smoothly declining intensity of the absorption tail. This structure is known as extended X-ray absorption fine structure (EXAFS)[110]. EXAFS is the fine structure which is developed in the absorption spectrum of the material under observation over an energy range up to 1 keV above the adsorption edge[111]. 1 keV corresponding to wavelengths of 10 Å is referring to the X-ray energy range. The cause of the EXAFS is the interference between the de Broglie wave representing the photoelectron travelling onwards from one atom, and the same wave scattered by a neighbouring atom. The interference pattern from the EXAFS depends on the internuclear distance of the atoms, thus giving information such as bond distance, and neighbouring atoms.

2.3.5 X-ray Absorption Near Edge Structure

The region of the XAFS spectra within 50 eV of the absorption edge is called the X-ray absorption near edge structure (XANES), where the electron's kinetic energy is small,

therefore scattering on the neighbouring atoms is strong and inelastic losses are relatively weak[112]. When the photon energy is low, photoelectrons can populate either the unfilled or partially filled electronic states, thus electron transition can be observed as s → p, or p → d. This strongly depends on local geometry (coordination number and ligand symmetry), with the absorption edge, position and shape providing information on the oxidation state of the absorber.

Pre-edge transitions are found in the XANES spectra, where three features can appear:

- The absorption edge, E_o – defines the onset of continuum states. The energy of the edge is specific to the element analysed. E_o is a function of the oxidation state of the absorbing atom, and this increases in eV with increase in oxidation state
- The pre-edge – result of electronic transitions to empty bound states, providing information about local geometry and electronic state around the absorber
- The post-edge – reliant on multiple scatterings, providing information regarding the local atomic structure and geometry

Experimental

XAFS data was collected at the B18 beamline at the Diamond Light Source in Harwell, UK. The measurements were performed in transmission mode at Fe and Ni K edge. A Si(111) double crystal monochromator was used to select the energies. A Pt coated mirror was used to reject higher harmonics from the beam. The photon flux of the incoming and outgoing X-ray beam was detected with two ionisation chambers I_0 and I_t, respectively, filled with appropriate mixtures of N_2/Ar. A third ionisation chamber (I_{ref}) was used in series to simultaneously measure the corresponding reference metal foil. Data was processed and interpreted by Professor Andrew Beale and Dr Wilm Jones (UCL) using Athena software.

2.3.6 X-ray Photoelectron Spectroscopy

X-ray photoelectron spectroscopy (XPS) is useful for gaining information about the surface of the material, and one of the most frequently used techniques in catalysis. It helps enable the elemental composition of the surface, chemical species and oxidation states of the elements on the surface. The signal measured by XPS is an exponentially surface weighted signal, therefore exhibits an analysis depth of up to 5-10 nm below the surface.

XPS is based on the photoelectronic effect; an atom absorbs a photon of energy ($h\nu$) after which a core or valence electron with binding energy E_b is ejected with kinetic energy[107] via the Eq. 2.3.

$$E_k = h\nu - E_b - \varphi \qquad \textit{Eq. 2.3}$$

Where:

E_k - kinetic energy of the photoelectron

h - Plank's constant

ν - frequency of the exciting radiation

E_b - binding energy of the photoelectron with respect to the Fermi level of the sample

φ - work function of the spectrometer

An incident X-ray photon is absorbed ($h\nu$) and a photoelectron is then emitted ($E_b + \varphi + E_k$), photoemission results in electrons of a given kinetic energy, where the recorded energy is a combination of the binding energy of the electron and the characteristic energy of the X-ray source[113]. Considering the photo absorption has the same energy as the photoelectron emitted, measurement of this kinetic energy allows the binding energy of the photoelectron to be calculated. An XPS spectrum contains peaks due to Auger transition as well as photoelectron peaks. Following core ionisation by photoelectron emission the atom stays behind as an

unstable ion with a hole in one of the core levels, an outer shell electron can fill the created vacancy and relaxed the excited ion, the energy released can result in the emission of an electron. This electron is known as the Auger electron, and the energy released from this transition is element-specific, allowing the determination of the Auger peak from its keV value.

Photoelectron peaks are labelled according to the quantum numbers of the level from which the electron originates. An electron with orbital momentum l (0,1,2,3,.. indicated as *s,p,d,f*.) and spin momentum, *s*, has the total momentum $j = l + s$. A spin may be either up ($s = +½$) or down ($s = -½$), each level with $l \geq 1$ has two sublevels, with an energy difference called spin-orbit coupling. Thus, Pd 3d level gives two photoemission peaks, $3d_{5/2}$ (with $l = 2$ and $j = 2 + ½$) and $3d_{3/2}$ ($l = 2$ and $j = 2 - ½$).

The kinetic energy is the experimental quantity measured by the instrument, but it is dependent on the photon energy of the X-rays employed and therefore not an essential property of the material. The binding energy is a parameter which identifies the electrons specifically, in terms of the atomic energy level of the parent element, therefore the XPS spectra are usually plotted as intensity in function of binding energy.

Experimental

X-ray photoelectron spectroscopy (XPS) was performed on a Thermo Fisher Scientific K-alpha+ spectrometer and analysed with the help of Dr David Morgan. Samples were analysed using a micro-focused monochromatic Al X-ray source (72 W) over an elliptical area of approximately 400 μm. Data were recorded at pass energies of 150 eV for survey scans and 40 eV for high resolution scan with 1 eV and 0.1 eV step sizes respectively. Charge neutralisation of the sample was achieved using a combination of both low energy electrons and argon ions. Data analysis was performed in CasaXPS using a Shirley type background and Scofield cross sections, with an energy dependence of -0.6.

2.3.7 Raman Spectroscopy

A form of vibrational spectroscopy, Raman spectroscopy exploits the inelastic scattering of photons, which lose energy by exciting vibrations in the sample, known as Raman scattering. Monochromatic light of a certain frequency (ν_0) falls onto a sample. However, a vibration can be excited causing the molecule to gain energy (stokes scattering, $\nu_0 - \nu_{vib}$) or a vibration can be de-excited causing the molecule to lose energy (anti-stokes, $\nu_0 + \nu_{vib}$), see Figure 2.3 for a schematic representation. Only a small fraction of the photons that are present are due to Raman scattering, the majority of photons will undergo no energy change, known as Raleigh scattering, this is elastic scattering.

In infrared spectroscopy, not all vibrations are observable, certain selection rules must be met. For example, for a molecule to be IR active it must be able to have a change in the dipole moment. A vibration is only Raman active if it changes the polarisability of the molecule, this relates to how the electronic structure in a molecule deforms in an electric field. In this way, symmetrical molecules can be Raman active, but not IR active, as for a molecule to be IR active.

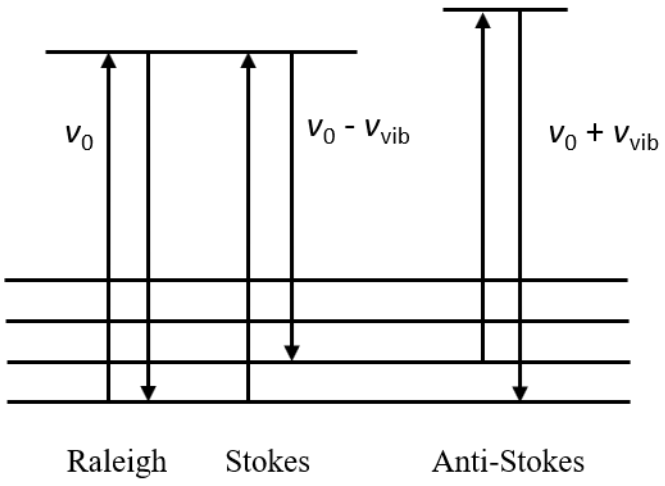

Figure 2.3: Schematic diagram of the Raman Effect.

Experimental

Raman spectroscopy was carried out using a Renishaw ramascope using spectrophysics 514 nm HeNe laser at a power of 1-10 mW. Spectra were obtained in the region of 100 – 1500 cm^{-1}.

2.3.8 Thermogravimetric Analysis

Thermogravimetry is a technique to determine the thermal stability of a material in which the mass of a sample is monitored against time or temperature, performed on a Thermogravimetric analyser (TGA). Usually a gas flow is present, nitrogen or air. TGA can reveal more information towards the material's composition and how it behaves at specific temperatures and gas flow. This is done by measuring mass gain and/or loss. In this case, when a material is heated under air, mass gain can occur from oxide formation. Mass loss can occur in the case of volatilisation of liquids or decomposition, concluding with evolution of gases from the material. The basic instrumental requirements for TGA are a precision balance and a furnace that is programmed for a linear rise of temperature with time. An empty crucible is first tared, before loaded with a small amount of sample, so its exact weight can be measured. The crucible is then connected to a high precision balance within the analyser that tracks the variation in mass as the temperature rises.

Experimental

Thermogravimetric analysis was carried out using a Perkin Elmer TGA 4000 with autosampler, under air or nitrogen flow (50 mL/min) in the range of temperature 30-900 °C with a constant heating of 5 °C/min.

2.3.9 Scanning Electron Microscopy

The scanning electron microscope (SEM) is a type of imaging technique that provides information on elemental composition and structure of the material, it is the most widely used

of all electron beam instruments. An electron beam is produced by a field emission gun, emitted by a cathode, then formed and concentrated by a system of magnetic lenses, typically within the range of 0.1-30 keV. The sample is probed by a focused beam of accelerated electrons, scanned rapidly across the surface. The beam electrons interact with the specimen atoms, transferring energy to the specimen atoms, altering the beams direction of travel. This beam electron-specimen interaction produce secondary electrons (SE) and backscattered electrons (BSE), and X-rays[114] (illustrated in Figure 2.4):

Secondary electrons – created when inelastic scattering of the beam electrons ejects weakly bound valence of conduction electrons, which have binding energies of ~ 1-15 eV to the parent atom(s). The SE are ejected with low kinetic energy and only travel short distances in the specimen, proving information about the surface topography and morphology with higher resolution at lower kinetic energies.

Backscattered electrons – a fraction of the incident beam electrons undergo sufficient elastic scattering deep within the atom, causing the electrons to return to the entrance surface and exit from the specimen in a direction approaching 180 ^{o} of the initial electron beam. The yield of BSE is dependant on the atomic number of the specimen, larger atoms produce a higher quantity of BSEs to lighter atoms thus creating a higher signal. Therefore, BSE gives information on compositional contrast between elements of the specimen[115].

The beam electron-specimen electrons also generate electron holes upon electron emission during scattering. The electron holes are filled by electrons in higher energy shells, releasing X-ray emission characteristic to the atom. This gives elemental surface information, known as X-ray energy dispersive (EDX) analysis.

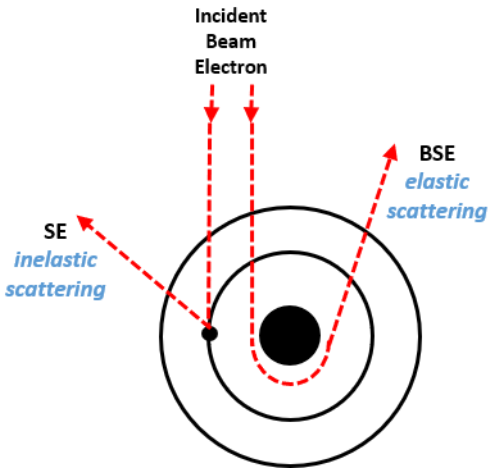

Figure 2.4: Diagram illustrating the possible interaction of electrons with the specimen during scanning electron microscopy.

Experimental

With the help of Dr Thomas Davies, scanning electron microscopy was performed on a Tescan Maia3 field emission gun scanning electron microscope (FEG-SEM) fitted with an Oxford Instruments X-MaxN 80 energy dispersive X-ray detector (EDX). Images were acquired using the secondary electron and backscattered electron detectors. Samples were prepared by dispersion in ethanol by sonication and deposited on 300 mesh copper grids coated with holey carbon film.

2.3.10 Transmission Electron Microscopy

Like SEM, Transmission electron microscopy (TEM) employs free electrons discharged from an electron gun to act on the atomic nuclei of a specimen. However, the TEM image is formed by electrons passing through the specimen (transmission), whereas for SEM, an image is created by detecting reflected or knocked off electrons from the specimen. A high energy beam of free electrons is emitted in a vacuum by a pointed filament and condensed by an electromagnetic lens, to a small spot on the specimen. Electrons are transmitted through the specimen, the resultant beam contains some of the original free electrons that have not been changed in velocity of direction, and some that have been changed in either way or both.

Another electron lens focuses the transmitted beam to an intermediate image which is enlarged by the projector lenses to form an image on a fluorescent screen. The corresponding images can be given in the so-called bright field (response of the transmitted electrons) or dark field (response of the diffracted electrons) [116].

Experimental

Operated by Dr Thomas Davies, transmission electron microscopy (TEM) were performed on a JEOL JEM-2100 operating at 200 kV. Energy dispersive X-ray analysis (EDX) was done using an Oxford Instruments X-MaxN 80 detector and the data analysed using the Aztec software. Samples were prepared by dispersion in ethanol by sonication and deposited on 300 mesh copper grids coated with holey carbon film.

2.3.11 Microwave Plasma - Atomic Emission Spectroscopy

Microwave plasma atomic emission spectroscopy (MP-AES) is a spectroscopic method used to identify and quantify dissolved metallic species present in solutions. In atomic spectroscopy, the analyte is atomised in a flame. The liquid is passed over a rapid flow of air, creating a fine mist. The mist is then directed into a spray chamber and nebulized in a nebulizer creating a fine aerosol. The steam then enters a high temperature plasma flame. This causes electrons to enter into their excited state, and the subsequent relaxation generates photon radiation. The emitted radiation has a wavelength specific to each element, thus the spectrometer that constantly monitor the changing in emission can perform qualitative analysis. Moreover, the intensity of the signal is related to the number of atoms, allowing quantitative analysis to be performed[117].

Experimental

MP-AES (Agilent 4100) was used to quantitatively determine Pd and Ru content for calculating catalytic leaching and turn-over number. Catalyst was digested in aqua regia first

(HCl/HNO_3 = 3: 1) until all solid was dissolved, before being diluted with water and manually submitted into the instrument.

2.4 Catalyst Testing

The following section describes the reactors used for this project, including the reaction set-up and the conditions required to run all the catalytic reactions.

2.4.1 High Pressure PARR Autoclave using M/Mo_2C catalysts

The hydrogenation of CO_2 to formic acid was carried out in a high-pressure stainless-steel Parr autoclave (50 mL) reactor fitted with an overhead stirrer. See Figure 2.5 for a schematic representation. In a typical run, 150 mg of the catalyst was charged into a Teflon liner containing 15 mL of 1 M aqueous NaOH solution. Then the Teflon liner was placed inside the autoclave reactor before the reactor was closed airtight. The reactor with its contents was first purged with N_2 (3 times) and then with CO_2 (3 times) to remove traces of air or oxygen from the system and then charged with 30 bar CO_2. The CO_2 was left to dissolve for 20 minutes at room temperature to allow CO_2 dissolution to saturate the solvent, before the pressure was reduced to 10 bar, then finally H_2 (additional 10 bar) was added, increasing the final pressure to 20 bar (CO_2:H_2, 1:1) at room temperature. Then the reactor was heated to the reaction temperature (100 ^oC) while stirring at 800 rpm. At reaction temperature the reaction pressure reached 26 bar. After 19 h of the reaction time the reactor was cooled to < 10 ^oC using an ice bath, the liquid sample was collected and the solid catalyst was removed *via* centrifugation followed by filtration using a syringe filter fitted with a 45 µL filter tip.

The liquid products were analysed by high performance liquid chromatography. The identity of the products (HCOOH) were confirmed using ^{1}H-NMR.

When stability tests were conducted; 4 identical reactions were run using the procedure above, the solvent was removed by filtration and the catalyst was washed twice with H_2O and once again with acetone and left to dry in a vacuum oven. The remaining catalyst was reused using

the same reaction procedure as above, washed and dried again to continue the study. The turn over number (TON) was determined as the number of moles of formic acid produced per mole of metal nanoparticle, calculated using microwave plasma atomic emission spectroscopy (see section 2.3.11), present in the catalyst used. Catalyst was digested in aqua regia first (HCl/HNO_3 = 3: 1) until all solid was dissolved, before being diluted with water and manually submitted into the instrument.

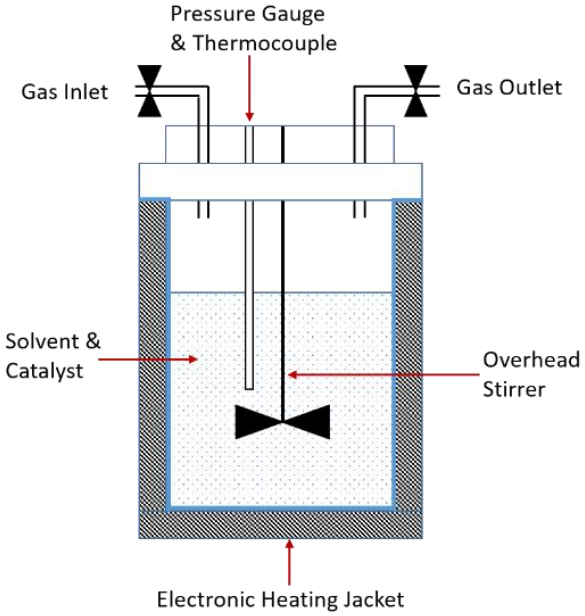

Figure 2.5: Schematic representation of an autoclave reactor.

2.4.2 High Pressure Autoclave using Iron Sulphide Catalysts

The hydrogenation of CO_2 to formic acid was carried out in a high-pressure stainless steel 10 mL autoclave. In a typical reaction, 20 mg of the catalyst was charged in a glass liner containing 4 mL of 1 M NaOH and a stirrer bar, the glass liner was placed inside the autoclave reactor before the reactor was closed air-tight. The reactor with its contents was first purged with N_2 (3 times) and then with CO_2 (3 times) to remove traces of air or oxygen from the system and then finally charged with 30 bar CO_2, the CO_2 was left to dissolve for 20 minutes at room temperature before the pressure was reduced to 10 bar, then H_2 (10 bar) was added,

resulting in a pressure of 20 bar (CO_2:H_2, 1:1) at room temperature. Then the reactor was heated to the reaction temperature (125 ^oC) while stirring at 1450 rpm. After 3 days of reaction time the reactor was cooled to < 10 ^oC using an ice bath, the liquid sample was collected and the solid catalyst was removed via centrifugation followed by filtration using a syringe filter fitted with a 45 µL filter tip. The identity of the products (HCOOH) were confirmed and quantified using proton nuclear magnetic resonance ^{1}H-NMR analysis, here 0.7 mL of reaction solution was mixed with 0.1 mL D_2O and a sealed glass tube insert containing 1 % tetramethylsilane (TMS) in $CDCl_3$ internal standard.

When stability tests were conducted; 4 identical reactions were run using the procedure above, the solvent was removed by filtration and the catalyst was washed twice with H_2O and once again with acetone and left to dry. The remaining catalyst was reused using the same reaction procedure as above, washed and dried again to continue the study.

2.4.3 Continuously Stirred Tank Reactor using M/Mo_2C Catalysts

Reactions performed in a 600 mL continuously stirred tank reactor (CSTR), were undertaken at the University of Cape Town, under the supervision of Prof. Michael Claeys. Funding for this project was provided by the ESRC/NRF-funded Newton Project.

To match the conditions of the high-pressure autoclave reaction conditions, a typical reaction proceeded as follows. The catalyst (3.5 g) was loaded into the reactor, containing 350 mL of a 1M NaOH solution. The reactor was sealed and purged with N_2 to remove any air. The reactor was then pressurised to 26 bar with He and heated to 100 ^oC. To initiate the reaction, the reactor was then fed with gas containing CO_2:H_2:N_2 = 4.5:4.5:1 (10 % N_2 required as an internal standard) at a flow rate of 18 mL/min controlled by gas regulators, and the reaction media was stirred at 500 rpm. Whilst maintaining a constant pressure, the tail-gas (resultant gas flow exiting the reactor) was fed into a gas chromatographer fitted with a thermal conductivity detector to analyse and quantify the fluctuation in gas concentrations. See Figure 2.6 for a schematic representation.

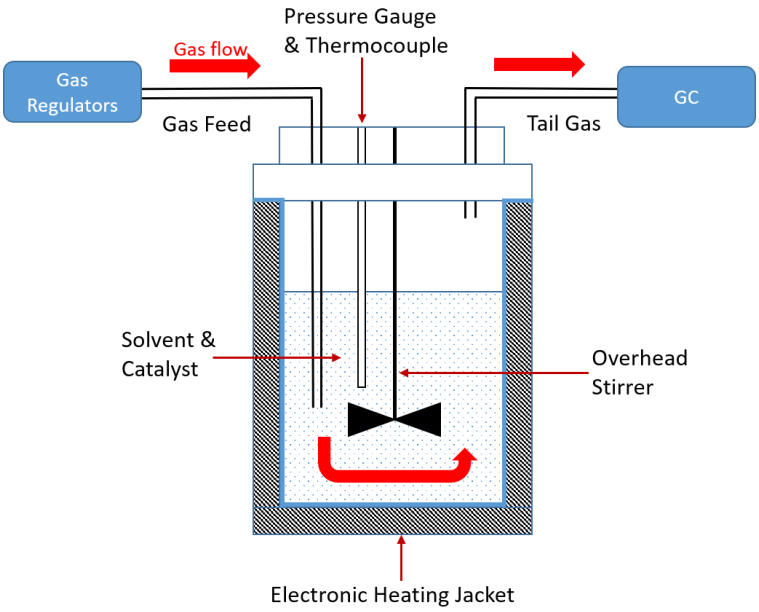

Figure 2.6: Schematic representation of a CSTR reactor.

2.5 Product Analysis

Liquid phase products were detected and quantified using high pressure liquid chromatography (HPLC) and ^{1}H-nuclear magnetic resonance (NMR). Gaseous samples were analysed using gas chromatography (GC).

2.5.1 High Performance Liquid Chromatography

Chromatography is a technique to separate a mixture of chemical compounds. High performance liquid chromatography (HPLC) represents a widely used chromatographic technique used for separation and quantification of liquid chemical mixtures, known as the eluent. The separation of eluent is determined by the affinity of the analytes to the stationary phase (the column). The length of time between injection of the sample and the elution of particular analyte is known as the retention time; thus the stronger the affinity between the analyte and the stationary phase, the longer its retention time[118].

The HPLC apparatus consists of four parts: the gas supply system (mobile phase), involving the pump to provide the high pressure required; the sample injector, the column (stationary phase) and the detector. A scheme of this is illustrated in Figure 2.7.

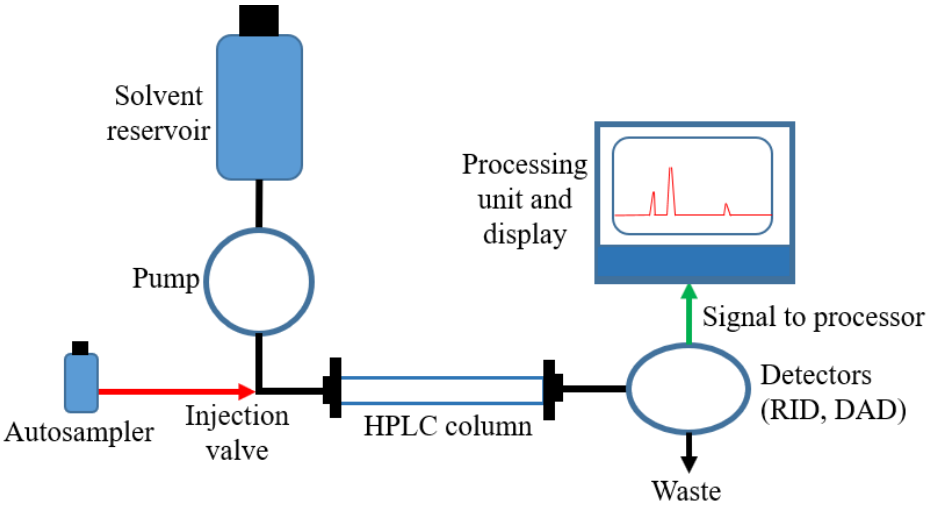

Figure 2.7: Schematic diagram of the HPLC for analysing the reaction products.

The column and the mobile phase represent the core of the separation process. The adsorption coefficient of the sample compounds between the column and mobile phase creates separation of particles, therefore effecting the time it takes the compounds to travel through the column and reach the detector. In order to minimise the diffusion time, the interaction between the column and mobile phase must be very efficient. In order to achieve this the column must be finely divided and homogeneously packed. To ensure the mobile phases passes through the column requires the use of a high-pressure pump.

There are two variants of operation in HPLC, normal phase and reversed phase HPLC; the application of these two variants depend on the relative polarity of the solvent and stationary phase.

- Normal Phase HPLC –The column is packed with tiny silica particles (polar), and the solvent is non-polar. The separation relies on adsorption coefficient. Polar compounds passing through the column will have a high affinity towards to polar silica, therefore

pass slowly through the column. Non-polar analytes will travel through with little interaction with the column, therefore achieving a shorter retention time.

- Reversed HPLC – The most commonly used form of HPLC and used in this project. This time the column is packed with modified silica particles with long hydrocarbon chains attached, making it non-polar. Therefore, here a polar solvent is used, for example water. In this case, separation relies on the partition coefficient, the polarity of the solvent effects the distribution coefficients therefore the retention factors of the analytes.

At the column exit, the flow is analysed by the detector(s):

- Refractive index detector (RID): measures the changes in refractive index of the analyte, relative to the solvent (the detector is used in this project).
- UV and diode array detectors (DAD). Spectrophometric detectors, where detection is based upon the Lambert-Beer law (the intensity of the absorption depends upon the molar absorption coefficient of the species detected).

Experimental

The HPLC used was an Agilent 1260 infinity, the liquid sample was injected into an Agilent Metacarb 67H column fitted with a refractive index detector. Method temperature ran at 25 °C with a flow rate of 0.25 mL/min with dilute phosphoric acid (0.1 vol. %) as the mobile phase. RID was used to analyse the analytes.

The HPLC was used to determine the concentration of formate formed within the reaction. For quantification, an external calibration method was used. 5 solutions of a known formate concentration were prepared (0.025 M, 0.5 M, 0.075 M, 0.1 M, 0.125 M) and injected into the HPLC, each three times. The peak area of the analyte is directionally proportional to the concentration; thus a calibration plot of concentration vs peak area can be plotted, as shown in Figure 2.8. The gradient of this plot is known as the calibration factor and can be used to calculate future unknown formate concentrations.

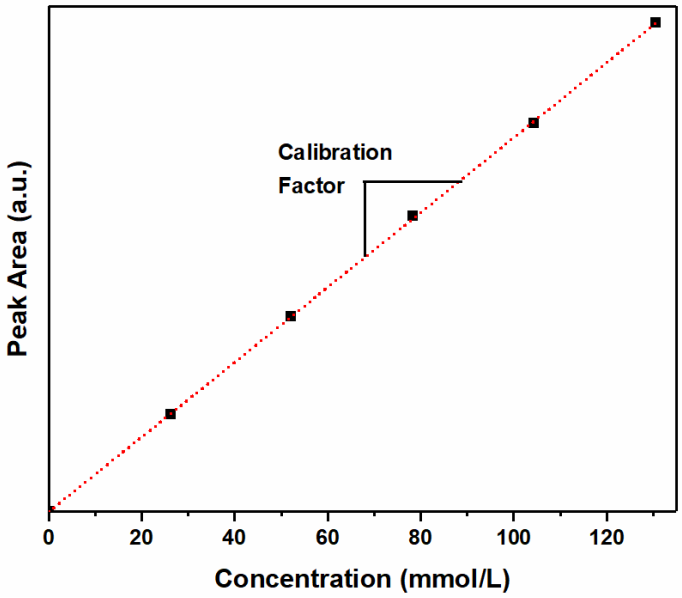

Figure 2.8: HPLC calibration plot used to calculate formate concentration of reaction mixture.

2.5.2 ^{1}H-Nuclear Magnetic Resonance Spectroscopy

Nuclear Magnetic Resonance (NMR) spectroscopy is a powerful non-destructive analytical technique enabling identification and quantification of liquid phase organic molecules, even at very low concentrations, by utilising the behaviour of the atomic nuclei in local magnetic fields. The atomic nucleus is a spinning charged particle which generates a magnetic field. The nuclei of ^{1}H has a non-zero characteristic net spin, therefore, in its natural state, the nucleus has two possible spin states: m = +1/2 (spin up) and m = -1/2 (spin down). These spin states are degenerate, *i.e.* possess the same energy. When an external magnetic field is applied, the nuclei align themselves either within or against the field of the external magnet, which leads to the removal of degeneracy (Figure 2.9). Protons that align with the external magnetic field are in a lower energy state (m_s = +1/2), protons that align against the external magnetic field are in a higher energy state (m_s = -1/2)[107].

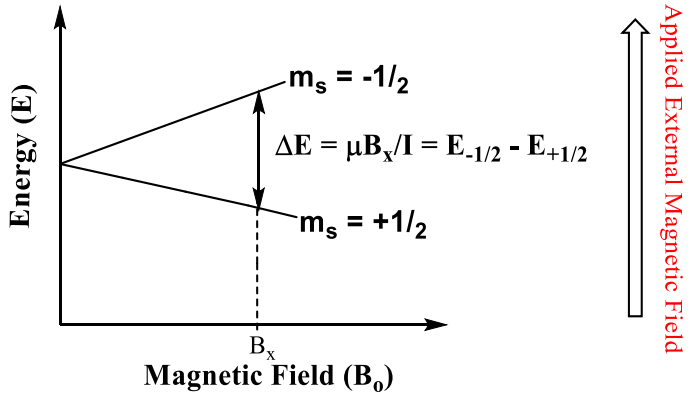

Figure 2.9: Energy level diagram illustrating effects of external magnetic field on nuclei spin states.

The energy difference of the spin states depends on the strength of the applied external magnetic field and the magnetic moment of the nuclei (μ). The greater the strength of the applied magnetic field, the larger the energy difference between the two spin states. When electromagnetic radiation, the same energy as ΔE is applied to the nucleus, the spin flips between spin states. Then the nuclei undergoes relaxation, and the nuclei return to their original state. This process emits an electromagnetic signal whose frequency depends on ΔE which is detected by the NMR spectrometer and plots a graph of signal frequency verses radiation.

The position of the signals in the NMR spectrum are based on how far they are from the signal of the reference compound tetramethylsilane (TMS), this information tells us the nature of the proton(s) responsible for the signal. The position of the signal is dependent on the "chemical shift". The magnetic field at the nucleus can be reduced due to the "shielding" effect created by the magnetic moment of the electrons that opposes the applied magnetic field. This causes the energy gap (ΔE) to reduce, creating a chemical shift in the signal. The resonant frequency is dependent on the external magnetic field, and since no two magnets have exactly the same magnetic field, different resonance signals will be obtained for the same molecule. Hence, the importance of the internal standard (TMS) is used as a reference, and any resonance signals are reported in relation to TMS, for which the signal is always equal to zero (δ = 0 ppm).

Experimental

^{1}H-NMR (Bruker 500 MHz) was used to identify and quantify the liquid phase reaction products when the signal was below the detection limit of HPLC. The chemicals shifts of the analytes were reported in ppm relative to TMS. The only product specified was formate (δ = 8.4 ppm) as shown in Figure 2.10. The NMR is equipped with a solvent suppression system to prevent the signals arising from water to dominate the spectra.

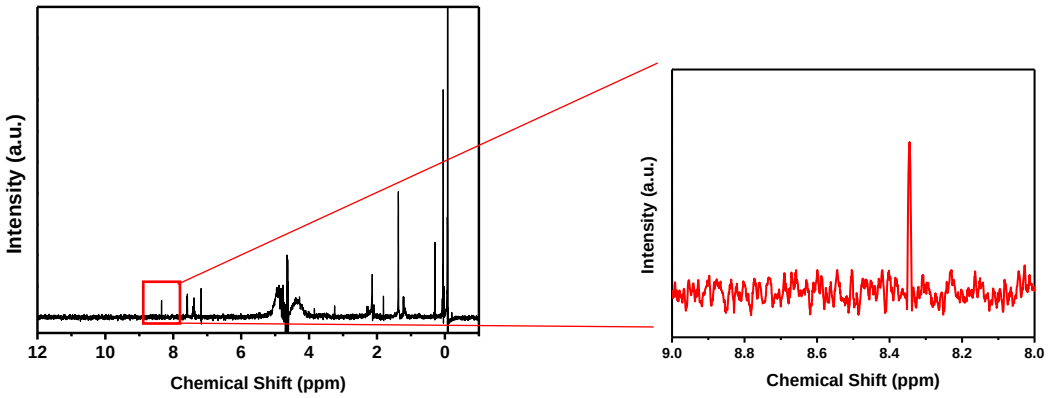

Figure 2.10: ^{1}H-NMR spectrum obtained from a typical reaction mixture. Species identified was formate (δ = 8.4 ppm). Other signals present correspond to; $CHCl_3$ (δ = 7.3 ppm), acetone (δ = 2.05 ppm), H_2O in $CDCl_3$ (δ = 1.5 ppm), TMS (δ = 0 ppm).

^{1}H-NMR analysis was performed as follows. Typically, 0.7 mL of sample with 0.1 mL of D_2O were placed in an NMR tube for analysis. The D_2O is necessary to act as a frequency lock for the H_2O solvent and generate a homogeneous magnetic field to shim the sample. The formate present were quantified against an internal standard in the form of a TMS insert; a sealed glass capillary tube containing 1% tetramethylsilane in $CHCl_3$, which was also placed in the NMR tube. The internal standard was calibrated against a series of known standard solutions of formic acid to generate a calibration curve, Figure 2.11, and response factors (slope) which were used for quantitative analyses of the reaction mixtures.

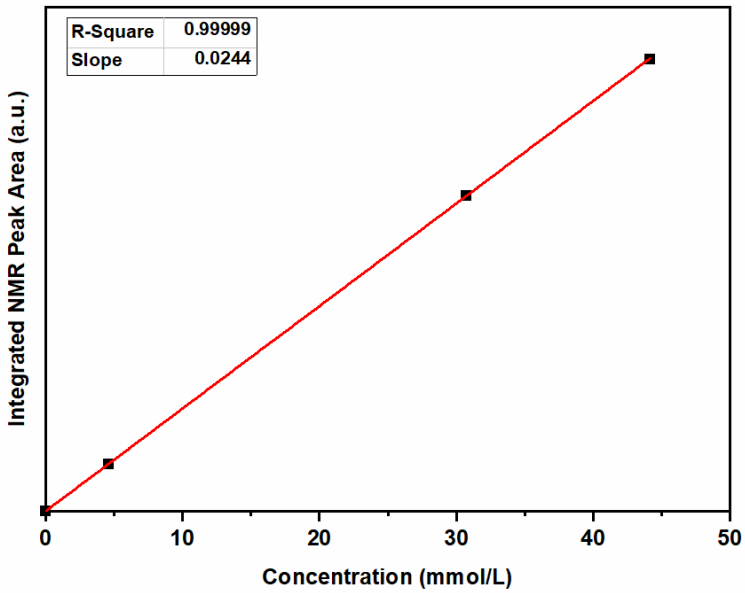

Figure 2.11: NMR calibration curve obtained from standard solutions of formate. Formate NMR peak area integrated against TMS internal standard.

2.5.3 Gas Chromatography

In addition to HPLC, gas chromatography (GC) is another chromatography technique. Instead of liquid samples, GC is used to detect and analyse mixtures of gases or products that can be easily vaporised, *i.e.* molecules possessing relatively low boiling point and sufficient thermal stability. A quantity of sample is introduced into the injector, which mixes the sample with the carrier gas, in this case He, selected for its low weight and chemical inertness. The sample then passes through a coiled temperature-controlled column, where separation between different analytes occurs.

The detector employed for this project was a thermal conductivity detector (TCD), a typical detector used in gas chromatography, which senses the thermal conductivity of the column effluent in comparison to a reference flow of carrier gas (in this case He). The TCD is composed of two thermistors. One thermistor is exposed to the carrier gas, while the other is exposed to the gas evolving from the column containing the eluted species. In the steady state, a thermal equilibrium is established between the thermal conductivity of the carrier gas and electrical current of the thermistor. When a solute elutes from the column, the composition of

the carrier gas changes resulting in modification of its thermal conductivity and consequently in the thermal equilibrium of the thermistor. This variation is proportional to the concentration of the solute. [119]

Experimental

Within continuous flow conditions within CSTR reactions, the tail gas was analysed by an online GC equipped with a TCD detector. A small sample is extracted from the tail gas every 10 minutes and entered into the GC. In the resulting chromatogram, the area of the peak is related to molar flow rates in the gas mix by their respective calibration response factors and the known flow of a reference gas (in this case N_2). To calculate the response factors, gas mixtures of a known composition (*e.g.* 5 %, 10 %, 15 %) diluted in He are analysed, and the peak areas of each gas is obtained and divided by the area of the reference gas, to give a calibration plot.

3 Liquid Phase Hydrogenation of CO_2 to Formate Using Palladium and Ruthenium Nanoparticles Supported on Molybdenum Carbide

3.1 Introduction

3.1.1 Mo_2C based catalyst

Recently, transition metal carbides (TMCs) have been reported as useful catalysts for the transformation of CO_2 into CO, methanol, methane and other hydrocarbons. Due to their promising physical and chemical properties, and low cost, TMCs have become increasingly prevalent in heterogeneous catalysis in the last few decades, either as using them as a catalyst[120–122] or as a support for metal nanoparticles[123–127], with molybdenum carbide as one of the most studied TMC in catalysis. Mo_2C can adopt a variety of crystalline forms, but it is commonly seen in two types, β-Mo_2C with a hexagonal close-packed (hcp) structure, and α-MoC_{1-x} ($x < 0.5$) with a face-centred cubic (fcc) structure. The metal/C ratio is important to consider as it effects the chemical and catalytic properties of the material, Dubois *et al.* considered a range of TMCs; Mo_2C, Fe_3C, TaC & WC, and highlighted that a higher Metal/C ratio exhibited better catalytic activity for CO_2 hydrogenation to CO and CH_4[120]. They further reported that adding Cu to Mo_2C and Fe_3C substantially increased the CH_3OH selectivity. Posada-Perez *et al.* investigated CO_2 interaction with cubic α-MoC and orthorhombic β-Mo_2C surfaces by means of density functional theory (DFT) based calculations[128]. The results indicated that β-Mo_2C with Mo-termination allows for CO_2 adsorption upon the surface and provoked spontaneous cleavage of a C-O bond in CO_2, causing carbon monoxide formation. β-Mo_2C with C-termination or α-MoC surface, were effective for CO_2 adsorption and activation however C-O cleavage was not favourable. These results indicate that a high Mo/C ratio (2:1), is by far the most active surface, also impacting the selectively towards CO_2

decomposition products through the reverse water-gas shift reaction i.e. CO, CH_4, CH_3OH, and a low Mo/C ratio (1:1) requires hydrogenation of the adsorbed CO_2 molecule to form HOCO intermediate before decomposing to produce CO, which upon further hydrogenation forms only methanol, thus achieving a good selectivity at high temperatures, albeit with low yields. These findings correlated nicely with their experimental work using Cu nanoparticles supported on β-Mo_2C to assist hydrogenation to form methanol[122], and also within agreement with Dubois. The nature of the metal nanoparticle supported on β-Mo_2C also has an effect on the favoured CO_2 hydrogenation pathway, Xu *et al.* [124] resolved that Cu displayed a high selectivity towards CO and methanol production with only one C-O cleavage, whereas Ni and Co were active for the activation and full decomposition of CO_2, showing selectivity for the production of methane (Ni case) and C_nH_{2n+2} hydrocarbons (Co case). In all these mentioned cases, CO_2 hydrogenation is performed in the gas phase and using high temperatures, only CO_2 is considered as the reactant and formic acid is not thermodynamically favoured. It is more desirable to perform the hydrogenation of CO_2 at lower temperatures where CO (a product from an endothermic reaction) is not favoured. Chen *et al.* demonstrated this by performing the CO_2 hydrogenation at 200 °C in the liquid phase for the production of MeOH, they reported metal nanoparticles supported on Mo_2C using 1,4-dioxane as the solvent [127,129]. They synthesised a series of M/Mo_2C (M = Pd, Cu, Co and Fe) catalysts, here they discussed Mo_2C acted as a co-catalyst as well as a support during the formation of CH_3OH, C_2H_5OH and C_{2+} hydrocarbons, as it performed CO_2 conversion without any other metals present.

To understand the complete picture, we must also consider the underlying chemistry between H_2 adsorption and dissociation. H_2 is a non-polar molecule, therefore is not very soluble in water as it does not readily form hydrogen bonds with water. It has been widely reported that Pd readily adsorbs and dissociates H_2 gaseous molecules[130–132] but in many cases is the limiting step due to the high energy barrier for dissociative adsorption[90]. H_2 dissociation upon Pd will be discussed in more detail later. That being said, Mo_2C also has H_2 adsorbing properties. Wang *et al.* studied the gas phase hydrogenation of nitroarenes over Mo_2C-supported Au-Pd[133], and report using Mo_2C as a support enhanced H_2 chemisorption, and consequently the

rate of hydrogenation, in comparison with Pd supported on Al_2O_3. This additional H_2 chemisorption onto the Mo_2C support can dissociate and form active hydride species. DFT calculations determine a strong electronic interaction between the β-Mo surface and H_2 (-0.67 eV) [134], with H-H bond cleavage an essentially spontaneous process. The β-C surface can also chemisorb H_2, despite a weak interaction between surface and H_2 (-0.02eV) inclusion of van der Waals forces also suggests H_2 dissociation is also likely to occur. Consequently, these results indicate that H_2 dissociation, a necessary step for hydrogenation processes, would occur on both surface terminations. With these findings, it is clear that Mo_2C is an attractive support to investigate further its potential for CO_2 hydrogenation.

3.1.2 Aqueous Alkaline Conditions

Despite Chen *et al.*'s impressive results forming methanol and C_{2+} products[127,129], they report using 1,4-dioxane as their solvent of choice; derived from fossil fuel, a probable human carcinogen and a widely-found, non-biodegradable contaminant in water sources[135]. Other organic solvents have also been reported for the liquid phase hydrogenation of CO_2, including ethanol [136]. Organic solvents have the disadvantage of being involved in the reaction itself and may play a role in the synthesis of the targeted products; hence, it is better to avoid using them. It has been reported that addition of water is effective for improving CO_2 hydrogenation to formic acid [69,137]. With this in mind; an aqueous solvent, with the benefits of improved CO_2 activation, low cost and more environmentally friendly, make it a lot more attractive solvent of choice.

CO_2 (a non-polar gas) has poor solubility in pure water (a polar solvent) as the entropy of the system is decreased (0.00362 molar fraction at 6 bar, 25 °C)[138]. This solubility increases with pressure but decreases with increasing temperature[138] due to a lower Henry's law constant, K_H ($K_{H25} = 10^{-1.47}$, $K_{H140} = 10^{-2.06}$)[139]. For reactions performed in water, the dissolution of CO_2 forms carbonic acid (H_2CO_3) which sequentially deprotonates to form bicarbonate (HCO_3^-) then carbonate (CO_3^{2-}) ions. (Eq. 3.1-3)

$CO_{2(aq)} + H_2O$	$\leftrightarrow H_2CO_{3(aq)}$	pH = 4-6	*Eq. 3.1*
$H_2CO_{3(aq)}$	$\leftrightarrow H^+_{(aq)} + HCO_3^-{}_{(aq)}$	pH = 6-10	*Eq. 3.2*
$HCO_3^-{}_{(aq)}$	$\leftrightarrow H^+_{(aq)} + CO_3^{2-}{}_{(aq)}$	pH > 10	*Eq. 3.3*

Scheme 3.1: Carbon dioxide – Carbonic acid equilibrium.

Because of these equilibria, different species dominate the aqueous medium at different pH. For example, between pH 4 and 6 CO_2 is predominantly undissociated; between pH 6 and 10, HCO_3^- predominates, achieving its maximum concentration at around pH = 8. Above pH = 10, the concentration of CO_3^{2-} progressively increases [140]; therefore increasing the pH pushes the equilibrium to increase CO_2 dissolution thereby satisfying Le Chatelier's principle. From these equilibria, and kinetic studies performed on the hydrogenation of bicarbonates at different pH values[141], it is apparent that the reaction is favourable in basic media, conditions where the actual substrate is HCO_3^- or CO_3^{2-}. The few who have used an alkaline solvent for the formation of formate from CO_2 hydrogenation include Mori *et al.* using a ruthenium-based catalyst within predominantly a $NaHCO_3$ solvent [92], Song *et al.*, using a Na_2CO_3 base, catalysed by palladium supported on chitin[91], and Patel *et al.*, using a KOH solvent for a cobalt supported on graphitic carbon catalyst[142] and lets not dismiss a large number of homogeneous catalysis systems either [141,143,144]. It should be brought to attention that when considering carbonated salts, i.e. $NaHCO_3$, Na_2CO_3, formation of formate can derive either from CO_2 reactant, or the bicarbonate/carbonate already within solution. While HCO_3^- from the sodium bicarbonate is able to form formate in the absence of CO_2 [145–148], it can be argued that the presence of CO_2 can replace any consumed bicarbonate maintaining the equilibrium, thus increasing the formate productivity.

3.1.3 Bicarbonate to Formate reaction mechanism

Studies have shown that the attack of the adsorbed H onto the HCO_3^- species is the rate determining step rather than the dissociative adsorption of H_2[90] which is a relatively

spontaneous process[134].The hydrogenation of bicarbonate can proceed through two pathways, either an active H will attack the O in HCO_3^-, forming two OH^- groups followed by release of two H_2O molecules, or the C is attacked forming HCO_3H intermediate followed by the release of one H_2O molecule. Chuan-Shu *et al.* considered both pathways *via* DFT calculations and determined that bicarbonate ion hydrogenation has a lower energy barrier when the hydride attacks the C atom rather than the O atom[149]. These results are complimented by Mori *et al.*, reporting a plausible reaction mechanism for the hydrogenation to formic acid within a $NaHCO_3$ solution[93], catalysed by palladium nanoparticles supported on TiO_2, as represented in Figure 3.1. The reaction is initiated when molecular H_2 adsorbs and dissociates on the surface creating active metal-hydride species (step I), HCO_3^- generated under basic conditions, then adsorbs onto the catalyst active site (step II) and undergoes hydrogenation form an active H to give a formate intermediate (step III). The reduction of HCO_3^- is energetically more favourable if active H attacks at the C atom of HCO_3^- rather than the O atoms. Finally, the remaining active H attacks the hydroxyl group, reducing the intermediate and formate is produced, which is desorbs off the surface along with a H_2O molecule (step IV), regenerating the initial active species. FT-IR studies of the catalyst after treatment in $NaHCO_3$ solvent and CO_2 pressure, found adsorbed HCO_3^- species, confirming the catalytic system proceeds mainly via the reduction of HCO_3^- transformed from gaseous CO_2 under basic conditions, while the involvement of the direct CO_2 activation is the minor pathway.

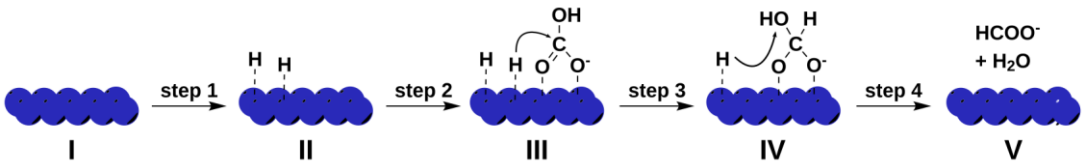

Figure 3.1: Schematic diagram representing a plausible mechanism for CO_2 hydrogenation to formate within alkaline conditions on a metal nanoparticle. Reproduced with permission from (J. Am. Chem. Soc, 2018, 140, 8902–8909). [reference 93] Copyright (2020) American Chemical Society.

3.1.4 Pd and Ru Supported Nanoparticles

We can presume from previous study that the HCO_3^- adsorbs onto the Mo_2C support before reduction with a hydride species, it is now important to also understand how H_2 plays an initial role in this mechanism. H_2 is relatively insoluble in water therefore in heterogeneous catalysis it is necessary to find a metal that readily adsorbs and dissociates the H_2 into hydride species, thus activated for further reactivity. Despite Mo_2C already presenting ability for H_2 adsorption, the amount is only minimal, and a metal species will play the role a lot more effectively. As mentioned in Chapter 1, Pd supported nanoparticles have played a dominant role as a catalytic metal for CO_2 hydrogenation, unsurprisingly so as palladium is well known metal for H_2 activation[150]. Stadler[86], Su[87], Lee[151] and Zhang[90] all demonstrate Pd's superior performance for CO_2 hydrogenation, therefore Pd is a good metal to begin this investigation with. Wang *et al.* studied palladium nanoparticles supported on nitrogen-doped mesoporous carbon[152], here they report the metallic palladium nanoclusters help the dissociative adsorption of H from H_2, the resulting Pd-H bond activates the adsorbed bicarbonate by inserting the adsorbed H into the C-OH group of the bicarbonate, before continuing the already discussed reaction pathway. Bimetallic nanoparticles have shown promise to improve catalytic activity in many cases and it is well documented that the addition of a second metal to Pd can dramatically improve the stability and resistance to sintering of supported Pd catalysts [153–155], alloying of two metals are likely to involve charge transfer between metals within close proximity driven by the differences in electronegativity of the two metals. These synergetic effects are found to stabilise the metal-support interaction and maintaining the oxidation state of the active species. As already mentioned in section 1.5, Ru also has a reputation for its catalytic CO_2 hydrogenation[82–84], when alloyed with Pd, reports have shown supported bimetallic RuPd nanoparticles enhance the stability of the nanoparticle, thus improving its catalytic activity, as found for the hydrodeoxygenation of levulinic acid to γ-valerolactone[156,157].

If we consider metallic Pd and/or Ru supported on Mo_2C, both metal and support playing an active role in H_2 splitting and HCO_3^- activation respectively, this support/metal interface is already showing huge potential for an interesting catalyst to investigate.

3.1.5 Aim of the Chapter

In this work I aimed to begin the study of CO_2 hydrogenation in the liquid phase, beginning by understanding the effect of CO_2 dissolution within an alkaline base, thus studying the role of $NaHCO_3$, Na_2CO_3 and NaOH in more detail, and selecting the correct base for the duration of the work. Molybdenum carbide is selected as an appropriate support to begin the study and palladium is confirmed as the most effective metal for catalysis. Optimising the preparation of Pd nanoparticles supported on Mo_2C was an important step, via a simple wet impregnation method as explained in Chapter 2. The study continues by focusing on the deactivation of the catalyst, understanding the deactivation using FEG-SEM, HR-TEM and XPS characterisations and finding ways of improving the stability of the material by adding a second metal as a bimetallic catalyst. Other catalyst characterisations also include XRD and MP-AES.

3.2 CO_2 hydrogenation – High Pressure Autoclave

3.2.1 Preliminary Catalytic Tests

Monometallic M/Mo_2C (M= Pd, Ru, Au, Ni, Cu, Fe, Co) were prepared *via* the modified wet-impregnation method with a 1 weight % loading and tested for the CO_2 hydrogenation reaction, using an aqueous 1M $NaHCO_3$ solution as solvent. Results presented in Figure 3.2 show that Pd/Mo_2C is by far the most active catalyst for CO_2 hydrogenation producing 1.30 mmol of formate, followed by Ru/Mo_2C (0.24 mmol) and Ni/Mo_2C (0.025 mmol). No other products were detected in the liquid phase or gaseous phase, *via* HPLC or GC analysis respectively. Based on this result, Pd/Mo_2C was used as the catalyst for further tests.

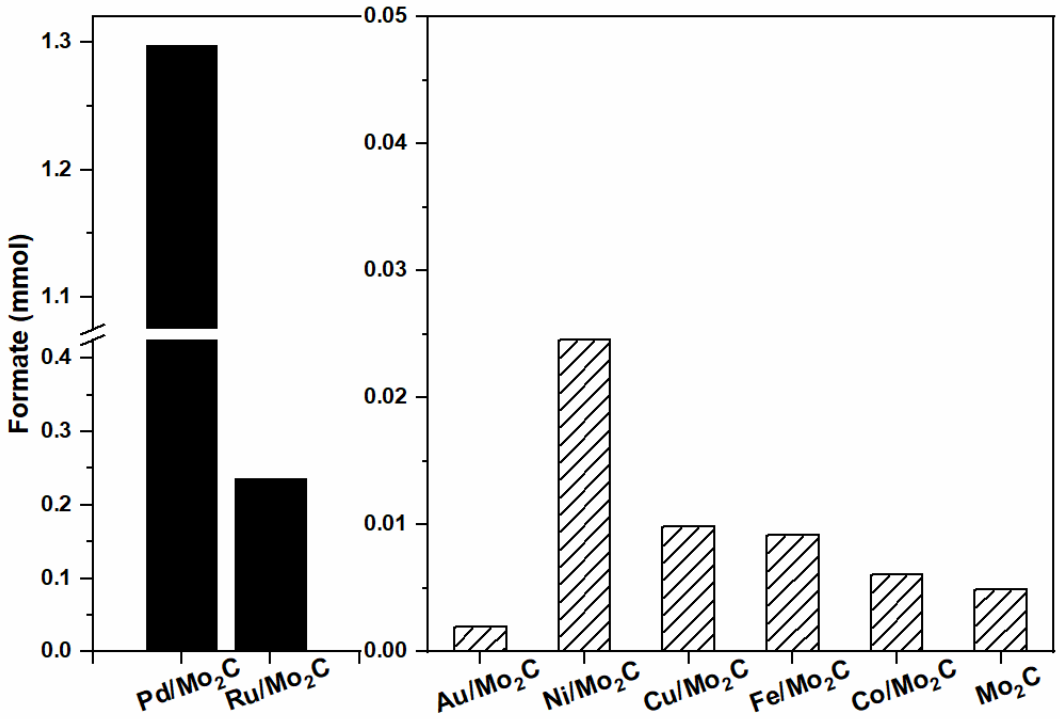

Figure 3.2: Screening of different monometallic nanoparticles supported on Mo_2C for CO_2 hydrogenation reaction. Reaction conditions: 1 wt.% M/Mo_2C: 200 mg; stirring speed: 800 rpm; 1 M aqueous $NaHCO_3$ solution: 20 mL; pCO_2: 10 bar (at 25 °C); pH_2: 10 bar (at 25 °C); reaction temperature: 100 °C; reaction time: 24 h. Black bars refer to first y-axis, lined bars refer to second y-axis.

A blank reaction of usual reaction conditions but no catalyst resulted in no product formation. Mo_2C alone managed to produce formate with no supported metal, confirming that although only a small amount of product was formed (0.0049 mmol), the support material holds catalytic activity. Therefore, when acting as a support for metal nanoparticles, it also acts as a co-catalyst for the reaction. To confirm Mo_2C was an appropriate support material for this reaction, Pd supported on CeO_2, a comparable basic metal oxide support, was also tested and found that it was approx. 5x less active than Pd/Mo_2C, forming only 0.204 mmol of formate (Table 3.1 on page 67).

3.2.2 Selecting an Appropriate Base

As discussed in the introduction section, for CO_2 hydrogenation reactions, an alkaline solution is vital to improve the solubility and reactivity of CO_2 and thereby increase the yield of desired product(s). In order to choose the most appropriate base, the hydrogenation reaction was carried out using different bases ($NaHCO_3$, Na_2CO_3 and NaOH), at a 1M concentration with and without CO_2, using 1% Pd/Mo_2C catalyst at 100 ^oC for 19 h. Under our reaction conditions, it was a surprise to observe more formate was formed from an aqueous $NaHCO_3$ solution without the presence of CO_2 (1.91 mmol) compared to the reaction with CO_2 (1.18 mmol), a decrease of approximately 38% (Figure 3.3). This effect may be due to the dissolution of acidic CO_2 affecting the pH and thus the equilibrium of the carbonate species, reducing the amount of HCO_3^- active species available in solution for further hydrogenation. Na_2CO_3 again produces formate in the absence of CO_2, but more formate was formed in the presence of CO_2 (0.75 mmol) than in the absence of CO_2 (0.52 mmol). When NaOH was used, needless to say, formate was formed only in the presence of CO_2 (0.82 mmol). With this in mind, it was clear to choose NaOH as an appropriate solvent for the rest of the study, giving clarity that 100% of formate formed is resolved indirectly from the reactant CO_2 gas.

A 1M NaOH solution situates as pH=14. To gain a better understanding of the pH of the reaction system, the reactor was loaded with 1M NaOH solvent and charged with the usual amount of CO_2 and H_2. After 10 minutes of stirring, the reactor was depressurised, opened and the pH of the solvent was quickly measured, obtaining a value of pH 8. It should be noted that this test is not an accurate representation of the true pH within reaction conditions, as during depressurisation some CO_2 will exit the solvent, increasing the pH by approximately 1-2 pH units. It is well established that between pH 6-10, the dissolved CO_2 forms predominantly HCO_3^- species, hence with confidence, HCO_3^- is considered as the intermediate in the formation of formate.[140]

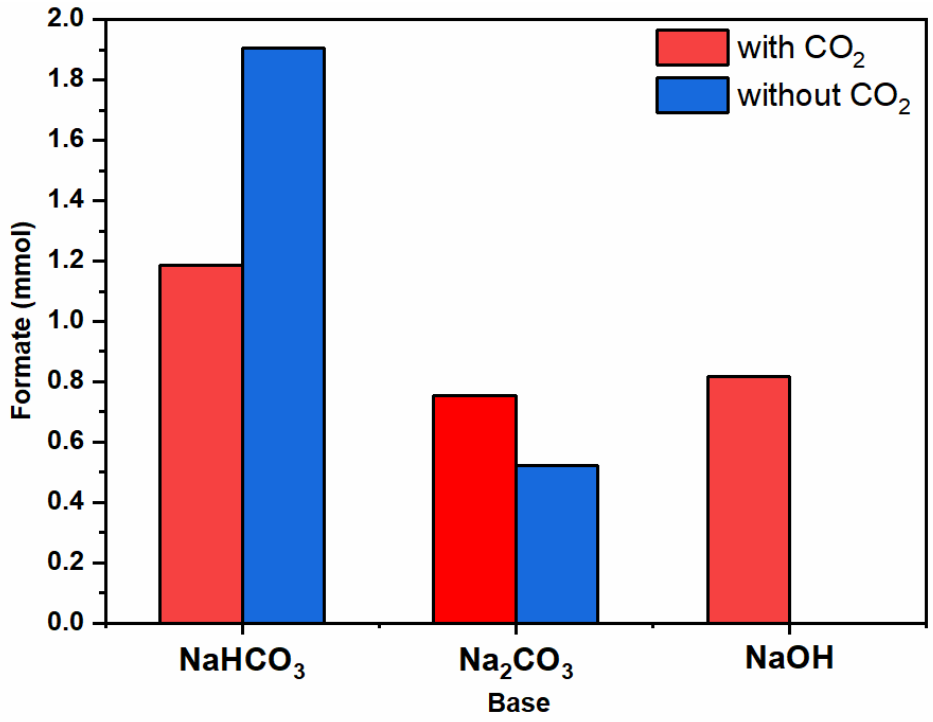

Figure 3.3: Production of formate using different bases ($NaHCO_3$, Na_2CO_3 and NaOH) with CO_2 (red) and without CO_2 (blue). Reaction conditions: 1% Pd/Mo_2C: 200 mg (Pd: 0.018 mmol); 1 M aqueous base: 20 mL; pCO_2: 10 bar (25 °C); pH_2: 10 bar (25 °C) for reaction with CO_2; pN_2 10 bar (25 °C) pH_2: 10 bar (25 °C) only for reaction without CO_2; reaction temperature: 100 °C; reaction time: 24 h.

3.2.3 Optimising Catalyst Preparation

The catalytic properties of any supported metal catalyst depend on its structural properties, such as particle size and morphology for monometallic catalysts and additional composition and nanostructure for bimetallic catalysts [105,158–161]. A number of synthesis strategies can be tested to control these structural properties of monometallic and bimetallic supported Pd catalysts. In an effort to tune the structural properties of the Pd/Mo_2C catalyst, four different Pd/Mo_2C structures were synthesised using modified wet-impregnation (MIm) and sol-immobilisation (SIm) methods [104,156,162]. The first two catalysts, 1% Pd/Mo_2C and 5% Pd/Mo_2C were prepared using MIm method. Here an aqueous solution of Pd precursor was used, where $PdCl_2$ is dissolved in 0.58M HCl solution. By altering the acid content of the precursor, and metal weight loading supported on the catalyst, are all factors that may affect the activity of the catalyst. For the purpose of simplicity these will be labelled 1% Pd/Mo_2C-

MIm (0.58M) and 5% Pd/Mo_2C-MIm, respectively. Another 1% Pd/Mo_2C was prepared using another precursor solution where $PdCl_2$ was dissolved in a 2M HCl solution, labelled 1% Pd/Mo_2C-MIm (2M). Previous reports show that addition of excess of Cl^- ions (*via* the addition of either HCl or NaCl) during the wet-impregnation procedure controls the particle size and morphology of supported AuPd catalysts [104]. Recently Li *et al.* reported the beneficial effect of the addition of excess chloride during the preparation of bimetallic PdRe catalyst for glycerol hydrogenolysis [163]. Finally, the fourth catalyst was synthesised using SIm also using an aqueous solution of Pd precursor, where $PdCl_2$ is dissolved in 0.58M HCl solution. This catalyst is be labelled 1% Pd/Mo_2C-SIm.

All the four Pd catalysts were tested for CO_2 hydrogenation and the formate yields are presented in Table 3.1. The 1% Pd/Mo_2C-MIm (2M) prepared from the precursor in 2M HCl was found to be much more active (1.53 mmol) in comparison to the 1% Pd/Mo_2C-MIm (0.58M) prepared from 0.58M HCl (1.09 mmol). However, 5% Pd/Mo_2C-MIm catalyst gave only 2.14 mmol of formate under the same reaction conditions. For this catalyst, in spite of a 5-fold increase in Pd content compared to 1% Pd/Mo_2C-MIm (0.58M) catalyst, the increase in formate yield is less than 2-fold. 1% Pd/Mo_2C-SIm was the least successful for formate production of the four catalysts (0.39 mmol). To normalise the formate productivity the turnover number (TON) must be calculated. TON is a useful calculation to determine the catalytic productivity with respect to the amount of available active sites per unit mass or volume, therefore can be regarded as a universal measure within catalysis. Usually, the turnover number is calculated using the number of available active sites determined indirectly using chemisorption techniques. Catalyst surface area and Pd surface content analysis was attempted *via* CO chemisorption, however this proved unsuccessful, due to the low surface area of the support likely resulting in low surface area of large nanoparticles. Therefore, the next available method for determining TON is by calculating the total number of moles of Pd, rather than the number of active metal atoms. However, this will result in a lower TON than the true value, as many Pd atoms are not active on the surface of the nanoparticle. The total number of Pd moles can be determined by catalyst digestion and MP-AES, presented in Table

3.1. Actual Pd contents of all the MIm catalysts were found to be closer to the nominal loading (calculated from the amount of Pd precursor added during the catalyst preparation). The actual loading of the SIm catalyst (1% Pd/Mo_2C-SIm) was found to be less than the expected nominal loading, likely due to inefficient immobilisation of Pd nanoparticles onto the support and their subsequent loss during the washing of catalyst. The TON of all the catalysts were calculated as moles of formate produced per mole of Pd, based on the actual amount of Pd. These TON results presented in Figure 3.4, indicate that 1% Pd/Mo_2C-MIm (2M) catalyst prepared from a 2M HCl solution is the most active catalyst exhibiting a TON of 109. Chen *et al.*, who have previously reported M/Mo_2C for CO_2 hydrogenation, have avoided the use of $PdCl_2$ precursor during catalyst preparation as they report that the chlorine ions poison the catalyst surface and consequently reduce their catalytic activities[129], which is not the first time Cl^- ions has considered as a poison[164,165]. However, a contradicting report by Sankar *et al*. found Cl^- ions aid the dispersion of metal nanoparticles along the support surface[104]. Our results clearly suggest that the addition of an excess of Cl^- ions, during the preparation of 1% Pd/Mo_2C-MIm (2M) catalyst, is beneficial and 1% Pd/Mo_2C-MIm (2M) was thus selected for the continuing studies in this report.

Table 3.1: Calculated Pd weight percentage and formate productivity using different Pd/Mo2C catalysts

Catalyst	**Pd loading (wt. %)[b]**	**Formate [a] (mmol)**
1% Pd/Mo_2C-MIm (0.58M)	1.09	1.09
5% Pd/Mo_2C-MIm	5.16	2.14
1% Pd/Mo_2C- MIm (2M)	1.02	1.53
1% Pd/Mo_2C-SIm	0.80	0.39
1% Pd/CeO_2	1.00	0.204

[a] Reaction conditions: Pd/Mo_2C: 150 mg; 1 M aqueous NaOH: 15 mL; pCO_2: 10 bar (at 25 °C); pH_2: 10 bar (at 25 °C); reaction temperature: 100 °C; reaction time: 19 h.

[b] Determined by MP-AES. Catalysts were digested in aqua regia to dissolve the metal and diluted in H_2O prior to analysis.

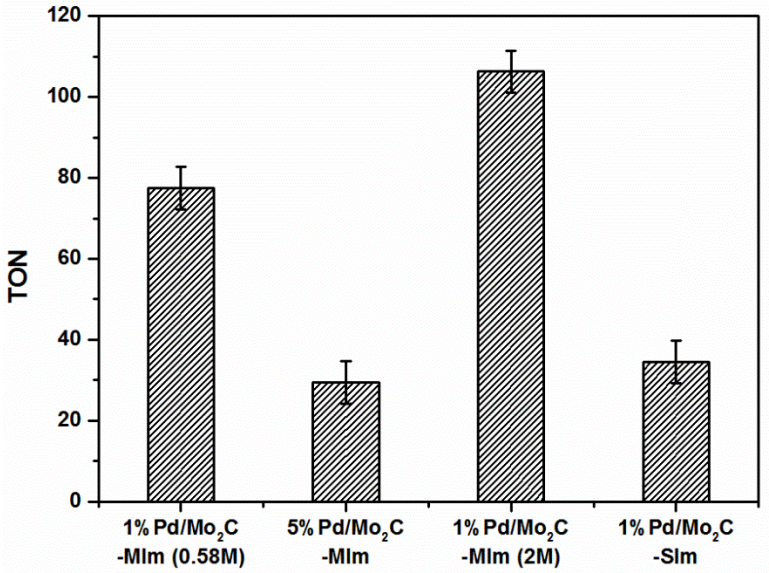

Figure 3.4: Comparison of TON for different Pd/Mo_2C catalysts for the hydrogenation of CO_2 to produce formate. TON is the mol of formate produced per mol of Pd calculated from MP-AES. Reaction condition: Pd/Mo_2C: 150 mg (1 wt.% = 0.014 mmol Pd, 5 wt.% = 0.7 mmol Pd); 1 M aqueous NaOH: 15 mL; pCO_2: 10 bar (at 25 °C); pH_2: 10 bar (at 25 °C); reaction temperature: 100 °C; reaction time: 19 h.

3.2.4 Investigating Catalytic Activity and Optimisation

Time on line (TOL) data (Figure 3.5a) for 1% Pd/Mo_2C-MIm (2M) catalyst, show that the formation of formate increases steadily with time until 19 h (1.53 mmol of formate) after which time the productivity starts to plateau (1.58 mmol after 24 h). The hydrogenation of CO_2 was also tested at different temperatures (75, 100, 125 and 150 °C) and the formate productivity also increases (Figure 3.5b) with increase in reaction temperature, which is in line with many reported trend.[81,85] At 75 °C, 0.81 mmol of formate was produced and increasing the temperature to 125 °C, sees a remarkable increase in formate productivity, achieving 4.30 mmol of formate, with a TON of 307. At 150 °C, formate production increases again to 5.26 mmol. The initial activity (turn over frequency, TOF) for the CO_2 hydrogenation is calculated from the data presented on page 82. TOF was calculated as moles of formate produced with per mole of metal per unit of time (hours). The TOF of 1% Pd/Mo_2C-MIm (2M) at 100 °C is ~ 14.1 h^{-1} during the first initial 2 hours. It then decreases steadily in an approximately exponential way, until it reaches a final activity of 4.6 h^{-1} after 19 hours. For a

125 °C reaction, we see a TOF of approximately 42.5 h^{-1} during the first 2 hours, and after 19 hours this drops to 16.2 h^{-1}. This result is comparable to Mori *et al*'s Pd/TiO_2 and $PdAg/TiO_2$ catalysts, achieving TOFs of 12 and 31 h^{-1} respectively[93], also their Ru/LDH catalyst, with TOF of 29. However, this catalyst indeed has a lot of competition and achieves TOFs less than Song *et al.*'s Pd/Chitin (TOF=257 h^{-1})[91] and Maru *et al.'*s Pd/g-C_3N_4 (TOF=660 h^{-1})[89] both achieving results at higher pressure but lower temperatures.

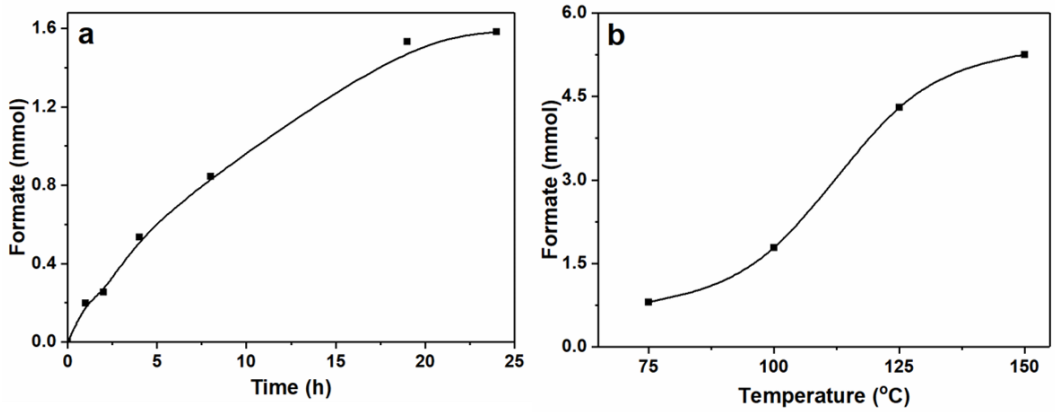

Figure 3.5: [a] Time on line evolution of formate over 1% Pd/Mo_2C catalyst. Reaction condition: 1% Pd/Mo_2C-MIm (2M): 150 mg (0.014 mmol Pd); 1 M aqueous NaOH: 15 mL; pCO_2: 10 bar (at 25 °C); pH_2: 10 bar (at 25 °C); reaction temperature: 100 °C. [b] Effect of temperature on the production of formate. Reaction condition: 1% Pd/Mo_2C-MIm (2 M): 150 mg (0.014 mmol Pd); 1M aqueous NaOH: 15 mL; pCO_2: 10 bar (at 25 °C); pH_2: 10 bar (at 25 °C); reaction time: 19 h.

A weight loading of 5% Pd supported on Mo_2C proved less effective than a 1% weight loading (Figure 3.4). This is likely due to agglomeration effects; higher weight loadings means more Pd atoms within a close proximity to each other, initiating agglomeration of nanoparticles. This can create larger nanoparticles exhibiting low surface areas, limiting active sites available for reaction. Therefore, weight loading optimisation is key. Catalysts with weight loadings <1% were also prepared and tested for their catalytic activity, the results are presented in Figure 3.6. 1% Pd/Mo_2C-MIm (2M) produces the best TON in comparison to all tested catalysts. Therefore a 1% Pd weight loading was continued throughout the study.

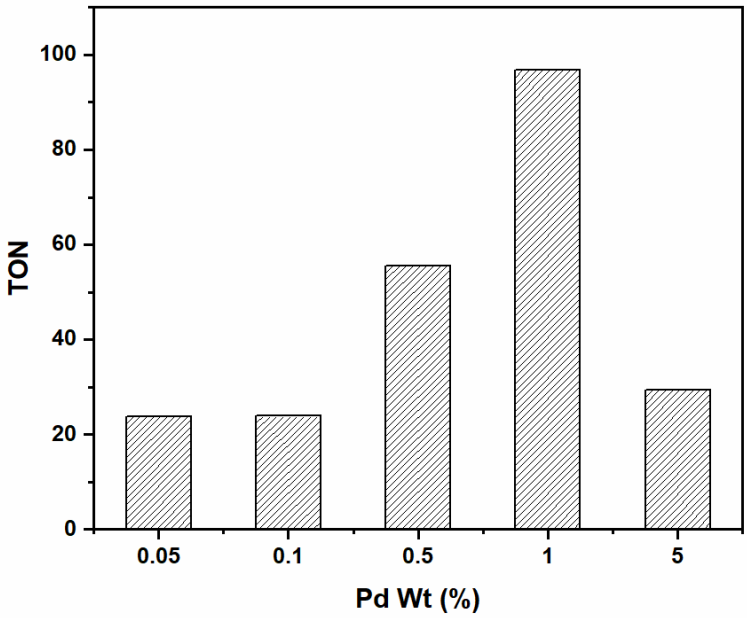

Figure 3.6: Effect of Pd loading (weight percentage), on formate production represented as TON (Formate mmol/Pd mmol). Actual Pd wt. % calculated by MP-AES. Reaction condition: Pd/Mo_2C-MIm: 150 mg (0.05 %, 0.1 %, 0.5 %, 1 % & 5 % Pd); 1 M aqueous NaOH: 15 mL; pCO_2: 10 bar (at 25 ^oC); pH_2: 10 bar (at 25 ^oC); reaction temperature: 100 °C.

The pH of the reaction medium is an important parameter for the dissolution, activation and hence the hydrogenation of CO_2. As mentioned previously, upon CO_2 dissolution, the pH of 1M NaOH solution (pH = 14), dropped to ~pH 8 within 10 minutes as bicarbonate species formed in solution. Hence the hydrogenation of CO_2 to formate can be represented as HCO_3^- + H_2 → HCO_2^-, releasing a water molecule. The concentration of NaOH will effect the pH of the solution, therefore effecting the concentration of CO_2 active species dissolved within solution. Different concentrations of NaOH solution (1, 0.5, 0.1 & 0.05M) were compared. In comparison to a 1M NaOH, reducing the concentration by half (0.5 M), halved the amount of $HCOO^-$ formed and the same effect occurred with 0.1 and 0.05 M NaOH solutions (Figure 3.7); when no base is added to the reaction solution, the formate production is negligible, resulting in direct correlation between NaOH concentration and formate production.

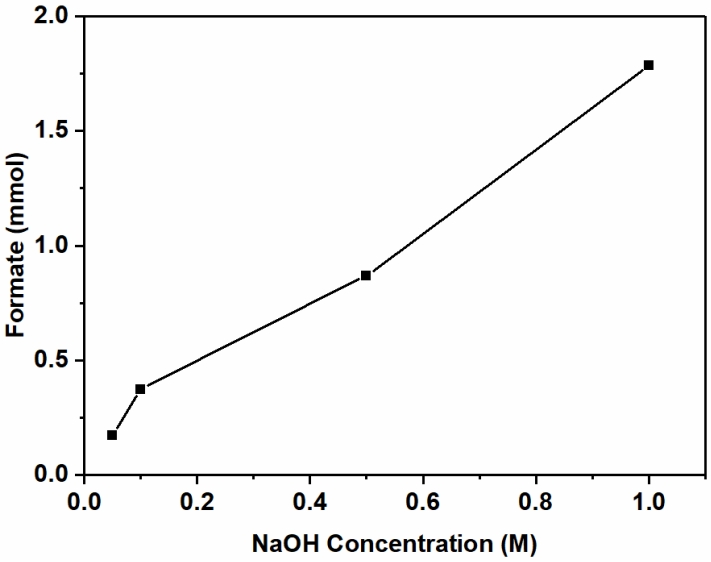

Figure 3.7: Effect of NaOH concentration on the production of formate. Reaction conditions: 1% Pd/Mo_2C-MIm (2M): 150 mg (0.014 mmol Pd); aqueous alkaline solution of various NaOH concentration: 15 mL; pCO_2: 10 bar (at 25 ^oC); pH_2:10 bar (at 25 ^oC); temperature: 100 ^oC; reaction time: 19 h.

3.2.5 Deactivation Studies

After optimising the reaction conditions, the heterogeneous nature of 1% Pd/Mo_2C-MIm (2M) catalyst was studied using the hot filtration method. Under the usual reaction set up, the catalyst was removed by filtration after 4 h of reaction while the reaction media was still warm, the reaction media was then re-entered into the reactor and the reaction continued in the absence of the catalyst. After 4 hours of reaction, 0.6 mmol of formate was produced. After 20 h of further reaction without catalyst, there was no increase in the formate yield, Figure 3.8 . This provides evidence that any leached Pd ions dissolved within the reaction media (if any) were insufficient for catalytic activity, thus proving the heterogeneous nature of the 1% Pd/Mo_2C-MIm (2M) catalyst.

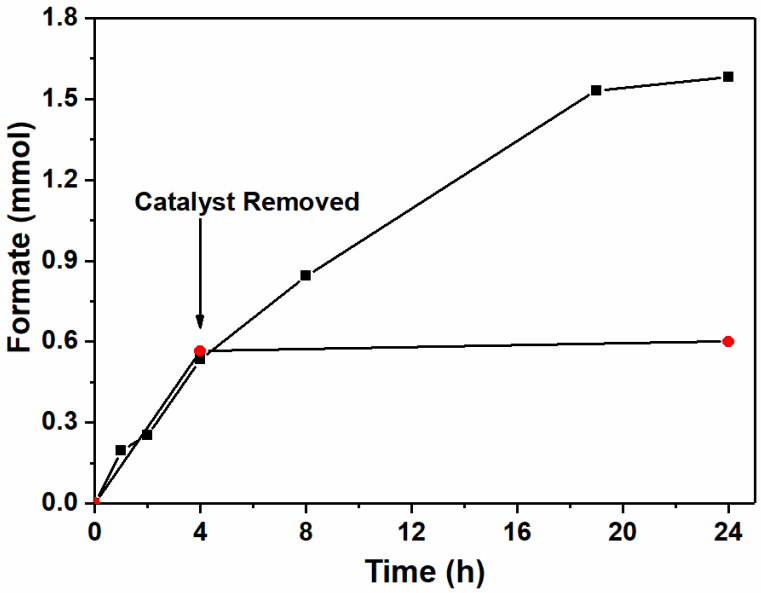

Figure 3.8: Catalyst filtration study to show that leaching of Pd is not responsible for the catalytic activity. 1% Pd/Mo_2C catalyst was filtered after 4 h of the reaction and the reaction was continued with the filtrate until the overall reaction time reaches 24 h (circle). A time-on-line profile of the hydrogenation of CO_2 in the presence of the catalyst is also given for comparison (square). Reaction conditions: 1% Pd/Mo_2C-MIm (2M): 150 mg (0.014 mmol Pd); 1 M NaOH: 15 mL; pCO_2: 10 bar (at 25 °C); pH_2: 10 bar (at 25 °C); reaction temperature: 100 °C.

A robust catalytic material with the stability for repetitive uses is a key component for a good catalyst. The stability and reusability of the Pd/Mo_2C catalyst was tested by recycling the catalyst two times for CO_2 hydrogenation reactions under identical reaction conditions, as represented in Figure 3.9a. The 1% Pd/Mo_2C-MIm (2M) catalyst displayed a large drop in the catalytic activity from 1.54 mmol of formate for the fresh catalyst to the 0.28 mmol after the 2nd reuse; an 82% drop in the catalytic activity (Figure 3.9a). Despite this unfortunate result, methods can be employed to try and improve the reusability of the catalyst. Commercial Mo_2C is typically found to have very low surface area (area of <1 m^2/g), in this instance Brunauer-Emmett-Teller (BET) and CO chemisorption results of Pd/Mo_2C was below the detection limit of the analyser. It has been reported that synthesised Mo_2C can have a much higher surface area of 151 m^2/g [129]. Therefore, increasing the support surface area would be expected to decrease the size of the supported metal nanoparticles and thus improve the catalyst stability. In an effort to improve the stability of the Pd/Mo_2C catalyst, a fresh batch of β-Mo_2C was

synthesised in the lab, sourced from Glasgow university. These materials were found to have a slightly improved surface area of approximately 13 m^2g^{-1} compared to commercial source and was used as the support for the synthesis of 1% Pd/Mo_2C catalyst. For the purpose of simplicity, this catalyst will be labelled 1% Pd/Mo_2C-Sy. Another approach to improve catalytic performance is to synthesise a Pd-based bimetallic catalyst, as discussed in the introduction of this chapter. Two Pd catalysts were prepared, in an attempt to improve the stability of Pd/Mo_2C catalyst, based on the two approaches mentioned above; 1% Pd/Mo_2C-Sy was prepared using home-made β-Mo_2C and a bimetallic 1% RuPd/Mo_2C (commercially sourced Mo_2C). Ruthenium was chosen as it was found the second most active metal within this reaction as a monometallic catalyst (Figure 3.2). Lab-synthesised β-Mo_2C support neither improved the catalytic activity nor the stability of 1% Pd/Mo_2C (Figure 3.9d). Bimetallic 1% RuPd/Mo_2C displayed lower activity, however, a much better stability is observed compared to the monometallic 1% Pd/Mo2C-MIm (2M) catalyst. For the monometallic catalyst, after the 2nd reuse, an 82% overall reduction in activity was observed, whereas for the bimetallic RuPd catalyst, only a 30% overall drop in activity was observed (Figure 3.9c). It should be noted that loading the lab synthesised β-Mo_2C with RuPd bimetallic nanoparticles was dismissed as the commercial and synthesised supports produced the similar results when loaded with Pd monometallic nanoparticles.

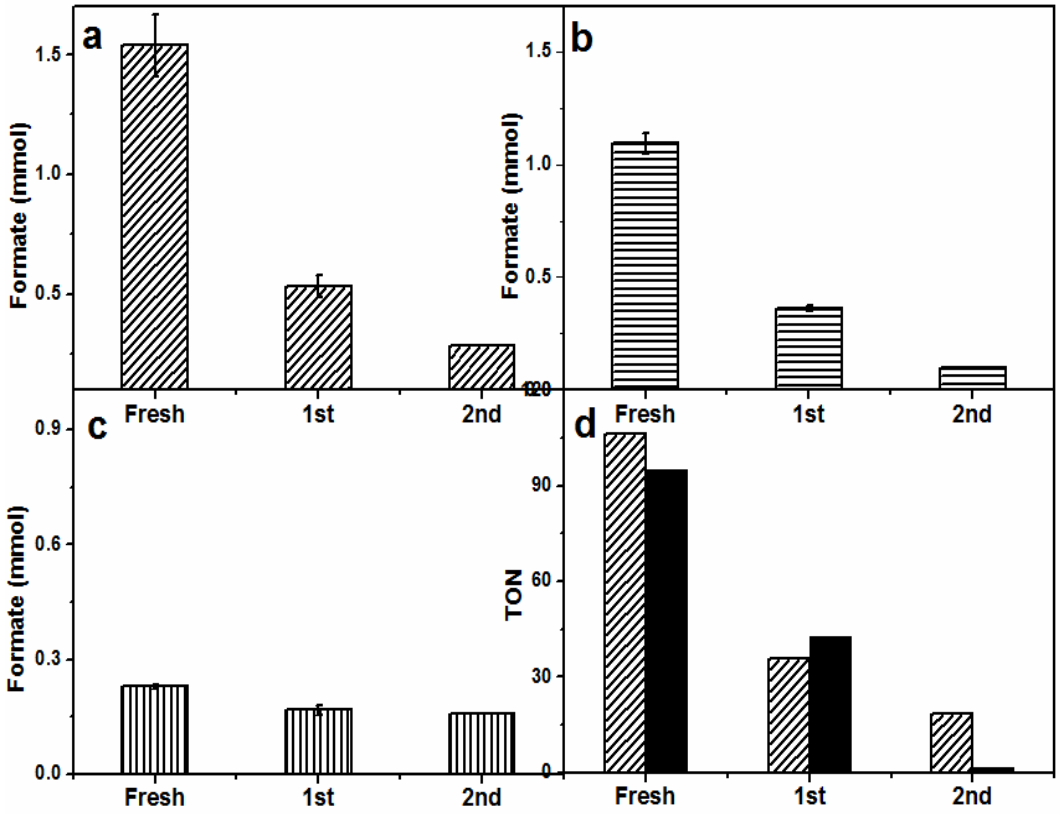

Figure 3.9: Stability studies of Pd/Mo_2C and RuPd/Mo_2C catalysts. All catalysts were reused 2x. (a) Formate formed with 1% Pd/Mo_2C-MIm (2M), (b) Formate formed with Pd/Mo_2C-MIm (0.58M), (c) Formate formed with 1% RuPd/Mo_2C, (d) TON of formate production from 1% Pd/Mo_2C-MIm (2M) with commercially sourced Mo_2C (patterned bar) and 1% Pd/Mo_2C-Sy with lab synthesised Mo_2C (solid bar). Reaction conditions (a-c+d (patterned bar)): M/Mo_2C: 150 mg (monometallic: 0.014 mmol Pd) (bimetallic 0.007 mmol (Pd,Ru)); 1 M NaOH: 15 mL; pCO_2: 10 bar (at 25 °C); pH_2: 10 bar (at 25 °C); temperature: 100 °C; reaction time: 19 h. Reaction conditions (d (solid bar)):10 mL stainless steel autoclave: M/Mo_2C: 40 mg; 1M NaOH: 4 mL; pCO_2: 10 bar (at 25 °C); pH_2: 10 bar (at 25 °C); reaction temperature: 100 °C; reaction time:19 h. "Fresh repeated" x4, "1st" repeated x2.

In an effort to understand the reason for this deactivation, the particle sizes of Pd within the fresh and used catalysts, were analysed by TEM and SEM. When observing catalysts synthesised using a commercially sourced Mo_2C, TEM image (Figure 3.10a), showed large, highly crystalline Mo_2C particles, which implies that the support has a very small surface area and few defects on the surface for Pd nanoparticles to bind to, resulting in large Pd particles on the surface. Due to the density of the Mo_2C support, the TEM images give minimal information as the material was blocking any transmission through the bulk of the material. SEM provides more detail with respect to the size of the metal particles and the nature of the support surface. The LE-BSE detector was used for distinguishing the palladium from the

molybdenum surface. The BSE is strongly related to atomic number, with heavier elements backscattering more electrons, thereby contributing to a brighter signal. Large Pd nanoparticles can be observed (Figure 3.10b) with a size range of approximately 50-70 nm and a good dispersion. When analysing the elemental composition of the Mo_2C surface, EDX showed a Pd wt. % of 0.5-0.8 %, which is a good result for a 1 wt. % loading. Characterising the used Pd/Mo_2C samples less even particle distribution is observed, also large agglomerations of palladium particles with sizes of approx. 1 µm (Figure 3.10c). Additionally, phase separated agglomerations were also found isolated from the support (Figure 3.10d) and surface decomposition or reconstruction of Mo_2C is observed (Figure 3.10e). This implies that during reaction, due to a weak metal-support interaction and surface decomposition or reconstruction, palladium nanoparticles sinter, and in turn, are lost from the support as heterogeneous particles, explaining the drop in catalytic activity. This did not show in the leaching studies as the particles are too large to be retained in the filtrate solution, as shown in Table 3.2. Tests were run to confirm that these Pd particles were not the catalyst for formate production; $PdCl_2$ and Pd colloids were catalytically tested and compared to 1% Pd/Mo_2C-MIm (2M), using the same palladium weight and reaction conditions. Formate productivities of 0.06 and 0.09 mmol were observed for $PdCl_2$ solution and Pd colloids respectively (Figure 3.11), compared to 0.42 mmol produced from 1% Pd/Mo_2C-MIm (2M). This confirms that the metal-support interactions are indeed causing an increase in catalytic activity of the palladium. Observing fresh bimetallic 1% RuPd/Mo_2C under TEM and SEM shows a larger range of metal nanoparticle sizes, *c.a.*10-85 nm, with an even dispersion over the support (Figure 3.12a). Analysing recycled 1% RuPd/Mo_2C, it was found that the metal particles had increased in size (Figure 3.12c), exceeding 100 nm. However, no metal particles, palladium or ruthenium, were found isolated from the support. This implies that, although there was sintering along the support surface during reaction, the addition of the ruthenium creates a stronger metal-support interaction and as a result, no metal particles are lost from the support, explaining the improved stability compared to the monometallic 1% Pd/Mo_2C. Simulations based on DFT produced by Dr Umberto Terranova found that the adsorption energies of Ru

on the Mo_2C surfaces are significantly lower (more negative) than Pd[166]. As such, Ru atoms have a stronger affinity towards the Mo_2C support, this evidence also supports the crucial role of Ru acting as a link to improve Pd stability. The reduced catalytic activity in the bimetallic catalyst in comparison to the monometallic catalyst is likely the result of Pd dilution, less Pd active sites available for reaction.

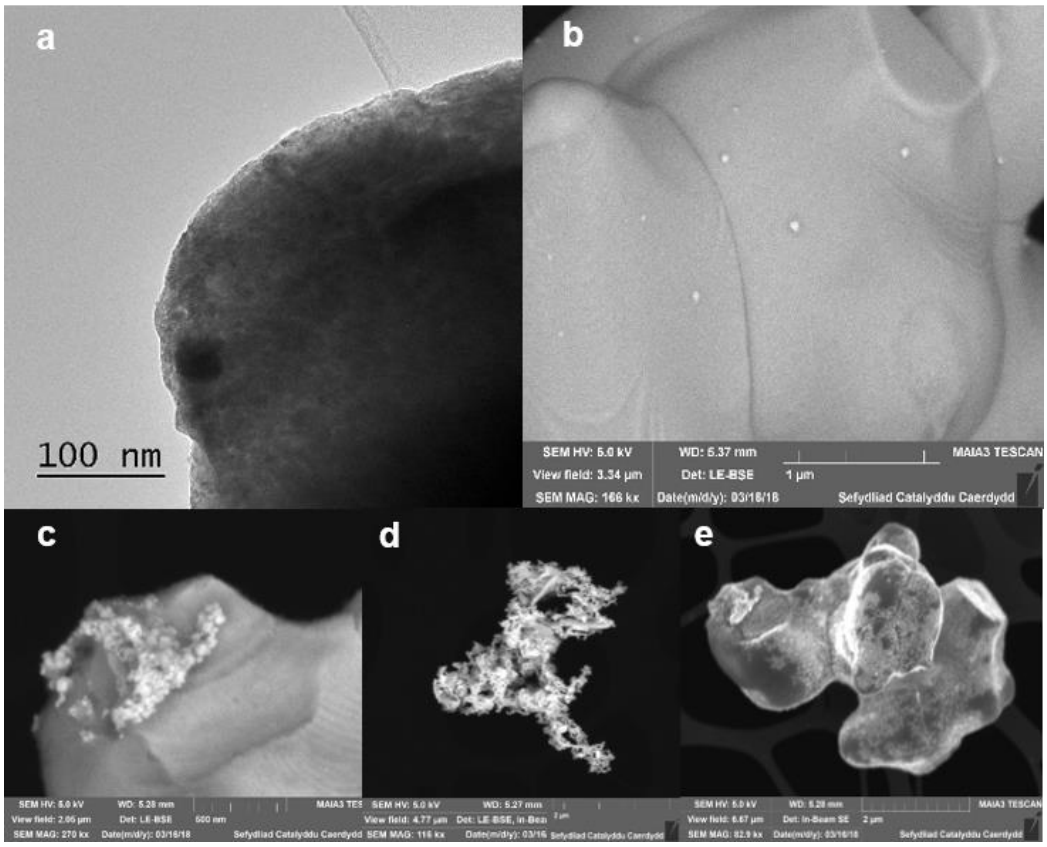

Figure 3.10: [a] HR-TEM images of fresh 1% Pd/Mo_2C-MIm (2M). FEG-SEM images of [b] fresh 1% Pd/Mo_2C-MIm (2M) LE-BSE [c] used 1% Pd/Mo_2C-MIm (2M) LE-BSE [d] Pd cluster LE-BSE [e] used 1% Pd/Mo_2C-MIm (2M) In-Beam SE.

Table 3.2: Pd weight percentages of catalysts during stability study, calculated using MP-AES.

	Weight Percentage			
Re-use	**1% Pd/Mo_2C -MIm (2M)**	**1% Pd/Mo_2C -MIm (0.58M)**	**1% RuPd/Mo_2C**	**1% Pd/Mo_2C -Sy**
Fresh	1.02	1.09	0.99	1.02
1st	1.05	1.13	0.96	1.01
2nd	1.07	1.15	1.00	1.12

Catalysts were digested in aqua regia to dissolve the metal and diluted in H_2O prior to analysis as mentioned in section 2.3.11.

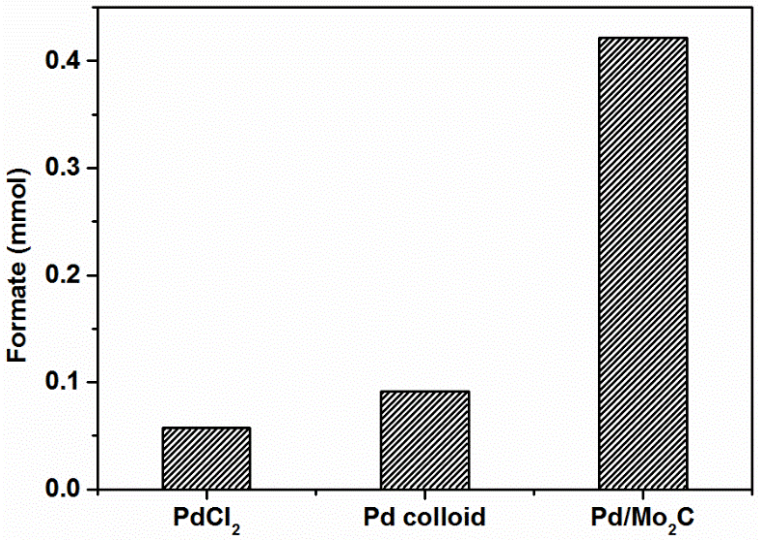

Figure 3.11: Elemental Pd in solution testing to confirm that metal-support interactions are improving the activity for CO_2 hydrogenation. Reaction conditions in 10mL stainless steel autoclave: Pd: 0.4 mg; 1 M NaOH: 4mL; pCO_2: 10 bar (at 25 °C); pH_2: 10 bar (at 25 °C); reaction temperature: 100 °C; reaction time: 19 h.

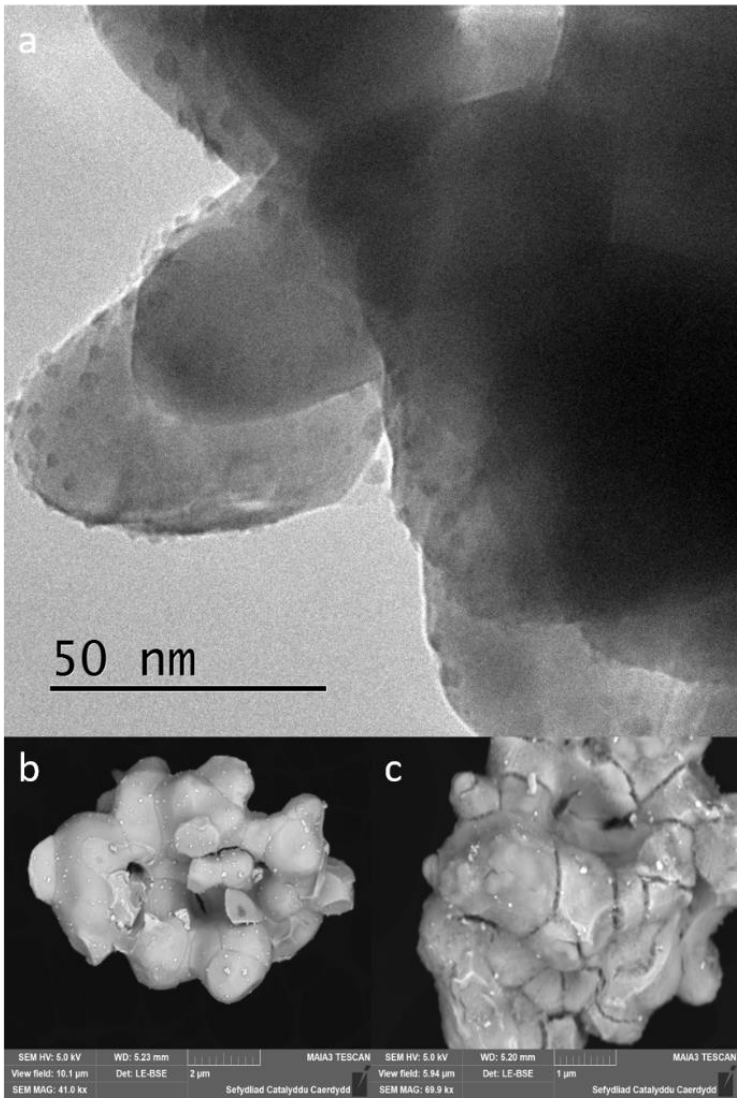

Figure 3.12: [a] HR-TEM image of fresh 1% RuPd/Mo_2C; FEG-SEM images: [b] Fresh 1% RuPd/Mo_2C LE-BSE, [c] used 1% RuPd/Mo_2C LE-BSE.

Pd/Mo_2C and RuPd/Mo_2C catalysts were characterised by XPS. From previous XPS studies of Mo_2C catalysts, Moon *et al.* concluded that the deactivation of a Mo_2C catalyst is caused by the transformation of Mo_2C (Mo^{2+}) to MoO_3 (Mo^{6+}) on the surface of the catalyst in the presence of H_2O during WGS reaction [167]. X-ray photoelectron spectroscopic data (Mo 3d) of 1% Pd/Mo_2C-MIm (2M) (Figure 3.17) reveals that the support is predominantly oxidised with several oxidation states of molybdenum ranging from Mo($^{\delta+}$) to Mo($^{6+}$) ($1<\delta<4$). However, these oxidised species do not show much deviation between the fresh and used samples. More details will be discussed further in section 3.2.7

In respect of the metal, palladium is observed as a well resolved doublet, with the $Pd3d_{5/2}$ centred at 335.7 eV, and exhibiting shake-up structure to higher binding energies indicative of metallic Pd [133] and $Pd3d_{5/2}$ centred at 337 eV indicative of Pd(II) (Figure 3.13). Post-reaction we only see Pd(0) present in the sample possibly accounting to the hydrogenation conditions of the reaction process. XPS of bimetallic samples shows ruthenium (Figure 3.13) is observed as an asymmetric doublet with $Ru3d_{5/2}$ centred at *ca.* 281 eV indicative of RuO_2[168]. The amount of Pd(II) increases post-reaction (Figure 3.13d) which may be a result of some charge transfer from Pd to Ru. Zhang *et al.* has studied PdRu bimetallic samples and reports that addition of Ru creates an increase in Pd(II) species[169], which can be observed in the post-reaction RuPd catalyst (Figure 3.13d). Ru(IV) has a higher standard electrode potential (+1.12 E^o/V) than Pd(II) (+0.95 E^o/V) causing an electron transfer explaining this Pd(II) formation post-reaction, which will also explain the drop in activity of the catalyst in comparison to the monometallic. A positive shift (+0.5eV) of the Pd 3d binding energy can be observed for the RuPd bimetallic catalyst with respect to the mono-Pd (Table 3.3), indicating that a change in the electronic properties of Pd atom modified upon alloying with Ru[169]. Comparing the fresh and used RuPd bimetallic catalyst, shifts for the Pd 3d binding energies are within experimental error, however a negative shift (-0.3eV) for the Ru 3d binding energy in the post reaction catalyst is observed, suggesting that there are still some alloy properties even after 3 uses, but it has decreased. It is this alloying affect that may be the reason of the bimetallic increased stability, as this metal-metal interaction is contributing to stronger metal-support interaction for Pd. Unfortunately, due to the similar atomic number of Pd, Ru and Mo it has proved very difficult to confirm this alloying through EDX.

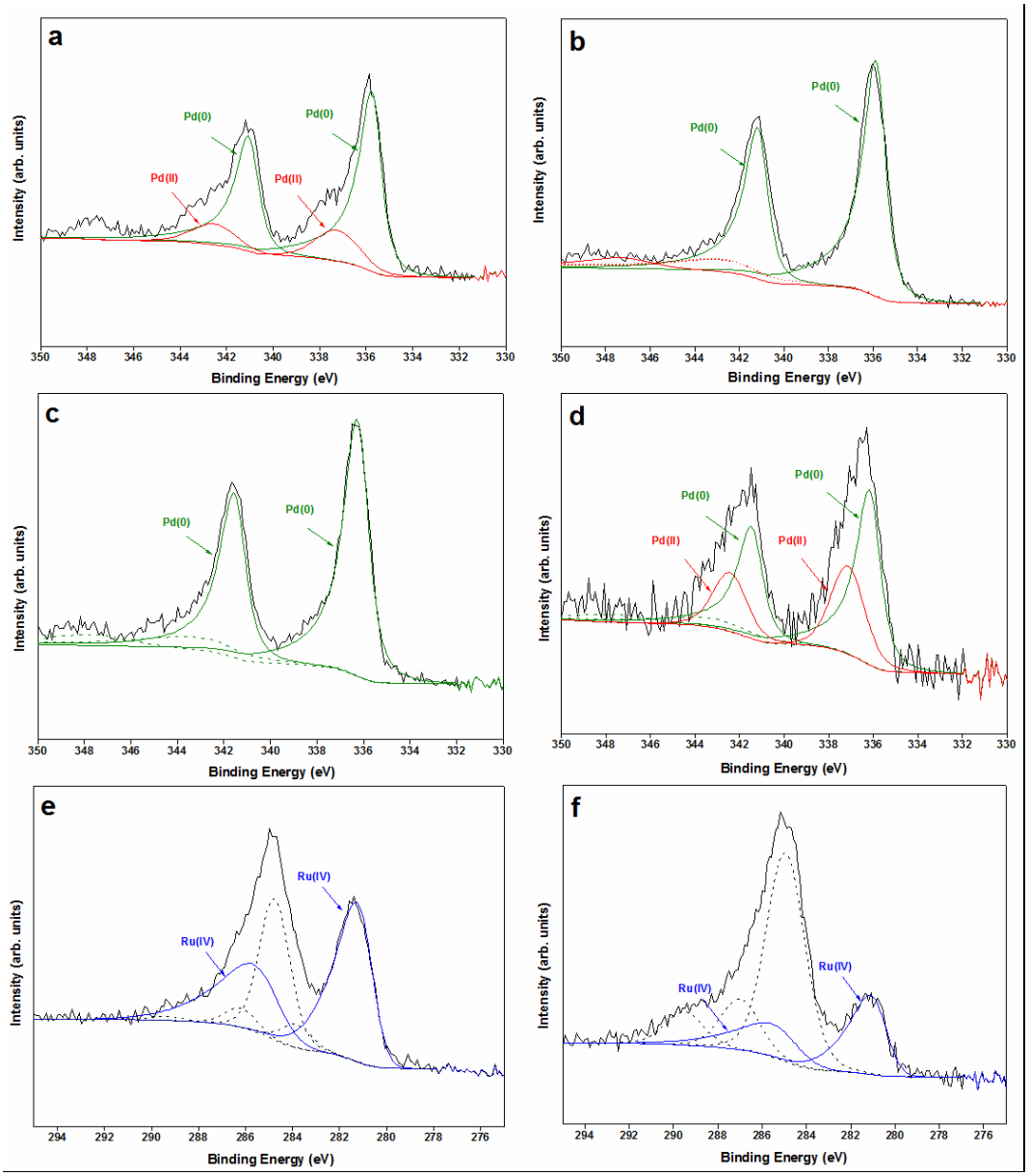

Figure 3.13: Pd 3d XPS spectra of 1% Pd/Mo_2C-MIm (2M) [a] fresh sample [b] 3x used sample, and 1% RuPd/Mo_2C [c] fresh sample [d] 3x used sample; displaying Pd(0) (green) and Pd(II) (red). Ru 3d XPS spectra of 1% RuPd/Mo_2C [e] fresh sample [f] 3x used sample, displaying RuO_2 (blue) species.

Table 3.3: Binding energies (eV) and curve-fitting results of Pd and Ru 3d XPS spectra.

Sample	**Pd(0)**		**Pd(II)**		**Ru(IV)**	
	$3d_{5/2}$, eV	**$3d_{3/2}$, eV**	**$3d_{5/2}$, eV**	**$3d_{3/2}$, eV**	**$3d_{5/2}$, eV**	**$3d_{3/2}$, eV**
1%Pd/Mo_2C-MIm (2M) Fresh	335.7	341.0	337.3	342.6	-	-
1%Pd/Mo_2C-MIm (2M) Used	335.8	341.1	-	-	-	-
1% RuPd/Mo_2C Fresh	336.2	341.5	-	-	281.0	285.2
1% RuPd/Mo_2C Used	336.1	341.4	337.1	342.4	280.7	284.9

3.2.6 Rate of Formation Study

The initial rate of formation of formate for Pd/Mo_2C and RuPd/Mo_2C were compared and studied at different temperatures (75, 100 & 125 ^oC) under standard conditions for the first 2 hours of the reaction. As already acknowledged in Figure 3.5b, the reaction rate is dependent on reaction temperature, following Arrhenius law. The activation energies for 1%Pd/Mo_2C and 1%RuPd/Mo_2C were calculated as +36 kJ mol^{-1} and +43 kJ mol^{-1} respectively. These were determined from Arrhenius plots using the temperature dependant rate constants. To calculate the activation energy (Ea), rates of conversion of substrate at different temperatures are required. In this system, quantification of CO_2 and H_2 is extremely challenging. Hence, the concentration of formate can be used instead to calculate the rate of the reaction since formate is the only product detected and we are assuming 100% selectivity. By defining the reaction as zero order, the integrated rate law is written as Equation 3.1, where [A] is concentration of formate and t is time.

$$[A] = kt + [A]_0 \qquad \textit{Eq. 3.1}$$

We can therefore obtain the value of k from the slope of the linear regression applied to the relationship between concentration of formate and t, as shown in Figure 3.14. The rate constants were calculated for three different temperatures: 75, 100 and 125 °C for both monometallic Pd/Mo_2C and bimetallic RuPd/Mo_2C catalysts, Figure 3.14.

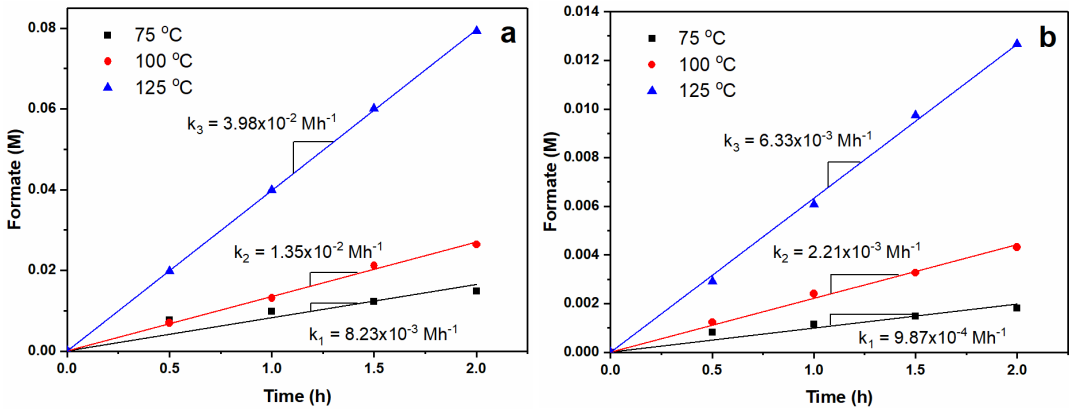

Figure 3.14: Effect of temperature on the catalytic hydrogenation of CO_2 using [a] 1% Pd/Mo_2C-MIm (2M) [b] 1% RuPd/Mo_2C at 75, 100 and 125 °C and varying reaction times. Reaction conditions: catalyst 150 mg (monometallic, 0.014 mmol (Pd); bimetallic, 0.007 mmol (Pd, Ru)); 1 M aqueous base: 15 mL; pCO_2: 10 bar (25 °C); pH_2: 10 bar (25 °C).

The activation energy, E_a, of the reaction can be determined using the Arrhenius equation, Equations 3.2 and 3.3, by plotting lnk and 1/T as shown in Figure 3.15.

$$k = Ae^{\frac{-E_a}{RT}} \qquad \textit{Eq. 3.2}$$

$$lnk = lnA - \frac{E_a}{R}.\frac{1}{T} \qquad \textit{Eq. 3.3}$$

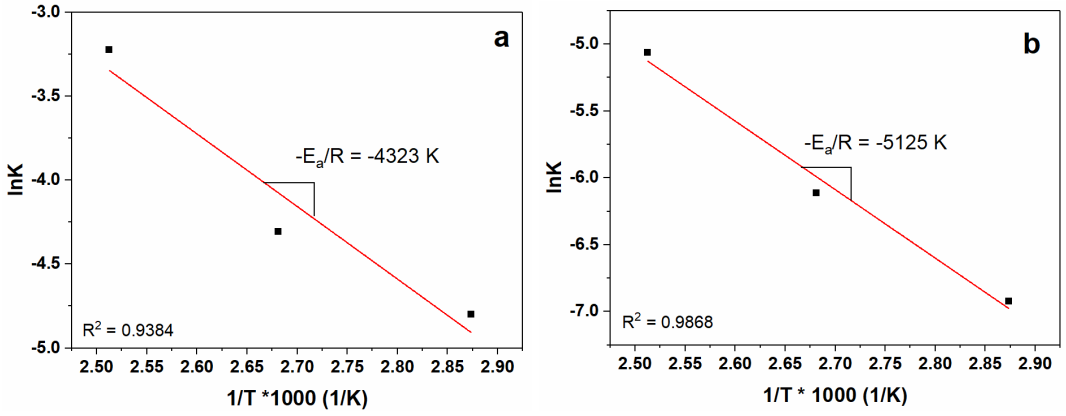

Figure 3.15: Arrhenius plot of the temperature dependence of the rate constant for [a] 1%Pd/Mo_2C-MIm (2M) [b] 1%RuPd/Mo_2C.

Using the gas constant R = 8.314 J/(mol·K), the activation energies for the catalysts 1%Pd/Mo_2C-MIm (2M) and 1%RuPd/Mo_2C are:

Pd/Mo2C	+35.9 kJ/mol
RuPd/Mo2C	+42.6 kJ/mol

RuPd/Mo_2C is found to have a higher activation energy, suggesting that the rate determining steps involves different active sites. Luo *et al.*[156] reported that alloying RuPd results in Ru diluting and isolating certain active sites of Pd, which may result in this increase in activation energy as well as creating stabilising effects. In comparison with the literature, these results are lower than Chen *et al.*'s work, reporting CO_2 hydrogenation to methanol Fe and Cu supported on Mo_2C within an organic solvent, with activation energies of +96 and +105 kJ mol^{-1} respectively[129]. However, in other catalytic systems known for hydrogenation of CO_2 and HCO_3^- salts, the reported activation energy values are larger than our Pd/Mo_2C catalyst, for example +54.3 kJ mol^{-1} for Ru/LDH [92], +39 kJ mol^{-1} with Pd/C catalyst [86,146]. The activation energy is similar to certain homogeneous catalysts $[RhCl(TPPMS)_3]$[67] with +36 kJ mol^{-1}. But higher than others for example with K[RuCl(EDTA-H)] [170] it is +31 kJ mol^{-1}, and $[RhCl(TPPTS)_3]$[64] it is 25 kJ mol^{-1}.

3.2.7 Further Catalyst Characterisation

XRD diffraction patterns of all samples (Figure 3.16) have all shown the pattern correlating to hexagonal β-Mo_2C (JCPDS 35-0787) with no extra peaks correlating to the metal nanoparticles (Pd or Ru), this can be assumed because the nanoparticles are too small to detect. The lab synthesised Mo_2C has a lower intensity than the commercial Mo_2C, as the material is less crystalline in nature, accounting for the slightly higher surface area as found from BET.

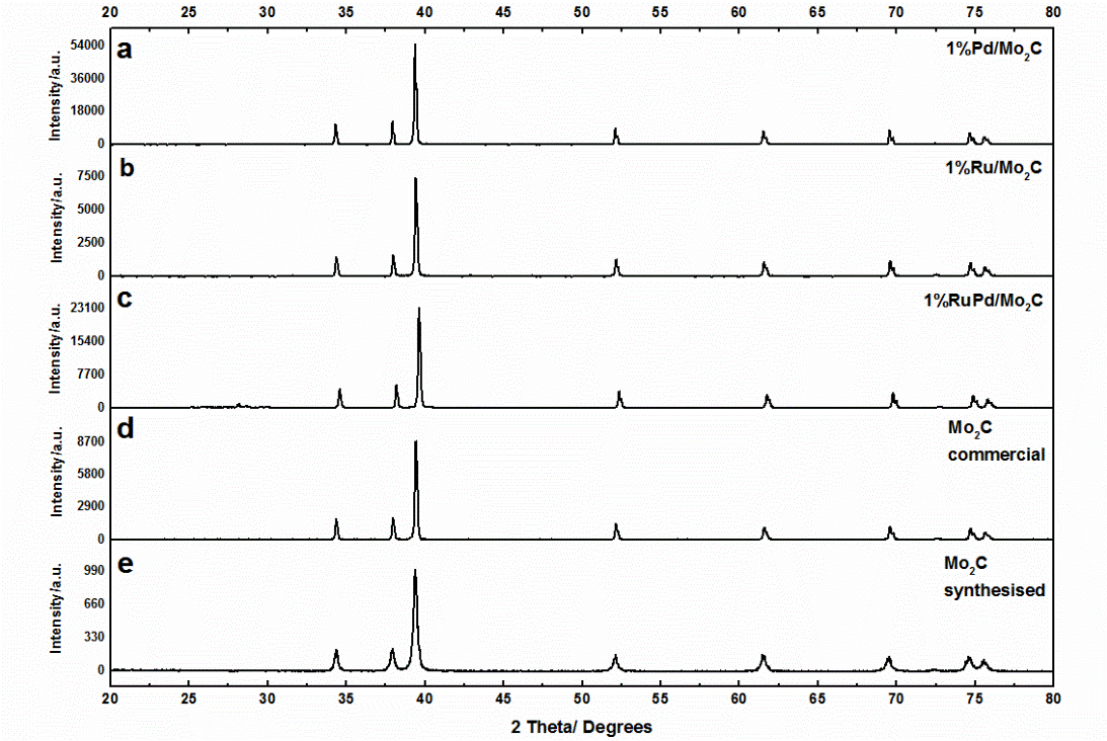

Figure 3.16: Powder XRD patterns for [a] 1% Pd/Mo_2C-MIm (0.58) [b] 1% Ru/Mo_2C [c] 1% RuPd/Mo_2C [d] Mo_2C (commercial) and [e] Mo_2C (lab synthesised).

X-ray photoelectron spectroscopic data (Mo 3d) of 1% Pd/Mo_2C-MIm (2M) (Figure 3.17a & b) reveals that the support is predominantly oxidised with several oxidation states of molybdenum ranging from Mo($^{\delta+}$) to Mo($^{6+}$) ($1<\delta<4$). The two main peaks at 232.8 and 235.9 eV can be attributed to the $3d_{5/2}$ and $3d_{3/2}$ transitions of Mo^{6+}, in MoO_3. Molybdenum carbide found at peaks 232.87 and 232.1 eV, attributed to the transitions of $3d_{5/2}$ and $3d_{3/2}$ transitions of $Mo^{\delta+}$ [171]. A number of smaller peaks are found in the range 235-240 eV which are attributed to molybdenum oxides of lower Mo valency, or more likely Mo^{5+}/Mo^{4+} oxycarbides. Similar results are obtained by Griboval-Constant *et al.*[172] and Xiang *et al.*[173]. The presence of these partial and/or total oxidation species of molybdenum can be attributed to surface oxidation and/or passivation of the catalyst prior to exposure to air during the Mo_2C synthesis [173]. It should be mentioned that no bulk MoO_2 or MoO_3 is found by XRD [174]. 1% RuPd/Mo_2C presents a similar Mo 3d XPS spectra (Figure 13c) to 1% Pd/Mo_2C-MIm (2M), revealing a range of molybdenum carbide and molybdenum oxide species. However, a used 1%

RuPd/Mo_2C sample (Figure 3.17d) has no carbide visible, suggesting a thick oxide film at the surface greater than 10nm.

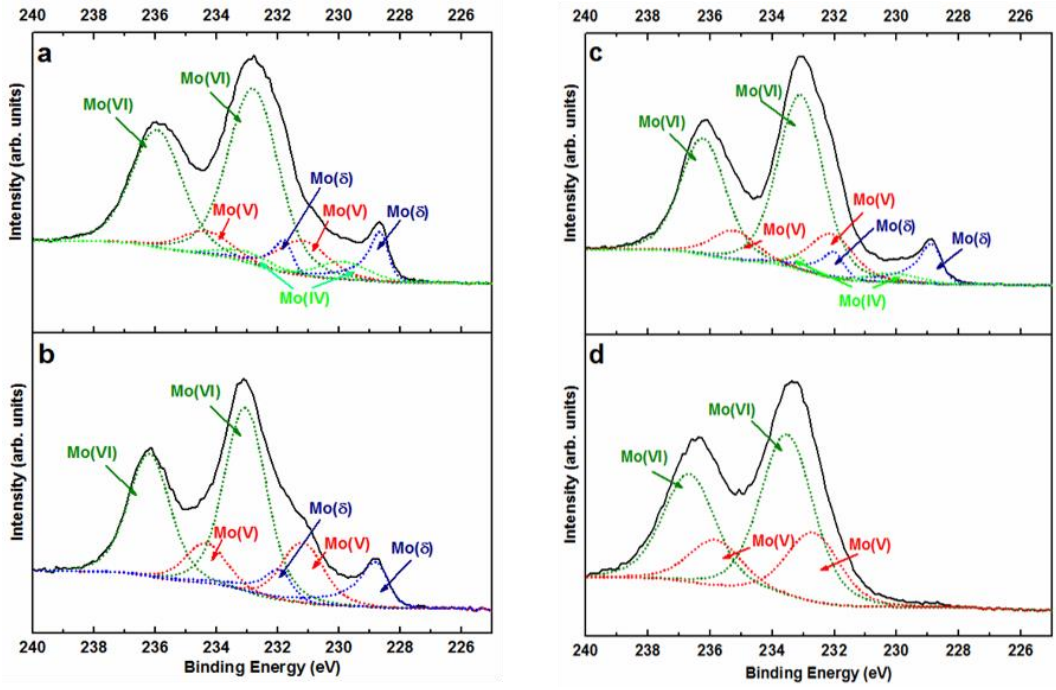

Figure 3.17: Mo 3d XPS spectra of 1% Pd/Mo_2C-MIm (2M) [a] fresh sample [b] used sample and 1% RuPd/Mo_2C [c] fresh sample [d] used sample.

3.3 CO_2 hydrogenation - Continuously Stirred Tank Reactor

3.3.1 Solving High Pressure Autoclave Limitations

One of the main difficulties faced when using a batch reactor is the ability to calculate the amount of CO_2 dissolved in solution and studying the long-term stability of the catalyst. It is very important for our study to calculate the CO_2 conversion, and this cannot be done without knowledge of how much CO_2 has been dissolved and how much HCO_3^- species is present. One option of solving this problem, is by first determining the pH. By a series of calculations considering the equilibrium, pressure and temperature of the reaction, the concentration of HCO_3^- can be calculated. However, for a precise representation, the pH must be accurately

measured within the conditions of the reaction, an error of pH 1 will alter the concentration of HCO_3^- species by a magnitude of 10. Unfortunately, the equipment to measure the pH was not available within a batch high-pressure autoclave reactor. Another question yet to be answered is the role of the proton source, as mentioned previously, CO_2 reacts with H_2O to form the bicarbonate through the deprotonation of carbonic acid, Eq. 3.4 & Eq. 3.5.

$$CO_{2(g)} + H_2O_{(l)} \leftrightarrow H_2CO_{3(aq)} \qquad \textit{Eq. 3.4}$$

$$H_2CO_{3(aq)} \leftrightarrow H^+_{(aq)} + HCO_3^-{}_{(aq)} \qquad \textit{Eq. 3.5}$$

It also must be considered if there is an alternative way of forming the bicarbonate, necessary for the intermediate of the reaction, the CO_2 can react with hydroxyl ions of the solvent NaOH, Eq. 3.6:

$$CO_{2(aq)} + OH^-_{(aq)} \rightarrow HCO_3^- \qquad \textit{Eq. 3.6}$$

This then leads to the question of the true hydrogen source. Is the CO_2 reacting with hydroxyl ions, concluding with the reaction slowing after 19h as a matter of pH as the ^-OH ions deplete (not deactivation of the catalyst), or is the H_2 gas adsorbing onto the catalytic surface and sequentially replacing any protons used in the formation of formate, maintaining the pH and hydroxyl concentration?

In order to better our understanding of the gaseous reactants, the reaction of CO_2 hydrogenation was performed in a continuously stirred tank reactor (CSTR), situated at the University of Cape Town. Set up very similarly to a batch reactor employing high temperature and pressure, yet the reaction is fed with a constant flow of gaseous reactants entering the tank, followed by a constant flow of gaseous products, and unreacted gases exiting the tank, whilst maintaining a constant pressure and temperature throughout the reaction. The flow of CO_2 and H_2 was kept at a controlled flow of 18 mL per minute; connected to the gas outlet is

a GC which enables the quantification of CO_2, H_2 and any potential products using N_2 as an inert reference. Therefore, by being able to quantify the gas inlet and gas outlet throughout the reaction, allows one to quantify the amount of gas dissolved and/or consumed.

3.3.2 Quantifying CO_2 dissolution

The first step to take was to calculate the amount of gas dissolved in the solution. This was done by running a blank reaction, with the same reaction conditions, in the absence of the catalyst, thus eliminating any catalytic activity. From this, one can calculate the amount of CO_2 and H_2 dissolved in the solution by monitoring the change in the GC peaks from the actual gas quantity in comparison to the expected gas quantity under a full flow of 18 mL per minute. Figure 3.18 represents the CO_2 flow outlet, which allows to calculate the total amount of CO_2 left behind in the reactor, dissolved in solution. Using this plot, the total dissolved CO_2 can be calculated. It was found that 1.42 M of CO_2 was dissolved at 100 ^oC, in a 1 M NaOH solution under 26 bar pressure (note: 20 bar pressure applied within the autoclave reactor is at room temperature, upon reaction temperature, the pressure increases to 26 bar).

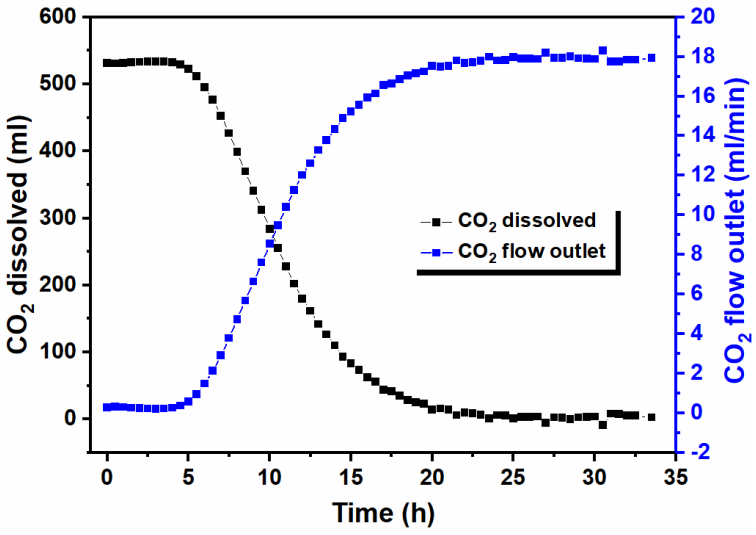

Figure 3.18: Plot representing the CO_2 dissolution of a blank reaction. (Blue) the quantified CO_2 flow outlet (mL/min), (black) Dissolved CO_2 in mL over 30 minute intervals. Reaction conditions;1 M NaOH: 350ml, reaction time: 30 hours, reaction temperature: 100 ^oC, stirring speed: 500 rpm, gas flow: 40 mL/min, CO_2:H_2:N_2 4.5:4.5:1, pressure: 26 bar.

3.3.3 Catalysis results

Two Pd/Mo_2C catalysts, 1 wt.% and 5 wt.% palladium, were tested for their activity within the CSTR, and the volume of CO_2 and H_2 within the tail gas were calculated. In order to be able to compare results from the CSTR and batch reactor reactions, the pressure and temperature of the reactions were kept the same (26 bar at 100 ^oC) and the solvent to catalyst ratio was also kept the same (10 mg of catalyst per 1 mL solvent). Figure 3.19a displays the CO_2 behaviour of the two catalysts with time in comparison to a blank run with no catalyst. Both catalysts show CO_2 consumption when compared to the blank. 5% Pd/Mo_2C catalyst is quite clearly the superior catalyst, as a lot more CO_2 is consumed in comparison to 1% Pd/Mo_2C.

The results displayed in Figure 3.18 is used as a blank run and can be used to take into account CO_2 dissolution for further catalytic tests. By measuring the CO_2 flow outlet for a catalytic reaction and comparing it to the blank reaction as displayed in Figure 3.19a, it can be seen that more CO_2 is consumed in the presence of a catalyst. Additionally, 5% Pd/Mo_2C consumes more CO_2 than 1% Pd/Mo_2C. Then, by calculating the amount of CO_2 dissolution/consumption in the presence of a catalyst and subtracting the calculated CO_2 dissolution obtained in the blank, it is possible to measure the total consumed CO_2 and thus calculate percentage conversion of CO_2, Figure 3.20. For 5% Pd/Mo_2C a percentage conversion of up to ~30% is observed, whereas for 1% Pd/Mo_2C only up to ~5% CO_2 conversion is observed. The 5 wt.% catalyst also stayed active for a longer period of time, holding activity for up to 15 hours, before the rate of CO_2 conversion drops suddenly. The 1 wt.% Pd catalyst only held activity for approximately 10 hours before the activity dropped, however a less sudden decrease in rate of conversion is observed for the higher weight percentage. For both reactions the rate of CO_2 conversion increases over the first ~10 hours, this will be due to the increase in HCO_3^- available for conversion as the CO_2 is slowly dissolved in solution, note that it takes over 20 hours before the solution is saturated with CO_2 (Figure 3.18). An induction period of up to 5 hours is observed with both catalysts due to the

same reasons. At time 0, there is no CO_2 species dissolved in solution, therefore, the initial induction period is the time it takes for the dissolved CO_2 to reach a high enough concentration for enough bicarbonate species to be within close proximity to the catalytic surface.

The same process of CO_2 calculation was applied to H_2, as displayed in Figure 3.19b. First to notice is during a blank run, the H_2 tail gas runs constant. Within the presence of a catalyst, both reactions observed immediate hydrogen consumption, which can be seen by a low H_2 concentration observed in the tail gas. After a period of time, H_2 consumption drops as the tail gas H_2 concentration increases. For the 1% Pd/Mo_2C reaction, H_2 consumption dropped after the first hour, whereas the 5% Pd/Mo_2C reaction held high H_2 consumption for the first 5 hours. This initial H_2 consumption can be seen as the result of H_2 adsorption saturating the catalytic surface, whereas the 10 hour delay of CO_2 consumption can be directly related to the conversion of bicarbonate to formate. The blank reaction of H_2 confirmed that little to no hydrogen is actually dissolved in the solvent under reaction conditions in the absence of catalyst. Knowing that Pd is an effective catalyst for H_2 activation, the large H_2 consumption provides evidence that H_2 is immediately adsorbed onto the surface of Pd, quickly saturating the catalytic surface, which then dissociates thus available for reducing the bicarbonate. The H_2 plot shows when the volume of H_2 in the tail gas increases from a low H_2 volume after the catalytic surface has been saturated, the high H_2 volume sequentially appears to overshoot, far exceeding the controlled H_2 flow of 18 mL/minute as seen in the blank. This is likely due to the gas regulators struggling to maintain a steady H_2 flow after the sudden change in H_2 consumption during the reaction. Because of this, it is impossible to accurately calculate H_2 conversion, as calculated for CO_2.

It can be theorised that as soon as a proton is utilised for formate production and removed off the surface, it is immediately replaced by another dissociated hydride from a H_2 molecule, however this is unable to be detected by GC. These results also reveal information regarding the surface area of the catalysts, the increased H_2 consumption at a higher weight percentage may be the result of a larger surface area of Pd, allowing more H_2 adsorption.

Usually the case for higher weight percentages results in larger nanoparticles, not necessarily a larger surface area, with subsequent limited stability due to a low metal/support interactions, however in this case increased H_2 consumption and CO_2 consumption for 5% Pd/Mo_2C leads to contradicting findings from the previous comparison between 1 wt.% and 5 wt.% catalysts within batch conditions, Figure 3.4. Implying that there are different catalytic effects/mechanisms occurring between the two reactors.

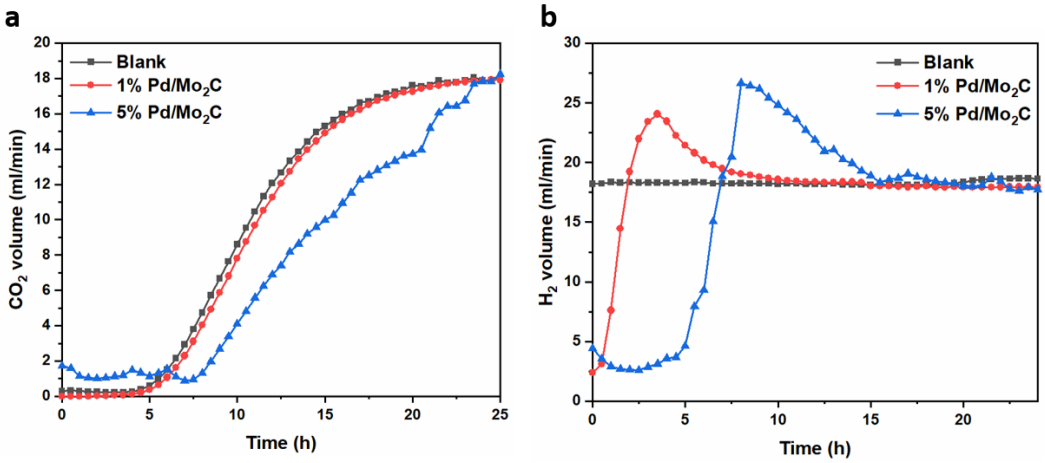

Figure 3.19: Plots displaying gas flow (mL/min) of tail gas of [a] CO_2 and [b] H_2. Blank run (black) 1% Pd/Mo_2C reaction (red) and 5% Pd/Mo_2C reaction (blue). Reaction conditions; 3.5 g catalyst, 26 bar pressure (CO_2:H_2:N_2 4.5:4.5:1) 40mL/min, 100 ^oC, 25 hours.

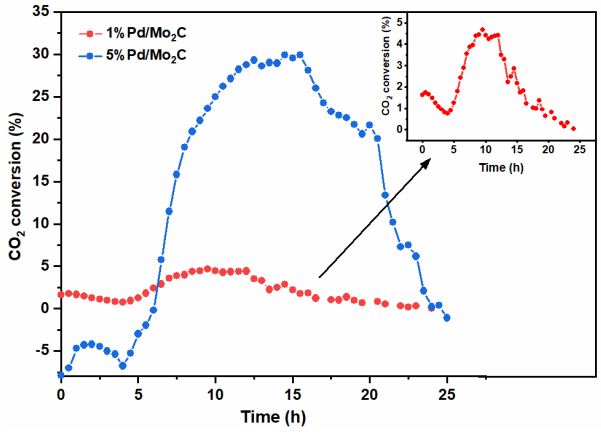

Figure 3.20: CO_2 percentage conversion, calculated from results obtained in Figure 3.20 Reaction conditions; Solvent: 300 mL 1 M NaOH, 3.5 g catalyst, 26 bar pressure (CO_2:H_2:N_2 4.5:4.5:1) 40 mL/min, 100 ^oC, 25 hours.

Focusing on overall CO_2 and H_2 conversion, we revert back to our initial question of the true H_2 source. Clearly H_2 gas is involved in the reaction and adsorbing on the catalytic surface providing an active proton source. Thus, confirming that the reaction limits are not a consequence of pH and diminishing OH^- ions, but due to catalyst deactivation. A liquid sample of the 1% Pd/Mo_2C post-reaction media was retained and run through the HPLC to find 0.067 M of formate present, see Table 3.4 (unfortunately the 5% Pd/Mo_2C post-reaction media was damaged), this value is very similar to the calculated value for CO_2 conversion. This result provides evidence that the gaseous calculations are correctly determined and seeing as no other gaseous of liquid products have been found from both GC and HPLC analysis, confirms a 100% CO_2 to formate selectivity.

Table 3.4: CO_2 and H_2 consumption for 1% Pd/Mo_2C and 5% Pd/Mo_2C reactions. Reaction conditions; 3.5 g catalyst, 26 bar pressure (CO_2:H_2:N_2 4.5:4.5:1) 40 mL/min, 100 ^oC, 25 hours.

	1% Pd/Mo_2C	**5% Pd/Mo_2C**
CO_2 volume converted	528.4 mL **0.062 M**	3649 mL **0.435 M**
Predicted formate formation	**0.062 M**	**0.435 M**
Formate detected	**0.067 M**	**-**

It should be noted that $RuPd/Mo_2C$ (1 wt. % and 5 wt. % Mo_2C) catalysts were also prepared and tested within CSTR conditions, with the hope to learn more about the stability of the bimetallic catalysts. Unfortunately however, any results concerning CO_2 and H_2 consumption for these catalysts were below the detection limit of the GC, and no quantifiable results could be obtained.

3.3.4 SEM analysis

SEM imaging of the fresh and used catalysts used within CSTR conditions are presented in Figure 3.21. The surface topology of 1% Pd/Mo_2C material, revels a very poorly distributed dispersion of Pd nanoparticles on the surface, finding nanoparticles of 100nm, showing a 21 wt.% through EDX. 5% Pd/Mo_2C also revealed large nanoparticles, but more consistent in size with a better nanoparticle distribution. A lower weight percentage would expect a better particle distribution, however, here seems to be not the case. These finding may be a consequence of an inconsistency during synthesis and reducing the material, as many parameters can affect the particle size including the temperature ramp rate, and cooling rate. Due to the time pressures of this particular study, catalyst preparation parameters were not optimised and found difficult to control. Imaging the post-reaction samples showed sintering of palladium with both catalysts, as expected and previously observed from the batch reactor study. This agglomeration will be the main cause of the deactivation of the catalyst.

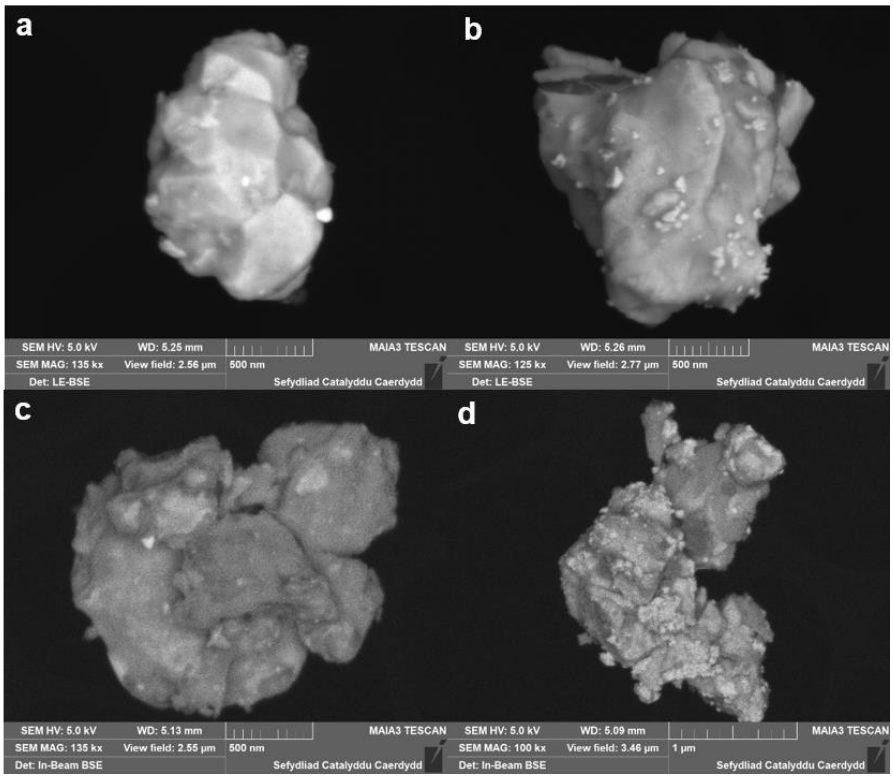

Figure 3.21a-d FEG-SEM imaging of [a] fresh 1%Pd/Mo_2C [b] fresh 5%Pd/Mo_2C [c] used 1%Pd/Mo_2C [d] used 5%Pd/Mo_2C, LE-BSE.

3.4 Conclusions

Mo_2C has been reported as an effective support and co-catalyst for CO_2 hydrogenation due to its CO_2 activation and H_2 adsorption properties. In this work, it has been shown palladium supported on molybdenum carbide is an active catalyst for the hydrogenation of CO_2 within aqueous alkaline conditions.

This study began with selecting the optimal metal supported on Mo_2C for the catalytic hydrogenation of CO_2. Comparing a number of supported metal catalysts, 1% Pd/Mo_2C has proved the best active catalyst for the liquid phase hydrogenation of CO_2 to formate.

For improved CO_2 dissolution in aqueous conditions, a basic solvent is necessary. Different basic solvents, NaOH, $NaHCO_3$ and Na_2CO_3 were tested and a 1M NaOH solvent was selected as the most suitable as it allowed 100% of formate formed to be derived from the CO_2 reactant. pH studies determined that after CO_2 dissolution, the reaction solvent situates around pH 6-8, within this region HCO_3^- is the dominant carbon species therefore concluded as the intermediate for CO_2 conversion.

Next, catalyst preparation optimisation was undertaken to achieve the most active catalyst. The modified impregnation technique was found the best method for catalyst preparation, when acidifying the $PdCl_2$ precursor solution, increasing the HCl concentration from 0.58M to 2M, increased the catalytic activity by more than 70%. Different palladium weight loadings were tested, determining that a 1% weight loading produced the best catalyst producing 1.5 mmol of formate with a TON of 109 at 100 ^oC. Increasing or decreasing the weight loading only decreased the TON. Increasing the reaction temperature to 125 ^oC increased TON to 307 after 19 hour reaction, with a TOF of 42.5 h^{-1} over the first 2h. Analysing the post-reaction filtrate for palladium content, and conducting a catalyst filtration study showed negligible palladium leaching and confirmed the catalytic activity is form heterogenous origin.

Stability studies and electron microscopy data found that monometallic 1% Pd/Mo_2C has a poor reusability as Pd nanoparticles easily sinter and can be partially lost from the support. However, when introducing ruthenium in a bimetallic 1% $RuPd/Mo_2C$ catalyst, although a

less active, greatly improves its reusability, exhibiting only a 30% drop in activity after 3 uses, in comparison to an 82% drop with monometallic palladium. XPS have found that due to reducing conditions of the reaction, Pd maintains its Pd (0) active state, however aggressive sintering forming large Pd nanoparticles that consequently detaches from the support explains the drop in activity. Analysing the bimetallic catalyst, alloying effects are observed between Pd and Ru. Thus, in the bimetallic catalyst the Ru atoms act like a link between the Pd and Mo_2C surface, reducing the amount of metal sintering, resulting in an increased stability for the RuPd/Mo_2C catalyst. Rate of formation of these two catalysts found 1% Pd/Mo_2C achieved an activation energy of +36 kJ mol^{-1}, while 1% RuPd/Mo_2C achieved +43 kJ mol^{-1}. From these results overall, 1% Pd/Mo_2C catalyst is in good competition with many other reported heterogenous and homogeneous catalysts within similar reaction conditions, despite its instability which can be helped by alloying with ruthenium.

Pd/Mo_2C catalysts were also briefly tested in a CSTR to test its catalytic ability in a continuous reactor, and to gain more of an understanding of the gaseous reactants and their behaviour in aqueous conditions. Using this reactor led to the quantification of dissolved CO_2 species at 1.42M, in a 1M NaOH solvent at reaction temperature and pressure. H_2 was found to immediately saturate the catalytic surface, a dissociative adsorption providing a direct source of hydrogen, and secondarily gave more information of the catalysts surface area. This knowledge then allowed the subsequent calculations for CO_2 conversion for corresponding formate formation reactions within the same reaction conditions. The results of CO_2 conversion/formate production found for the high-pressure autoclave and the CSTR were comparable for 1% Pd/Mo_2C, however results for 5% Pd/Mo_2C was shown to outperform 1% weight loading achieving higher formate production and stability, showing contradicting results between the two reactors.

4 Pyrrhotite and the role of surface oxygen on the catalytic activity for CO_2 hydrogenation

4.1 Introduction

4.1.1 Origin of Life Theory

Given the aqueous nature of the living cell, it follows that life itself must have begun in water, presumably in the Hadean ocean, a geologic eon of the earth, 4.6 billion years ago.

Fe-S phases have been hypothesised as potential membrane catalysts, reducing aqueous carbon dioxide for the formation of prebiotic molecules and life's emergence on early Earth, an idea first introduced by Wachtershauser in 1988[97,175]. From 1994, Russel produced a series of reports proposing an alternative hypothesis, by giving a deeper understanding of the Hadean Ocean[94,98,99]. Environmental conditions during this time period is uncertain. A 10-bar CO_2 atmosphere is proposed, constituting in an acidic ocean of a high concentration of dissolved CO_2, around pH 5.5[176]. Hydrothermal vents operated as natural electrochemical reactors in which warm, alkaline (pH 9-11)[177], hydrogen rich fluids mixed with cool, acidic, CO_2-rich waters, separated by a labyrinth of catalytic Fe(Ni)S micropores. Springs of acidic hydrothermal vents, termed 'black smokers' are located directly above magma chambers, leaching dissolved ionic complexes, particularly Fe(II) and Ni(II) ions[99] into the ocean. Fe(Ni)S minerals spontaneously precipitated at the interface between the alkaline hot water springs rich in bisulphide (HS^-) and hydrogen, and the iron and nickel rich Hadean ocean, encapsulated within the walls of hydrothermal vents. These hydrothermal vents are highly porous, consisting of a labyrinth of interconnected micropores, creating an inorganic interface between the hydrothermal fluids and the ocean waters[178]. These Fe(Ni)S precipitates served as juxtaposed primitive membranes, naturally separating the low pH ocean water with the high pH spring effluents[179]. This natural osmotic potential derived from the pH gradient is thought

to drive the reduction of CO_2 by H_2, a process analogous to autotrophic cells specifically to the chemistry of the acetyl Co-A pathway. Russel and Hall suggested the mineral phases greigite (Fe_3S_4) and violarite ($FeNi_2S_4$) as probable catalysts situated in these vents, based on the fact that both minerals contain [4Fe-4S] cubane and [Fe_3S_4] structures, superficially similar in structure to four iron ferredoxins[99,180] specifically within carbon monoxide dehydrogenase and acetyl Co-A synthetase, enzymes employed to dissociate H_2 and reduce CO_2 within the acetyl-CoA pathway[99,181].

4.1.2 Catalysis Using Iron Sulphide

Replication of these oceanic discussed conditions, within a benchtop experimental setup is impossible. Nonetheless, experimental attempts to drive the reaction of H_2 and CO_2 electrochemically using Fe_xS_y catalysts have been reported, albeit with limited results even at high pressures[182]. The reduction potential of the $H_2/2H^+$ couple is not sufficiently low to reduce CO_2 to CO, formate ($HCOO^-$), formaldehyde (HCHO) or similar organics with equivalent reduction potentials[183]. Previous work from Roldan *et al.* has involved replicating and adapting this theory of iron sulphide CO_2 conversion into small organic molecules mainly via mechanistic studies[100,102,103]. Combined computational and experimental work, involved electrochemical CO_2 hydrogenation using greigite-modified electrodes in CO_2 saturated aqueous solutions[100]. Within these conditions they report low concentrations of formic acid, acetic acid and methanol were detected; substantially more formic acid generated at pH 6.5, accounting to the majority of dissolved CO_2 present as HCO_3^- (the active species) at this pH.

The origin of life theory aside, iron sulphides are certainly interesting materials. Due to the high natural abundance, very low cost and low toxicity of iron and sulphur, iron sulphide structures including pyrrhotite ($Fe_{1-x}S$), pyrite (FeS_2) and greigite (Fe_3S_4) have brought attention for catalytic application in the development of green catalysts and energy storage within the last decade. The stoichiometric ratio between Fe and S atoms and crystalline structure, allows iron sulphide minerals to display interesting magnetic and electrical

properties[102]. Iron sulphide catalysis have been reported for hydrogen evolution reaction[184–187] oxygen reduction reaction[188], hydrodesulphurisation,[189,190] potential for photovoltaic devices[191] and an effective magnetic sorbent for the recovery of contaminant metals[192].

4.1.3 Pyrrhotite Structure

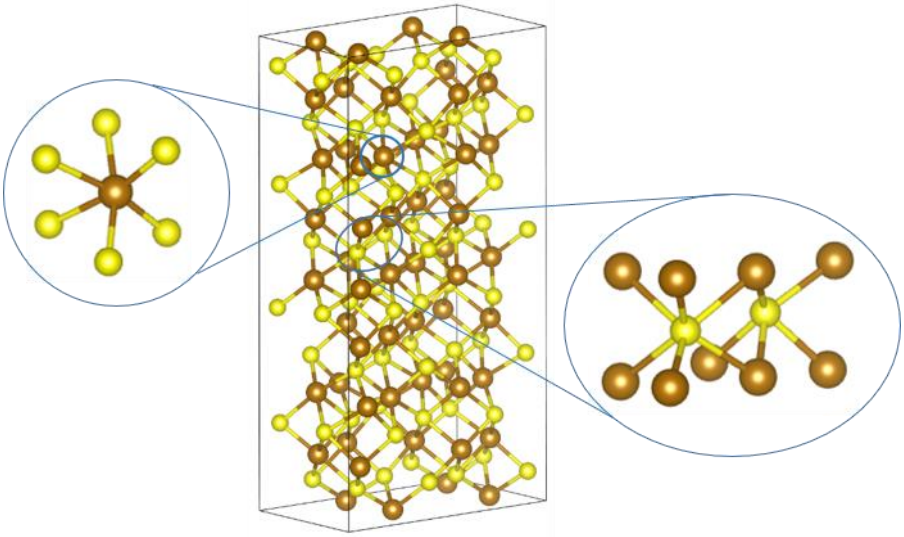

Figure 4.1: Crystal structure of pyrrhotite, brown: Fe atom; yellow: S atom. Generated from Vesta[193] using pyrrhotite cif file from [American Mineralogist (1972) 57, 7-8, 1066–1080][194].

Greigite is rare in nature because of the instability imparted by the large number of electrons in antibonding orbitals, and only found in relatively recent sediments where it has been well protected from oxidation to pyrite, or reduction to pyrrhotite[195]. After pyrite, pyrrhotite is the most common and abundant iron sulphide mineral in nature, occurring as accessory minerals in many rocks and found in a wide range of hydrothermal deposits[196,197]. Pyrrhotite covers a wide range of iron sulphide "superstructures" based on the NiAs structure[198] with the general composition $Fe_{1-x}S$, where x varies from 0 (FeS, troilite) to 0.125 (Fe_7S_8). Pyrrhotite can be synthesised in two types of crystal structures: hexagonal or monoclinic, and these can be defined by their iron percentage, increasing the iron content above 47% moves the structure from monoclinic (Fe_7S_8) to hexagonal ($Fe_{11}S_{12}$) [199]. Exhibiting octahedral iron sites while

sulfur exhibits five-fold and six-fold coordination due to vacancies on metal sites[200], as represented in Figure 4.1. Pyrrhotite is nonstoichiometric, it has an iron deficiency within the Fe layers, with 1/8 metal ions absent, creating Fe vacancy ordering. It is these vacancies that form pyrrhotites magnetic behaviour, crystalline structure[201], and potential active sites for catalysis. Gronvold *et al.* are the first to report that a high atomic percentage of Fe (50%) (FeS) will have a constant composition of hexagonal FeS, and a constant composition of monoclinic $Fe_{1-x}S$ is formed at a low Fe atom percentage (46.73%) (Fe_7S_8)[202]. Consequently, increasing the amount of iron changes the magnetic behaviour from ferromagnetic (monoclinic) to antiferromagnetic (hexagonal).

4.1.4 Pyrrhotite Oxidation

Pyrrhotite is well reported to oxidise upon contact with air or moisture. Several authors have shown that the oxidation of pyrrhotite involves the transfer of electrons from the crystal lattice and diffusion of iron towards the pyrrhotite surface resulting in a coating of ferric hydroxides[203–206], represented by Eq. 4.1-3;

$$Fe_{1-x}S + (2-0.5x)O_2 + xH_2O \rightarrow (1-x)Fe^{2+} + SO_4^{2-} + 2xH^+ \quad \textit{Eq. 4.1}$$

$$2Fe^{2+} + 0.5O_2 + 2H^+ \rightarrow 2Fe^{3+} + H_2O \quad \textit{Eq. 4.2}$$

$$Fe^{3+} + 3H_2O \rightarrow Fe(OH)_{3(s)} + 3H^+ \quad \textit{Eq. 4.3}$$

Scheme 4.1: Sequential oxidation of pyrrhotite

Oxidation causes the formation of SO_4^{2-} ions (Eq. 4.1)and the release of protons, causing the oxidation of Fe^{2+} to Fe^{3+} (Eq. 4.2), precipitating as ferric hydroxide (Eq. 4.3). Steger *et al.* studied the oxidation of pyrrhotite at temperatures up to 50 °C and their results indicated that the oxidation proceeded by a sequence of intermediates; $FeSO_4$, $(Fe(OH)SO_4)_xH_2O$ and ultimately gave ferric oxide and elemental sulphur[205]. Using the surface characterisation technique XPS, Buckley *et al.*[207] found that exposure of pyrrhotite to air leads to the consecutive formation of iron(II) oxide, iron(III) hydroxyl-oxide or hydrated iron(III) oxide

along the surface of the material within the first few seconds of exposure. Fe(2p) studies indicated that more than half the iron within a 5nm depth became bonded to oxygen, finding peaks consistent with $Fe_2O_3.xH_2O$ and the remaining high spin iron(II) bonded to sulphur. Fe(2p) and Fe(3p) spectra indicated the diffusion of iron from the lattice towards the surface to form the observed oxidation products, thus leaving a higher number of iron vacancies than in the pre-oxidised material. Pratt *et al.*[208] also studying pyrrhotite oxidation report that the elemental structure of pyrrhotite is a combination of Fe(II)-S and Fe(III)-S species, however upon exposure to air, within the near-surface, the Fe(III)-S bonds will break for form Fe(III)-O bonds, leaving only Fe(II) bonded to sulphur in the lattice. Suggesting an oxygen-rich, sulphur-depleted outermost layer, as a consequence, a sulphur rich layer is developed beneath the ferric oxyhydroxide layer, likely forming disulphide bonds[209].

4.1.5 Aim of this chapter

Including the previous work using electrochemistry for CO_2 hydrogenation[100,210], iron sulphides are rarely reported for their catalytic activities. For this work, lab-synthesised pyrrhotite has been tested for its activity for CO_2 hydrogenation in an alkaline liquid phase media to produce formate. These alkaline conditions are vital for two reasons. First, pyrrhotite oxidation is considerably reduced under neutral or alkaline conditions[204], under acidic conditions $Fe_{1-x}S$ dissolution occurs[211]. Secondly CO_2 is poorly soluble in water, however increasing the pH significantly improves the solubility[166]. After investigation concerning the alkaline base in chapter 3, these important findings are reflected in the following chapters. NaOH base will again be used within this chapter to increase the pH and increase the presence of HCO_3^- within solution.

For this work, the same reaction conditions employed in Chapter 3 are applied. This study investigates pyrrhotite as a novel candidate for CO_2 hydrogenation, inspired by the 'Origin of Life theory'. Characterisation of pyrrhotite and embracing its air oxidation properties has provided new and crucial understanding towards its application as a catalyst.

4.2 Results and Discussion

4.2.1 Material Characterisation

XRD

To initiate the study, the pyrrhotite synthesis procedure was first optimised. Pyrrhotite samples with good crystallinity were synthesised using a range of reaction temperatures and times, as presented in Table 4.1. XRD patterns of the samples 1-6 (Figure 4.2) show a range of crystallinities depending on the reaction conditions, but all show a pattern confirming the pyrrhotite structure, The XRD pattern presents 5 major reflections at $2\theta \approx 31$, 34, 44, 53 and 71 °. It shows peaks with planes of (002), (101), (102), (110) and (104) corresponding with the reference to the JCPS 01-079-5974 PDF file, a hexagonal crystal phase, cell with lattice constraints of a = b = 3.44, c = 5.87 and angles are $\alpha = \beta = 90$ ° and $\gamma = 120$ °. It should also be noticed that no other phase of iron sulphide (marcasite, pyrite or greigite) was found. As reported by Yund *et al.*[212] and Lauretta *et al.*[213], the Fe/S atomic ratio can be calculated using the mean d_{102} spacings using the Eq. 4.4:

$$\text{Atom-\% Fe} = 45.212 + 72.86(d_{102} - 2.0400) + 311.5(d_{102} - 2.0400)^2 \qquad \textit{Eq. 4.4}$$

Gronvold *et al.* determined that a high atomic percentage of Fe (50%) will have a constant composition of hexagonal FeS, and a constant composition of monoclinic $Fe_{1-x}S$ is formed at a low Fe atom percentage (46.73%)[202]. Therefore, by determining the Fe atomic percentage from XRD (Table 4.1), results have found that increasing the synthesis temperatures and synthesis times during the iron sulphide synthesis increases the Fe atomic percentage transforming the structure from monoclinic (samples 1-3) into a hexagonal pure structure (samples 4-6), reaching an Fe:S ratio closer to 1:1, an unsurprising outcome as monoclinic

begins to lose their stability above 254 ^{o}C [214]. Sample 6 has the most crystallinity, a product of the highest temperature (310 ^{o}C) and reaction time (12h).

Table 4.1: Experimental Parameters for Pyrrhotite synthesis.

Sample	**Reaction Temperature (°C)**	**Reaction Time (hour)**	**Composition[a]**	**Fe atomic %**
1	280	0.5	$Fe_{0.85}S$	45.83
2	280	4	$Fe_{0.88}S$ (Fe_7S_8)	46.89
3	310	0.5	$Fe_{0.88}S$ (Fe_7S_8)	46.89
4	310	4	$Fe_{0.93}S$ (FeS)	48.26
5	310	8	$Fe_{0,94}S$ (FeS)	48.51
6	310	12	$Fe_{0.96}S$ (FeS)	48.98

[a]Product was determined using p-XRD patterns (Figure 4.2) to find the d_{102} to determine the Fe/S atomic ratio using equation given by Yund *et al.*[213].

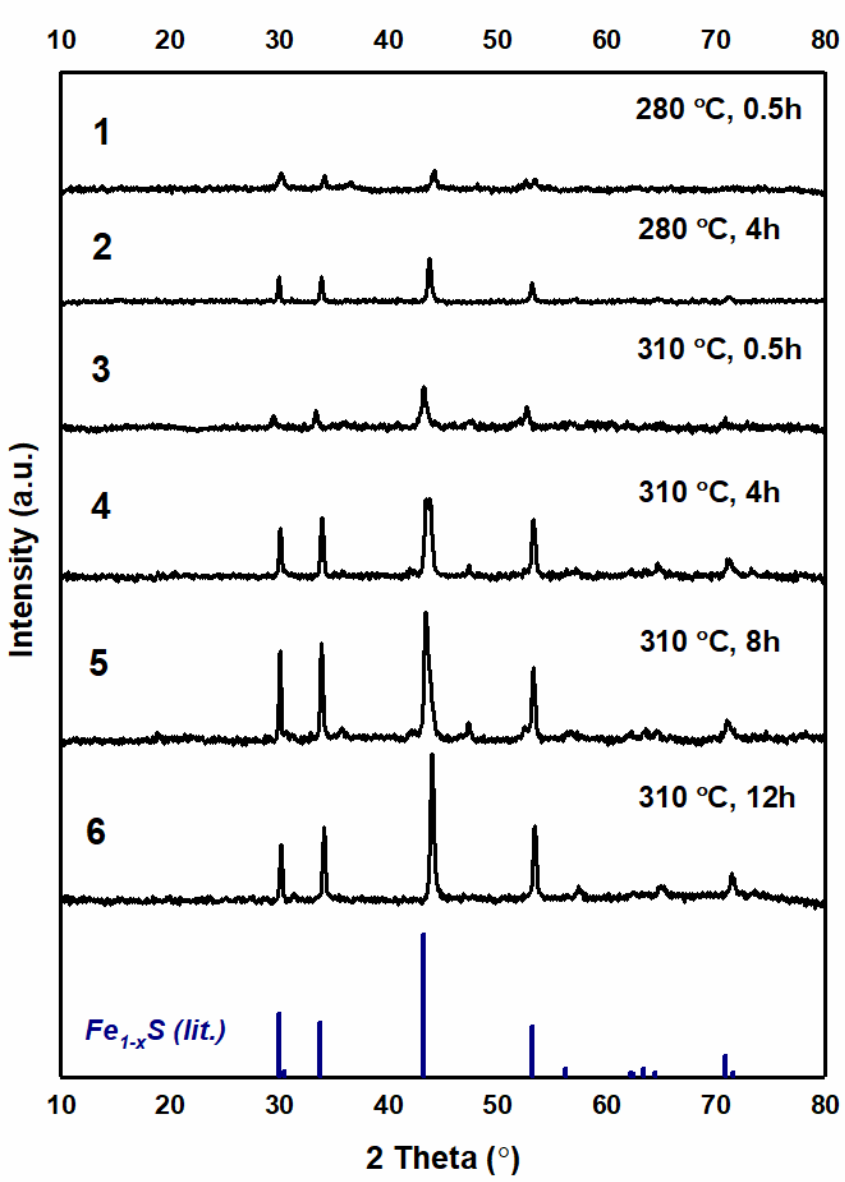

Figure 4.2: XRD patterns of pyrrhotite samples 1-6. Additional information listed in table Table 4.1.

Raman Spectroscopy

Raman spectroscopy was also used to confirm the structure of the iron sulphide for all 6 samples of pyrrhotite synthesised. The Raman spectra of sample 6 (Figure 4.3) shows peaks at 215, 277 and 384 cm^{-1} and the results perfectly correlated with reported Raman spectra of natural pyrrhotite[215]. Results for all 6 samples show very similar results, as reported in Appendix Figure 7.1, confirming that pyrrhotite is the correct iron sulphide phase synthesised.

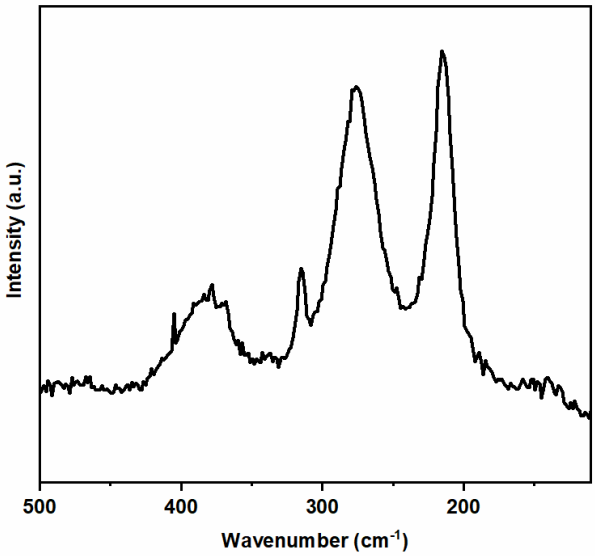

Figure 4.3: Raman analysis of pyrrhotite sample 6.

4.2.2 Pyrrhotite Catalysis for CO_2 Hydrogenation

Prepared pyrrhotite was tested for liquid phase CO_2 hydrogenation using a similar reaction procedure to Chapter 3; 1M NaOH solution as a solvent under the reaction conditions of 125 ^oC and 20 bar pressure (CO_2:H_2, 1:1). Initial tests revealed that the most crystalline pyrrhotite material, sample 6, resulted in the highest formate productivity, therefore the synthesis procedure for sample 6 was continued for the rest of the study. Also, the maximum reaction time of 3 days allowed the best product formation as shown by the largest NMR peak area, unfortunately these initial tests were not quantified. Freshly synthesised pyrrhotite was found active for CO_2 hydrogenation, although formate was quantified at a small amount of 0.19 µmol. However, upon investigation it was found that if the catalyst was stored in air for some time, the activity of the catalyst greatly improved (Figure 4.4), achieving 0.54 µmol after 30 days of ageing. XRD analysis shown in Figure 4.5 revealed that this aging process also caused a decrease in peak intensity, correlating to a loss of crystallinity within the structure. This is contradicting to the initial tests, as it was found that the sample with the highest crystallinity held the highest catalytic activity. The increase in activity with aging may be due to the formation of new chemical species, which results in a loss in crystallinity. As discussed,

pyrrhotite is well known for oxidation in air; leading to the hypothesis that this oxidation may be the cause for the improved catalytic performance of the material and decline in crystallinity.

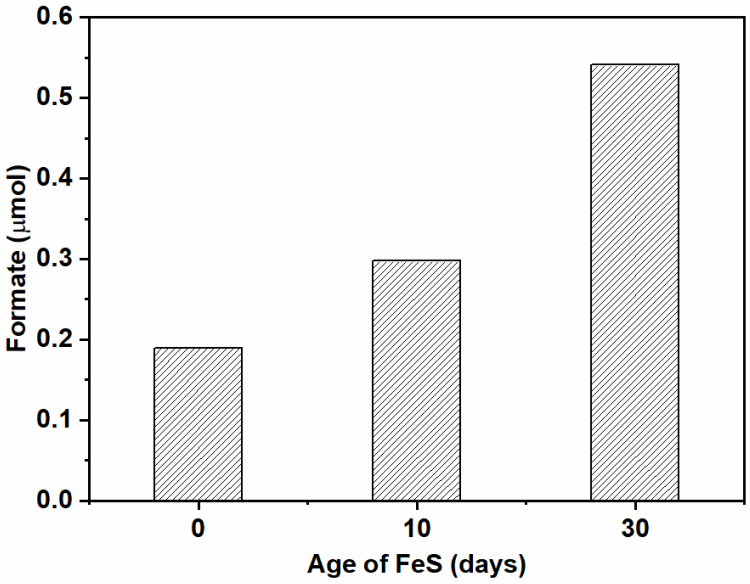

Figure 4.4: Formate production of pyrrhotite samples, stored in air for 0, 10 & 30 days.

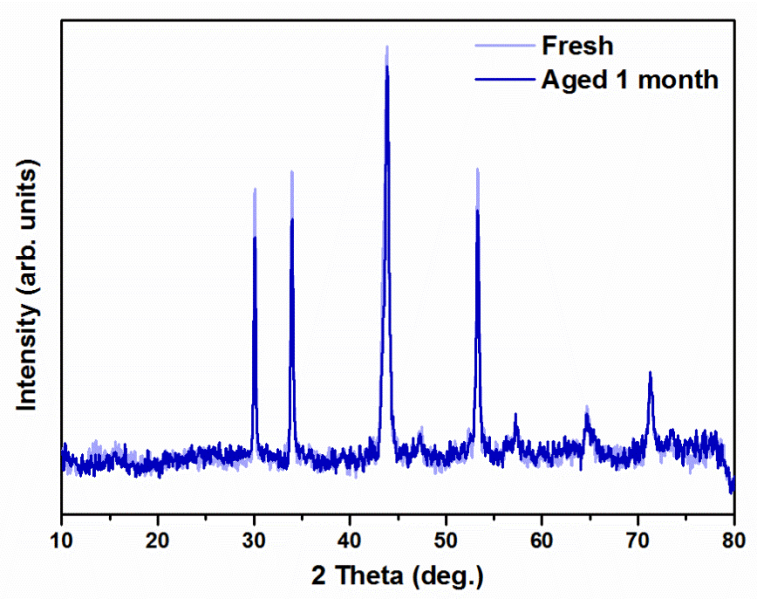

Figure 4.5: XRD spectra of pyrrhotite sample fresh (light blue), and aged 1 month (dark blue).

TGA and in situ XRD

To investigate this ageing further, freshly synthesised pyrrhotite was analysed under TGA and *in situ* XRD, analysing how the sample responds to thermal oxidation, under a steady increase in temperature up to 800 ºC under flowing air. These results are presented in Figure 4.6 (TGA) and Figure 4.7 (*in situ* XRD). XRD coupled with TGA helped define the changes in phase during calcination. Increasing the temperature of pyrrhotite under air from 100-800 ºC caused an overall steady phase change from pyrrhotite to iron oxide. Studying the techniques in detail provides more understanding of these phase changes. Initial mass loss (up to ~150 ºC) is the result of water and residual toluene evaporation off the surface. When increasing temperature from 150 ºC up to 302 ºC, the material gained 2.5% of its original weight from the formation of S-O and Fe-O species, although from 150 ºC to 240 ºC, there is only a small mass gain of 0.6%. At 200 ºC, pyrrhotite begins to lose crystallinity as oxygen becomes integrated into the bulk. At 250 ºC, the pyrrhotite phase is lost as the material becomes an amorphous $Fe_xS_yO_x$ species. From 240 ºC to 302 ºC a large weigh gain of 1.9%, where at 300 ºC a phase change is revealed in XRD, Figure 4.8. Steger *et al*. reported that oxidation of pyrrhotite proceeds by a sequence of intermediates; $FeSO_4$, $Fe(OH)SO_4.xH_2O$ and ultimately gave ferric oxide and elemental sulphur[205]. In this case, at 300 ºC begins with the formation of a solid 'soup' of a variety of iron sulphide/oxide species, dominantly marcasite & pyrite (FeS_2) and Fe_2O_3, which is showed more intensely at 350 ºC. Above 360 ºC displays large mass loss of 25.1%, sulphoxides are unstable at high temperatures so these decompose rapidly releasing SO_2. XRD at 400 ºC revealed the temporary formation of $FeSO_4$, $Fe_2(SO_4)_3$, Fe_3O_4 and Fe_2O_3 species, involving the transition of iron oxidation states from Fe(II) to Fe(III) (Figure 4.9). From 500-640 ºC, another large mass drop of 19.1% is observed, as remaining sulphur is removed from more SO_2 evolution, until only ferric oxide remains, corresponding suitably with XRD. Once 800 ºC is reached, the XRD diffraction pattern presents a strong pattern directly correlating to Fe_2O_3. Eight major reflections are observed at $2\theta \approx 24, 33, 35, 40, 49, 54, 62$ & 64 °, consistent with the reference to the Fe_2O_3 JCPS 01-085-0987 PDF file. Any additional peaks were attributed to the sample stage, as the same peaks also occurred during the background scan.

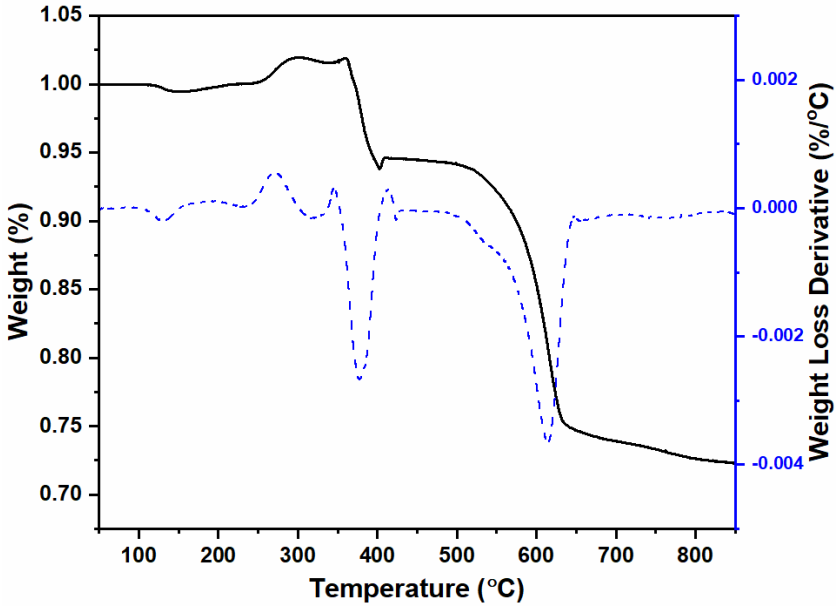

Figure 4.6: TGA of pyrrhotite heated under air from room temperature to 800 °C, 5°C/min. Percentage weight loss (black) and the first derivative of weight loss (blue).

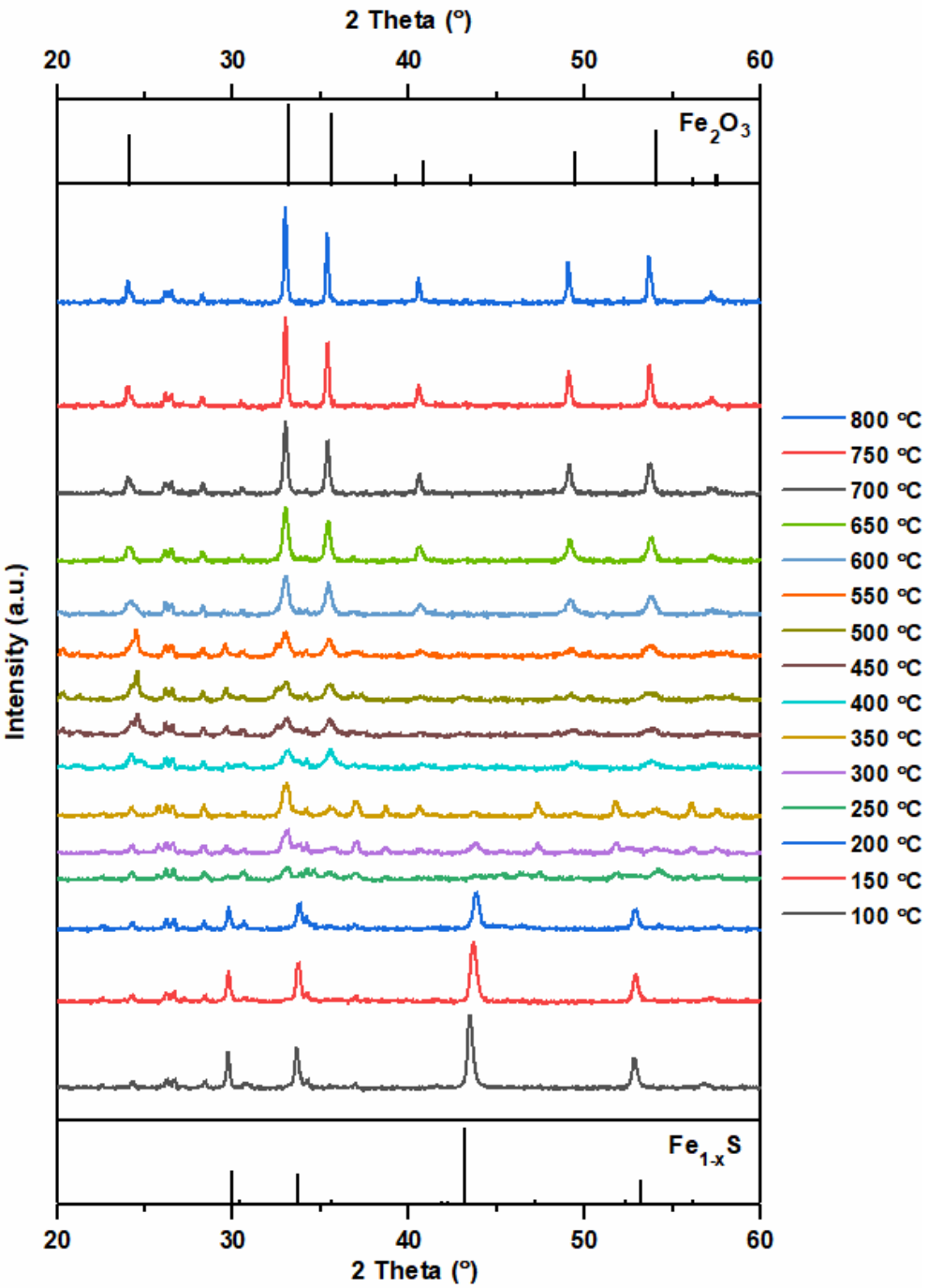

Figure 4.7: In-situ XRD, pyrrhotite sample heated in air room temperature - 800 °C, 5 °C min^{-1}. XRD analysis run every 50 °C.

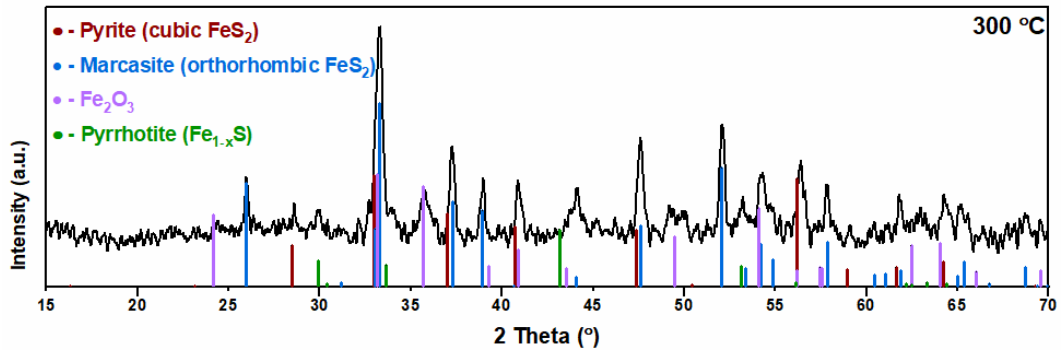

Figure 4.8: XRD of pyrrhotite sample calcined at 300 °C during in situ conditions. Compared to JCPS PDF files. (Brown)- Pyrite, FeS_2, 01-088-2293, (Blue) – Marcasite, FeS_2, 01-074-1051, (Purple) – Fe_2O_3, 01-085-0987, (Green) – Pyrrhotite, $Fe_{1-x}S$, 01-079-5974.

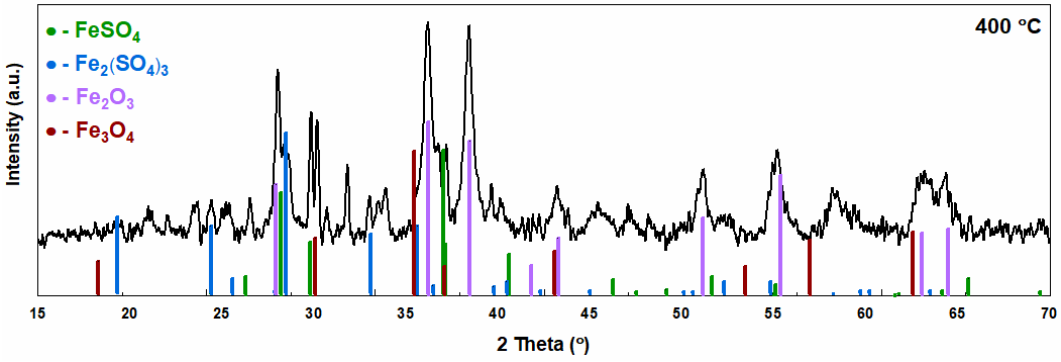

Figure 4.9: XRD spectra of pyrrhotite calcined at 400 °C (during in situ conditions) compared to corresponding XRD patterns sourced from JCPDS files. (Green) – $FeSO_4$, 01-073-1057; (Blue) – $Fe_2(SO_4)_3$, 00-033-0679; (Purple) – Fe_2O_3, 01-085-0987; (Brown) – Fe_3O_4, 01-074-1909.

4.2.3 Pyrrhotite Calcination Optimisation

Considering oxidation creates many different iron sulphide/oxide structures, samples of pyrrhotite were calcined at different temperatures in a furnace under flowing air to re-create these structures, especially focusing around 150-300 °C where the material transforms from pyrrhotite to amorphous iron sulphide. They were then tested for catalytic activity, presented in Figure 4.10. It was found that calcining the material at 200 °C proved the optimal calcination temperature, achieving the best formate production of 1.00 µmol, greatly improving the catalytic activity of fresh pyrrhotite (0.29 µmol). Increasing the calcination temperature further, drops the activity back down to its original activity. TGA and *in situ* XRD has already

determined that increasing the calcination from 150 °C to 200 °C to 250 °C causes an increase in oxygen incorporation, and a drop in crystallinity. However, more characterisation is necessary to determine the active species for this catalyst under a 200 °C calcination. An *In-situ* XRD experiment proceeding at 200 °C for 12h, revealed that when calcined even for 12 hours, very little change in the crystal structure is observed after 4 hours of calcination, exhibiting the stability of this crystal phase (Appendix Figure 7.2). Blank reaction without catalyst present observed no formate production. To eliminate the possibility of pure iron oxides or iron sulphoxides performing the catalytic activity within the sample, commercial sources of Fe_2O_3, Fe_3O_4 and $FeSO_4$ were tested for CO_2 hydrogenation, and although they all produced formate, these materials were found significantly less active than pyrrhotite.

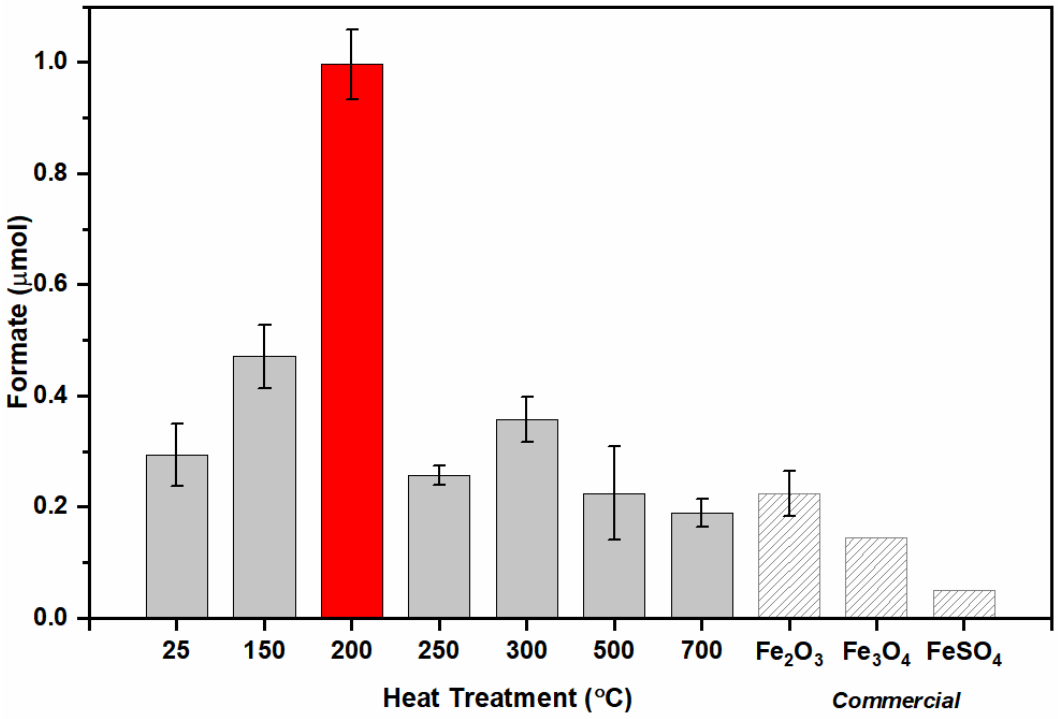

Figure 4.10: Comparison of the effect of different calcination temperatures of pyrrhotite catalyst for the hydrogenation of CO_2 to produce formate. (red) most active material, (grey) less active synthesised materials, (striped) commercial materials. Reaction conditions: $Fe_{1-x}S$: 20 mg, 1 M aqueous NaOH: 4 mL pCO_2: 10 bar (at 25 °C); pH_2: 10 bar (at 25 °C); reaction temperature: 125 °C; reaction time: 3 days. All data points (except Fe_3O_4 & $FeSO_4$) repeated at least twice. 200 °C repeated x4.

Reaction temperature study at 100 °C, 125 °C and 150 °C is presented in Figure 4.11. Results found a linear trend, increasing temperature increased formate productivity up to 150 °C. A reaction temperature remained at 125 °C for the rest of the study as reaching 150 °C was close to the limit of the reactor.

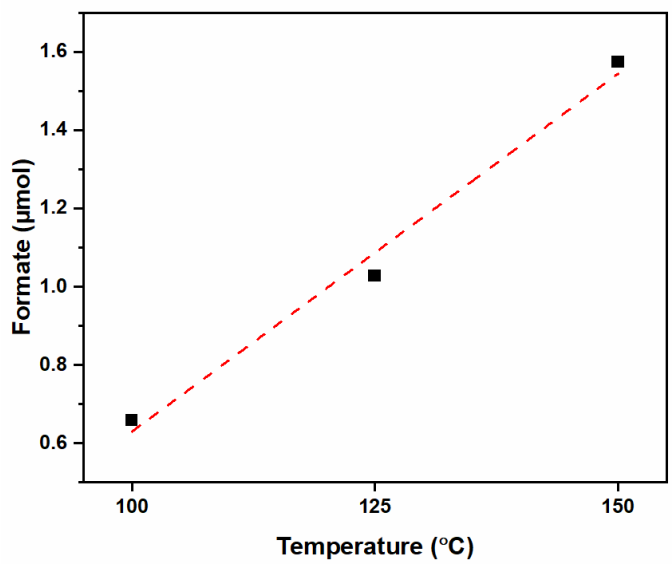

Figure 4.11: Reaction temperature study; usual reaction conditions proceeding at varying temperatures (black square) fitted with a linear trendline (red). Reaction conditions: $Fe_{1-x}S$: 20 mg, 1 M aqueous NaOH: 4 mL, pCO_2: 10 bar (at 25 °C); pH_2: 10 bar (at 25 °C); reaction time: 3 days.

4.2.4 Catalyst Characterisation

pXRD, Raman, elemental analysis and XAFS were run over the pyrrhotite materials individually calcined over varying temperatures to achieve greater insight into the effects this heat treatment has towards the phase morphology, elemental composition and chemical species of the bulk of the material. SEM imaging and XPS analysis of fresh and calcined samples also gave more information of the physical morphology and chemical species along the surface of the catalyst.

XRD & Raman studies

Individually calcined samples were characterised using pXRD, Figure 4.12, and Raman spectroscopy, Figure 4.13. pXRD revealed a slight difference to *in situ* XRD, a 200 ^{o}C calcination revealed a more amorphous structure, due to differences in calcination procedures (*in situ + ex situ*). As found previously through *in situ* XRD, using pXRD we again see a steady transformation from pyrrhotite to Fe_2O_3 with increasing temperature. XRD spectra of pyrrhotite calcined at 300 ^{o}C, Figure 4.8, reveals the phase structure is dominantly a mixture of FeS_2 polymorphs; pyrite (cubic) and marcasite (orthombic). We also see the presence of Fe_2O_3, and remaining pyrrhotite character. This gives the indication that increasing the temperature from 200 ^{o}C to 300 ^{o}C causes iron oxidation resulting in Fe-S bond cleavage, to create FeS_2 and Fe_2O_3.

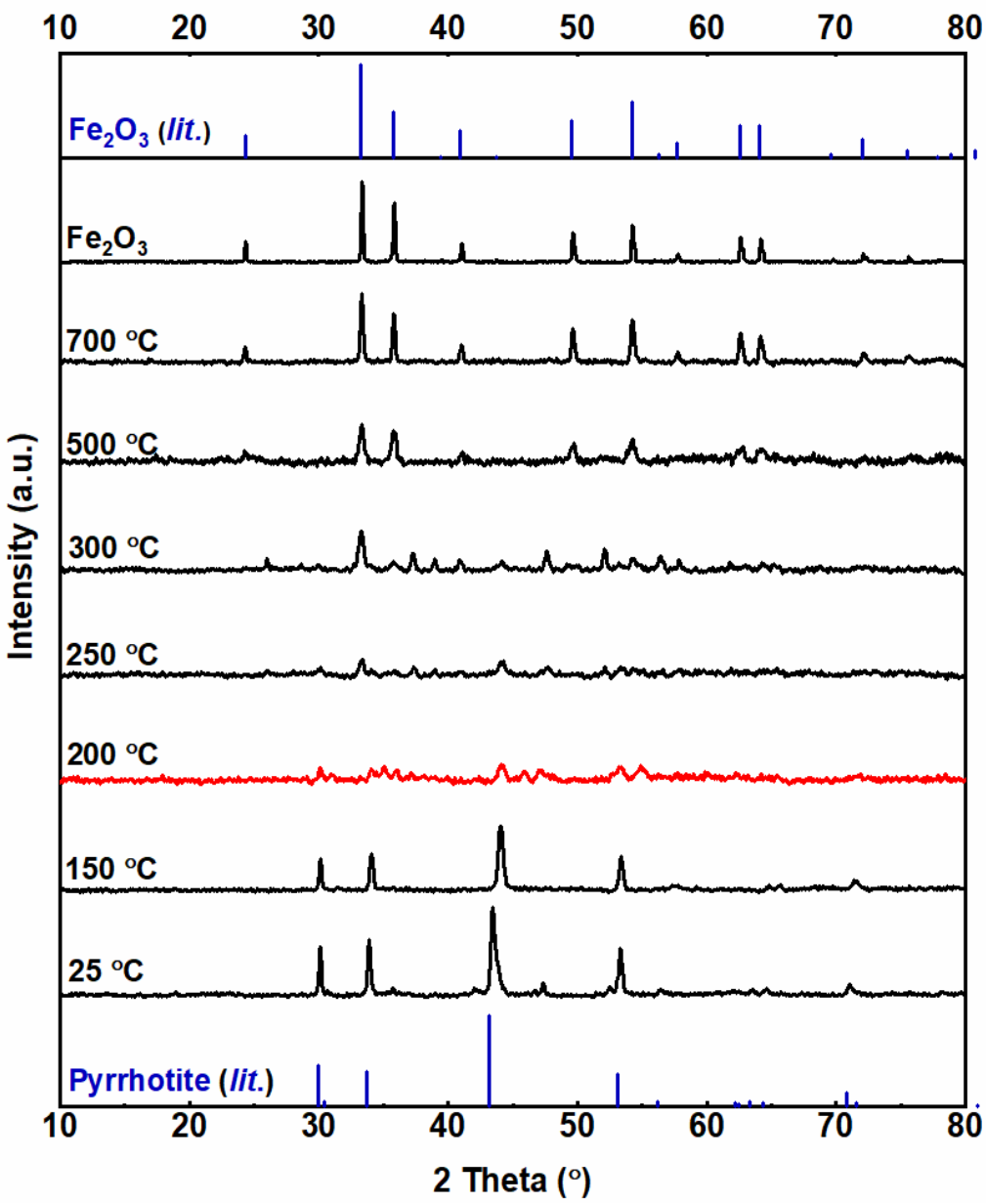

Figure 4.12: pXRD of pyrrhotite material calcined at different temperatures from fresh – 700 °C. (red)-most catalytically active species (blue) reference peaks.

Raman spectroscopy, Figure 4.13, detects pyrrhotite at approximately 408 cm^{-1}, 291 cm^{-1} and 223 cm^{-1} [215], which dominates the spectra throughout all calcination temperatures. This implies that Fe-S species are still present even after a high temperature calcination. This was not detected in XRD, implying these Fe-S species transforms into the amorphous phase. At 500 °C the presence of Fe_2O_3 is observed, as seen from the peak at approximately 1314 cm^{-1}, in addition, small quantities of Fe_3O_4 species at 612 cm^{-1} and elemental sulphur, S_8, 493 cm^{-1} are

also present. These findings are within agreement with Genchev's work[216], and their study of mackinawite ($Fe_{1+x}S$) oxidation. Here they express Fe_3O_4 as an intermediate for the transformation of the iron sulphide to the Fe_2O_3. Their findings discuss upon further laser heating (oxidation), all the Fe_3O_4 in their sample became completely oxidised and transformed into the more stable Fe_2O_3.

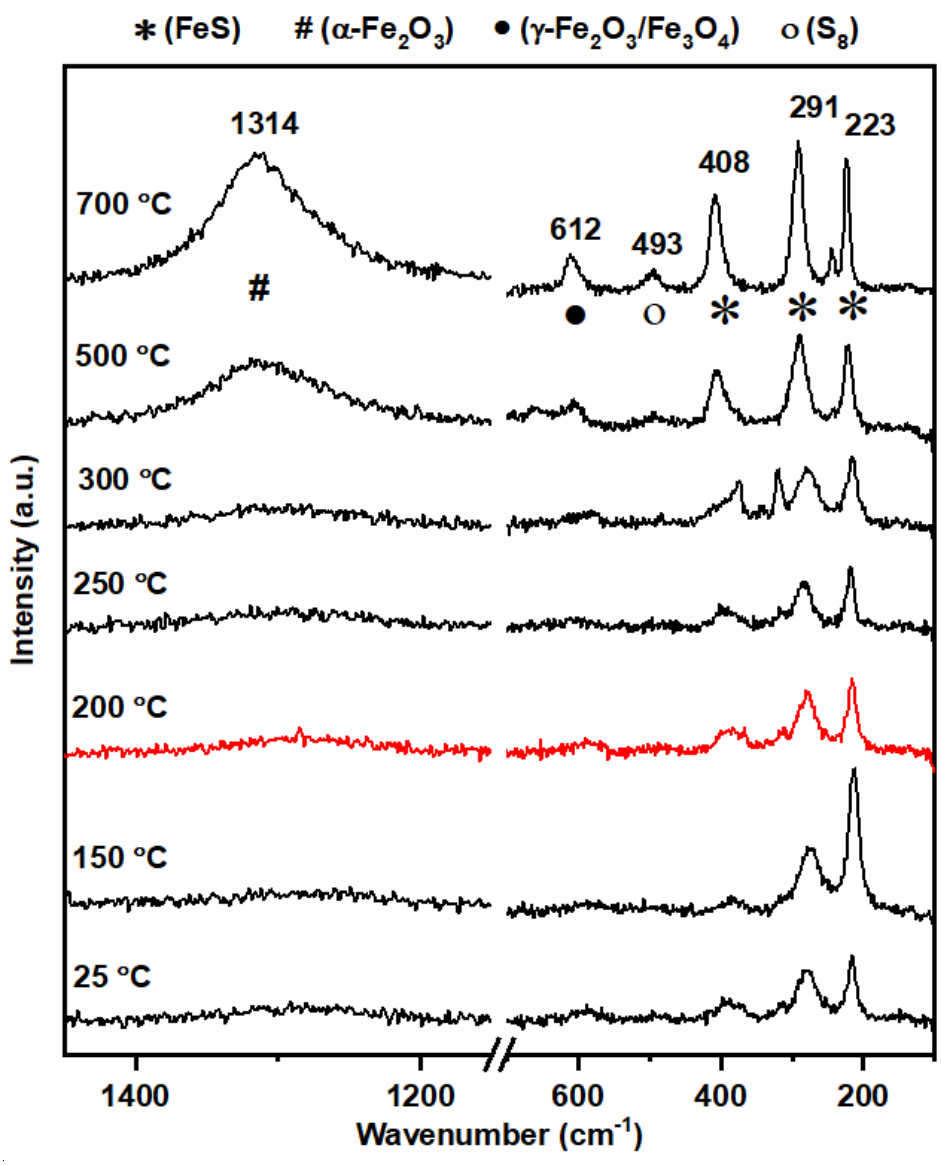

Figure 4.13: Raman spectroscopy of pyrrhotite material calcined at different temperatures from fresh – 700 °C. (red)-most catalytically active species. (star)-$Fe_{1-x}S$, (hash)-α-Fe_2O_3, (dot)-γ-Fe_2O_3/Fe_3O_4, (hollow circle)-S_8.

FT-IR of the beforementioned calcined pyrrhotite samples were also employed, presented in the Appendix Figure 7.3, however, these results contributed very little.

Elemental Analysis

Elemental analysis was performed by Exeter Analytical using ICP-OES analysis. These results shown in Table 4.2 calculates the relative concentration of Fe, S and O within the fresh and calcined samples. Iron shows a small drop in concentration after calcination, which may be within instrumentational error. There is very little change in concentration of sulphur, confirming that no sulphur is removed off the surface during calcination. Oxygen more than doubles in concentration after calcination, an atom percentage of 10% predominantly distributed along the surface.

Table 4.2: Elemental Analysis of fresh and calcined samples of pyrrhotite.

Sample	**Weight %**			**Atom %**			
	Fe	**S**	**O**	**Fe**	**S**	**O**	**$Fe_xS_yO_z$**
Pyrrhotite Fresh	61.62	36.63	1.75	46.8	48.5	4.7	$Fe_{0.96}SO_{0.1}$
Pyrrhotite calcined 200 ^oC	59.35	36.65	4	43.3	46.5	10.2	$Fe_{0.93}SO_{0.2}$

SEM

Typical SEM micrographs are shown in Figure 4.14a+b, a fresh sample of pyrrhotite shows a surface of clusters of crystallites ranging from 50-450 nm. Calcination of 200 ^{o}C shows a decrease in crystallite size ranging from 40-300 nm. As the crystal structure becomes more amorphous, a more porous structure arises proposing a higher surface area.

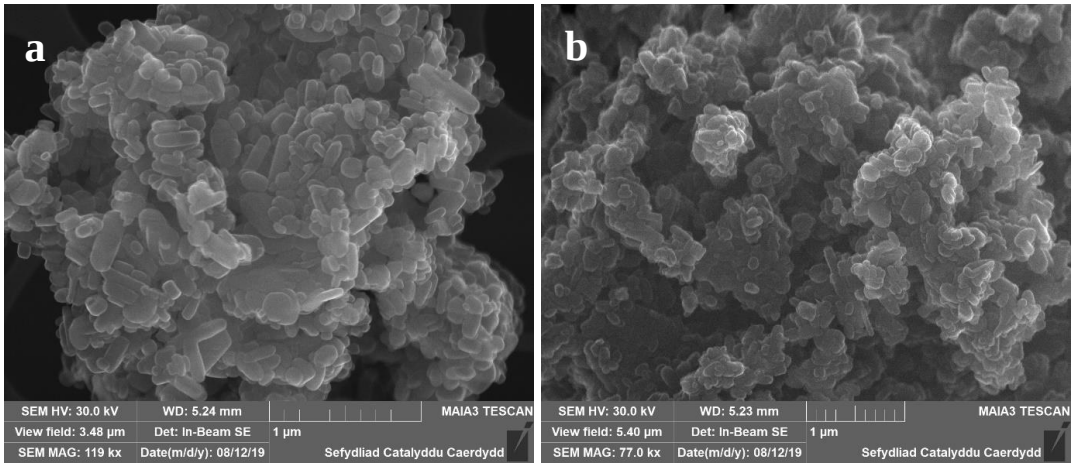

Figure 4.14: SEM imaging of Pyrrhotite samples [a] fresh [b] calcined 200 °C.

A pyrrhotite sample was heated at 200 °C under nitrogen gas and tested for catalytic activity to test how the sample behaves with heat treatment without the presence of oxygen. XRD analysis reveals that heating the sample under N_2 maintains the crystalline phase of pyrrhotite (Figure 4.15a), and the activity of the catalyst is decreased (Figure 4.15b). These results confirm that oxygen has a vital role in the activity of this material and the structural changes, not just the heat treatment.

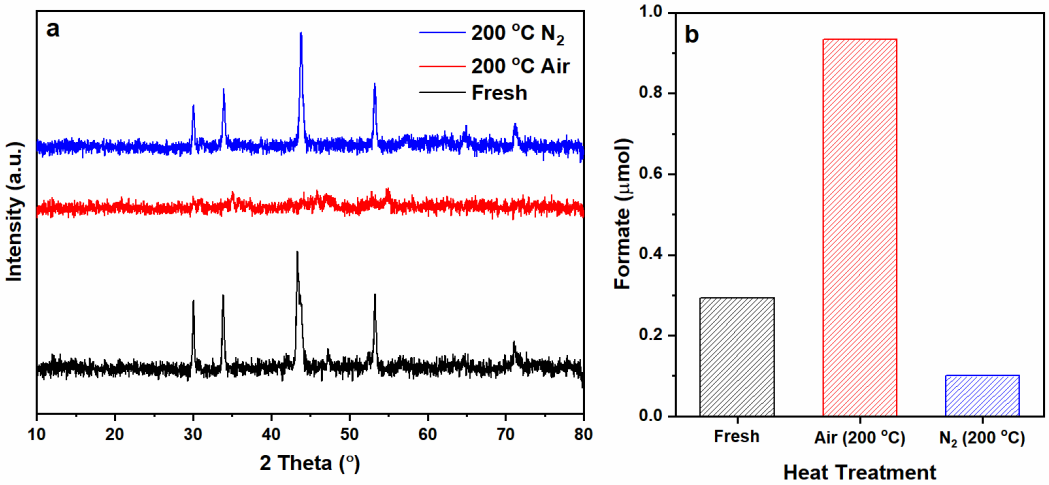

Figure 4.15: [a] XRD and [b] formate production as a result of different heat treatments. (black) none (red) 200 °C under air (blue) 200 °C under nitrogen. Reaction conditions: $Fe_{1-x}S$: 20 mg, 1 M aqueous NaOH: 4 mL, pCO_2: 10 bar (at 25 °C); pH_2: 10 bar (at 25 °C); reaction temperature: 125 °C; reaction time: 3 days.

XPS

To understand the chemical species upon the surface, and how they change with oxidation, XPS was used to compare a fresh sample, and a sample calcined at 200 ºC. The atomic ratio of pyrrhotite fresh Fe : S: O was 12 : 39 : 49 and calcined Fe : S : O was 13 : 7 : 80 approximately. The analysis depth of XPS measurement is approximately 5nm, and not a representation of the bulk. The fresh sample was analysed a few days after synthesis, and the already high oxygen content revealing how sensitive the surface of pyrrhotite is to air oxidation, despite the oleylamine capping agent during the synthesis. Calcination induces this oxidation further, to a dominantly oxygen coated surface. Sulphur has a 39% surface coverage, which drops significantly to 7% as the surface becomes consumed with oxygen. This sulphur is not removed from the material, as already confirmed by elemental analysis. As pyrrhotite is very air sensitive, exposure to oxygen forces Fe atoms to diffuse from the interior to the surface to combine with oxygen[208] leading to a slight increase in Fe content after calcination.

Fe2p analysis of fresh pyrrhotite surfaces shown in Figure 4.16a has three distinct peaks at 710.1-713.3eV indicating the presence of oxidised iron. Another, smaller peak at 707.3 eV, indicating the presence of Fe(II)-S species. These results correspond within measurability to those by summarised by Pratt *et al.*[208] and Buckley *et al.*[207,217]. Pyrrhotite is known to have a mixed valency of iron, involving Fe(III)-S and Fe(II)-S species. Fe(III)-S species can have a binding energy of 709 eV[218], however this is not present in the spectra, therefore any Fe(III)-S present in the sample is below the analysis depth of the spectrometer. Calcination of the surface indicates enhanced Fe-O species, and depleted Fe-S (Figure 4.16c), however, there is still a significant amount present for catalytic activity as found in the S2p spectra. Calcination of the surface exhibits a small positive shift in binding energies for the Fe2p and S2p spectra, as a result of oxidation of the iron and sulphur species.

The S2p spectra (Figure 4.16b+d) are fitted with a doublet representing the spin-orbit splitting of $S2p_{3/2}$ and $S2p_{1/2}$ lines. There shows a dominance of monosulphide (S^{2-}), indicated by the peaks 161.2 eV ($2p_{3/2}$), also disulphides (S_2^{2-}) with peaks at 162.2 eV ($2p_{3/2}$) indicating the

presence of S-Fe bonds. We also find a presence of polysulphides (S_n^{2-}) at 163.2 and elemental sulphur (164.1 eV) originating from S-S bonds. Finally, sulphate $2p_{3/2}$ peaks can be found with binding energies of 166.6 and 168.2 eV corresponding to SO_3^{2-} and SO_4^{2-} respectively. These binding energies are similar to those of Buckley *et al.*[207] and Pratt *et al.*[208]. For fresh pyrrhotite, the monosulphide species has by far the highest abundance, Figure 4.16b, compared to disulphides and polysulphides. Migration of Fe towards the surface to combine with oxygen, as already discussed, leaves Fe vacancies within the structure, forcing the formation of disulphide and polysulphide bonds. The formation of disulphides and polysulphides require the oxidation of some sulphide (S^{2-}) to S^0, so it can be deduced that there is little or no disulphide or polysulphide in pyrrhotite without exposure to air and the S_2^{2-} and S_n^{2-} may have formed during surface oxidisation upon contact with air, leading to cleavage of some S-Fe bonds and the formation of S-S bonds[208]. Hence, calcining the sample alters the ratio of sulphur species significantly. Figure 4.16d shows that upon calcination the presence of SO_x species increase, whilst sulphides decrease in concentration; this time leaving disulphide as the dominant sulphide species as more Fe-S cleavage occurs, also seen with the increase of elemental sulphur. The presence of strong Fe-S peaks in the S2p spectrum, but very weak in the Fe2p spectrum is because S2p photoelectrons have an analysis depth 50% greater than Fe 2p electrons[219]. Thus, showing evidence that a there is a small concentration of iron sulphide on the top layer, with a sulphide rich layer buried beneath the surface oxide dominated layer. From the information received using XPS it is clear that calcination greatly oxidises the surface of the material, leading us to assume that Fe-S bonds cleavage to account for the formation of iron and sulphur oxides, oxidising iron to Fe(III) in the process, a process previously reported from Mycroft *et al.*[209,220].

Calcination from 200 ºC to 300 ºC causes a large drop in activity, XPS results for sample after 300 ºC is also listed in Table 4.3 and presented in Figure 4.16 e&f. S2p spectra follows the same trend as the calcination at 200 ºC, the content of monosulphides decrease from 6% to 3%, where disulphides and polysulphide increase; S_2^{2-}, 15% to 25% S_n^{2-} 3% to 4%. Implying

further Fe-S cleavage and iron migration, forcing the formation of more S-S bonds. SO_3^{2-} decreases (11-5%) as SO_4^{2-} increases (54-61%) as sulphate species becomes more oxidised.

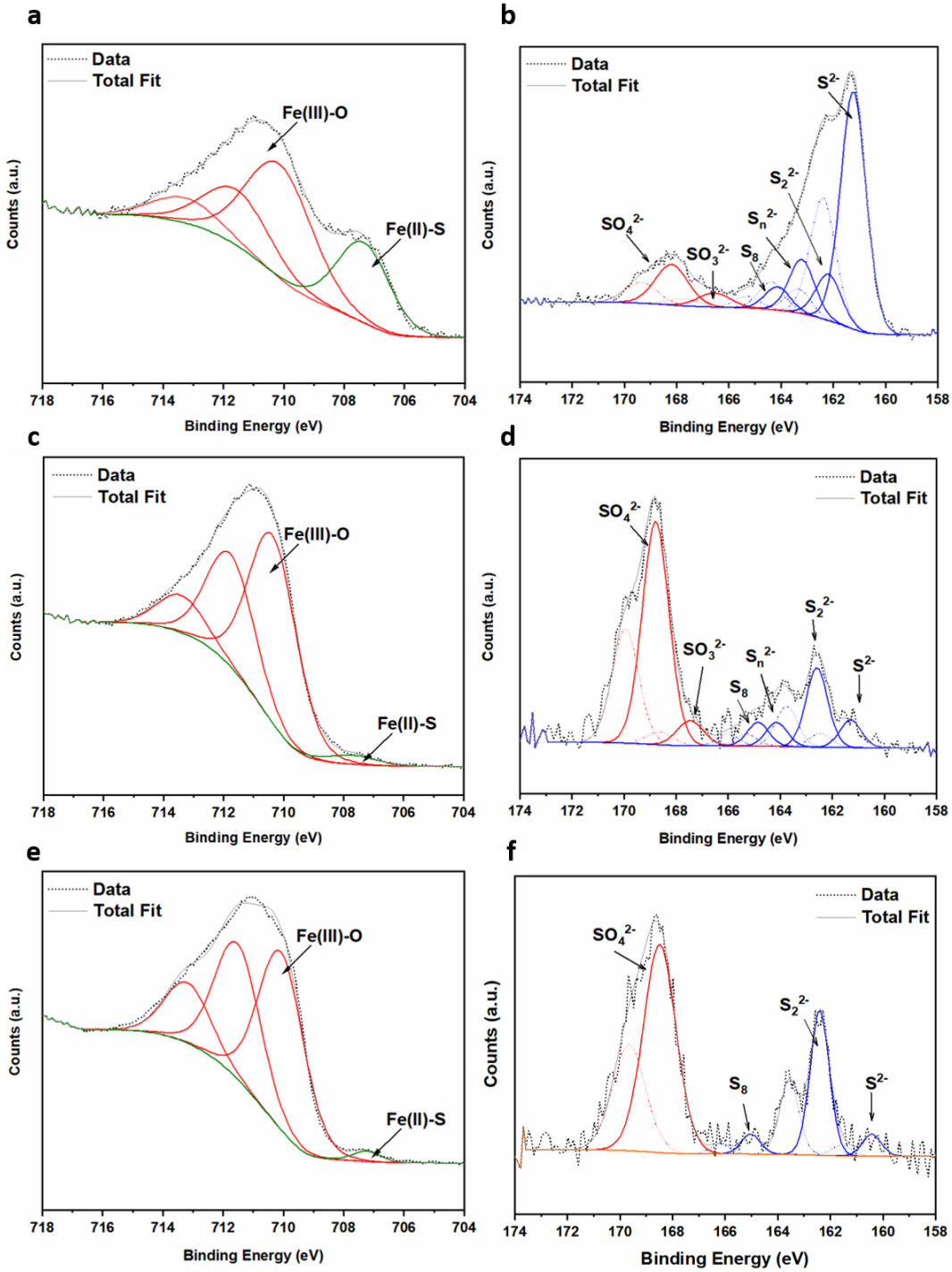

Figure 4.16: XPS spectra of fresh and calcined samples; Fresh [a] Fe2p [b] S2p; Calcined 200 ^oC [c] Fe2p [d] S2p; Calcined 300 ^oC [e] Fe2p [f] S2p. Plot details in (Table 4.3).

Table 4.3: Binding energy data, interpretations and atomic concentrations for the Fe2p and S2p spectra of fresh and calcined pyrrhotite samples. Peak reference correlating to spectra in Figure 4.16.

	Fresh			***Calcined 200 ºC***			***Calcined 300 ºC***		
XPS spectra	*B.E. (eV)*	*Chemical state*	*Atom Conc (%) (±10%)*	*B.E. (eV)*	*Chemical state*	*Atom Conc (%)(±10%)*	*B.E. (eV)*	*Chemical state*	*Atom Conc (%)(±10%)*
Fe2p	707.3	Fe(II)-S	24	707.6	Fe(II)-S	3	707.4	Fe(II)-S	2
	710.1	Fe(III)-O	44	710.4	Fe(III)-O	54	709.7	Fe(III)-O	46
	711.6	Fe(III)-O	21	711.8	Fe(III)-O	32	710.7	Fe(III)-O	36
	713.3	Fe(III)-O	10	713.4	Fe(III)-O	11	712.6	Fe(III)-O	16
S2p	161.2	S^{2-}	36	161.3	S^{2-}	4	160.5	S^{2-}	3
	162.4		19	162.5		2	161.6		1
	162.2	S_2^{2-}	7	162.6	S_2^{2-}	12	162.4	S_2^{2-}	18
	163.3		4	163.7		6	163.5		9
	163.2	S_n^{2-}	8	164.1	S_n^{2-}	4	163.9	S_n^{2-}	-
	164.4		4	165.3		2	165.0		-
	164.1	S_8	3	164.8	S_8	3	165.0	S_8	3
	165.3		2	166.0		2	166.2		1
	166.6	SO_3^{2-}	3	167.5	SO_3^{2-}	4	166.6	SO_3^{2-}	-
	167.7		2	168.6		2	167.7		-
	168.2	SO_4^{2-}	8	168.8	SO_4^{2-}	39	168.5	SO_4^{2-}	43
	169.4		4	169.9		20	169.6		22

X-ray Absorption Fine Structure

XAFS analysis was run for 4 samples; pyrrhotite fresh, calcined at 200 ºC, calcined at 300 ºC and a Fe_2O_3 reference. XANES analysis gave the opportunity to study the oxidation state of iron K-edge (Figure 4.17a). First to notice is a very characteristic pre-edge (feature A) from the contribution of Fe 1s to Fe 3d transition. There is a shoulder to the edge (B) indicating the coordination between Fe and S representing the normally forbidden Fe 1s to Fe 4s transition. There is also white line intensity (C), corresponding to the first allowed Fe 1s to Fe 4p transition[210,221]. Upon calcination at 200 ºC, there is a shift towards lower energy from B, indicating that iron is oxidising with calcination from Fe(II) to Fe(III), in particular loosing Fe-S character and acquiring more O ligands, supported by an increase in intensity at section C. This is re-enforced by the Fourier Transform EXAFS (Figure 4.17b), from a shift in radial

distance. Calcination forms a decrease in radial distance as Fe-S bonds are becoming replaced by Fe-O bonds. This effect is created due to the fact that Fe(II) and S^{2-} are larger ions than Fe(III) and O^{2-} therefore exhibiting a larger radial distance than Fe-S. Fe-S holds a bond distance in the range of 2.37–2.72 Å and Fe-O has a bond distance ranging from 1.81-1.93 Å, which correlates appropriately to the fresh pyrrhotite and Fe_2O_3 samples respectively. Note, elemental analysis has confirmed that sulphur content does not decrease with calcination, therefore any Fe-S cleavage does not mean sulphur loss. The Fourier transform EXAFS reveals something particularly interesting; when the sample is calcined at 300 ^oC, a peak at ~2.8 Å starts to form. As this peak is also present in Fe_2O_3 this can be noted as the Fe-Fe scattering component, which has been confirmed by XRD. This peak is not present for the fresh and 200 ^oC calcined samples, which denotes that there are no iron oxide/iron hydroxide species present within the bulk. It has already been confirmed that the 200 ^oC calcined sample shows oxidation has occurred and from the shoulder edge B, Fe-S character is still seen. Therefore, indicating newly formed S-Fe-O species. Increasing the calcination temperature to 300 ^oC separates these species into separate Fe-O Fe-S domains, this correlates to newly formed FeS_2 and Fe_2O_3 species, as previously found through XRD, Figure 4.8. As the formation of these Fe-O and Fe-S domains forms a drop-in catalytic activity, thus strongly suggesting that these unique S-Fe-O species is the active species of the catalyst which reaches its optimum capacity at 200 ^oC.

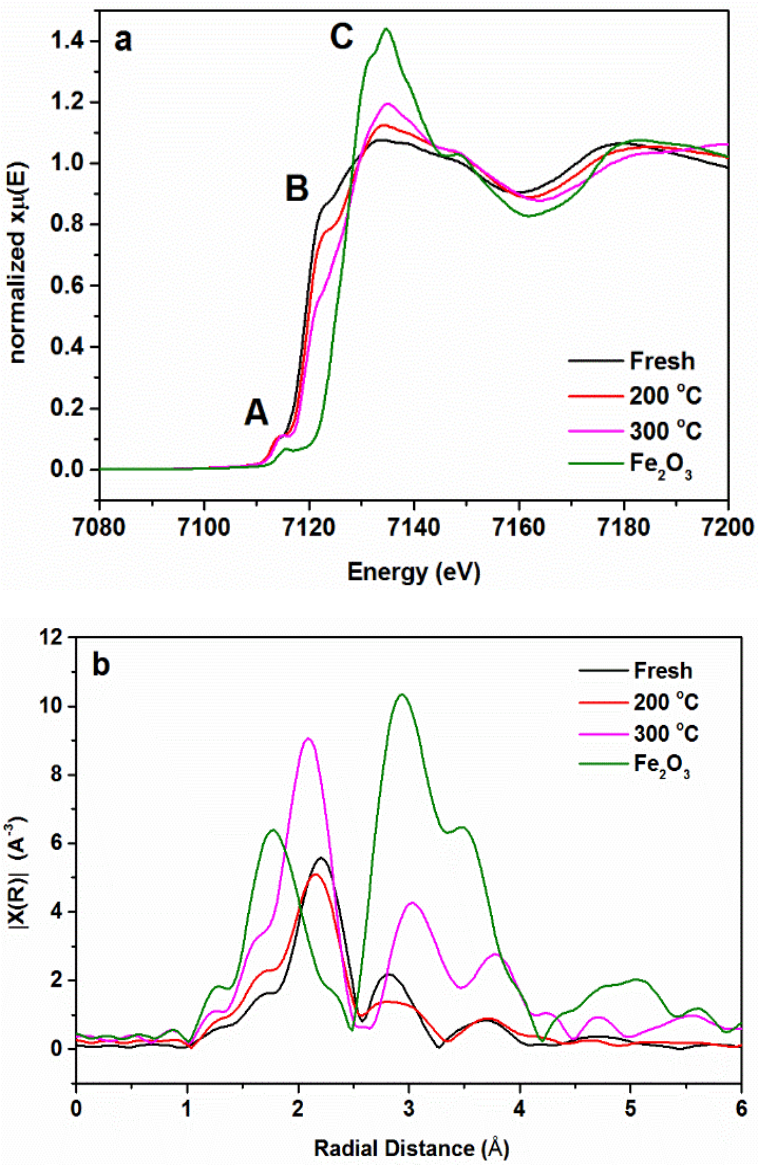

Figure 4.17: XAS data of Fe K-edge including [a] XANES and [b] Fourier Transform EXAFS for pyrrhotite samples; fresh (black), 200 °C calcination (red), 300 °C calcination (pink) and Fe_2O_3 reference sample (green).

Dr Umberto Terranova employed Density Functional Theory calculations, investigating the adsorption of bicarbonate species on (a) a fully oxidised Fe-O surface and (b) a partially oxidised surface containing S-Fe-O units. He concluded that hydrogenation of the carbon atom of HCO_3^- is not possible on a completely oxidised surface. However, replacement of O by 25% S atoms dramatically changes the geometry of the adsorbed HCO_3^-. In addition, the orientation of the sulphur bound hydrogen is more accessible that the oxygen bound hydrogen, making hydrogenation a favourable process. These findings clearly highlight the importance

of sulphur atoms for the HCO_3^- reduction process. The subsequent elimination of H_2O is endothermic with a low activation barrier therefore not hindering the reaction.

4.2.5 Reusability Study

Reusability is crucial for any heterogeneous catalyst, therefore a reusability study was conducted by recycling the catalyst for CO_2 hydrogenation under identical reaction conditions. This is important to determine how the catalyst withstands reaction conditions, and how long it can hold its activity for. Results found that with each reuse the catalyst dropped in formate productivity significantly from 0.85 µmol to 0.21 µmol after 3 uses (Figure 4.18). Characterising the catalyst post-reaction *via* XRD, shown in Figure 4.19, revealed that the crystal structure of the pyrrhotite phase increased in crystallinity with each use, most likely due to the elevated reaction temperature and pressure, forcing reorganisation of the crystal structure. Additional peaks within the diffraction pattern correlate to iron carbonate, $FeCO_3$, with major reflections at $2\theta \approx 25, 32, 46$ & 53 °; corresponding with the reference to the JCPS 00-012-0531 PDF file. This is likely the result of the reactant bicarbonate species irreversibly binding to Fe^{2+} sites on the surface of the catalyst forming iron carbonate, reducing the number of catalytic sites available for further bicarbonate hydrogenation, thus poisoning the catalytic surface. SEM images of the catalyst post-reaction reveals large crystalline structures, shown in Figure 4.20. This can be assumed as $FeCO_3$ crystals developed on the surface of the catalyst, similar imaging is reported by Barker *et al.*[222].

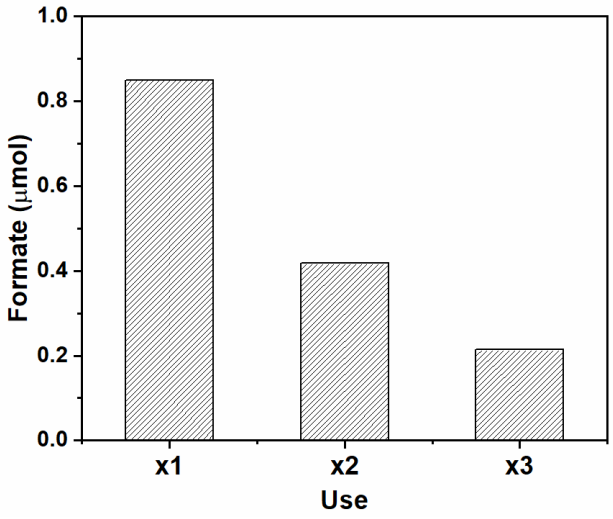

Figure 4.18: Reusability study of pyrrhotite catalyst, 3 consecutive reactions under identical reaction conditions. Reaction conditions: $Fe_{1-x}S$: 20 mg, 1 M aqueous NaOH: 4 mL, pCO_2: 10 bar (at 25 °C); pH_2: 10 bar (at 25 °C); reaction temperature: 125 °C; reaction time: 3 days. Catalyst retained, washed and dried after each reuse.

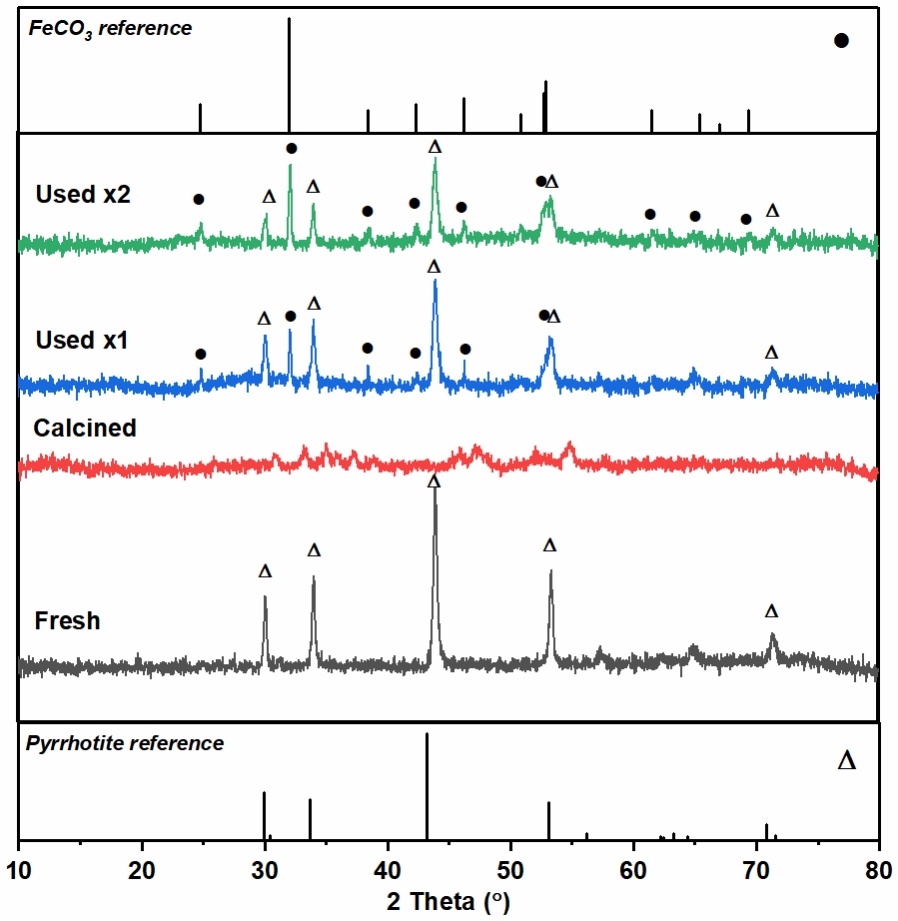

Figure 4.19: XRD spectra of pyrrhotite samples within reusability study, corresponding to Figure 4.18.; fresh (grey) and calcined (red), used x1 (blue) and used x2 (green) Identified peaks corresponding to pyrrhotite (hollow triangle) and $FeCO_3$ (filled circle).

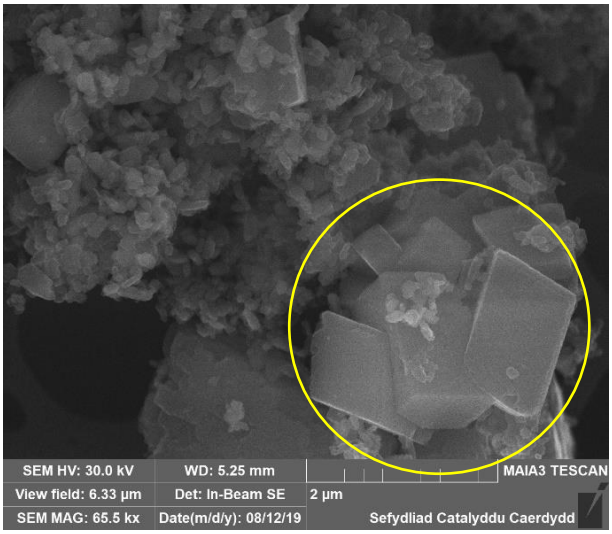

Figure 4.20: SEM image of a pyrrhotite sample, post reaction, revealing large $FeCO_3$ structures, inside the yellow circle.

To determine whether this iron carbonate formation is instantaneous, or develops throughout the reaction, a reaction was set up under the usual reaction conditions and terminated after 1 hour. The catalyst was then analysed by XRD, Figure 4.21. After 1 hour of reaction, the iron carbonate peak is already present, however not as intense as after a 72-hour reaction. This allows one to assume that CO_3^{2-} is always present throughout the reaction, albeit at low concentration, allowing the steady formation of $FeCO_3$. The amorphous crystal phase of the catalyst has little affect after 1-hour reaction. The pyrrhotite crystallinity forms over a long period of time of pressure and temperature.

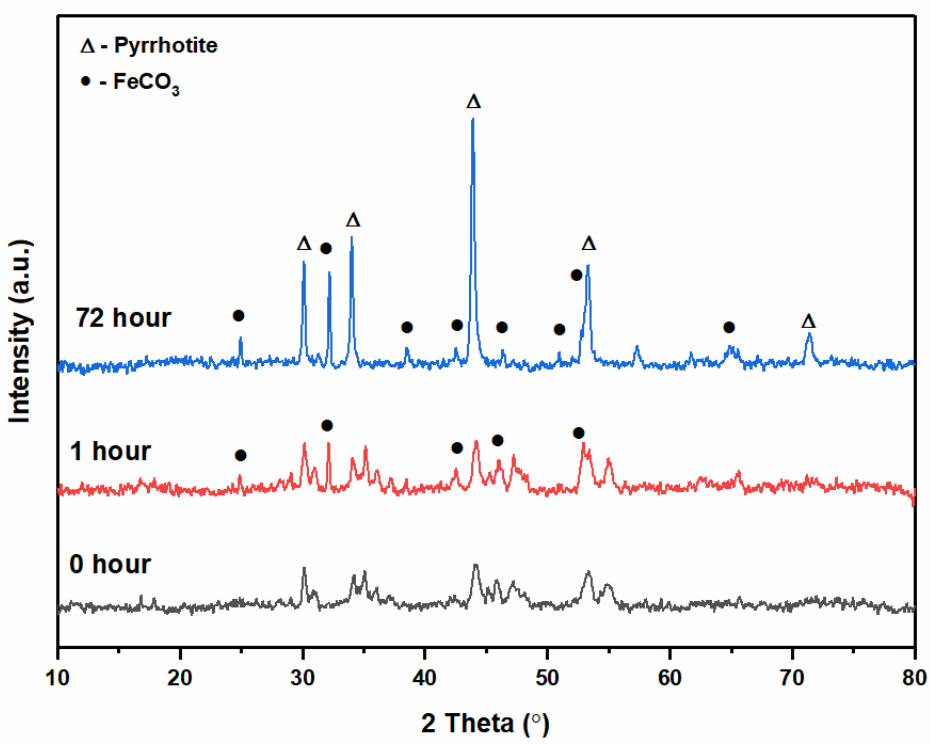

Figure 4.21: XRD spectra representing $Fe_{1-x}S$ catalyst structural change during reaction after 0 hour (red), 1 hour (purple) & 72 hours (blue). Identified peaks corresponding to pyrrhotite (hollow triangle) and $FeCO_3$ (filled circle).

Comparing the catalysts surface post-reaction using XPS, it appears that the reducing conditions of the hydrogenation reaction has decreased the amount of surface oxide species. When comparing pre-reaction and post-reaction samples, the Fe2p spectra (Figure 4.22a, Table 4.4) reveals a marginal increase in Fe(II)-S atomic concentration from 3% to 5%, but negligible change in Fe(III)-O. However, the S2p spectra (Figure 4.22b, Table 4.4) reveals a large decrease in SO_4^{2-} species from 54% to 19%, and increase in monosulphide from 6% to 22% complimenting the increase in pyrrhotite crystallinity. Disulphide and polysulphide species also receive a small increase in atomic concentration.

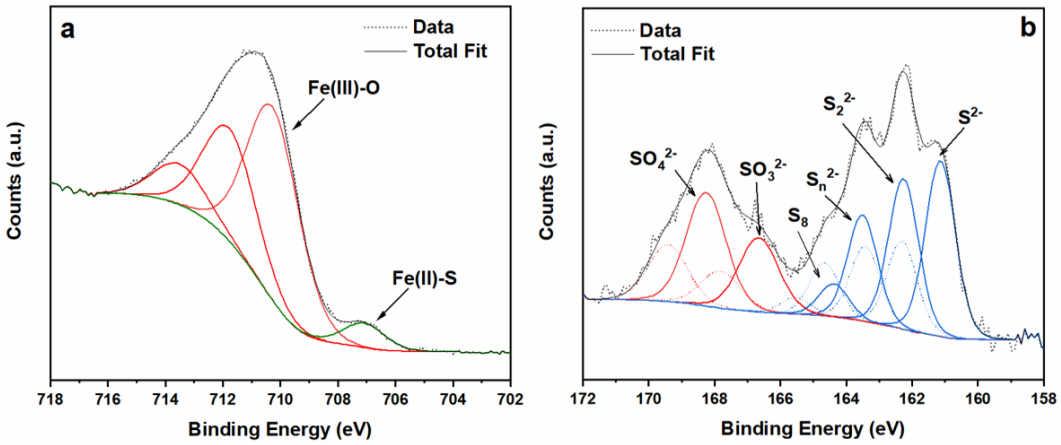

Figure 4.22: XPS spectra of used pyrrhotite catalyst [a] Fe2p [b] S2p. (Plot details in Table 4.4).

Table 4.4: Binding energy data, interpretations and atomic concentrations for the Fe2p and S2p spectra of fresh and calcined pyrrhotite samples. Peak reference correlating to spectra in Figure 4.22.

	Calcined			**Used x1**		
XPS spectra	**B.E. (eV)**	**Chemical state**	**Atom Conc (%)**	**B.E. (eV)**	**Chemical state**	**Atom Conc (%)**
Fe2p	707.3	Fe(II)-S	3	707.1	Fe(II)-S	5
	710.3	Fe(III)-O	54	710.3	Fe(III)-O	53
	711.4	Fe(III)-O	33	711.8	Fe(III)-O	31
	713.4	Fe(III)-O	11	713.5	Fe(III)-O	11
S2p	161.2	S^{2-}	4	161.1	S^{2-}	15
	162.4		2	162.3		7
	162.6	S_2^{2-}	10	162.3	S_2^{2-}	12
	163.7		5	163.4		6
	163.7	S_n^{2-}	2	163.5	S_n^{2-}	9
	164.9		1	164.7		4
	164.6	S_8	8	164.4	S_8	5
	165.8		4	165.5		2
	167.4	SO_3^{2-}	7	166.7	SO_3^{2-}	14
	168.6		3	167.8		7
	168.7	SO_4^{2-}	36	168.3	SO_4^{2-}	13
	170.0		18	169.4		6

A post-reaction sample was also analysed using XAFS, showing changes between the two samples. XANES analysis (Figure 4.23) reveals that there is some change in local Fe-S structure. The three main features of XANES include pre-edge (A) from the contribution of Fe 1s to Fe 3d transition, a shoulder to the edge (B) indicating the coordination between Fe and S representing the normally forbidden Fe 1s to Fe 4s transition and white line intensity (C), corresponding to the first allowed Fe 1s to Fe 4p transition[210,221]. Edge A has decreased, again confirming there has been a shift to higher symmetry. FT-EXAFS also shows a shift to larger radial distance, implying increase in Fe-S species. Additionally, there is no Fe-O domain formation, again implying there has been a change in Fe-S structure. Reformation of these Fe-S species and increase in pyrrhotite character implies that the unique S-Fe-O structures are lost during reaction conditions.

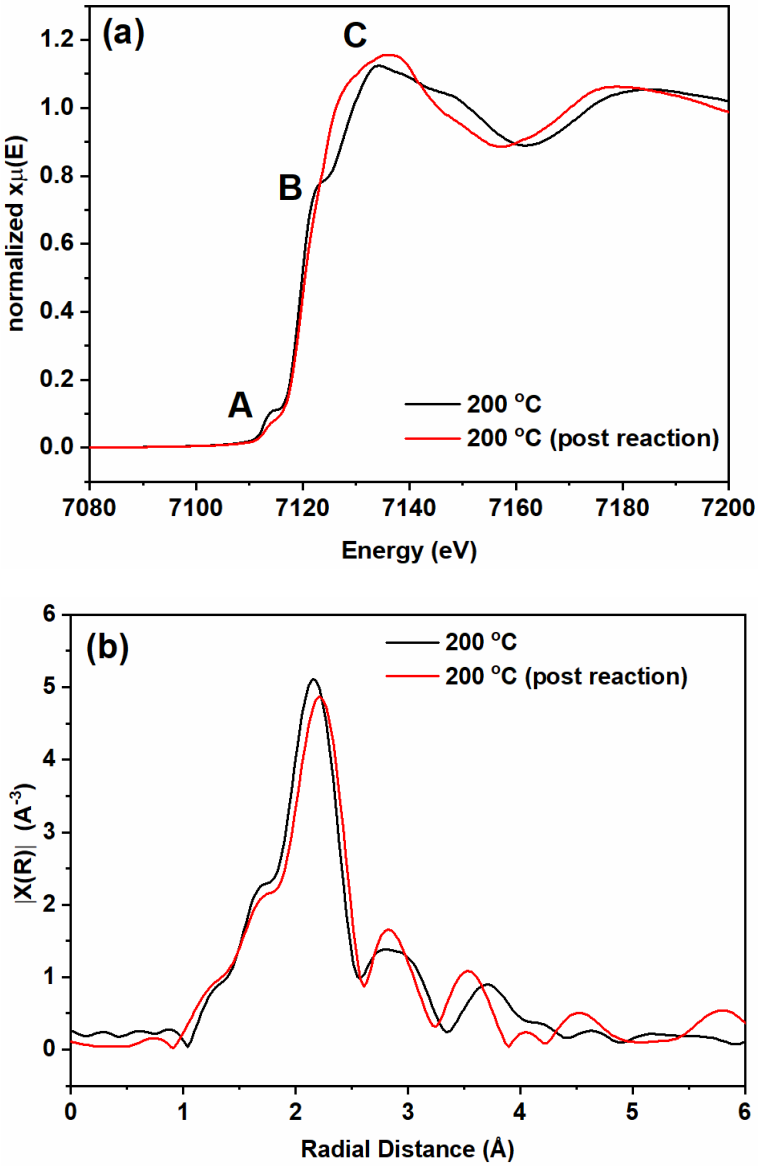

Figure 4.23: XAS data of Fe K-edge including [a] XANES and [b] Fourier Transform EXAFS for pyrrhotite sample calcined at 200 °C; (black) pre-reaction (red) post-reaction.

The catalytic deactivation of a heterogeneous catalyst is the result of loss of S-Fe-O species and the formation of $FeCO_3$; strong chemisorption of carbonate species on the iron catalytic sites may destroy the S-Fe-O species, the active site for catalytic reaction. $FeCO_3$ can be formed from the following reaction, Equation 4.5:

$$Fe^{2+}_{(s)} + CO_3^{2-}{}_{(aq)} \rightarrow FeCO_{3\,(s)} \qquad \textit{Eq. 4.5}$$

$$FeCO_{3\,(s)} \rightarrow FeO_{(s)} + CO_{2\,(g)} \qquad \textit{Eq. 4.6}$$

$$FeCO_{3\,(s)} + SO_4^{2-}{}_{(aq)} + 2H^+_{(aq)} \rightarrow FeSO_4 + CO_{2\,(g)} + H_2O_{(l)} \qquad \textit{Eq. 4.7}$$

Scheme 4.2: Formation of $FeCO_3$ from iron and carbonate species.

To regain the catalytic activity, it is essential to convert the post-reaction catalyst, back to its original state. Blocking of catalytic sites by surface carbonate can be reversed by heat treatments, to remove the carbon species off the surface. If the carbonate species formed during reaction conditions can be removed, there may be a chance for the catalyst to regain its activity. It may be possible to remove this iron carbonate in two ways; *via* thermal decomposition, Equation 4.6, or acid dissolution, Equation 4.7. First, a series of heat treatments were employed and analysed by XRD to see if a post-reaction sample can return to its amorphous crystallinity, and if possible, to remove the carbonate species from the structure, listed in Table 4.5:

Table 4.5: List of pre- and post-reaction samples exposed to a variety of heat treatments.

Sample		**Heat treatment**	
Reference	**Sample type**	**Gas**	**Conditions**
1	Fresh Pyrrhotite	None	None
2	Pre-reaction	Flowing Air	200 °C, 4h
3	Post-reaction	None	None
4	Post-reaction	Flowing N_2	200 °C, 4h
5	Post reaction	Flowing Air	200 °C, 4h

Figure 4.24 displays the XRD spectra of these samples. Freshly synthesised pyrrhotite (1) was calcined (2) and run under usual reaction conditions. This sample was extracted from the reaction media, washed and dried (3). The same post-reaction sample was then heated under flowing N_2 (4) or air (5). As discussed earlier, the reaction conditions cause recrystallisation

of the catalyst, and formation of iron carbonate, represented by the most intense diffraction peak at $2\theta \approx 32$ °. Heating the post-reaction sample under N_2 only promotes further crystallisation of $FeCO_3$ shown as intensified diffraction peaks. Heating the post-reaction sample under air reverts the crystallised pyrrhotite peaks back to an amorphous structure and loss in pyrrhotite structure, which is required for optimised catalytic activity. However, the iron carbonate peaks are still present within the sample. TGA of a post-reaction sample (sample 3) heated under air from room temperature to 900 °C is shown in Figure 4.25. Apart from a small weight loss seen up to 200 °C attributed to evaporation of moisture, there is no significant weight loss until approx. 400 °C, attributing to the decomposition of iron sulphide and the formation of iron oxides. Therefore, thermal decomposition of $FeCO_3$ is not an effective treatment for the regeneration of the catalyst.

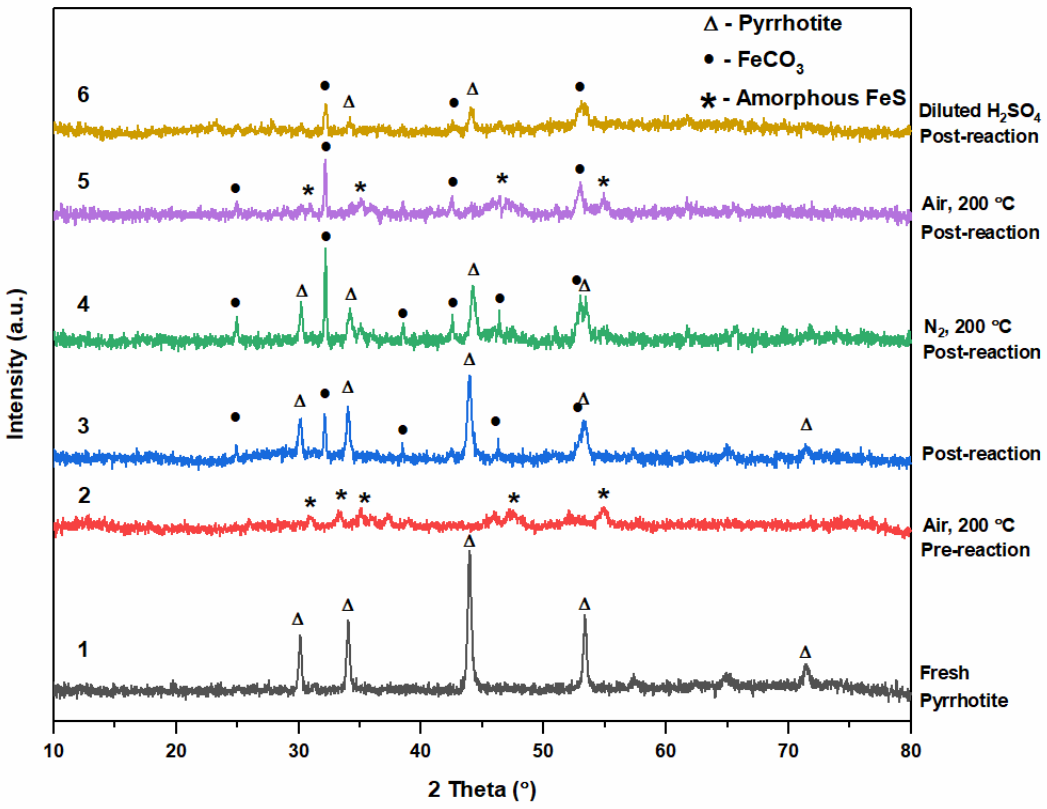

Figure 4.24: XRD spectra following attempt for $FeCO_3$ removal. Samples 1-5 treatment conditions listed in Table 4.5. Sample 6 – post reaction sample immersed in 0.00147M H_2SO_4, 40 °C stirred for 2 hours. Identified peaks corresponding to pyrrhotite (hollow triangle) and $FeCO_3$ (filled circle).

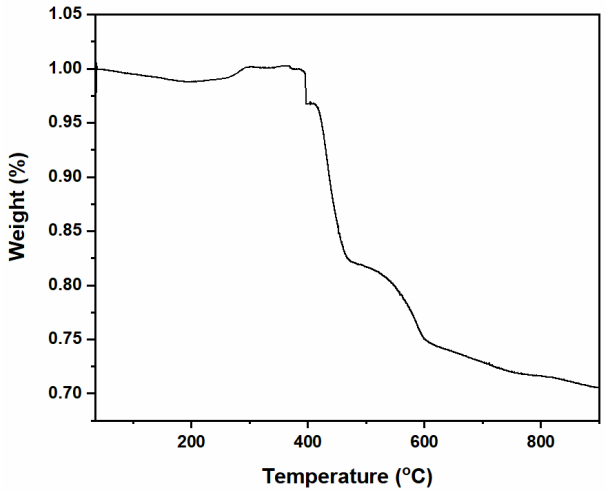

Figure 4.25: TGA of post-reaction sample (sample 3), heated under air from room temperature to 900 °C.

$FeCO_3$ can also be removed by dissolution within acidic conditions[223], therefore the last effort to remove $FeCO_3$ was to immerse a post-reaction sample within weakly concentrated sulphuric acid (H_2SO_4) (0.00147M, 40 °C, 2h), Eq. 4.7. The XRD analysis is presented in Figure 4.24, sample 6. The diffraction pattern shows a drop in $FeCO_3$ intensity however it also shows a loss in pyrrhotite crystal phase. Pyrrhotite has been reported to also dissolve within highly acidic conditions[211], therefore the reduction in the intensity of pyrrhotite peaks likely correlates to destruction of the crystal phase due to dissolution, a situation that must be avoided. Thus far, any attempt to remove the carbonate peak post-reaction without damaging the catalyst has been unsuccessful.

4.3 Conclusions

Herein, I report the synthesis of highly crystalline pyrrhotite ($Fe_{1-x}S$) samples, confirmed by XRD and Raman spectroscopy. Initial synthesis optimisation found that increasing the

reaction temperature and time increased the crystallinity of pyrrhotite and increased the Fe/S ratio. Therefore, a pyrrhotite synthesis procedure at 310 ^{o}C for 12 hours was selected.

These samples are found active for the hydrogenation of CO_2 to formate, albeit weakly active requiring long reaction times, these results are significant as the first iron sulfide materials active for CO_2 hydrogenation within hydrothermal conditions. Catalytic results show that simple high temperature calcination improves the activity of the catalyst further. Studying pyrrhotite oxidation in more detail, an *in situ* XRD study combined with TGA, calcining the sample from room temperature to 800 ^{o}C revealed that the material progressed through a variety of iron sulphide/sulphate/oxide phases. After testing the catalyst calcined at number of different calcination temperatures (room temperature – 700 ^{o}C), it was found that calcining pyrrhotite at 200 ^{o}C produced the most active catalyst for CO_2 hydrogenation. Increasing formate productivity from 0.29 μmol to 1.00 μmol. The same heat treatment involving N_2 instead of air decreased the activity of the catalyst, confirming oxygen has a vital role in the activity. This result was also compared to a number of other materials possibly present within the sample, iron oxide and iron sulphates which all resulted in a low activity, confirming this unique $Fe_xS_yO_z$ material is the source of activity.

XRD analysis of a 200 ^{o}C treatment showed the pyrrhotite material decreased in crystallinity into dominantly amorphous structure, however increasing the temperature to 300 ^{o}C showed the formation of FeS_2 and Fe_2O_3 structures, correlating to a drop in catalytic activity. From XPS, it was determined a fresh pyrrhotite sample already possessed iron oxide species, displaying the how sensitive the material is towards air oxidation. The surface when calcined at 200 ^{o}C presented an increased oxygen surface possessing a surface that is dominant with oxidised iron and sulphate species, a layer that is covering a sulphide rich underlayer. Increase in di/polysulphides is a result of iron migrating towards the surface, causing Fe-S cleavage, leaving a vacancy forcing S-S formation. Exceeding the calcination above 200 ^{o}C constitutes in a further increase of these oxygen containing species forming along the surface, correlating to a drop in catalytic activity. XAFS gave a deeper understanding of these oxygen-species by

confirming mild calcination steadily oxidises Fe-S forming S-Fe-O species up to 200 ºC, whereas any increase in 200 ºC, oxidises these species further causing the formation separate Fe-O and Fe-S domains, appropriately correlating to XRD. The theory of the importance of S within an Fe-O surface is confirmed by density functional theory calculations.

Therefore, from these results, we can denote with confidence that these S-Fe-O species are extremely important for catalytic activity and the likely active sites towards the hydrogenation of the HCO_3^- intermediate. A reusability study found that during reaction conditions caused the formation of iron carbonate and consequently the loss in S-Fe-O species, the likely culprit for the considerably drop in activity after each re-use. Attempts to remove the iron bicarbonate by decomposition or dissolution was unsuccessful. With that being said, the reaction conditions did little to affect the iron sulphide phase, only causing crystallisation of pyrrhotite, which can be easily transformed back into the active material *via* calcination. This result brings to light the potential for regeneration of this material and the motivation for further investigation into this relatively underexplored catalytic material.

5 Violarite and the role of surface oxygen on the catalytic activity for CO_2 hydrogenation

5.1 Introduction

5.1.1 Origin of Life theory

Chapter 4 focused on iron sulphide's catalytic activity for CO_2 hydrogenation. As previously mentioned, FeNiS structures are also proposed to partake a role within the origin of life theory, as Ni(II) ions are found within hydrothermal vents as well as Fe(II) ions. Violarite ($FeNi_2S_4$) has been discovered within these hydrothermal systems. This mineral is structurally similar to greigite, Fe_3S_4, a material already reported active for the electrocatalysis of CO_2 hydrogenation[100].

Gaining inspiration from sophisticated biological processes, Dobbek *et al.* discussed mixed Ni-Fe clusters also found within carbon monoxide dehydrogenase (CODH)[96]. In prokaryotes, the core enzyme within the acetyl-CoA pathway is carbon monoxide hydrogenase (CODH) coupled with acetyl-CoA synthase (ACS). This dual active site reaction is thought to entail the reduction of CO_2 to CO with the help of electrons at an Fe_4NiS_5 cluster called the 'C-cluster', and the subsequent condensation of the CO group at the 'A-cluster' with a methyl group donated by an FeS protein, to produce an acetyl group[94]. More specifically, these Fe_4NiS_5 clusters entail [4Fe-4S] clusters bridged to a Ni atom, revealing in asymmetric [Ni-4Fe-5S] clusters as an active site during the acetyl-CoA pathway, Figure 5.1. Spatial arrangement of these clusters provides a plausible electron-transfer pathway extending from the buried active site to the molecular surface. The structure of metal clusters within CODH-ACS are very similar to mineral forms of (Fe,Ni)S. It has been argued that structure and atomic coordination of catalytically essential (Fe,Ni)S centres of (Fe,Ni)S proteins are not inventions

of the biological world, rather they are mimics of minerals that are indisputably older and which themselves have catalytic activity in the absence of protein[94].

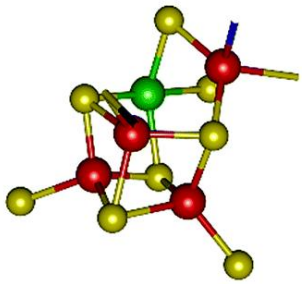

Figure 5.1: [Ni–4Fe–5S] cluster - active site in the nickel-containing CO dehydrogenase; red: Fe atom, green: Ni atom, yellow: S atom. Image reproduced with permission by S. Piontek, Chem. Sci., 2019, 10, 1075. [Reference [224]]. Published by The Royal Society of Chemistry.

5.1.2 Fe-Ni interaction

Ni is found vital to modulate an adequate redox potential in (Ni,Fe) complexes and its inclusion in enzymes is attributed to its flexibility in coordination and ability to shuttle between 3+, 2+ and 1+ oxidation states within a very small potential range[225], allowing electron transfer within the enzyme. These (Ni,Fe)S clusters can also be found in the active site [FeNi]-dehydrogenase, responsible for the catalysis to cleaves molecular hydrogen to a proton, H^+, and a hydride, H^-[99,181], contributing to the generation of formaldehyde by reducing CO_2 bound to an adjacent iron centre.

The electronic interaction between Fe and Ni has been well established within catalysis and alloying Fe with Ni is well known to enhance catalytic performance[226,227]. The Fe-Ni relationship has also been reported excellent catalytic performance for the reduction of CO_2 into methane[228] and CO[229], where the bimetallic interaction outperforms their analogous monometallic metals. Winter *et al.* summarise that this improvement in bimetallic activity is attributed to intermediate bond strengthening, also Ni contributed to the reduction of Fe oxides via enhancing H_2 dissociation and hydrogen spill-over to the Fe oxides[229]. Through theoretical study, Gong *et al.* evaluated the catalytic performance of NiFe-based nanoclusters for CO_2 reduction through a bicarbonate intermediate[230]. Their findings illustrated that the adsorption

of HCO_3^- outcompeted the adsorption of CO_2, also, the formation of CO was difficult through HCO_3^- on NiFe nanoclusters both thermodynamically and kinetically, resulting in the selective conversion of HCO_3^- to formic acid. In summary, the most thermodynamically favourable dissociative adsorption of H_2 and the strongest nanocluster-HCO_3^- interaction situated on the $Fe@Ni_{12}$ nanocluster, after which $HCOO^-$ formed spontaneously. HCO_3^- reacting with an active H atom of H_2 was determined as the rate determining step. The most energetically favourable bicarbonate adsorption occurred when two oxygen atoms are bonded through a Ni atom and an Fe atom (Figure 5.2a), moreover, the short Ni-O and Fe-O bonds indicated a strong interaction with the bicarbonate ion and the $Fe@Ni_{12}$ nanocluster. Adsorption of the bicarbonate ion on 2 Ni atoms of the same nanocluster (Figure 5.2b) deemed marginally less favourable. The NiFe alloy nanoclusters showed a better catalytic activity than a pure nickel, Ni_{13}, nanocluster, arguing that that the HCO_3^- and H_2 could stably co-adsorb, with interaction on the NiFe-alloy nanocluster stronger compared to the Ni_{13} one, resulting in easy intermediate activation.

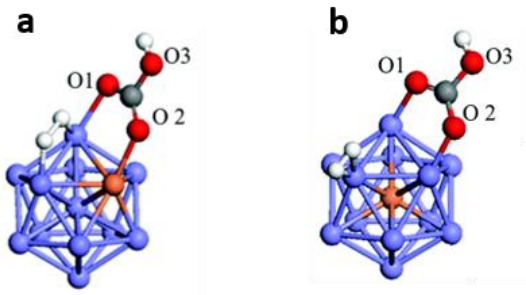

Figure 5.2: H_2 and HCO_3^- co-adsorption on [a] $Ni@Ni_{11}Fe$ and [b] $Fe@Ni_{12}$ nanoclusters; purple: Ni atom, gold: Fe atom, white: H atom, grey: C atom, and red O atoms). Image reproduced from: L. Gong, Phys. Chem. Chem. Phys. (2017) 19, 28344, [Reference [230]], with permission from the PCCP Owner Societies.

5.1.3 $Fe_xNi_yS_z$ catalytic activity

Scouring the literature, iron nickel sulphides have suggested potential for energy generation, oxygen evolution reaction (OER) and hydrogen evolution reaction (HER)[219,231–235], although results are relatively unremarkable. OER catalysis using binary metal oxides such as iron nickel hydroxide/oxide, established that the relationship between Ni^{3+} and Fe^{3+} exerted partial-

charge-transfer activation effect surrounding the Ni^{3+} sites, altering the local environment and average oxidation state, thus exhibiting increased catalytic activity[231]. It is this flexibility in coordination and charge transfer of Ni which demonstrates its important role in biological catalysis. Considering the observed natural performance and close resemblance of NiFe-sulphides to the enzyme CODH, remarkably little is reported for the performance of NiFe-sulphides for the hydrogenation of CO_2. One report by Fu *et al.* demonstrated the synthesis of alkane species catalysed by pentlandite ($Fe_{4.5}Ni_{4.5}S_8$) under hydrothermal conditions, within dilute NaCl/HCl fluid equivalent to that of seawater[236]. Formic acid served as a carbon and hydrogen source, was converted into C_1-C_3 hydrocarbons, albeit with low yields at the cost of high pressure and temperature (50 bar, 400 ^oC). In 2019, Piontek *et al.*[224] synthesised and developed pentlandite mineral to mimic these [NiFe] hydrogenase, which has been found to have the ability to successfully perform electrocatalytic carbon dioxide reduction reaction (CO_2RR). Using aprotic solvents, CO_2RR was favoured over HER with the main products of CO and methane. Although relatively unremarkable products, Piontek has shown the potential for these materials. Posada-Perez *et al.* studied the interaction of CO_2 with violarite via computational study[237], where they found a weak interaction, attributing to the repulsion between CO_2 oxygen atoms and the sulphur atoms. In comparison to greigite (Fe_3S_4) however, replacing an Fe atom with Ni did exhibit a strengthening effect on the binding, but not enough to activate the CO_2 molecule. In the instance regarding this thesis, CO_2 can be activated *via* HCO_3^- species, therefore from Posada-Perez's findings, iron nickel sulphides shows more potential for CO_2 hydrogenation than iron sulphide species.

5.1.4 Violarite Structure

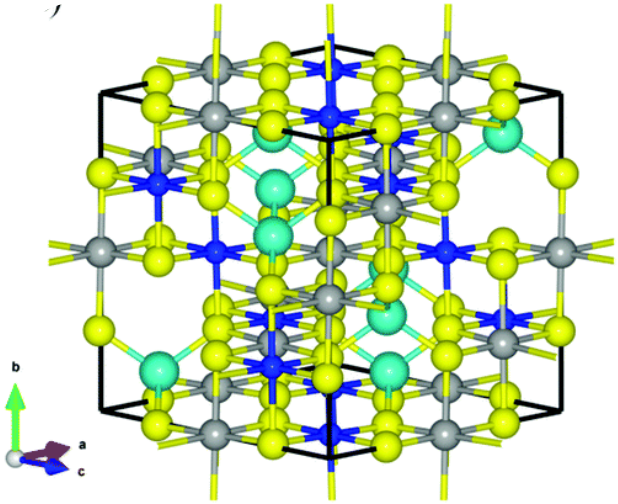

Figure 5.3: Crystal structure of violarite. Yellow: S atom, grey: Fe atom, light blue: Ni (tetrahedral) atom, dark blue: Ni (octahedral) atom, respectively. Image reproduced with permission from Phys. Chem. Chem. Phys. (2018) 20, 20439 [Reference [237]]. Published by The Royal Society of Chemistry (RSC) on behalf of the European Society for Photobiology, the European Photochemistry Association, and RSC.

Violarite is an economically important source of nickel, formation in nature usually occurs from the supergene alteration, a weathering process of the metal-rich pentlandite, $(Fe,Ni)_9S_8$[238,239], involving the oxidation of Fe(II) and Ni(II)[240]; and to a lesser extent the alteration of pyrrhotite ($Fe_{1-x}S$) and millerite (NiS). Violarite is found in an abundant supply, thus, if sufficiently pure is an extremely cost-effective material to work with little environmental expense. Violarite, as represented in Figure 5.3 is nonstoichiometric and adopts the thiospinel structure, a cubic close-packed array of S atoms occupying octahedral and tetrahedral sites, structurally similar to greigite (Fe_3S_4)[240]. Violarite is portrayed to have a high Fe/Ni ratio, an inverspinel structure, $(Ni)^{tet}[FeNi]^{oct}S_4$, with the formula $FeNi_2S_4$ metal oxidation states Fe(II) and Ni(III) are occupied. Although these are considered metastable with respect to the assemblage: $FeNi_2S_4$, $(Fe,Ni)S_2$ and $(Ni,Fe)_{1-x}S$ [241]. Violarite synthesis procedures are often a lengthy process, constituting high temperatures. Early methods report a three-month two-stage preparation, involving heating Fe, Ni and S powders together at 500 ^oC, followed by grinding

and re-annealing[242]. A hydrothermal coupled dissolution-reprecipitation method developed by Xia *et al.* involved the process of artificial pentlandite $(Fe,Ni)_9S_8$ preparation followed by the subsequent preparation of violarite[243]. By adjusting the temperature and pH, they could control the Fe/Ni ratio. Jørgensen *et al.* were the first to report the precipitation of violarite using aqueous Fe, Ni & S elemental components[239], a direct hydrothermal route using iron(II) acetate, nickel(II) acetate and DL-penicillamine. Indicating it is feasible for nickel-rich violarite to precipitate hydrothermally within a geochemical environment.

5.1.5 Violarite Oxidation

Dunn *et al.* meticulously studied the oxidation of violarite, where samples were heated in air up to 1000 ^oC[244]. Much like as previously explored with pyrrhotite, violarite forms a wide range of iron and nickel complexes when oxidised at high temperatures. Up to 405 ^oC, only minor sulfation occurred, above this temperature violarite decomposed into a monosulphide solid solution (MSS), a general formula of $(Ni,Fe)_{1-x}S$, pyrite (FeS_2) and vaesite (NiS_2). From 470 ^oC, iron oxidised into iron(III) sulphates before conversion to hematite (Fe_2O_3) at 585 ^oC. At 670 ^oC, further decomposition formed heazlewoodite ($(Ni,Fe)_3S_2$), sulphur and trevorite ($(Fe,Ni)_3O_4$). Above 725 ^oC, experienced sulphur dioxide evolution associated with the decomposition of nickel sulphate, then heazlewoodite melting above 785 ^oC until the final products trevorite, nickel oxide and hematite formed at 860 ^oC. A similar outcome was also reported from the oxidation of pentlandite ($(Ni,Fe)_9S_8$[245]. Dunn also discussed the preferential oxidation of iron; reporting that upon thermal oxidation, iron migrated from the sulphide core towards the surface forming dense iron oxide rings surrounding a nickel sulphide core. Lower temperatures exhibited oxidation of iron sulphides, followed by oxidation of nickel sulphides occurring at higher temperatures.

5.1.6 Aim of the Chapter

Following on from the success of pyrrhotite's catalytic activity and considering the reported electronic transfer properties and catalytic enhancement of iron and nickel interaction, the aim of this work is to study the effect of incorporating nickel into the iron sulphide structure. This work will investigate the synthesis of iron nickel sulphide, specifically violarite $(Fe,Ni)_3S_4$, and test its catalytic activity for the hydrogenation of CO_2 within alkaline hydrothermal conditions, again entering an unexplored area of research. Calcination of violarite will also be studied to analyse how thermal oxidation plays a role within the material, and in turn how it effects the material as a catalyst. Finally, surface and bulk characterisation of the material will be investigated to gain an understanding of the catalytic species.

5.2 Results and Discussion

5.2.1 Catalyst Synthesis Optimisation

To initiate this study, the catalyst synthesis procedure was first optimised. Thus, 3 different iron nickel sulphide materials were synthesised by altering the $Fe(acac)_2$: $Ni(acac)_2$ precursor ratios. The usual synthesis procedure used throughout chapter 4 with a 1:1 metal-precursor : sulphur ratio was continued for this work. Iron sulphide and nickel sulphide materials were also synthesised for comparison, maintaining the 1:1 metal-precursor : sulphur ratio. In total 5 catalysts were synthesised, as presented in Table 5.1.

Table 5.1: Catalyst precursor ratios used during catalyst synthesis.

Sample number	**$Fe(acac)_2$: $Ni(acac)_2$: Sulphur molar ratio**	**Sample name**
1	1:0:1	FeS
2	0.75:0.25:1	$Fe_{0.75}Ni_{0.25}S$
3	0.5:0.5:1	$Fe_{0.5}Ni_{0.5}S$
4	0.25:0.75:1	$Fe_{0.25}Ni_{0.75}S$
5	0:1:1	NiS

Furthermore, all 5 samples were calcined at 200 °C, these fresh and calcined catalysts were tested for CO_2 hydrogenation under the usual reaction conditions and produced positive results. As presented in Figure 5.4, the freshly prepared $Fe_xNi_yS_z$ catalysts provided good performance for CO_2 hydrogenation. The $Fe_{0.5}Ni_{0.5}S$ catalysts outperformed all synthesised catalysts, producing 1.8 µmol of formate, in comparison to FeS & NiS, producing formate at 0.3 µmol and 1.2 µmol respectively. Calcining the samples improved the catalytic activity for all samples, with $Fe_{0.5}Ni_{0.5}S$ providing the best catalytic performance, producing 4.9 µmol of formate.

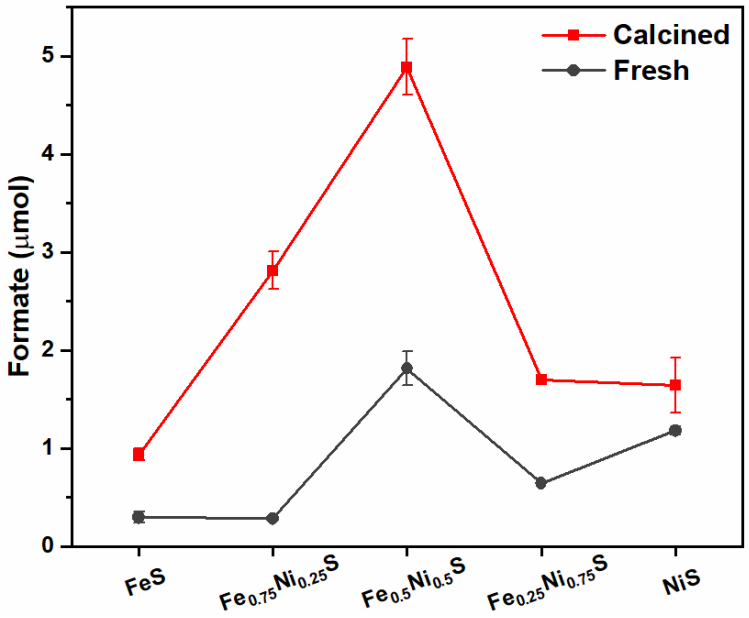

Figure 5.4: Catalyst comparison of fresh (black) and calcined 200 °C (red) iron nickel sulphides with altering Fe:Ni ratio during synthesis. Each data point repeated twice. Sample preparation and labelling described in Table 5.1.

All 10 fresh and calcined samples were analysed using XRD analysis, revealing that the fresh samples have a combination of diffraction peaks relating to pyrrhotite, $Fe_{1-x}S$ (JCPS 01-085-0987 PDF file), heazlewoodite, Ni_3S_2 (JCPS 01-076-1870 PDF file) and violarite, $(Fe,Ni)_3S_4$ (including Ni_3S_4) (JCPS 00-002-0779 PDF file) as shown in Figure 5.5a. However, upon

calcination the diffraction patterns for all $Fe_xNi_yS_z$ samples changed revealing new diffraction peaks correlating to violarite, Ni_3S_4 and millerite (NiS) whilst the presence of pyrrhotite and heazlewoodite diminished (Figure 5.5b). NiS sample revealed the diffraction pattern for Ni_3S_4. $Fe_{0.5}Ni_{0.5}S$ sample has the most intense diffraction pattern correlating to violarite, 4 major reflections are observed at $2\theta \approx 31$, 38, 50 & 55 °. A cubic crystal phase, cell with lattice constraints of $a = b = c = 9.46$ and angles are $\alpha = \beta = \gamma = 90$ °. It's broad peaks represent small particle size of the violarite crystallites. This sample is also the most active catalyst, suggesting that the violarite structure is the source of the catalytic activity. With violarite as the target crystal phase, synthesising the material using a 1:1 Fe:Ni ratio of pre-cursors will be the catalyst synthesis procedure used for the remaining of the study. To avoid confusion, $Fe_{0.5}Ni_{0.5}S$ catalyst will be referred to as $(Fe,Ni)_3S_4$, its true empirical formula, for the remainder of this report. Knowing that $Fe_{1-x}S$ and Ni_3S_4 has a lower activity, and calcination of $Fe_xNi_yS_z$ samples transforms the crystal structure towards violarite correlating with an increase in catalytic activity, suggests that there is some unique interaction between Fe and Ni atoms that allows an increase in activity. It should be noted that $(Ni,Fe)_3O_4$ XRD pattern is not observed within the sample. Whether additional oxygenated species from the calcination procedure plays a role within the active site is next to be investigated.

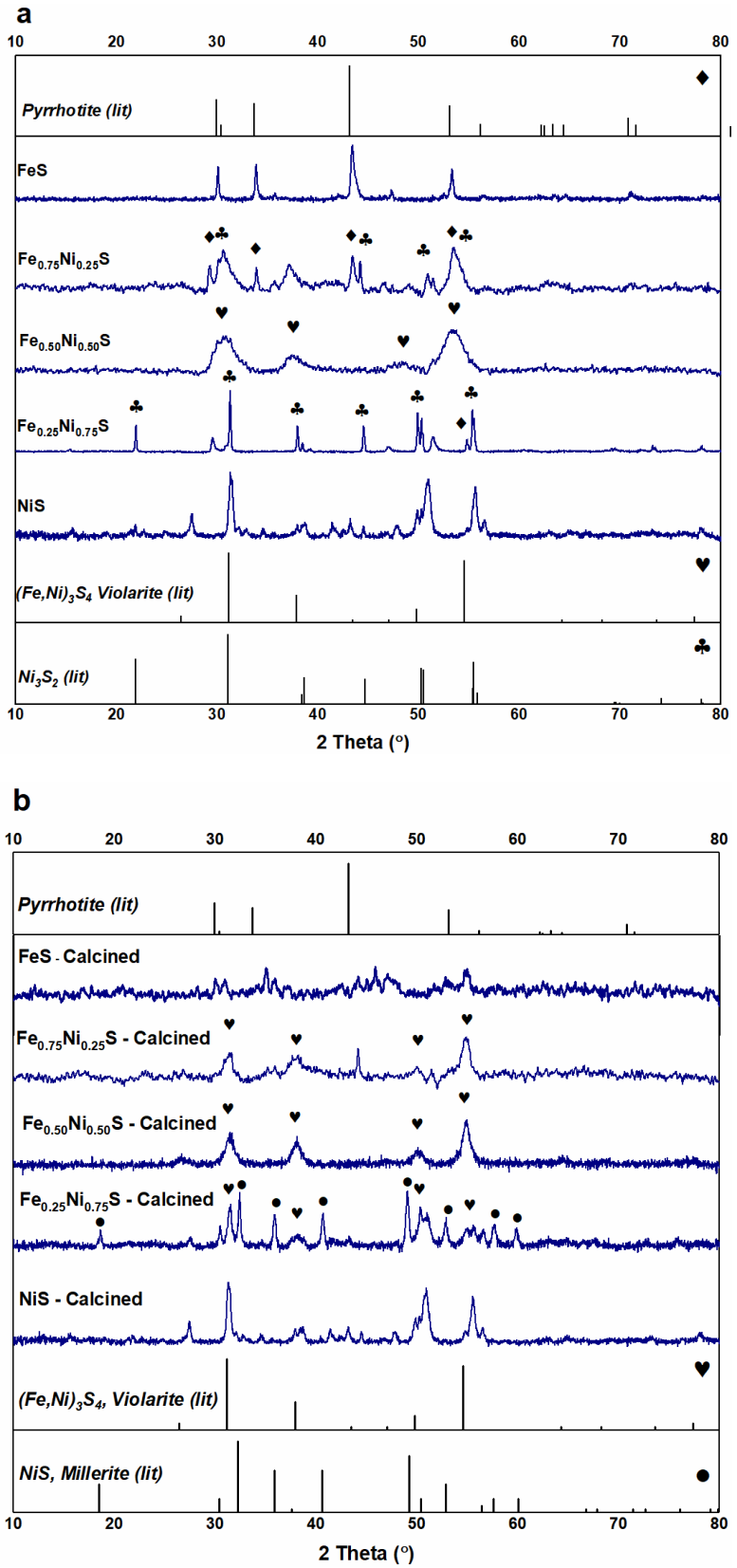

Figure 5.5: XRD spectra of [a] fresh and [b] calcined iron nickel sulphides with altering Fe:Ni ratio. Sample preparation and labelling described in Table 5.1 Diffraction patterns correlate to $Fe_{1-x}S$ (diamond), Ni_3S_2 (club), $(Fe,Ni)_3S_4$ (heart) and NiS (dot) reference patterns.

$(Fe,Ni)_3S_4$ calcined at 300 ºC and 450 ºC were also tested for CO_2 hydrogenation, to compare whether the amorphous or oxidised iron and nickel crystal structures held a higher activity than $(Fe,Ni)_3S_4$ calcined at 200 ºC. Figure 5.6a confirms that violarite calcined at 200 ºC is indeed the most active material thus far, as 300 ºC calcined and 450 ºC calcined catalyst decreased in formate production to 2.4 & 0.4 µmol respectively. The XRD spectra of the sample calcined at 300 ºC, Figure 5.6b, shows $(Fe,Ni)_3S_4$ dropping in crystallinity, and when calcined at 450 ºC the diffraction pattern correlates to the combination of Fe_3O_4 and $NiSO_4$, this will be discussed in more detail later. Commercial sources of Fe_3O_4, $NiSO_4$ and $FeSO_4$ were all tested for their catalytic activity within the same reaction conditions and were found to produce formate at a much lower quantity than all synthesised $Fe_xNi_yS_z$ samples, see Table 5.2. From these results it is possible to rule out iron oxides or nickel sulphates as active catalysts for CO_2 hydrogenation within these reaction conditions.

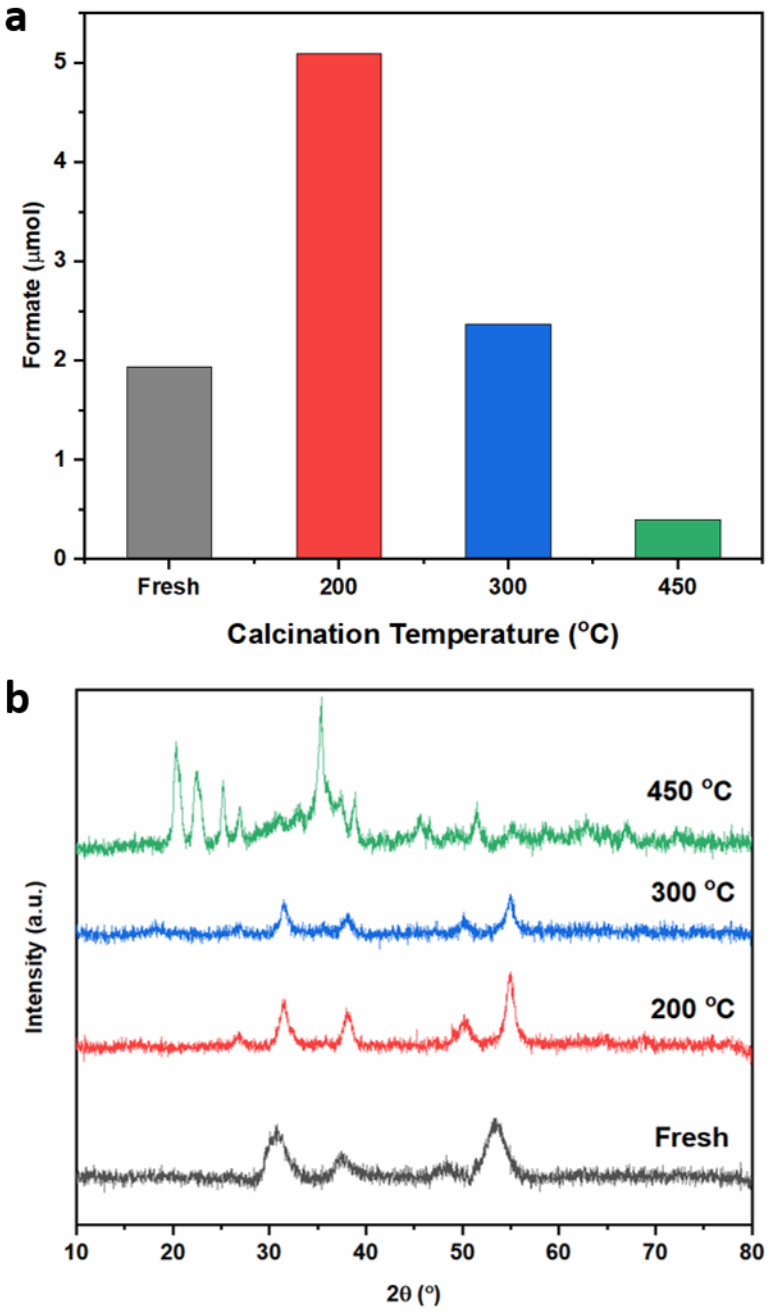

Figure 5.6: Comparison of [a] formate productivity and [b] XRD of $(Fe,Ni)_3S_4$ fresh (grey), calcined at 200 °C (red), 300 °C (blue) & 450 °C (green).

Table 5.2: Testing commercial materials for CO_2 hydrogenation.

Catalyst	Formate (µmol)
$(Fe,Ni)_3S_4$ (calcined 200 °C)	5.08
*Fe_3O_4**	0.14
*$FeSO_4$**	0.05
*$NiSO_4$**	0.04

*Commercially sourced

5.2.2 Calcination study

Violarite is well known to oxidise when heated[244]. To explore this, *in situ* XRD experiments were performed on $(Fe,Ni)_3S_4$ sample over increasing temperatures initiated from room temperature to 800 °C, with a ramp of 5 °C/min under a flow of air. This result is presented in Figure 5.7. This coupled with TGA experiment, Figure 5.8, supports the phase transformations of violarite under calcination. Initial mass loss (up to ~150 °C) is the result of water and residual toluene evaporation off the surface. From 25-200 °C, a steady increase in crystallisation of $(Fe,Ni)_3S_4$ can be observed and a stable mass, the structure then begins to lose its crystallinity and changes phase around 350 °C. Assuming with evolution of SO_2 and a small mass drop of 1% from 310 °C to 355 °C, a monosulphide solid solution (MSS) is formed; a mixture FeS_2, NiS_2, $Fe_{1-x}S$, as well as any remaining $FeNi_2S_4$, also metal oxide species Fe_3O_4 & NiO, Figure 5.9. From 355 °C to 492 °C, there is a mass increase of 7.1%, as oxygen is incorporated into the structure during sulfation, forming metal sulphates, $FeSO_4$ & $NiSO_4$, Figure 5.10. As temperature is increased from 620 °C another change in diffraction pattern arises. Sulphate decomposition releasing SO_2 and a mass loss of 3.2%, correlating with the final formation Fe_3O_4 and NiO crystal phases, Figure 5.11, and the increase in iron oxidation state to iron(III). $FeSO_4$/$NiSO_4$, Fe_3O_4 & NiO diffraction peaks are consistent with reference JCPS reference files; 00-013-0435, 01-074-1909, 00-003-0760, respectively. Allowing subtle

differences in temperature thresholds, these results are within good agreement to Dunn *et al.*[244].

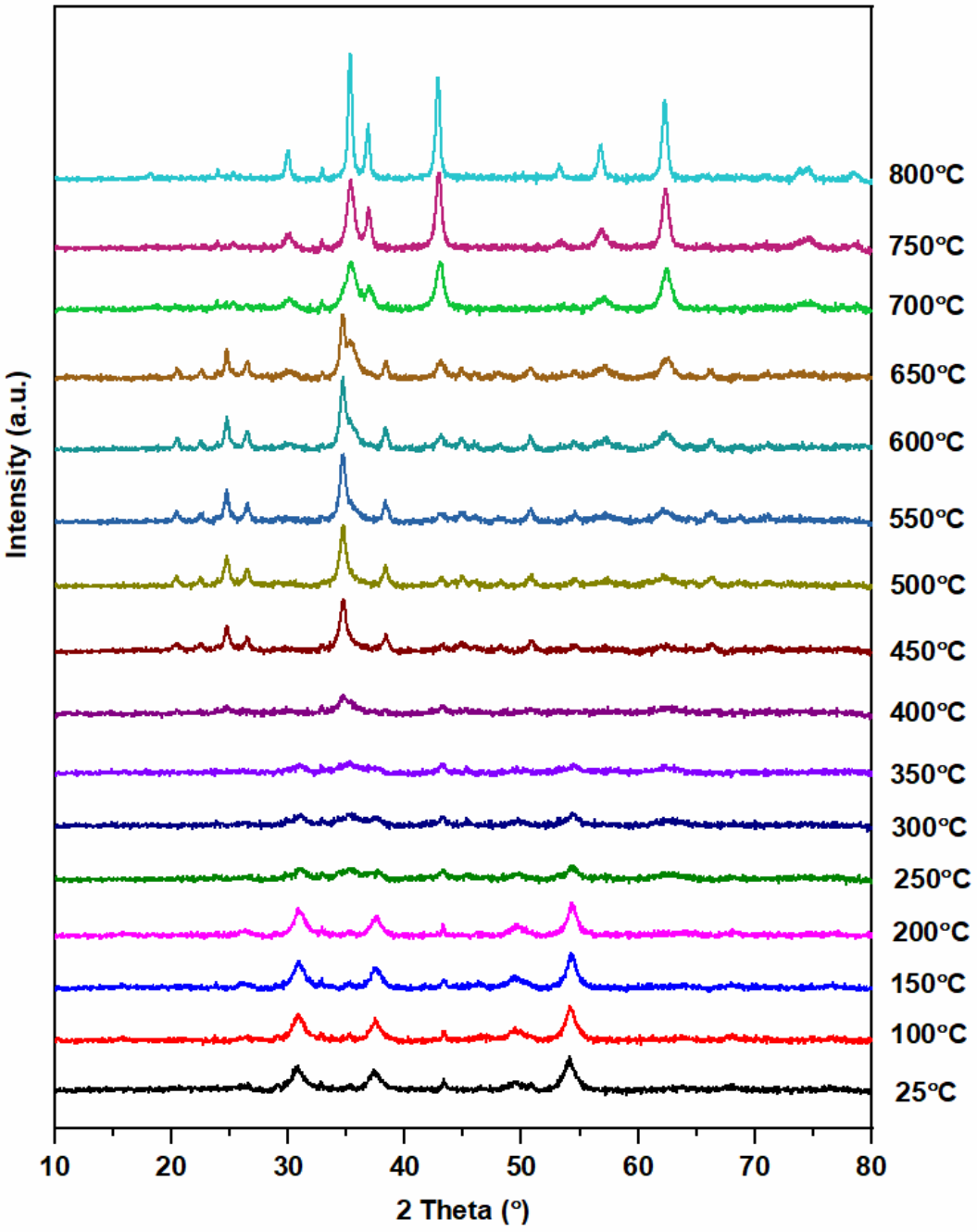

Figure 5.7: in situ XRD, $(Fe,Ni)_3S_4$ sample, from 25-800 °C under flowing air. 5 °C min^{-1}. XRD analysis run every 50 °C. Peaks analysed in more detail at specific temperatures within Figures 5.7-5.9.

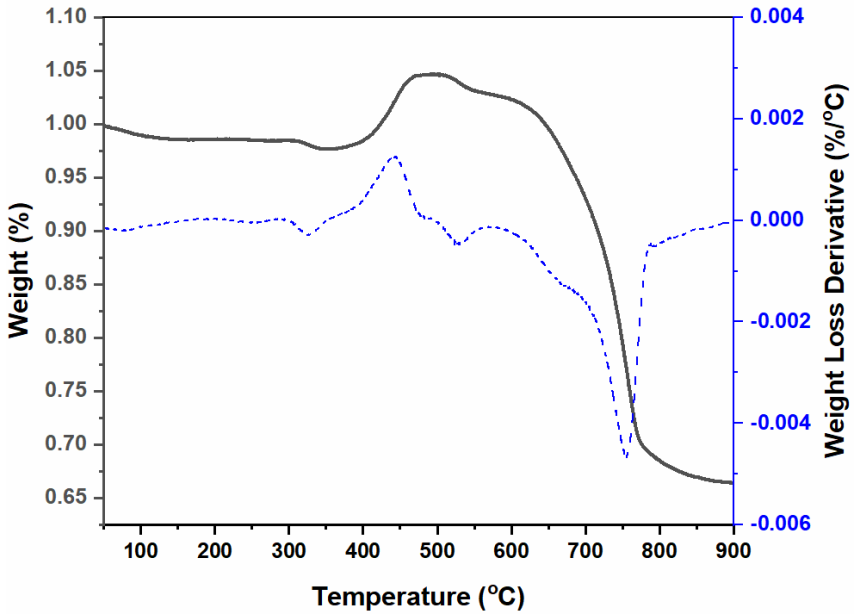

Figure 5.8: TGA of $(Fe,Ni)_3S_4$ sample heated under air from room temperature to 800 °C, 5 °C/min. Percentage weight loss (black) and the first derivative of weight (blue).

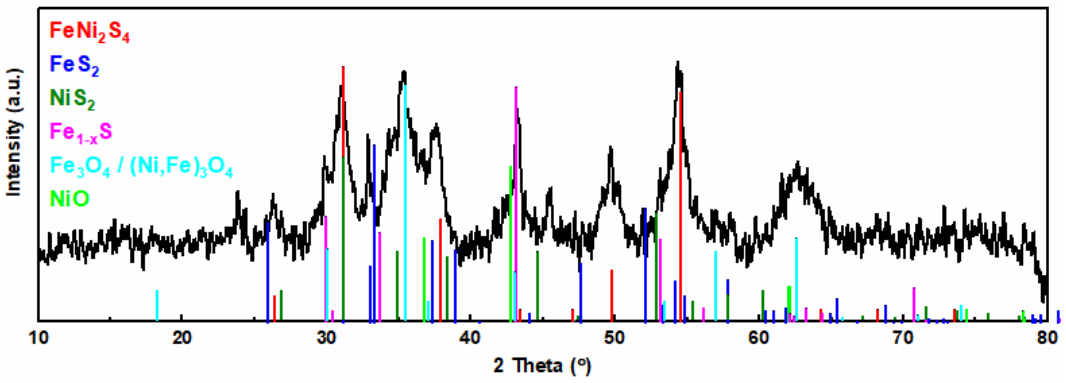

Figure 5.9: XRD spectra of violarite calcined at 350 °C, compared to corresponding XRD patterns sourced from JCPDS files. (Red) Violarite, $FeNi_2S_4$ 01-075-8684; (Dark Blue) – Marcasite, FeS_2 00-002-1342; (Dark Green) – Vaesite, NiS_2 01-071-4834; (Pink) – Pyrrhotite, $Fe_{1-x}S$ 01-079-5974; (Light Blue) – Magnetite Fe_3O_4 01-074-1909 / $(Ni,Fe)_3O_4$ 01-087-2336; (Light Green) - Nickel Oxide, NiO 01-078-4370.

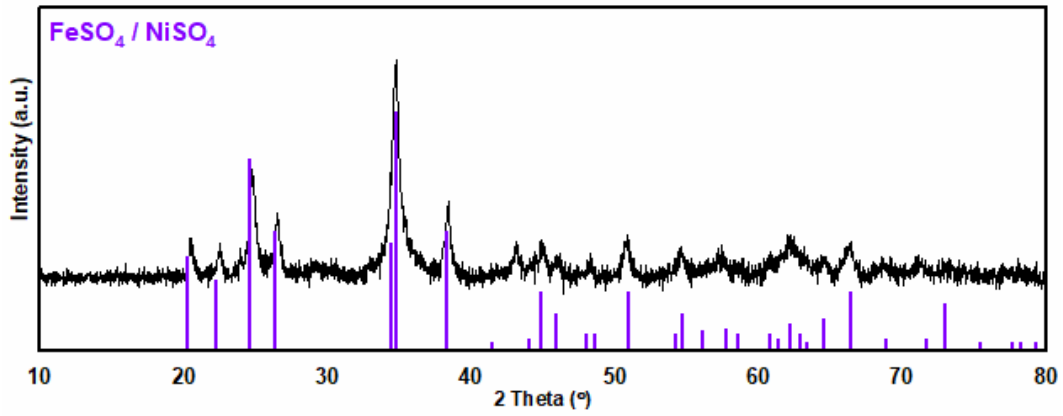

Figure 5.10: XRD spectra of violarite calcined at 500 °C, compared to corresponding XRD patterns sourced from JCPDS files. (purple) $FeSO_4$ / $NiSO_4$, 00-013-0435.

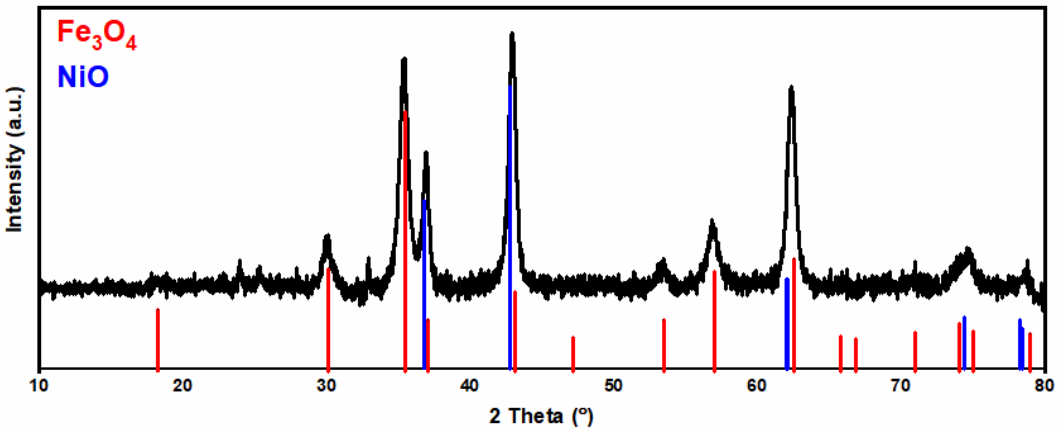

Figure 5.11: XRD spectra of violarite calcined at 750 °C, compared to corresponding XRD patterns sourced from JCPDS files. (red) Magnetite Fe_3O_4 01-074-1909 (blue) - Nickel Oxide, NiO 01-078-4370.

5.2.3 XPS analysis

XPS analysis was performed to determine the surface chemical composition and electronic structure between the fresh and calcined $(Fe,Ni)_3S_4$ samples. The substantial range of iron, nickel and mixed Fe/Ni oxide/hydroxide compounds, and the complexity of their photoelectron spectra (including multiplet splitting and satellite features), makes any interpretation of unknown species of iron nickel sulphides synthesised from iron and nickel precursors very difficult[219], therefore the XPS spectral interpretation must be considered within context. Fe2p analysis is presented in Figure 5.12 a&b. Oxidation of metal sulphides

when exposed to air or moisture is well known and result from the higher free energy of formation to form the metal oxides/hydroxides/sulphates[219]. The Fe2p spectra shows the presence of the Ni $L_3M_{2,3}M_{4,5}$ (^{1}P) Auger peak at ~712 eV and the Ni $L_3M_{2,3}M_{4,5}$ (^{3}P) Auger peak at ~716 eV, which is in agreement with a Ni-rich nature of this mixed metal oxide[219]. There are distinct Fe $2p_{3/2}$ peaks from 710 eV indicating the presence of Fe(III)-O, and a $Fe2p_{3/2}$ peak at 707 eV correlating to Fe(II)-S. Calcination of the sample enhanced the Fe(III)-O species, while Fe(II)-S species is depleted.

For the Ni2p spectrum (Figure 5.12 c&d), the dominant peaks at 853 eV and 855 eV correspond to Ni(II)-S and Ni(II)-O $2p_{3/2}$ peaks respectively. In this instance, calcination causes only a marginal increase in nickel oxide and a small decrease in nickel sulphides in comparison to iron. The specific Ni(II)-S binding energy of 853.1 eV corresponds to Ni_3S_4 / $(Fe,Ni)_3S_4$ coordination[246]. Ni(II)-O $2p_{3/2}$ peak for the fresh samples is observed at 854.9 eV which also according to McIntyre corresponds to and nickel and iron ratio of Ni:Fe=1:1, suggesting a composite of NiO and $NiFe_2O_3$. With calcination however, the Ni(II)-O peak shifts to 855.6 eV, corresponding to $NiFe_2O_4$ with Ni:Fe=1:2[247], implying that heating the surface with air causes enhanced Ni-Fe interaction, possibly coupled with Fe diffusion towards the surface.

S2p spectra is fitted with a doublet representing the spin-orbit splitting of $S2p_{3/2}$ and $S2p_{1/2}$ lines, Figure 5.12 e&f. These show the presence of monosulphides (161.3 eV), disulphides (162.7 eV), polysulphides (163.4 eV) and elemental sulphur (165.1 eV). There is also the presence of the sulphite, SO_3^{2-}, with a binding energy of 166.9 eV and sulphate, SO_4^{2-}, with a binding energy of 168.6 eV. These binding energies are within agreement to Buckley *et al.*[207] and Pratt *et al.*[208]. With exposure to air, the migration of Fe and Ni towards the surface to combine with oxygen, leaves metal-sulphur bond cleavage and metal vacancies within the structure. This forces the formation of S-S disulphide and polysulphide bonds. The formation of disulphides and polysulphides require the oxidation of some sulphide (S^{2-}) explaining the presence S_8[208]. The atomic ratio of $(Fe,Ni)_3S_4$ fresh Fe : Ni : S: O was 11 : 10 : 36 : 43 and

calcined Fe : Ni : S : O was 9 : 8 : 23 : 59 approximately. As previously discussed, studies have found that upon oxidation Fe diffuses from the interior to the surface to combine with oxygen leading to a dense iron oxide rings surrounding a nickel sulphide core[244], therefore it is expected for the Fe content to increase and Ni to decrease upon the surface, however here is not the case. This leads us to believe that Fe is stable within the crystal structure and does not yet diffuse to the surface with the mild calcination temperature of 200 ^{o}C, and only oxidation of surface Ni and Fe occurs, with the violarite bulk structure remaining. In the case of pyrrhotite, section 4.2.4, diffusion of Fe to the surface increasing the Fe surface concentration did occur at a 200 ^{o}C calcination. Loss in crystallinity was confirmed by XRD and from XPS analysis of S2p region (Figure 4.16), confirmed that this diffusion of Fe caused cleavage of the Fe-S monosulphide bonds and a large decrease in the monosulphide peak. This forced the formation of S-S bonds, with an increase in disulphide and elemental sulphur peaks. However, in the case of violarite, already confirmed by XRD, the crystallinity of the violarite increases with mild calcination. S2p XPS reveals the monosulphide peak at 161.3 eV does not drop to such an extent as pyrrhotite, with 66% of the original monosulphide concentration remaining. This is coupled with a small increase in sulphur and the majority of S resulting in SO_4^{2-}. This implies that only surface metal-sulphide bonds are cleaving, allowing for oxidation of metal and sulphur situated upon surface, with the bulk structure remaining intact. The binding energies of the chemical species listed in Table 5.3 also reveal an interesting discovery. The sulphate species exhibit a small negative shift in binding energy, where as Fe2p and Ni2p spectra exhibit positive shifts, this implies an interaction between the sulphate and metal species. Indicating an enhanced electron transfer from Fe and Ni to S via an O bridge coordination and accordingly an enhanced relative interaction through S-Fe-O and S-Ni-O surface species. Investigating further, these Fe 2p and Ni2p spectra of fresh $(Ni,Fe)_3S_4$ can be compared to the synthesised FeS and NiS samples (Table 5.1). The binding energies of all three samples are presented in Table 5.4. The $(Ni,Fe)_3S_4$ Fe2p peak corresponding to Fe(II)-S exhibited a negative shift compared to FeS, the $(Ni,Fe)_3S_4$ Ni2p peak corresponding to Ni(II)-

S exhibited a positive shift compared to NiS. These results suggests an electron transfer from Ni to Fe, and evidence for enhanced relative interaction of Ni, Fe and S within the structure.

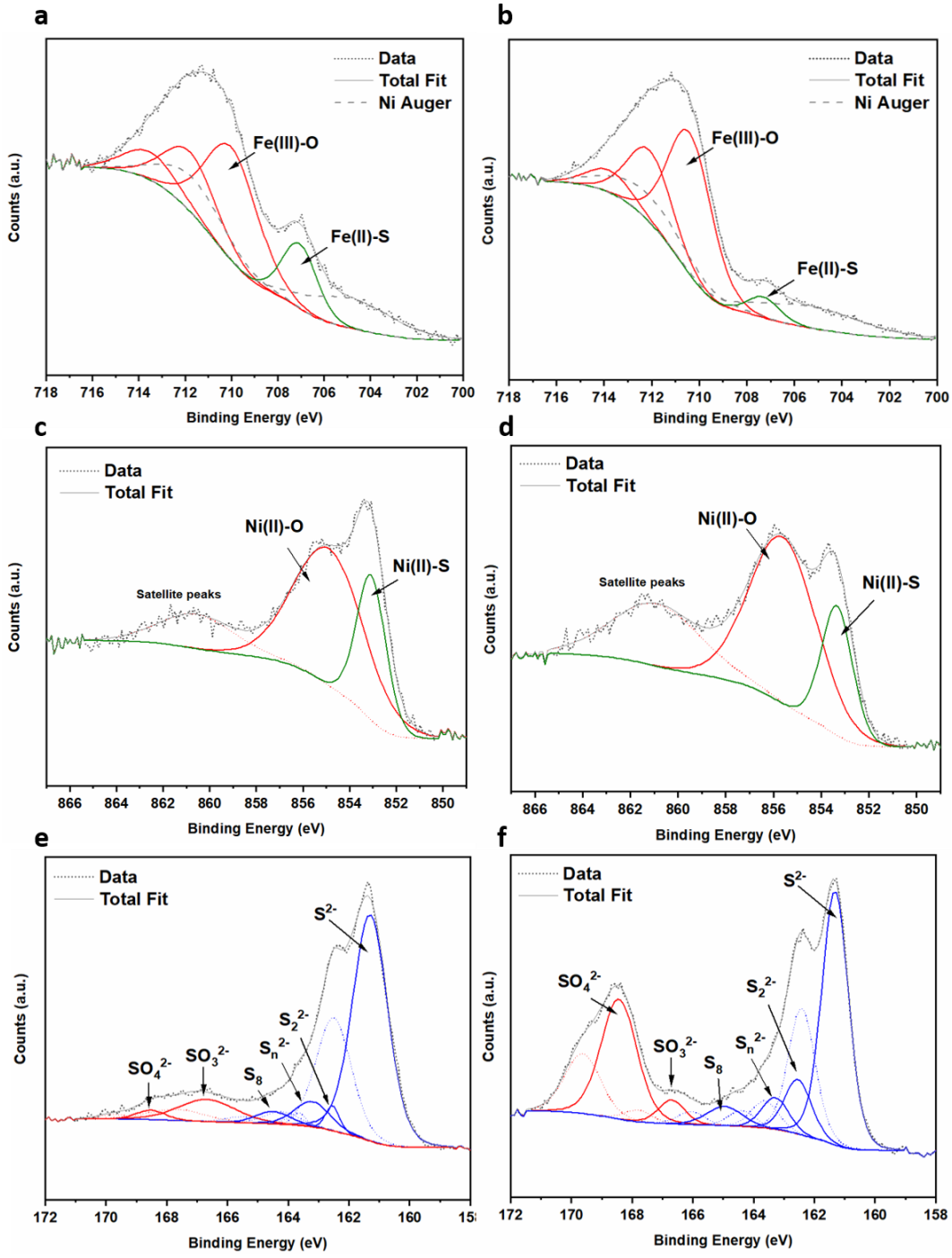

Figure 5.12: XPS spectra of $(Fe,Ni)_3S_4$; [a] Fe2p Fresh [b] Fe2p Calcined 200 °C [c] Ni2p Fresh [d] Ni2p Calcined 200 °C [e] S2p Fresh [f] S2p Calcined 200 °C.

Table 5.3: Binding energy data, interpretations and atomic concentrations for the Fe2p, Ni2p and S2p spectra of fresh and calcined $(Fe,Ni)_3S_4$ samples. Peak reference correlating to spectra in Figure 5.12.

	Fresh			Calcined		
XPS spectra	**B.E. (eV)**	**Chemical state**	**Atom Conc (%)**	**B.E. (eV)**	**Chemical state**	**Atom Conc (%)**
Fe2p	707.0	Fe(II)-S	17.6	707.3	Fe(II)-S	6.0
	710.0	Fe(III)-O	46.6	710.4	Fe(III)-O	56.5
	711.8	Fe(III)-O	24.4	712.1	Fe(III)-O	28.7
	713.5	Fe(III)-O	11.5	713.8	Fe(III)-O	8.9
Ni2p	853.1	Ni(II)-S	25.7	853.3	Ni(II)-S	19.5
	854.9	Ni(II)-O	58.6	855.6	Ni(II)-O	53.9
	860.6	satellite	15.7	860.9	satellite	26.6
S2p	161.3	S^{2-}	45.0	161.3	S^{2-}	29.9
	162.4		22.5	162.4		14.9
	162.7	S_2^{2-}	6.6	162.5	S_2^{2-}	6.4
	163.8		3.3	163.6		3.2
	163.4	S_n^{2-}	4.1	163.3	S_n^{2-}	3.7
	164.5		2.1	164.4		1.8
	165.1	S_8	2.1	165.0	S_8	5.0
	166.2		1.1	166.0		2.5
	166.9	SO_3^{2-}	7.7	166.7	SO_3^{2-}	2.8
	168.0		3.9	167.8		1.4
	168.6	SO_4^{2-}	1.0	168.4	SO_4^{2-}	18.9
	169.8		0.5	169.6		9.4

Table 5.4 Binding energy data, interpretations and atomic concentrations for the Fe2p, Ni2p and S2p spectra of fresh $(Fe,Ni)_3S_4$ NiS and FeS samples. Peak reference correlating to spectra in Figure 5.12.

	FeS (Fresh)			**FeNiS Fresh**			**NiS (fresh)**		
XPS spectra	**B.E. (eV)**	**Chemical state**	**At. Conc. (%)**	**B.E. (eV)**	**Chemical state**	**At. Conc. (%)**	**B.E. (eV)**	**Chemical state**	**At. Conc. (%)**
Fe2p	707.4	Fe(II)-S	26	707.1	Fe(II)-S	17.6	-	-	-
	710.2	Fe(III)-O	46	710.0	Fe(III)-O	46.6			
	711.7	Fe(III)-O	20	711.8	Fe(III)-O	24.4			
	713.3	Fe(III)-O	8	713.5	Fe(III)-O	11.5			
Ni2p	-	-	-	853.1	Ni(II)-S	25.7	852.7	Ni(II)-S	30.0
				854.9	Ni(II)-O	58.6	855.3	Ni(II)-O	46.8
				860.6	satellite	15.7	860.2	satellite	23.3
S2p	161.3	S^{2-}	34	161.3	S^{2-}	45.0	161.3	S^{2-}	36.7
	162.4		17	162.4		22.5	162.4		18.3
	162.3	S_2^{2-}	6	162.7	S_2^{2-}	6.6	161.9	S_2^{2-}	15.5
	163.4		3	163.8		3.3	163.0		7.8
	163.2	S_n^{2-}	7	163.4	S_n^{2-}	4.1	163.2	S_n^{2-}	8.2
	164.4		4	164.5		2.1	164.3		4.1
	164.2	S_8	5	165.1	S_8	2.1	164.9	S_8	2.1
	165.4		2	166.2		1.1	166.0		1.1
	166.6	SO_3^{2-}	3	166.9	SO_3^{2-}	7.7	165.9	SO_3^{2-}	2.5
	167.7		2	168.0		3.9	167.0		1.3
	168.2	SO_4^{2-}	11	168.6	SO_4^{2-}	1.0	167.5	SO_4^{2-}	1.6
	169.3		6	169.8		0.5	168.5		0.8

5.2.4 XAFS Analysis

The technique of XAFS has rarely been systematically applied to iron nickel sulphide minerals. On the basis of an EXAFS study of thiospinel minerals by Charnock *et al.*, evidence is reported that iron substitutes for nickel on the octahedral sites of violarite[248]. Charnock discusses a variety of violarite samples, exhibiting clear structural coordination. In the Fe spectra, these samples exhibit a presence of a peak at 3.2 Å, revealing octahedral coordination. The Ni spectra features characteristic peaks at 3.2 Å and 6.1 Å, revealing octahedral and tetrahedral coordination respectively. Turning our attention to the Fourier transforms EXAFS in Figure 5.13a (Fe) and Figure 5.14a (Ni) it is difficult to draw the same conclusions. The

XAFS data does however bring to light many new understandings towards these materials. Fe spectra Fourier transforms in Figure 5.13a shows fresh violarite sample exhibits a peak at 1.55 Å; a smaller radial distance than the Fe-S peak situated at 1.8 Å, and larger than Fe-O at 1.45 Å, revealing a mixture of Fe-S and Fe-O character. The same can be observed for the Ni spectra Fourier transforms in Figure 5.14a. With the violarite peaks at 1.75 Å, situated in between Ni-S and Ni-O peaks, implying a mixture of Ni-S and Ni-O character.

Upon calcination the beforementioned Fe violarite peak exhibits a negative shift, as Fe gains more oxygen ligands. This does not occur for Ni, as the radial distance is maintained. Peaks at 2.6 Å within the Fe spectra for violarite and Fe_2O_3 samples correlate to the Fe-Fe scattering component indicating the presence of iron oxides within the sample. This Fe-Fe scattering is also an indication of increased crystallinity and ordering, as found with XRD. The broad peak suggests a mixture of Fe coordination with a high number of Fe-O bonds compared to Fe-S bonds present within the violarite material. It should be noted; low-spin Fe(II) and high-spin Fe(III) species with similar ligand systems can have similar bond distances indicating that the radial distance at 1.55-1.65 Å may be the result of low-spin Fe(II)-S, not high-spin Fe(III)-O. This is discussed in more detail later. With the contribution of the beforementioned Fe-Fe scattering component at 2.6 Å, it is indeed possible a mixture of Fe(III)-O and Fe(II)-S is present. XRD reveals no presence of iron oxide within the bulk of the sample, suggesting these Fe-O bonds are incorporated within the phase of $(Fe,Ni)_3S_4$, where O is replacing S ligands, increasingly so with calcination. This is not observed within the Ni spectra, the absence of component at 2.6 Å shows nickel oxides are not present within the violarite samples, both fresh or calcined. Complimented by beforementioned XPS analysis, these results lead one to believe that only iron oxidises within the sample, while nickel remains stable. Note, TGA data revealed no SO_2 evolution at this calcination temperature, therefore sulphur still remains within the structure.

XANES analysis gives the opportunity to study the oxidation states of the iron K-edge and nickel K-edge, presented in Figure 5.13b and Figure 5.14b respectively. First to notice is a

very characteristic pre-edge (feature A) from the contribution of Fe/Ni 1s to Fe/Ni 3d transition. There is a shoulder to the edge (B) indicating the coordination between Fe/Ni and S representing the normally forbidden Fe/Ni 1s to Fe/Ni 4s transition. There is also white line intensity (C), corresponding to the first allowed Fe/Ni 1s to Fe/Ni 4p transition[210,221]. Fe oxide can be characterised by a sharp white line intensity (A), Figure 5.13b, while Fe/Ni sulphide displays a broad XANES edge. The increase in intensity at region C for the violarite samples from FeS confirms the presence of an oxide-like character within the violarite material. Violarite Ni XANES edge, Figure 5.14b, at region C is broad revealing no oxide character, which is not affected with calcination. Violarite at region B is situated at a lower energy than Ni_3S_2 and higher energy than NiO. Ni_3S_2 exhibits tetrahedral cooordiation[249], while NiO holds octahedral coordination. This effect for violarite is created because Ni holds a mixed valency of tetrahedral and octahedral coordination. Calcination appears to hold no effect on the coordination or oxidative state of nickel, implying stable Ni-S species within the bulk. The Fe XANES spectra in Figure 5.13b also reveals coordination information. Still focusing on B, violarite situates at a higher energy than $Fe_{1-x}S$ and Fe_2O_3. $Fe_{1-x}S$ and Fe_2O_3 iron adopts Fe(III) high-spin state octahedral coordination, while the higher energy of the violarite iron is the result of an octahedral coordination in the Fe(II) low-spin state[250]. Upon calcination, Fe shifts only marginally to a higher energy at B as Fe replaces sulphur with oxygen ligands whilst maintaining in the Fe(II) low-spin state.

Previously confirmed by XRD, there is no evidence of pure iron oxide phase situated within the bulk of the material, and calcination causes an increase in crystallinity within the violarite structure. Therefore, it may be deduced that Fe is oxidising to also form S-Fe-O species, as in the case in chapter 4. Although Fe and Ni occupy independent crystal lattice sites, the enhanced interaction of Ni and Fe as already confirmed by XRD and XPS, holds a very important role achieving the superior catalytic activity of these S-Fe-O sites. It must be reminded that the metal oxidation states exists as $Fe^{2+}Ni^{3+}{}_2S_4$ within the bulk. Fe(III) has a high redox potential situated at +0.77 eV meaning that it is easily reduced, while the redox potential of Ni(III) is rare and hard to define within this system, Ni(III) within biological

systems possesses charge transfer properties. Using supporting evidence from XPS and XAFS, we can summarise that Ni(III) within violarite is capable of maintaining Fe(II) in the lower oxidation state. This is vital for stabilising these important S-Fe-O active sites, resulting in an improved catalytic activity in comparison pyrrhotite structure, where nickel is absent.

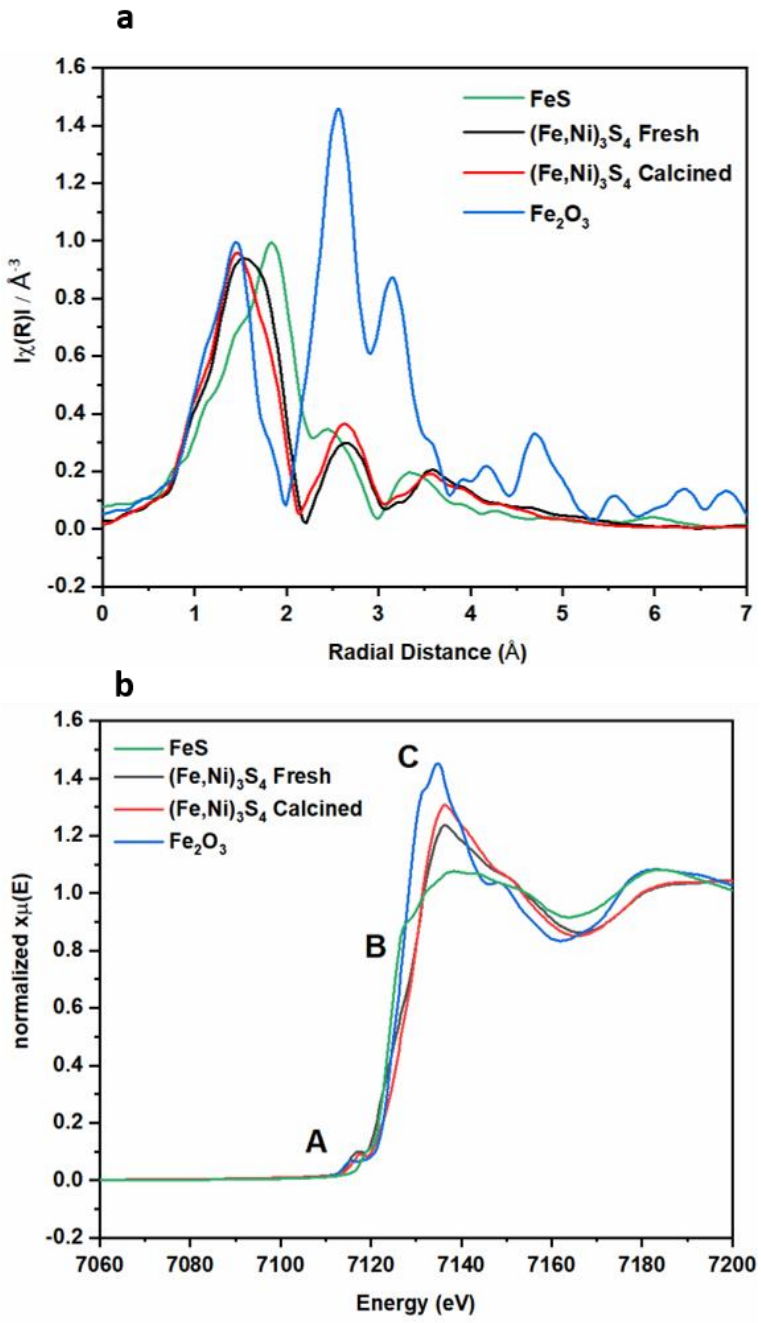

Figure 5.13: XAFS data, Fe K-edge analysis for violarite fresh (black) and calcined 200 °C (red) samples. Including [a] Fourier Transform EXAFS and [b] XANES for violarite samples. Including reference samples Fe_2O_3 (blue), FeS (green).

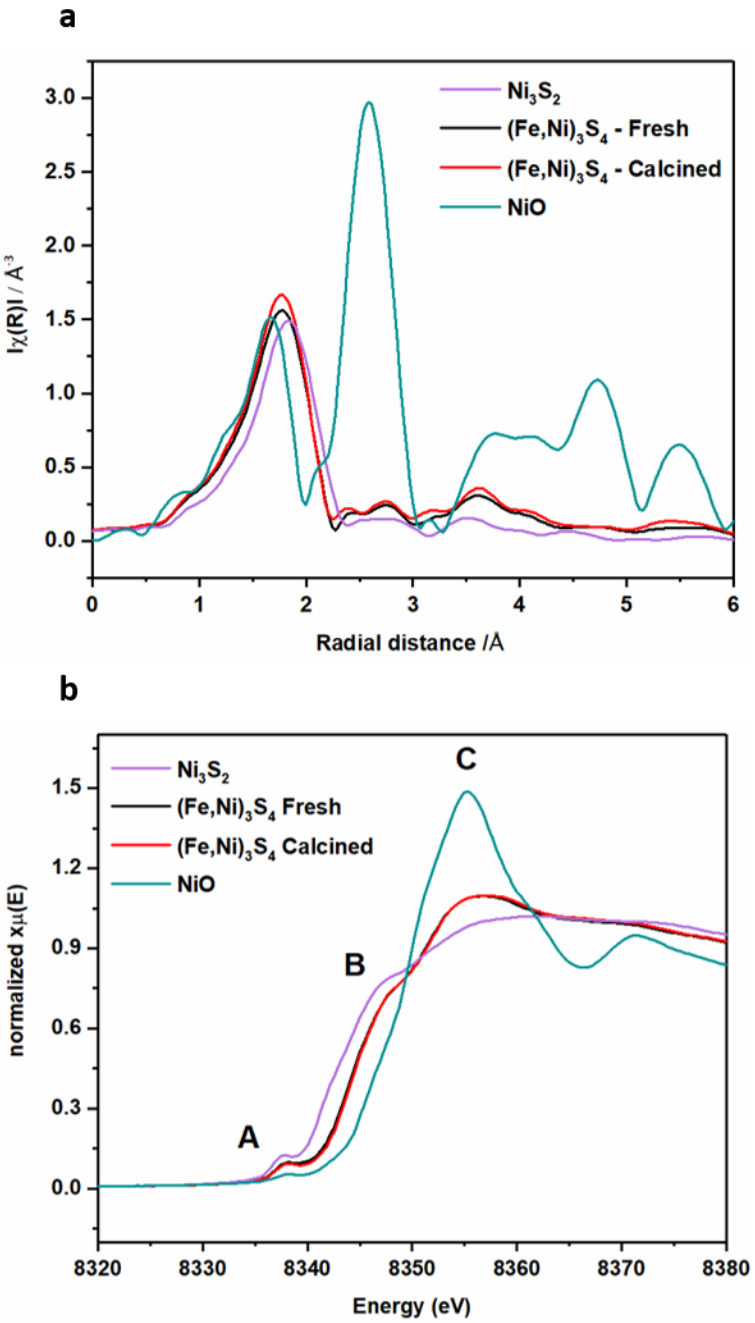

Figure 5.14: XAFS data, Ni K-edge analysis for violarite fresh (black) and calcined 200 °C (red) samples. Including (a) Fourier Transform EXAFS and (b) XANES, for violarite samples. Including reference samples NiO (teal) and Ni_3S_2 (purple).

5.2.5 Further Calcination XPS Study

$(Fe,Ni)_3S_4$ calcined at 300 °C was analysed by XPS and presented in Figure 5.15. Comparing these results to the optimised 200 °C calcination sample, can give further understanding of the active sites, and why increasing oxidation causes a drop in activity. The Fe 2p spectra, Figure

5.15a, shows only a further drop in Fe(II)-S content. The binding energies of Fe-S exhibits a +0.8 positive shift in binding energy to 708.1 eV. In this range, Fe-S is becoming more oxidised, forming more Fe(III)-S character[209]. Fe(III)-O species show a -0.2 negative shift in binding energies to 711.9 and 716.3 eV. Ni2p spectra exhibit a positive peak shift to 856.3 eV and a new peak at 585.6 eV corresponding to the formation of $NiSO_4$ species as correlating to Legrand's findings[251]. S2p spectra reveals another drop in monosulphide and another increase in disulphide as more metal-sulphide bonds are cleaved in favour of metal oxides.

The evidence for Fe(III)-S and $NiSO_4$ shows the enhanced interaction between Fe and Ni is lost. By loosing the relative interaction between Fe, Ni and S, confirms the importance of the Fe/Ni interaction, and the S-Fe-O bridges required for catalytic activity. The Fe : Ni : S : O surface atomic ratio was calculated as 8.5 : 8 : 17 : 66.5. The increase in oxygen and decrease in sulphur surface content compared to a 200 ^{o}C calcination reveals increased amount oxygen species formed, suffocating the active surface species. The Fe : Ni ratio still remains the same as fresh and calcined 200 ^{o}C samples, implying no Fe surface migration, despite the drop in violarite crystallinity.

Table 5.5: Binding energy data, interpretations and atomic concentrations for the Fe2p, Ni2p and S2p spectra of $(Fe,Ni)_3S_4$ calcined at 200 °C (Figure 5.12b,d&f) and 300 °C (Figure 5.15).

	Calcined 200 °C			**Calcined 300 °C**		
XPS spectra	**B.E. (eV)**	**Chemical state**	**Atom Conc (%)**	**B.E. (eV)**	**Chemical state**	**Atom Conc (%)**
Fe2p	707.3	Fe(II)-S	6.0	708.1	Fe(II)-S	3.0
	710.4	Fe(III)-O	56.5	710.5	Fe(III)-O	52.6
	712.1	Fe(III)-O	28.7	711.9	Fe(III)-O	32.7
	713.8	Fe(III)-O	8.9	713.6	Fe(III)-O	11.8
Ni2p	853.3	Ni(II)-S	19.5	853.6	Ni(II)-S	3.0
	855.6	Ni(II)-O	53.9	856.3	Ni(II)-SO_4	43.3
	860.9	satellite	26.6	858.6	Ni(II)-SO_4	11.1
				861.7-866.4	Satellite	57.4
S2p	161.3	S^{2-}	29.9	161.5	S^{2-}	9.3
	162.4		14.9	162.6		4.7
	162.5	S_2^{2-}	6.4	163.1	S_2^{2-}	10.1
	163.6		3.2	164.2		5.0
	163.3	S_n^{2-}	3.7	164.7	S_n^{2-}	0.7
	164.4		1.8	165.8		0.3
	165.0	S_8	5.0	165.5	S_8	1.4
	166.0		2.5	166.6		0.7
	166.7	SO_3^{2-}	2.8	167.2	SO_3^{2-}	3.5
	167.8		1.4	168.4		1.8
	168.4	SO_4^{2-}	18.9	168.7	SO_4^{2-}	41.7
	169.6		9.4	169.9		20.9

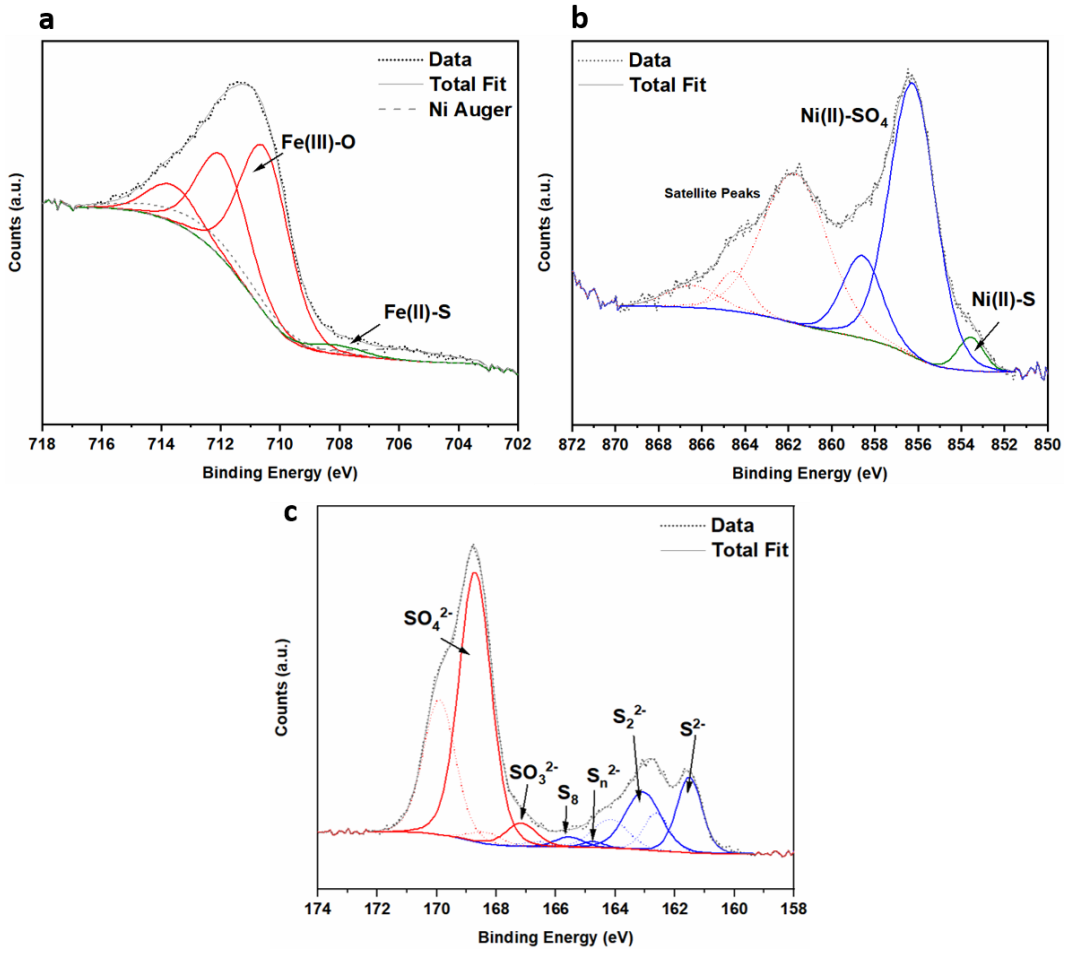

Figure 5.15: XPS spectra of $(Fe,Ni)_3S_4$ calcined at 300 °C [a] Fe2p [b] Ni2p [c] S2p.

5.2.6 Post-reaction catalyst characterisation

To finish this study, the catalyst was analysed post-reaction, to investigate how the catalyst behaves during reaction conditions. XRD analysis of the catalyst post-reaction reveals quite a different structure, as presented in Figure 5.16. Violarite character is still remaining in the sample, although the diffraction intensity has dropped significantly, $NiSO_4.6(H_2O)$ is also present within the sample, corresponding to JCPS file 01-079-0105. These findings realise that violarite is not stable under the reaction conditions. Like with the case of pyrrhotite, $FeCO_3$ has formed, which likely destroys S-Fe-O species and promotes the formation of nickel sulphate. XPS measurements were carried out to analyse the composition and chemical states of the surface (Figure 5.17). S2p region displays a large drop in sulphides situated along 161-166 eV binding energies. This is coupled with a large increase in SO_4^{2-} species, corresponding

to $S2p_{3/2}$ peak at 168.8 eV, correlating to $NiSO_4$ species. Ni2p spectra reveals the presence of $NiSO_4$ species at the $Ni2p_{3/2}$ peak at 856.7 eV. These results give an indication that catalyst regeneration would have its difficulties. Already studied in chapter 4, removal of $FeCO_3$ is yet to be successful.

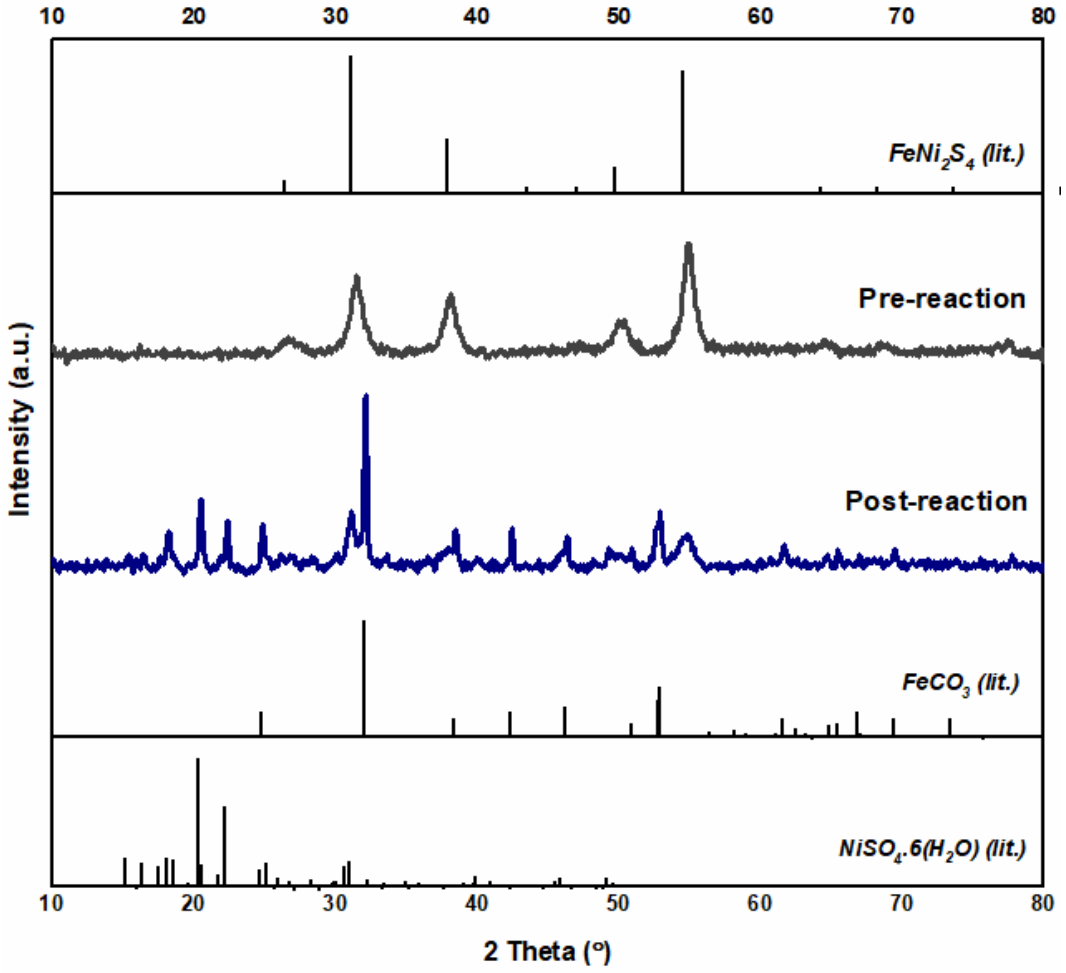

Figure 5.16: XRD of pre- and post-reaction $(Ni,Fe)_3S_4$ catalyst, compared to $FeNi_2S_4$, $FeCO_3$ & $NiSO_4.6H_2O$ JSPC files.

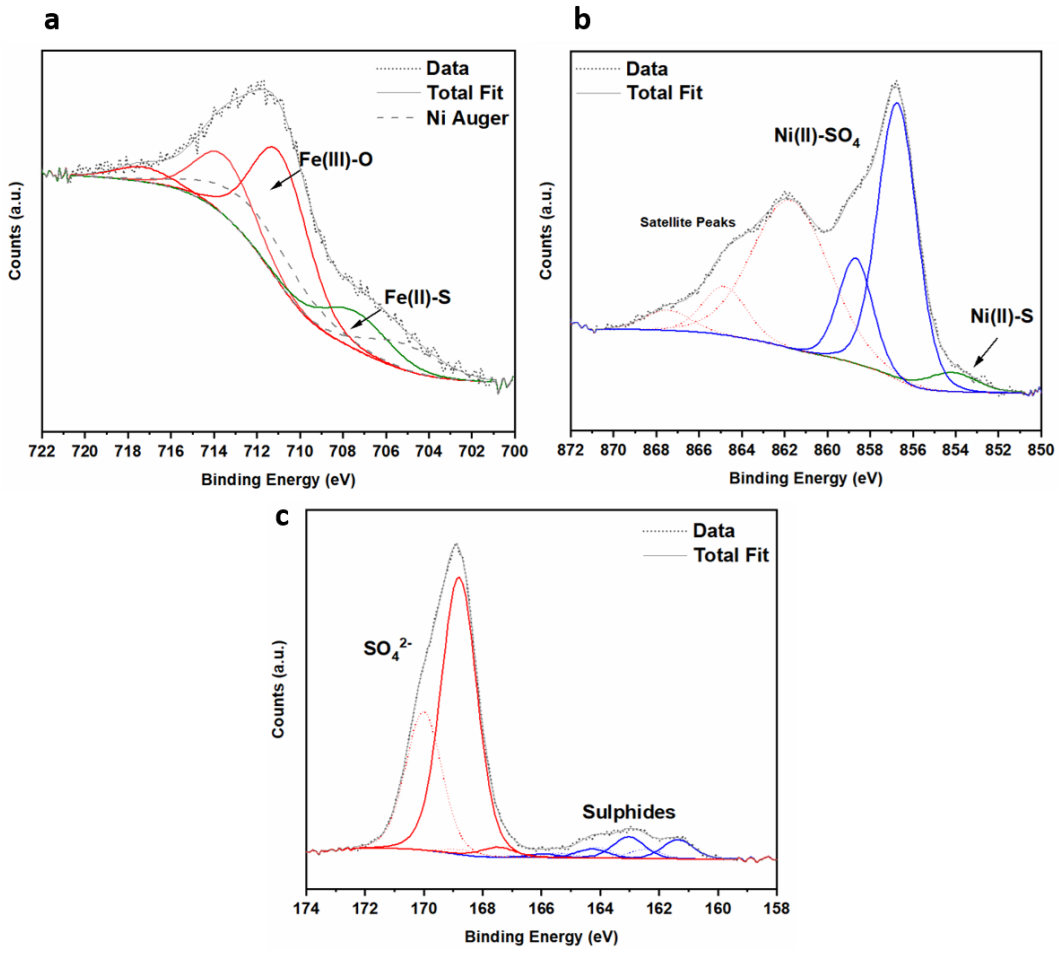

Figure 5.17: XPS spectra of post-reaction $(Ni,Fe)_3S_4$ sample; [a] Fe2p, [b] Ni2p & [c] S2p.

5.3 Conclusions

With the demand to produce a catalyst that is environmentally friendly, earth abundant, highly stable and an economically viable synthesis, iron nickel sulphide is certainly within that category. In this work violarite $(Fe,Ni)_3S_4$ has been synthesised within a shorter period of time (12h) than any of the other methods reported in the literature[239,242,243] albeit with smaller crystal sizes than the violarite reported by Jørgensen *et al.*[239], a synthesis procedure of 45 hours. From synthesis optimisation it was determined that a 1:1 Ni:Fe precursor ratio produced the most active catalyst for CO_2 hydrogenation, coinciding with highest violarite purity and crystallinity. Sample synthesised with 1:3 and 3:1 ratio displayed a mix of pyrrhotite and Ni_3S_2

as well as violarite character. Further investigation revealed that calcining this sample improved the catalytic activity further for all samples. This calcination exhibits favourability for violarite formation, and in some cases even transforming pyrrhotite and Ni_3S_4 into $(Fe,Ni)_3S_4$. After optimising the catalytic activity of violarite with calcination, it was determined that calcining the material at 200 ^oC achieved the best catalyst, much like the case with pyrrhotite. Producing 4.9 µmol of formate, a catalyst far superior to pyrrhotite and Ni_3S_4. Unlike pyrrhotite however, a calcination at this temperature resulted in the improved crystallinity of violarite. These findings confirm the Fe-Ni interaction has a vital role to play for the improved catalytic activity.

An *in situ* XRD study coupled with TGA analysis displayed the many metal sulphide/sulphate/oxide structures are formed and transformed during calcination up to 800 ^oC, concluding with fully oxidised Fe_2O_3 and NiO structures.

XPS revealed calcination formed a dominant metal oxide/sulphoxide surface. The limited Ni/Fe-S cleavage and metal migration to the surface accounts towards the stable structure of the material. When compared with $Fe_{1-x}S$ and Ni_3S_4 binding energies for Ni2p and Fe2p spectra, XPS showed freshly synthesised violarite material possessed enhanced Ni-Fe interaction and electron transfer. Calcination resulted in a new electron interaction between the metal and sulphate species, implying S-Fe-O interaction as with pyrrhotite, demonstrating the importance of calcination to create these S-O species. XAFS helped analyse the bulk structural characteristics and oxidative effects of nickel and iron within the structure. XAFS confirmed the mixed valency state of Ni, while revealing little change of coordination and oxidation state upon calcination. FT-EXAFS of Fe revealed largely Fe-O species compared to Fe-S species and XANES confirmed Fe is situated within octahedral coordination, in a Fe(II) low-spin state. This state is maintained upon calcination, confirming that Fe remains within the violarite crystal structure. The increase in crystallinity with calcination as confirmed by XRD indicates that this oxygen incorporated within the structure does not disrupt the crystal lattice. The bulk metal atoms occupy Fe(II) and Ni(III) oxidation states, of which Ni(III) can

facilitate charge transfer, essential for maintaining the Fe(II) oxidation state. Suggesting this role in nickel is vital for stabilising S-Fe-O species, the key for the superior catalytic performance in comparison to pyrrhotite.

Analysing the catalyst post-reaction revealed a similar outcome to pyrrhotite, with the formation of $FeCO_3$ species, with additional new $NiSO_4$ species detected. This presumes that regeneration of the violarite structure would be difficult to achieve.

6 Conclusions & Future Work

6.1 Summary of Work Motivation

Climate change is the result of rising greenhouse gas emissions. There has been a huge effort to reduce the amount of CO_2, the most abundant greenhouse gas, from being emitted into the atmosphere. Fossil fuel combustion as a source of energy is the main cause of CO_2 emissions; and as many large economies are still dependant on fossil fuels, further effects of atmospheric CO_2 levels are undeniable. One method of preventing CO_2 reaching the atmosphere is to catch it from the industrial source. This captured CO_2 can be utilised as a carbon feedstock towards the conversion of chemicals and fuels.

The aim of this PhD has continued along the idea of CO_2 utilisation, by investigating the hydrogenation of CO_2 within the alkaline liquid phase, to form formate, the simplest product of CO_2 hydrogenation. This thesis has studied the performance of two different types of catalysis. Chapter 3 investigated transition metals supported on molybdenum carbide, dominantly Pd/Mo_2C, while chapters 4 & 5 focused on iron (nickel) sulphide catalysis.

6.2 Summary of Chapter 3

Inspired by the work previously reported from Thompsons's research group[127,252], transition metals supported on molybdenum carbide system was studied for the hydrogenation of CO_2.

In this project a variety of transition metals were tested for the hydrogenation of CO_2 before a Pd/Mo_2C system was selected as the most active catalyst within aqueous conditions. A systematic study of monometallic Pd/Mo_2C samples was then conducted. In this project, the preparation of Pd supported on Mo_2C was compared, revealing a modified impregnation method was the best approach. With the knowledge that acidifying the $PdCl_2$ precursor can affect the size and distribution of the palladium nanoparticles. Preparing a catalyst with a 2M HCl $PdCl_2$ precursor solution achieved the best formate productivity.

After catalytic testing, it was essential to select appropriate the reaction conditions, keeping in mind these conditions would be used for the rest of the work in this thesis. A basic reaction solution is necessary to induce CO_2 dissolution, allowing carbon species available as aqueous intermediates. Therefore, three of sodium salt solutions were tested; $NaHCO_3$, Na_2CO_3 & NaOH, all of which are commonly reported within similar reaction systems. Despite NaOH solution exhibiting less formate formation than a $NaHCO_3$ solution, it was selected as the most appropriate solution knowing that all formate derived from the initial gaseous CO_2 reactant. Analysing the basic solvent further the molarity was optimised, and the pH of the reaction system was analysed. An optimal 1M NaOH solution situates at pH 14, however upon saturation of CO_2, the system immediately drops to pH 6-8. With the knowledge that HCO_3^- is the dominant carbonaceous species within this pH region. It is understood that bicarbonate ion is the intermediate for this reaction.

Reaction temperature and time tests concluded that increasing reaction temperature increased formate productivity up to 150 ^oC, increasing reaction time increased formate production up till 19 hours, where formate productivity began to diminish.

Stability of this catalyst however was poor. The low surface area of the support material resulted in a weak metal-support interaction. Allowing sintering of nanoparticles to occur, and catalyst deactivation. Adding a second metal, ruthenium, as a bimetallic catalyst (1% RuPd/Mo_2C) had a lower performance than its monometallic counterpart. However, Ru acted as a link to anchor Pd to the surface, allowing a stronger metal-support interaction and thus a much more stable material available for re-use.

Finally, this material was also tested within flow like conditions, within a slurry reactor. The flow of gas allowed more understanding of the behaviour of the reactant gases, and for the calculation of CO_2 and H_2 conversion. The 1% Pd/Mo_2C catalyst revealed results very similar to batch conditions, however the catalyst with a higher Pd loading (5% Pd/Mo_2C) exhibited a higher stability and activity, which was contradicting to results obtained from the batch reactor.

6.2.1 Future work

Work comparing the batch autoclave and flow like slurry reactors was interesting indeed however more efforts can be taken to optimise the catalyst synthesis and reaction conditions for this slurry reaction system. This work can be continued by testing how altering the H_2:CO_2 gas ratio effects the productivity, in an effort to increase productivity and gain a better understanding of how these gases behave in the system. For the bimetallic study, ruthenium was selected because it was the second most active metal as a monometallic catalyst, however, more bimetallic combinations can also be investigated. The main limitations of this catalyst is the poor stability and large size of the nanoparticles. To attempt to eliminate the catalytically inactive larger particles and reduce the overall size of the nanoparticles, a more thorough Pd weight loading and catalyst preparation study can be investigated. A usual catalyst was reduced at 400 ^{o}C for 4 hours, but by changing the temperature and ramp rate of the thermal reduction treatment, it is possible to tune the size of the nanoparticles, therefore altering the surface area of the nanoparticles. This study could have a large impact on improving the catalytic activity and stability of the material.

6.3 Summary of Chapters 4 & 5

Iron, nickel and sulphur are cheap, non-toxic, and readily available elements ideal for large scale use. Iron (nickel) sulphides have been long since hypothesised as potential membrane catalysts, reducing aqueous carbon dioxide for the formation of prebiotic molecules and life's emergence on early Earth. Therefore, synthesising these materials and testing them for the catalytic hydrogenation of CO_2 showed promise for interesting catalytic abilities. Working within the optimised reaction conditions studied in Chapter 3, iron sulphide (Chapter 4) and iron nickel sulphide (Chapter 5) were next investigated.

This study began with the iron sulphide, Pyrrhotite, $Fe_{1-x}S$. The synthesis of pyrrhotite was first optimised, concluding that the highest reaction temperatures (310 ^{o}C) and reaction time (12h) formed the most crystalline structure. This material was found active for CO_2 hydrogenation, however resting the material in air over a long period of time, caused an increase in catalytic activity. This increase in catalytic activity was believed to be the result of surface oxidation, forming new chemical species. A

calcination study was employed, to analyse how the material behaves under flowing air and elevated temperatures. Results showed that when pyrrhotite is calcined at 200 ^{o}C, the optimum catalytic activity is achieved, increasing formate productivity from 0.29 µmol to 1.00 µmol. Further investigations found up to 200 ^{o}C of heat treatment the material decreases in crystallinity creating an amorphous structure. Increasing the temperature then transforms the material through a range of iron sulphide/sulphate/oxide structures until finally Fe_2O_3 is formed along with SO_2 evolution. XPS characterisation revealed that calcination caused the evolution of FeO_x and SO_x species forming on the surface, coating a sulphide rich underlayer. XAS analysis revealed this incorporation of oxygen is also implemented within the bulk of the material creating S-Fe-O species. Further calcination above 200 ^{o}C destroys these S-Fe-O sites, which coincides with a drop in catalytic activity. These results confirm that these unique S-Fe-O species are active sites within the catalyst for CO_2 hydrogenation.

Chapter 5 worked on developing this material further by investigating the effects of incorporating nickel within the iron sulphide structure. Initial tests of material synthesis found that a 1:1 ratio of Fe:Ni precursor formed violarite $(Fe,Ni)_3S_4$ with good purity. This material was found the most active catalyst, significantly outperforming pyrrhotite, (and nickel sulphides Ni_2S_3) by more than 3x the formate productivity, producing 4.9 µmol of formate compared to pyrrhotite's 1.00 µmol. With calcination at 200 ^{o}C, violarite increases in crystallinity coupled with increase in catalytic activity.

Like pyrrhotite, violarite was also analysed under flowing air and elevated temperatures, again revealing an interesting formation and destruction of a variety of iron/nickel sulphide/sulphate/oxides. As soon as the violarite structure decreases in crystallinity, this is correlated with a drop in catalytic activity and the formation of nickel and iron sulphate.

XAFS analysis reveal that within the bulk of the material, Ni remains within a stable Ni(III)-S state even after calcination, while Fe occupies Fe(II) octahedral character. While the coordination is maintained during calcination, Fe gains Fe-O character with calcination, while the violarite crystal lattice is enhanced as supported by XRD. Supported with XPS, it may be concluded that S-Fe-O species are formed with calcination, with the crucial role of a strong iron – nickel interaction maintaining these

S-Fe-O species. The enhanced interaction of nickel within violarite results in impressive catalytic activity when compared to pyrrhotite material with the absence of nickel.

Reusability studies found that these catalysts has a poor reusability, owing to the formation of $FeCO_3$ within the structure, formed from the reaction of aqueous carbonate species and Fe(II) during the reaction. Any efforts to remove this catalytic poison and regenerate the catalyst was ineffective.

Despite the weak catalytic activity these materials possess and the limitation of catalyst regeneration, this study of pyrrhotite and violarite has by far exceeded initial expectations. Beginning with previous reports covering poor catalytic performance of and limited structural characterisation, this thesis has revealed new catalytic data towards these iron (nickel) sulphide's ability for the hydrogenation of CO_2 into formate. Through thorough investigation this report reveals new knowledge towards pyrrhotite's and violarite's oxidative behaviours and never reported before catalytic abilities. By enhancing this oxidative feature, these findings introduce these materials as exciting new candidates for catalysts towards the hydrogenation of CO_2.

6.3.1 Future Work

This abundant and cheap material has provided some interesting catalytic results that before now was relatively underexplored. Despite its limitation of reusability thus far, this work focusing on calcined pyrrhotite for the hydrogenation of CO_2 is certainly maintained as an exciting material to be studied further. Of course, at this stage this catalyst is by no means within competition of the many successful catalysts previously reported; however, this project and the concept of Fe(Ni)S catalysis for CO_2 hydrogenation is only in its infancy. Developing and optimising this material will likely find enhanced catalytic abilities. Improving this catalytic system can been focused down two pathways; first by focusing on preventing the formation of $FeCO_3$, and secondly, improving the catalytic surface area.

$FeCO_3$ forms when there is a supersaturation of CO_3^{2-} species within solution. Due to the chemical equilibrium of dissolved CO_2, it may be impossible to remove all CO_3^{2-}. However, the concentration of CO_3^{2-} species can certainly be reduced. As discussed, the pH of the reaction media determines the concentration of specific carbon species. During this work it has been impossible to measure the pH of

the reaction media within reaction conditions. However, enabling a flow reaction with a specific and controlled reaction solution passing over the catalyst could enable the pH to be maintained around 6-8 pH units. Here, the concentration of bicarbonate ions would be high, and the concentration of carbonate ions would be negligible, thus limiting the formation of $FeCO_3$ ions.

The main limitation of my work thus far is the result of the low surface area of the material, resulting in a majority of inactive metal sulphide species situated within the bulk. Increasing the reactive surface areas of these sulphides is crucial in improving its catalytic performance. This can be done in a number of ways, by introducing mesoporousity in these materials[186], or by supporting the active species upon another material. Zeolites are a family of materials with nanodimensional pores, considered to be good templates for preparing small nanoparticles of a restricted size, thus producing a large surface area of catalytic sites. FeS and NiS nanocomposites have been previously incorporated within zeolite structures for catalytic application[253,254], even as a bimetallic sulphide nanocomposite[255,256]. Thus, incorporating metal sulphide within a zeolite host could be another avenue for investigation.

Past success of CO_2 hydrogenation using greigite[100] and pentlandite $(Fe,Ni)_9S_8$[224] were produced under electrocatalytic conditions. Therefore, calcined pyrrhotite and violarite can also be tested under electrocatalytic application. With the aid of an electrochemical charge potential, this gives the thermodynamic push towards higher value produces such as methanol, ethanol, acetic acid and pyruvic acid.

Once again seeking inspiration from hydrothermal vents, within the concept of the origin of life theory, cobalt, manganese and zinc cations are also present within these hydrothermal fluids along with Fe(II) and Ni(II)[257]. Cobalt sulphide is a widely occurring mineral, existing in a variety of structures; Co_9S_8, CoS, Co_3S_4, and CoS_2. All of these structures have exhibited chemical stability and catalytic activity for electrocatalytic applications[258]. Siegenite $(Ni,Co)_3S_4$, a spinel-type mineral structurally similar to violarite and greigite (Fe_3S_4)[250], also occurs within hydrothermal systems, associated with iron sulphides previously mentioned. Siegenite is scarcely reported for catalytic applications, however from previous successes of violarite and greigite, siegenite holds a case for investigation alongside CoS_x minerals for the hydrogenation of CO_2

7 Appendix

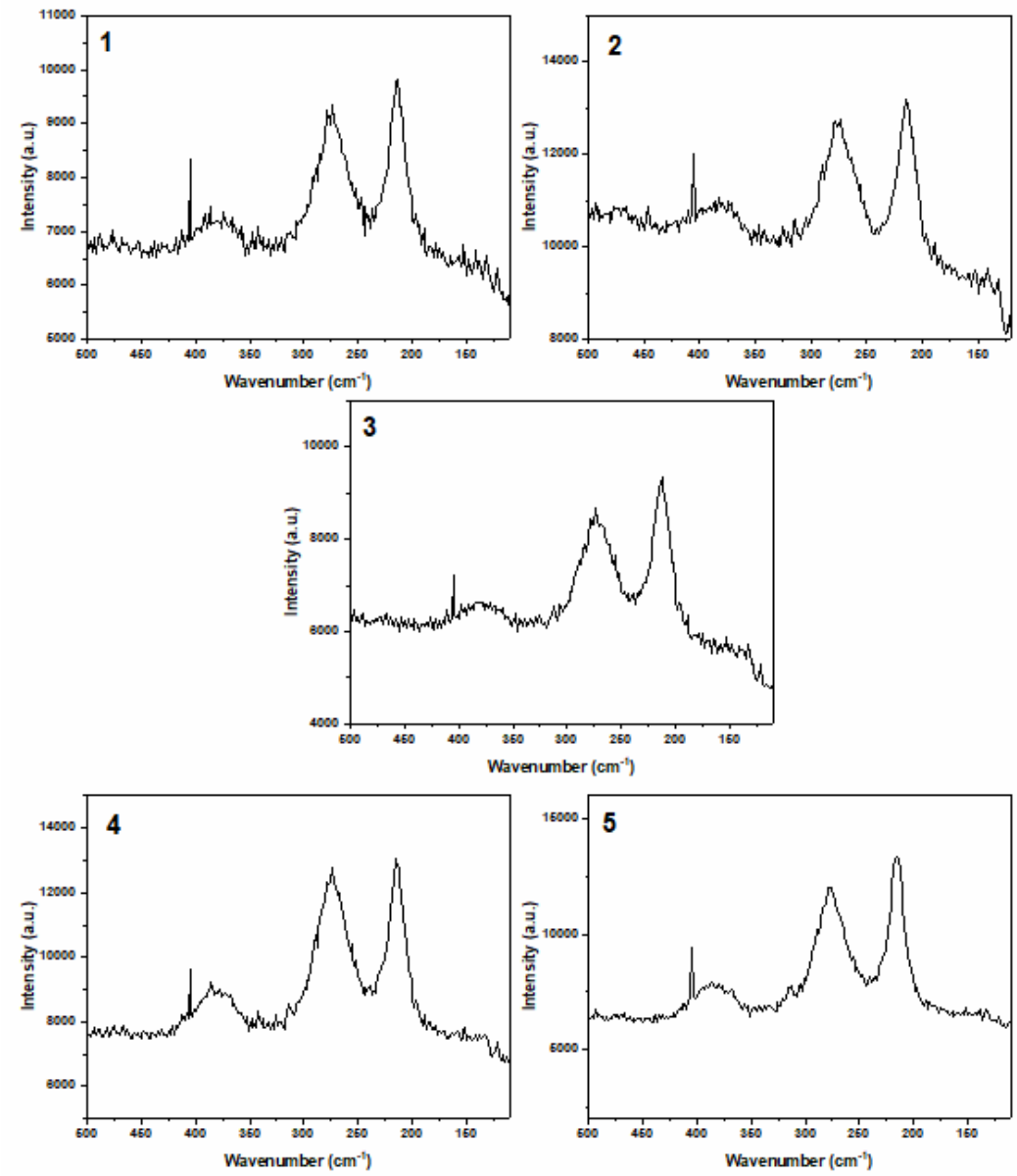

Figure 7.1: Raman spectra of samples 1-5, pyrrhotite samples synthesised at different synthesis temperatures and times. Synthesis conditions presented in Table 4.1

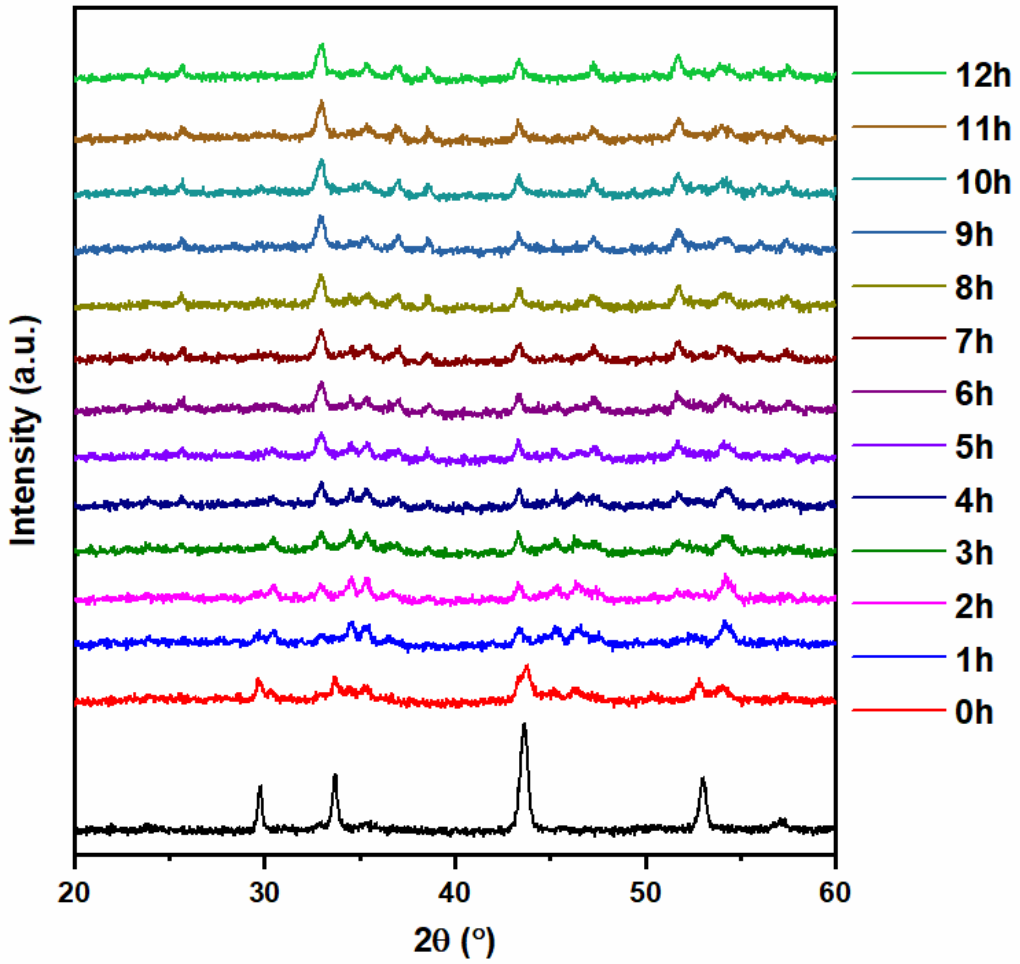

Figure 7.2: In situ XRD of Pyrrhotite heated at 200 °C under flowing air for 12 hours. XRD analysis every hour during heat treatment.

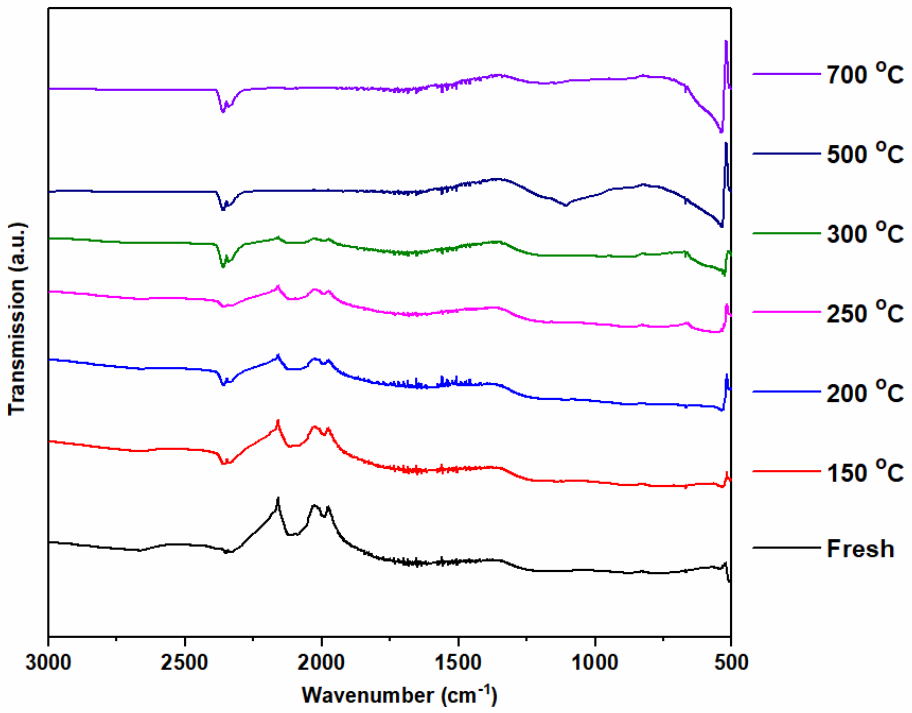

Figure 7.3: FT-IR spectra of pyrrhotite material calcined at different temperatures from fresh – 700 °C

A transmission within the region of 500-700 cm^{-1} corresponds to the presence of iron (III) oxides. Iron sulphates can be are usually found within the region between 1210 and 1040cm^{-1}. Fe-S bonds are usually located at lower energies than 500 $^{-1}$, the limit of this instrument. These findings are reported by Dunn *et al.*[259]. The results presented in Figure 7.3 show a slight increase in transmission within the Fe-O regions, corresponding to iron oxide formation, however, there is little else to conclude.

8 References

1 Nasa, The Causes of Climate Change, https://climate.nasa.gov/causes/.

2 C. Quéré, R. Andrew, P. Friedlingstein, S. Sitch, J. Hauck, J. Pongratz, P. Pickers, J. Ivar Korsbakken, G. Peters, J. Canadell, A. Arneth, V. Arora, L. Barbero, A. Bastos, L. Bopp, P. Ciais, L. Chini, P. Ciais, S. Doney, T. Gkritzalis, D. Goll, I. Harris, V. Haverd, F. Hoffman, M. Hoppema, R. Houghton, G. Hurtt, T. Ilyina, A. Jain, T. Johannessen, C. Jones, E. Kato, R. Keeling, K. Klein Goldewijk, P. Landschützer, N. Lefèvre, S. Lienert, Z. Liu, D. Lombardozzi, N. Metzl, D. Munro, J. Nabel, S. I. Nakaoka, C. Neill, A. Olsen, T. Ono, P. Patra, A. Peregon, W. Peters, P. Peylin, B. Pfeil, D. Pierrot, B. Poulter, G. Rehder, L. Resplandy, E. Robertson, M. Rocher, C. Rödenbeck, U. Schuster, I. Skjelvan, R. Séférian, I. Skjelvan, T. Steinhoff, A. Sutton, P. Tans, H. Tian, B. Tilbrook, F. Tubiello, I. Van Der Laan-Luijkx, G. Van Der Werf, N. Viovy, A. Walker, A. Wiltshire, R. Wright, S. Zaehle and B. Zheng, *Earth Syst. Sci. Data*, 2018, **10**, 2141–2194.

3 R. Kawase, Y. Matsuoka and J. Fujino, *Energy Policy*, 2006, **34**, 2113–2122.

4 P. Nejat, F. Jomehzadeh, M. M. Taheri, M. Gohari and M. Z. Abd. Majid, *Renew. Sustain. Energy Rev.*, 2015, **43**, 843–862.

5 L. Suganthi and A. A. Samuel, *Renew. Sustain. Energy Rev.*, 2012, **16**, 1223–1240.

6 International Energy Agency, *Global Energy and CO2 Status Report 2018*, 2018.

7 Adoption of the Paris Agreement, http://unfccc.int/resource/docs/2015/cop21/eng/l09r01.pdf, (accessed 11 April 2019).

8 European Comission, A Roadmap for moving to a competitive low carbon economy in 2050, http://eur-lex.europa.eu/LexUriServ/LexUriServ.do?uri=COM:2011:0112:FIN:en:PDF, (accessed 9 April 2018).

9 European Comission, Energy Efficiency Plan 2011,

https://ec.europa.eu/clima/sites/clima/files/strategies/2050/docs/efficiency_plan_en.pdf, (accessed 9 April 2018).

10 International Energy Agency, *Technology Roadmap - Carbon Capture and Storage*, 2013.

11 P. A. Okken, R. J. Swart and S. Zwerver, *Climate and Energy: The Feasibility of Controlling CO2 Emissions - Google Books*, Kluwer Academic Publishers, 1989.

12 E. A. Quadrelli, G. Centi, J.-L. Duplan and S. Perathoner, *ChemSusChem*, 2011, **4**, 1194–1215.

13 International Energy Agency, *Energy Technology Analysis - CO2 Capture and Storage*, 2008.

14 Zero Emissions Platform, *The Costs of CO_2 Capture, Transport and Storage*, 2011.

15 Element Energy Limited, *Carbon Capture and Storage (CCS) Costs for UK Industry: High Level Review*, 2013.

16 M. A. Celia and S. Bachu, in *6th International Conference on Greenhouse Gas Control Technologie*, 2003, pp. 477–482.

17 H. Deng, J. M. Bielicki, M. Oppenheimer, J. P. Fitts and C. A. Peters, *Clim. Change*, 2017, **144**, 151–163.

18 NOAH Friends of Denmark, Information about Carbon Capture and Storage - CCS, http://ccs-info.org/liability.html, (accessed 1 July 2020).

19 N. Mac Dowell, N. Florin, A. Buchard, J. Hallett, A. Galindo, G. Jackson, C. S. Adjiman, C. K. Williams, N. Shah and P. Fennell, *Phys. Chem. Chem. Phys.*, 2010, 1–28.

20 S. Ó. Snæbjörnsdóttir, B. Sigfússon, C. Marieni, D. Goldberg, S. R. Gislason and E. H. Oelkers, *Nat. Rev. Earth Environ.*, 2020, 90–102.

21 K. M. S. Cartier, *Eos (Washington. DC).*, 2020.

22 L. A. Curtiss, K. Raghavachari, P. C. Redfern and J. A. Pople, *J. Chem. Phys*, 1997, **106**, 1063.

23 *Gaseous Carbon Waste Streams Utilization*, National Academies Press, 2019.

24 M. Aresta, C. F. Nobile, V. G. Albano, E. Forni and M. Manassero, *J.C.S. Chem. Comm*, 1975, 636–637.

25 B. Metz, O. Davidson, H. de Coninck, M. Loos and L. Meyer, *Carbon dioxide capture and storage*, 2005.

26 International Energy Agency, *Global Energy and CO2 status report*, 2017.

27 P. Styring, D. Jansen, H. de Coninck, H. Reith and K. Armstrong, *Carbon Capture and Utilisation in the green economy*, 2011.

28 S. Ghazali-Esfahani, H. Song, E. Păunescu, F. D. Bobbink, H. Liu, Z. Fei, G. Laurenczy, M. Bagherzadeh, N. Yan and P. J. Dyson, *Green Chem.*, 2013, **15**, 1584.

29 E. Alper and O. Yuksel Orhan, *Petroleum*, 2017, **3**, 109–126.

30 A. Dibenedetto, A. Angelini and P. Stufano, *J. Chem. Technol. Biotechnol.*, 2014, **89**, 334–353.

31 T. Sakakura, J. C. Choi and H. Yasuda, *Chem. Rev.*, 2007, 107, 2365–2387.

32 J. G. de Vries and S. D. Jackson, *Catal. Sci. Technol.*, 2012, **2**, 2009.

33 S. Y. Tee, K. Y. Win, W. S. Teo, L.-D. Koh, S. Liu, C. P. Teng and M.-Y. Han, *Adv. Sci.*, 2017, **4**, 1600337.

34 P. Nikolaidis and A. Poullikkas, *Renew. Sustain. Energy Rev.*, 2017, **67**, 597–611.

35 M. Ni, M. K. H. Leung, D. Y. C. Leung and K. Sumathy, *Renew. Sustain. Energy Rev.*, 2007, **11**, 401–425.

36 K. Mazloomi, N. B. Sulaiman and H. Moayedi, *Int. J. Electrochem. Sci*, 2012, **7**, 3314–3326.

37 A. Weilhard, M. I. Qadir, V. Sans and J. Dupont, *ACS Catal.*, 2018, **8**, 1628–1634.

38 G. Peng, S. J. Sibener, G. C. Schatz and M. Mavrikakis, *Surf. Sci.*, 2012, **606**, 1050–1055.

39 T. Maihom, S. Wannakao, B. Boekfa and J. Limtrakul, *J. Phys. Chem. C*, 2013, **117**,

17650–17658.

40 D. Mellmann, P. Sponholz, H. Junge and M. Beller, *Chem. Soc. Rev.*, 2016, **45**, 3954–3988.

41 A. Amir and N. Afshar, *Chemical profile: Formic acid*, 2014.

42 J. Klankermayer, S. Wesselbaum, K. Beydoun and W. Leitner, *Angew. Chemie Int. Ed.*, 2016, **55**, 7296–7343.

43 S. A. Burgess, K. Grubel, A. M. Appel, E. S. Wiedner and J. C. Linehan, *Inorg. Chem.*, 2017, **56**, 8580–8589.

44 S. Moret, P. J. Dyson and G. Laurenczy, *Nat. Commun.*, 2014, **5**, 4017.

45 F. Joó, *ChemSusChem*, 2008, **1**, 805–808.

46 A. K. Singh, S. Singh and A. Kumar, *Catal. Sci. Technol.*, 2016, **6**, 12–40.

47 A. Boddien, C. Federsel, P. Sponholz, D. Mellmann, R. Jackstell, H. Junge, G. Laurenczy and M. Beller, *Energy Environ. Sci.*, 2012, **5**, 8907–8911.

48 X. Yu and P. G. Pickup, *J. Power Sources*, 2008, 182, 124–132.

49 C. Rice, S. Ha, R. I. Masel, P. Waszczuk, A. Wieckowski and T. Barnard, *J. Power Sources*, 2002, **111**, 83–89.

50 Y. Zhu, Z. Khan and R. I. Masel, *J. Power Sources*, 2005, **139**, 15–20.

51 N. M. Aslam, M. S. Masdar, S. K. Kamarudin and W. R. W. Daud, *APCBEE Procedia*, 2012, **3**, 33–39.

52 M. Rumayor, A. Dominguez-Ramos and A. Irabien, *Appl. Sci.*, 2018, **8**, 914.

53 W. Reutemann and H. Kieczka, in *Ullmann's Encyclopedia of Industrial Chemistry*, Wiley-VCH Verlag GmbH & Co. KGaA, Weinheim, Germany, 2000.

54 M. Pérez-Fortes, J. C. Schöneberger, A. Boulamanti, G. Harrison and E. Tzimas, *Int. J. Hydrogen Energy*, 2016, **41**, 16444–16462.

55 T. Schaub and R. A. Paciello, *Angew. Chemie - Int. Ed.*, 2011, 50, 7278–7282.

56 P. G. Jessop, T. Ikariya and R. Noyori, *Chem. Rev.*, 1995, **95**, 259–272.

57 S. Enthaler, J. von Langermann and T. Schmidt, *Energy Environ. Sci.*, 2010, **3**, 1207.

58 K. C. Waugh, *Catal. Today*, 1992, **15**, 51–75.

59 Y. Inoue, H. Izumida, Y. Sasaki and H. Hashimoto, *Chem. Lett.*, 1976, **5**, 863–864.

60 R. Tanaka, M. Yamashita and K. Nozaki, *J. Am. Chem. Soc.*, 2009, **131**, 14168–14169.

61 R. Tanaka, M. Yamashita, L. W. Chung, K. Morokuma and K. Nozaki, *Organometallics*, 2011, **30**, 6742–6750.

62 C. Ziebart, C. Federsel, P. Anbarasan, R. Jackstell, W. Baumann, A. Spannenberg and M. Beller, *J. Am. Chem. Soc.*, 2012, **134**, 20701–20704.

63 P. Munshi, A. D. Main, J. C. Linehan, C. C. Tai and P. G. Jessop, *J. Am. Chem. Soc.*, 2002, **124**, 7963–7971.

64 F. Gassner and W. Leitner, *J. Chem. Soc. Chem. Commun.*, 1993, **0**, 1465.

65 F. Joó, J. Kovács, A. C. Bényei and Á. Kathó, *Catal. Today*, 1998, **42**, 441–448.

66 F. Joó, G. Laurenczy, L. Nádasdi and J. Elek, *Chem. Commun.*, 1999, 971–972.

67 Á. Kathó, Z. Opre, G. Laurenczy and F. Joó, *J. Mol. Catal. A Chem.*, 2003, **204**–**205**, 143–148.

68 P. G. Jessop, T. Ikariya and R. Noyori, *Nature*, 1994, **368**, 231–233.

69 P. G. Jessop, Y. Hsiao, T. Ikariya and R. Noyori, *J. Am. Chem. Soc.*, 1996, **118**, 344–355.

70 E. J. Beckman, *J. Supercrit. Fluids*, 2004, **28**, 121–191.

71 W. Leitner, *Angew. Chem., Int. Ed. Engl.*, 1995, **34**, 2207–2221.

72 G. H. Gunasekar, K. Park, K.-D. Jung and S. Yoon, *Inorg. Chem. Front.*, 2016, **3**, 882–895.

73 Q. Liu, X. Yang, L. Li, S. Miao, Y. Li, Y. Li, X. Wang, Y. Huang and T. Zhang, *Nat. Commun.*, 2017, **8**, 1407.

74 M. W. Farlow and H. Adkins, *J. Am. Chem. Soc.*, 1935, **57**, 2222–2223.

75 M. N. Mahmood, D. Masheder and C. J. Harty, *J. Appl. Electrochem.*, 1987, **17**, 1159–

1170.

76 Y. Zhang, J. Fei, Y. Yu and X. Zheng, *Catal. Commun.*, 2004, **5**, 643–646.

77 S. Wesselbaum, U. Hintermair and W. Leitner, *Angew. Chemie Int. Ed.*, 2012, **51**, 8585–8588.

78 Z. Xu, N. D. McNamara, G. T. Neumann, W. F. Schneider and J. C. Hicks, *ChemCatChem*, 2013, **5**, 1769–1771.

79 N. D. McNamara and J. C. Hicks, *ChemSusChem*, 2014, **7**, 1114–1124.

80 J. Su, M. Lu and H. Lin, *Green Chem.*, 2015, **17**, 2769–2773.

81 D. Preti, C. Resta, S. Squarcialupi and G. Fachinetti, *Angew. Chemie Int. Ed.*, 2011, **50**, 12551–12554.

82 C. Hao, S. Wang, M. Li, L. Kang and X. Ma, *Catal. Today*, 2011, **160**, 184–190.

83 N. Liu, R. J. Du and W. Li, *Adv. Mater. Res.*, 2013, **821**–**822**, 1330–1335.

84 T. Umegaki, Y. Enomoto and Y. Kojima, *Catal. Sci. Technol*, 2016, **6**, 409.

85 L. T. M. Nguyen, H. Park, M. Banu, J. Y. Kim, D. H. Youn, G. Magesh, W. Y. Kim and J. S. Lee, *RSC Adv.*, 2015, **5**, 105560–105566.

86 C. J. Stalder, S. Chao, D. P. Summers and M. S. Wrighton, *J. Am. Chem. Soc.*, 1983, **105**, 6318–6320.

87 J. Su, L. Yang, M. Lu and H. Lin, *ChemSusChem*, 2015, **8**, 813–816.

88 A. C. Dillon and M. J. Heben, *Appl. Phys. A Mater. Sci. Process.*, 2001, **72**, 133–142.

89 M. S. Maru, S. Ram, J. H. Adwani and R. S. Shukla, *ChemistrySelect*, 2017, **2**, 3823–3830.

90 Z. Zhang, L. Zhang, S. Yao, X. Song, W. Huang, M. J. Hülsey and N. Yan, *J. Catal.*, 2019, **376**, 57–67.

91 H. Song, N. Zhang, C. Zhong, Z. Liu, M. Xiao and H. Gai, *New J. Chem.*, 2017, **41**, 9170–9177.

92 K. Mori, T. Taga and H. Yamashita, *ACS Catal.*, 2017, **7**, 3147–3151.

93 K. Mori, T. Sano, H. Kobayashi and H. Yamashita, *J. Am. Chem. Soc.*, 2018, **140**, 8902–8909.

94 M. J. Russell and W. Martin, *Trends Biochem. Sci.*, 2004, **29**, 358–363.

95 A. Volbeda and J. C. Fontecilla-Camps, *Coord. Chem. Rev.*, 2005, 249, 1609–1619.

96 H. Dobbek, *Science (80-.).*, 2001, **293**, 1281–1285.

97 G. Wächtershäuser, *Prog. Biophys. Mol. Biol.*, 1992, 58, 85–201.

98 M. J. Russell, R. M. Daniel, A. J. Hall and J. A. Sherringham, *J Mol Evol*, 1994, **39**, 231–243.

99 M. J. Russell and A. J. Hall, *J. Geol. Soc. London.*, 1997, **154**, 377–402.

100 A. Roldan, N. Hollingsworth, A. Roffey, H.-U. Islam, J. B. M. Goodall, C. R. A. Catlow, J. A. Darr, W. Bras, G. Sankar, K. B. Holt, G. Hogarth and N. H. de Leeuw, *Chem. Commun.*, 2015, **51**, 7501–7504.

101 A. Yamaguchi, M. Yamamoto, K. Takai, T. Ishii, K. Hashimoto and R. Nakamura, *Electrochim. Acta*, 2014, **141**, 311–318.

102 A. Roldan, D. Santos-Carballal and N. H. De Leeuw, *J. Chem. Phys.*, 2013, **138**, 204712.

103 D. Santos-Carballal, A. Roldan and N. H. de Leeuw, *J. Phys. Chem. C*, 2016, **120**, 8616–8629.

104 M. Sankar, Q. He, M. Morad, J. Pritchard, S. J. Freakley, J. K. Edwards, S. H. Taylor, D. J. Morgan, A. F. Carley, D. W. Knight, C. J. Kiely and G. J. Hutchings, *ACS Nano*, 2012, **6**, 6600–6613.

105 P. Paalanen, B. M. Weckhuysen and M. Sankar, *Catal. Sci. Technol.*, 2013, **3**, 2869.

106 J. H. L. Beal, P. G. Etchegoin and R. D. Tilley, *J. Solid State Chem.*, 2012, **189**, 57–62.

107 J. W. Niemantsverdriet, *Spectroscopy in catalysis*, Wiley-VCH, 2007.

108 J. E. Penner-Hahn, *Coord. Chem. Rev.*, 1999, **190**–**192**, 1101–1123.

109 A. Mihelič Mentor and A. Kodre, *XANES spectroscopy*, 2002.

110 J. M. Hollas, *Modern spectroscopy*, Wiley.

111 B. Moraweck, *X-Ray Absorption Spectroscopy: EXAFS and XANES*, 1994.

112 J. J. Rehr and A. L. Ankudinov, *Coord. Chem. Rev.*, 2005, 249, 131–140.

113 The Nature of X-ray Photoelectron Spectra, http://www.casaxps.com/help_manual/XPSInformation/IntroductiontoXPS.htm, (accessed 7 November 2019).

114 J. I. Goldstein, D. E. Newbury, J. R. Michael, N. W. M. Ritchie, J. H. J. Scott and D. C. Joy, *Scanning Electron Microscopy and X-Ray Microanalysis*, 2018.

115 S. Amelinckx, D. van Dyck, J. van Landuyt and G. van Tendeloo, Eds., *Handbook of Microscopy (Methods II)*, Wiley, 1996.

116 T. G. Rochow and P. A. Tucker, in *Introduction to Microscopy by Means of Light, Electrons, X Rays, or Acoustics*, Springer US, Boston, MA, 1994, pp. 1–21.

117 D. C. Harris, *Quantitative Chemical Analysis*, W. H. Freeman and Company, 7th edn., 2007.

118 L. R. Snyder, J. J. Kirkland and J. W. Dolan, *Introduction to Modern Liquid Chromatography*, John Wiley and Sons, 2010.

119 G. D. Christian, P. K. Dasgupta and K. A. Schug, *Analytical Chemistry, 7th Edition | Wiley*, 2013.

120 J.-L. Dubois, K. Sayama and H. Arakawa, *Chem. Lett.*, 1992, **1**, 5–8.

121 M. G. Quesne, A. Roldan, N. H. de Leeuw and C. R. A. Catlow, *Phys. Chem. Chem. Phys.*, 2018, **20**, 6905–6916.

122 S. Posada-Pérez, P. J. Ramírez, R. A. Gutiérrez, D. J. Stacchiola, F. Viñes, P. Liu, F. Illas and J. A. Rodriguez, *Catal. Sci. Technol.*, 2016, **6**, 6766–6777.

123 J. A. Rodriguez, P. Liu, D. J. Stacchiola, S. D. Senanayake, M. G. White and J. G. Chen, *ACS Catal.*, 2015, **5**, 6696–6706.

124 W. Xu, P. J. Ramírez, D. Stacchiola, J. L. Brito and J. A. Rodriguez, *Catal. Letters*, 2015, **145**, 1365–1373.

125 A. B. Vidal, L. Feria, J. Evans, Y. Takahashi, P. Liu, K. Nakamura, F. Illas and J. A. Rodriguez, *J. Phys. Chem. Lett.*, 2012, **3**, 2275–2280.

126 S. Wannakao, N. Artrith, J. Limtrakul and A. M. Kolpak, *ChemSusChem*, 2015, **8**, 2745–2751.

127 Y. Chen, S. Choi and L. T. Thompson, *ACS Catal.*, 2015, **5**, 1717–1725.

128 S. Posada-Pérez, F. Viñes, P. J. Ramirez, A. B. Vidal, J. a Rodriguez and F. Illas, *Phys. Chem. Chem. Phys.*, 2014, **16**, 14912–21.

129 Y. Chen, S. Choi and L. T. Thompson, *J. Catal.*, 2016, **343**, 147–156.

130 H. Conrad, G. Ertl and E. E. Latta, *Surf. Sci.*, 1974, **41**, 435–446.

131 I. Cabria, M. J. Lópezlópez, S. Fraile and J. A. Alonso, *J. Phys. Chem. C*, 2012, **116**, 21179–21189.

132 T. Mitsui, M. K. Rose, E. Fomin, D. F. Ogletree and M. Salmeron, *Nature*, 2003, **422**, 705–707.

133 X. Wang, N. Perret, L. Delannoy, C. Louis and M. A. Keane, *Catal. Sci. Technol.*, 2016, **6**, 6932–6941.

134 S. Posada-Pérez, F. Viñes, R. Valero, J. A. Rodriguez and F. Illas, *Surf. Sci.*, 2017, **656**, 24–32.

135 S. D. Richardson and S. Y. Kimura, *Environ. Technol. Innov.*, 2017, **8**, 40–56.

136 I. U. Din, M. S. Shaharun, A. Naeem, S. Tasleem and M. Rafie Johan, *Chem. Eng. J.*, 2018, **334**, 619–629.

137 C. Yin, Z. Xu, S.-Y. Yang, S. Man Ng, K. Yin Wong, Z. Lin and C. Po Lau, *Organometallics*, 2001, **20**, 1216–1222.

138 F. Lucile, P. Cézac, F. Contamine, J.-P. Serin, D. Houssin and P. Arpentinier, *J. Chem. Eng. Data*, 2012, **57**, 784–789.

139 K. Gilbert, P. C. Bennett, W. Wolfe, T. Zhang and K. D. Romanak, *Appl. Geochemistry*, 2016, **67**, 59–67.

140 O. Pedersen, T. D. Colmer and K. Sand-Jensen, *Front. Plant Sci.*, 2013, **4**, 140.

141 L. Gábor, J. Ferenc and L. Nádasd, *Inorg. Chem.*, 2000, **39**, 5083–5088.

142 P. Patel, S. Nandi, M. S. Maru, R. I. Kureshy and N. U. H. Khan, *J. CO2 Util.*, 2018, **25**, 310–314.

143 Y. M. Badiei, W.-H. Wang, J. F. Hull, D. J. Szalda, J. T. Muckerman, Y. Himeda and E. Fujita, *Inorg. Chem.*, 2013, **52**, 12576–12586.

144 E. Fujita and Y. Himeda, *Biochim. Biophys. Acta - Bioenerg.*, 2013, **1827**, 1031–1038.

145 C. J. Stalder, S. Chao, D. P. Summers and M. S. Wrighton, *J. Am. Chem. Soc.*, 1983, **105**, 6318–6320.

146 H. Wiener, J. Blum, H. Feilchenfeld, Y. Sasson and N. Zalmanov, *J. Catal.*, 1988, **110**, 184–190.

147 J. Su, L. Yang, M. Lu and H. Lin, *ChemSusChem*, 2015, **8**, 813–816.

148 M. Wang, J. Zhang and N. Yan, *Front. Chem.*, , DOI:10.3389/fchem.2013.00017.

149 C. S. He, L. Gong, J. Zhang, P. P. He and Y. Mu, *J. CO2 Util.*, 2017, **19**, 157–164.

150 W. Wang, S. Wang, X. Ma and J. Gong, *Chem. Soc. Rev.*, 2011, **40**, 3703.

151 J. H. Lee, J. Ryu, J. Y. Kim, S. W. Nam, J. H. Han, T. H. Lim, S. Gautam, K. H. Chae and C. W. Yoon, *J. Mater. Chem. A*, 2014, **2**, 9490–9495.

152 F. Wang, J. Xu, X. Shao, X. Su, Y. Huang and T. Zhang, *ChemSusChem*, 2016, **9**, 246–251.

153 X. Nie, X. Jiang, H. Wang, W. Luo, M. J. Janik, Y. Chen, X. Guo and C. Song, *ACS Catal.*, 2018, **8**, 4873–4892.

154 R. K. Rai, K. Gupta, D. Tyagi, A. Mahata, S. Behrens, X. Yang, Q. Xu, B. Pathak and S. K. Singh, *Catal. Sci. Technol.*, 2016, **6**, 5567–5579.

155 A. García-Trenco, A. Regoutz, E. R. White, D. J. Payne, M. S. P. Shaffer and C. K.

Williams, *Appl. Catal. B Environ.*, 2018, **220**, 9–18.

156 W. Luo, M. Sankar, A. M. Beale, Q. He, C. J. Kiely, P. C. A. Bruijnincx and B. M. Weckhuysen, *Nat. Commun.*, 2015, **6**, 1–10.

157 E. Nowicka and M. Sankar, *J. Zhejiang Univ. A*, 2018, **19**, 5–20.

158 G. J. Hutchings and C. J. Kiely, *Acc. Chem. Res.*, 2013, **46**, 1759–1772.

159 D. Wu, K. Kusada and H. Kitagawa, *Sci. Technol. Adv. Mater.*, 2016, **17**, 583–596.

160 J. Yang, C. Tian, L. Wang and H. Fu, *J. Mater. Chem.*, 2011, **21**, 3384.

161 M. L. Toebes, J. A. van Dillen and K. P. de Jong, *J. Mol. Catal. A Chem.*, 2001, **173**, 75–98.

162 N. Dimitratos, A. Villa and L. Prati, *Catal. Letters*, 2009, **133**, 334–340.

163 Y. Li, H. Liu, L. Ma and D. He, *Appl. Catal. A Gen.*, 2016, **522**, 13–20.

164 T. Narita, H. Miura, M. Ohira, H. Hondou, K. Sugiyama, T. Matsuda and R. D. Gonzalez, *Appl. Catal.*, 1987, **32**, 185–190.

165 V. Ragaini, R. Carli, C. L. Bianchi, D. Lorenzetti and G. Vergani, *Appl. Catal. A Gen.*, 1996, **139**, 17–29.

166 C. Mitchell, U. Terranova, I. AlShibane, D. J. Morgan, T. Davies, Q. He, J. Hargreaves, M. Sankar and N. H. De Leeuw, *New J. Chem.*, 2019, **43**, 13985–13997.

167 D. J. Moon and J. W. Ryu, *Catal. Letters*, 2004, **92**, 17–24.

168 D. J. Morgan, *Surf. Interface Anal.*, 2015, **47**, 1072–1079.

169 J. Zhang, K. Gao, S. Wang, W. Li and Y. Han, *RSC Adv.*, 2017, **7**, 6447–6456.

170 M. M. T. Khan, S. B. Halligudi and S. Shukla, *J. Mol. Catal.*, 1989, **57**, 47–60.

171 E. T. Liakakou and E. Heracleous, *Catal. Rev. Eng.*, 2016, **6**, 1106–1119.

172 A. Griboval-Constant, J.-M. Giraudon, G. Leclercq and L. Leclercq, *Appl. Catal. A Gen.*, 2004, **260**, 35–45.

173 M. Xiang and J. Zou, *J. Catal.*, 2013, **2013**, 1–5.

174 J. Baltrusaitis, B. Mendoza-Sanchez, V. Fernandez, R. Veenstra, N. Dukstiene, A.

Roberts and N. Fairley, *Appl. Surf. Sci.*, 2015, **326**, 151–161.

175 G. Wächtershäuser, *Syst. Appl. Microbiol.*, 1988, **10**, 207–210.

176 G. Macleod, C. McKeown, A. J. Hall and M. J. Russell, *Orig. Life Evol. Biosph.*, 1994, **24**, 19–41.

177 N. T. Arndt and E. G. Nisbet, *Annu. Rev. Earth Planet. Sci.*, 2012, **40**, 521–549.

178 M. J. Russell, *Science (80-.).*, 2003, 302, 580–581.

179 V. Sojo, B. Herschy, A. Whicher, E. Camprubí and N. Lane, *Astrobiology*, 2016, **16**, 181–197.

180 U. P. Apfel and W. Weigand, *Angew. Chemie - Int. Ed.*, 2011, **50**, 4262–4264.

181 K. A. Vincent, A. Parkin and F. A. Armstrong, *Chem. Rev.*, 2007, 107, 4366–4413.

182 E. Shock and P. Canovas, *Geofluids*, 2010, 161–192.

183 N. Lane, *Cold Spring Harb. Perspect. Biol.*, 2014, **6**, a015982.

184 C. Di Giovanni, W. A. Wang, S. Nowak, J. M. Grenèche, H. Lecoq, L. Mouton, M. Giraud and C. Tard, *ACS Catal.*, 2014, **4**, 681–687.

185 C. Di Giovanni, Ál. Reyes-Carmona, A. Coursier, S. Nowak, J. M. Greneche, H. Lecoq, L. Mouton, J. Rozière, D. Jones, J. Peron, M. Giraud and C. Tard, *ACS Catal.*, 2016, **6**, 2626–2631.

186 R. Miao, B. Dutta, S. Sahoo, J. He, W. Zhong, S. A. Cetegen, T. Jiang, S. P. Alpay and S. L. Suib, *J. Am. Chem. Soc.*, 2017, **139**, 13604–13607.

187 M. S. Faber, M. A. Lukowski, Q. Ding, N. S. Kaiser and S. Jin, *J. Phys. Chem. C*, 2014, **118**, 21347–21356.

188 D. Susac, L. Zhu, M. Teo, A. Sode, K. C. Wong, P. C. Wong, R. R. Parsons, D. Bizzotto, K. A. R. Mitchell and S. A. Campbell, *J. Phys. Chem. C*, 2007, **111**, 18715–18723.

189 H. Li, J. Liu, J. Li, Y. Hu, W. Wang, D. Yuan, Y. Wang, T. Yang, L. Li, H. Sun, S. Ren, X. Zhu, Q. Guo, X. Wen, Y. Li and B. Shen, 2017, **7**, 4805–4816.

190 T. A. Pecoraro and R. R. Chianelli, *J. Catal.*, 1981, **67**, 430–445.

191 R. Dasbach, G. Willeke and O. Blenk, *MRS Bull.*, 1993, **18**, 56–60.

192 Y. Yang, T. Chen, M. Sumona, B. Sen Gupta, Y. Sun, Z. Hu and X. Zhan, *Rev. Environ. Sci. Biotechnol.*, 2017, 16, 289–308.

193 K. Momma and F. Izumi, *J. Appl. Crystallogr.*, 2011, **44**, 1272–1276.

194 M. Tokonami, K. Nishiguchi and N. Morimoto, *Am. Mineral.*, 1972, **57**, 1066–1080.

195 B. J. Skinner, R. C. Erd and F. S. Grimaldi, 1964, **49**, 543–555.

196 P. Toulmin III and P. B. Barton Jr, *Geochim. Cosmochim. Acta*, 1964, **28**, 641–671.

197 N. Belzile, Y.-W. Chen, M.-F. Cai and Y. Li, *J. Geochemical Explor.*, 2004, **84**, 65–76.

198 U. Becker, A. W. Munz, A. R. Lennie, G. Thornton and D. J. Vaughan, *Surf. Sci.*, 1997, **389**, 66–87.

199 R. G. Arnold, *Can. Mineral.*, 1967, **9**, 31–50.

200 H. W. Nesbitt, A. G. Schaufuss, M. Scaini, G. M. Bancroft and R. Szargan, *Am. Mineral.*, 2001, **86**, 318–326.

201 L. Argueta-Figueroa, N. Torres-Gómez, R. García-Contreras, A. R. Vilchis-Nestor, O. Martínez-Alvarez, L. S. Acosta-Torres and M. C. Arenas-Arrocena, *Prog. Nat. Sci. Mater. Int.*, 2018, **28**, 447–455.

202 F. Gronvold and H. Haraldsen, *Acta Chem. Scand.*, 1952, **6**, 1452–1469.

203 J. D. Miller, J. Li, J. C. Davidtz and F. Vos, *Miner. Eng.*, 2005, **18**, 855–865.

204 H. F. Steger and L. E. Desjardins, *Chem. Geol.*, 1978, **23**, 225–237.

205 H. F. Steger, *Chem. Geol.*, 1982, **35**, 281–310.

206 M. P. Janzen, R. V. Nicholson and J. M. Scharer, *Geochim. Cosmochim. Acta*, 2000, **64**, 1511–1522.

207 A. N. Buckley and R. Woods, *Appl. Surf. Sci.*, 1985, **20**, 472–480.

208 A. R. Pratt, I. J. Muir and H. W. Nesbitt, *Geochim. Cosmochim. Acta*, 1994, **58**, 827–

841.

209 J. R. Mycroft, H. W. Nesbitt and A. R. Pratt, *Geochim. Cosmochim. Acta*, 1995, **59**, 721–733.

210 S. N. A. Zakaria, N. Hollingsworth, H. U. Islam, A. Roffey, D. Santos-Carballal, A. Roldan, W. Bras, G. Sankar, G. Hogarth, K. B. Holt and N. H. De Leeuw, *ACS Appl. Mater. Interfaces*, 2018, **10**, 32078–32085.

211 P. Chiriţă and J. D. Rimstidt, *Appl. Geochemistry*, 2014, **41**, 1–10.

212 R. A. Yund and H. T. Hall, *Econ. Geol.*, 1969, **64**, 420–423.

213 D. S. Lauretta, D. T. Kremser and B. Fegley, Jr., *Icarus*, 1996, **122**, 288–315.

214 A. Kontny, H. de Wall, T. G. Sharp and M. Posfai, *Am. Mineral.*, 2000, **85**, 1416–1427.

215 Y. El Mendili, A. Abdelouas, H. El Hajj and J.-F. Bardeau, *RSC Adv.*, 2013, **3**, 26343.

216 G. Genchev and A. Erbe, *J. Electrochem. Soc.*, 2016, **163**, 333–338.

217 A. N. Buckley and R. Woods, *Appl. Surf. Sci.*, 1985, **22**–**23**, 280–287.

218 Y. L. Mikhlin, Y. V. Tomashevich, G. L. Pashkov, A. V. Okotrub, I. P. Asanov and L. N. Mazalov, *Appl. Surf. Sci.*, 1998, **125**, 73–84.

219 C. Zhao, C. Zhang, S. Bhoyate, P. K. Kahol, N. Kostoglou, C. Mitterer, S. Hinder, M. Baker, G. Constantinides, K. Polychronopoulou, C. Rebholz and R. K. Gupta, *Catalysts*, 2019, **9**, 597.

220 J. R. Mycroft, W. Nesbitt and A. R. Pratt, *Geochemica Cosmochim. Acta*, 1994, **59**, 721–733.

221 Y. Mikhlin, Y. Tomashevich, S. Vorobyev, S. Saikova, A. Romanchenko and R. Félix, *Appl. Surf. Sci.*, 2016, **387**, 796–804.

222 R. Barker, I. Al Shaaili, R. A. De Motte, D. Burkle, T. Charpentier, S. M. Vargas and A. Neville, *Appl. Surf. Sci.*, 2019, **469**, 135–145.

223 J. Bruno, P. Wersin and W. Stumm, *Geochim. Cosmochim. Acta*, 1992, **56**, 1149–1155.

224 S. Piontek, K. junge Puring, D. Siegmund, M. Smialkowski, I. Sinev, D. Tetzlaff, B. Roldan Cuenya and U.-P. Apfel, *Chem. Sci.*, 2019, **10**, 1075–1081.

225 M. E. Pandelia, W. Nitschke, P. Infossi, M. T. Giudici-Orticoni, E. Bill and W. Lubitz, *Proc. Natl. Acad. Sci. U. S. A.*, 2011, **108**, 6097–6102.

226 L. Wang, D. Li, M. Koike, S. Koso, Y. Nakagawa, Y. Xu and K. Tomishige, *Appl. Catal. A Gen.*, 2011, **392**, 248–255.

227 T. Zhang, Z. Liu, Y. A. Zhu, Z. Liu, Z. Sui, K. Zhu and X. Zhou, *Appl. Catal. B Environ.*, 2020, **264**, 118497.

228 D. Pandey and G. Deo, *J. Mol. Catal. A Chem.*, 2014, **382**, 23–30.

229 L. R. Winter, E. Gomez, B. Yan, S. Yao and J. G. Chen, *Appl. Catal. B Environ.*, 2018, **224**, 442–450.

230 L. Gong, J. J. Chen and Y. Mu, *Phys. Chem. Chem. Phys.*, 2017, 19, 28344–28353.

231 J. Jiang, S. Lu, H. Gao, X. Zhang and H. Q. Yu, *Nano Energy*, 2016, **27**, 526–534.

232 J. Yu, G. Cheng and W. Luo, *J. Mater. Chem. A*, 2017, **5**, 15838–15844.

233 M. Chatti, A. M. Glushenkov, T. Gengenbach, G. P. Knowles, T. C. Mendes, A. V. Ellis, L. Spiccia, R. K. Hocking and A. N. Simonov, *Sustain. Energy Fuels*, 2018, **2**, 1561–1573.

234 P. Ganesan, A. Sivanantham and S. Shanmugam, *J. Mater. Chem. A*, 2016, **4**, 16394–16402.

235 B. Konkena, K. junge Puring, I. Sinev, S. Piontek, O. Khavryuchenko, J. P. Dürholt, R. Schmid, H. Tüysüz, M. Muhler, W. Schuhmann and U.-P. Apfel, *Nat. Commun.*, 2016, **7**, 12269.

236 Q. Fu, D. I. Foustoukos and W. E. Seyfried, *Geophys. Res. Lett.*, 2008, **35**, 0.

237 S. Posada-Pérez, D. Santos-Carballal, U. Terranova, A. Roldan, F. Illas and N. H. De Leeuw, *Phys. Chem. Chem. Phys.*, 2018, **20**, 20439–20446.

238 A. N. Buckley and R. Woods, *Surf. Interface Anal.*, 1991, **17**, 675–680.

239 W. H. Jørgensen, H. Toftlund and T. E. Warner, *Hydrometallurgy*, 2012, **115**–**116**, 98–103.

240 C. Tenailleau, A. Pring, B. Etschmann, J. Brugger, B. Grguric and A. Putnis, *Am. Mineral.*, 2006, **91**, 706–709.

241 D. J. Vaughan and J. R. Craig, *Am. Mineral.*, 1985, **70**, 1036–1043.

242 J. R. Craig, *Am. Mineral.*, 1971, **56**, 1303–1311.

243 F. Xia, J. Zhou, J. Brugger, Y. Ngothai, B. O'Neill, G. Chen and A. Pring, *Chem. Mater.*, 2008, **20**, 2809–2817.

244 J. G. Dunn and V. L. Howes, *Thermochim. Acta*, 1996, **282**–**283**, 305–316.

245 H. Zhu, J. Chen, J. Deng, R. Yu and X. Xing, *Metall. Mater. Trans. B Process Metall. Mater. Process. Sci.*, 2012, **43**, 494–502.

246 R. Karthikeyan, D. Thangaraju, N. Prakash and Y. Hayakawa, *CrystEngComm*, 2015, **17**, 5431–5439.

247 N. S. McIntyre, D. G. Zetaruk and D. Owen, *Appl. Surf. Sci.*, 1978, **2**, 55–73.

248 J. Charnock, C. D. Garner, R. A. D. Pattrick and D. J. Vaughan, *Am. Mineral.*, 1990, **75**, 247–255.

249 R. T. Wilkin and D. G. Beak, *Chem. Geol.*, 2017, **462**, 15–29.

250 D. J. Vaughan, R. G. Burns and V. M. Burns, *Geochim. Cosmochim. Acta*, 1971, **35**, 365–381.

251 D. L. Legrand, H. Wayne Nesbitt and G. M. Bancroft, *Am. Mineral.*, 1998, **83**, 1256–1265.

252 Y. Chen, S. Choi and L. T. Thompson, *J. Catal.*, 2016, **343**, 147–156.

253 Q. Z. Zhai, T. S. Jiang, W. H. Hu, X. Guan, W. Wang and S. Qiu, *Mater. Res. Bull.*, 2002, **37**, 1837–1842.

254 A. Nezamzadeh-Ejhieh and S. Moeinirad, *Desalination*, 2011, **273**, 248–257.

255 S. Sohrabnezhad, A. Pourahmad, M. S. Sadjadi and M. A. Zanjanchi, *Mater. Sci. Eng.*

C, 2008, **28**, 202–205.

256 S. Sohrabnezhad, A. Pourahmad, M. S. Sadjadi and B. Sadeghi, *Phys. E Low-Dimensional Syst. Nanostructures*, 2008, **40**, 684–688.

257 M. J. Russell, *Acta Biotheor.*, 2007, **55**, 133–179.

258 X. Ma, W. Zhang, Y. Deng, C. Zhong, W. Hu and X. Han, *Nanoscale*, 2018, **10**, 4816–4824.

259 J. G. Dunn, W. Gong and D. Shi, *Thermochim. Acta*, 1992, **208**, 293–303.